The Jahn-Teller Effect in Magneto-optical Spectroscopy of Axial Radicals

A thesis submitted in partial fulfilment of the
requirement for the degree of

Doctor of Philosophy in Chemistry

at the
University of Canterbury

by
Kirsten Clare Lake Taylor
2000

CONTENTS

LIST OF FIGURES ..... **IX**

LIST OF TABLES ..... **XIII**

ABSTRACT ..... **XV**

ACKNOWLEDGMENTS ..... **XVII**

GLOSSARY OF ACRONYMS ..... **XIX**

1 INTRODUCTION **1**

1.1 VIBRONIC COUPLING AND THE JAHN-TELLER EFFECT 1

1.2 SPECTROSCOPY 3

1.3 THESIS LAYOUT 5

1.4 REFERENCES 7

2 SYMMETRY AND QUANTUM MECHANICS OF AXIAL MOLECULES 9

2.1 GROUP THEORY 9

2.1.1 Definitions *9*

2.1.2 Categories of Irreps *15*

2.1.3 The Axial Groups *17*

2.2 QUANTUM-MECHANICAL APPLICATIONS OF GROUP THEORY 20

2.2.1 Equivalence of Rotational Symmetry and Angular Momentum *23*

2.2.2 Equivalence of Rotational Symmetry and Angular Momentum in Axial Groups *26*

2.2.3 Quantum Mechanical Operators and Group Theory *29*

2.2.4 Coupling Coefficients and Their Applications *32*

2.3 REFERENCES 35

3 ELECTRONIC AND VIBRATIONAL WAVEFUNCTIONS AND MATRIX ELEMENTS OF AXIAL MOLECULES **37**

3.1 VIBRONIC COUPLING 37

3.1.1 Nuclear Coordinates *37*

3.1.2 Vibronic Hamiltonian *38*

3.1.3 The Born-Oppenheimer Approximation 39
3.2 ELECTRONIC STATES 41
3.2.1 Nuclear-coordinate Dependence of Electronic Wavefunctions 41
3.2.2 Many-electron Wavefunctions 43
3.3 ELECTRONIC MATRIX ELEMENTS 49
3.3.1 Reduction to One-electron Form 49
3.3.2 Electronic Angular Momenta 50
3.3.3 Spin-orbit Coupling 55
3.3.4 The Zeeman Effect 57
3.3.5 Electronic Transition Moments 59
3.4 VIBRATIONAL STATES 62
3.4.1 Non-degenerate Vibrations 63
3.4.2 Doubly Degenerate Vibrations 65
3.5 VIBRATIONAL MATRIX ELEMENTS 70
3.5.1 Non-degenerate Vibrations 70
3.5.2 Doubly Degenerate Vibrations 71
3.6 VIBRONIC BASIS FUNCTIONS IN THE BORN-OPPENHEIMER APPROXIMATION 72
3.7 REFERENCES 73

4 MAGNETO-OPTICAL SPECTROSCOPY 75

4.1 THE ORIGIN OF MCD 75
4.2 THE ABSORPTION COEFFICIENT 76
4.3 ABSORPTION AND MCD 81
4.4 MCD MAGNETIC-FIELD AND TEMPERATURE DEPENDENCE 82
4.4.1 Faraday Terms and Parameters 84
4.4.2 Extraction of Molecular Parameters from Experimental Data 87
4.5 MOLECULE FIXED OPERATORS AND ORIENTATIONAL AVERAGING 89
4.6 SATURATION OF $\mathcal{C}$ TERMS 92
4.7 REFERENCES 94

5 THE JAHN-TELLER EFFECT 95

5.1 INTRODUCTION 95
5.1.1 Breakdown of the Born-Oppenhiemer Approximation 95
5.1.2 The Vibronic (Dynamic) Jahn-Teller Problem 96

5.1.3 The Electronic (Static) Jahn-Teller *98*
5.2 E ⊗ E JAHN-TELLER COUPLING 99
5.2.1 The Electronic (Static) Jahn-Teller Effect *100*
5.2.2 The Vibronic Jahn-Teller Effect *111*
5.3 ZEEMAN MATRIX ELEMENTS 123
5.3.1 g Values *125*
5.4 LOW-TEMPERATURE SPECTROSCOPY 126
5.4.1 Non-zero Transition Moments from the Ground State *127*
5.4.2 Absence of a Ground-State Jahn-Teller Effect *131*
5.4.3 Absorption and MCD Moments over all Bands *131*
5.5 SPECTRAL SIMULATION PROGRAMME: DYNAMO 133
5.6 REFERENCES 137

6 EXPERIMENTAL APPARATUS AND PROCEDURES 139

6.1 THE SPECTROMETER: MOD4 139
6.1.1 Optical Layout *141*
6.1.2 Circular Polarisation Modulation *143*
6.1.3 The Detector *144*
6.1.4 Signal Processing *144*
6.2 MATRIX-ISOLATION/CRYOMAGNET SYSTEMS 148
6.2.1 Deposition Windows *148*
6.2.2 Helium Refrigerator/Electromagnet System *148*
6.2.3 SM4/Matrix Injection System *151*
6.3 SAMPLE PREPARATION: ISOLATION OF RADICALS IN ARGON MATRICES . 160
6.4 SOLUTION SPECTRA 165
6.5 REFERENCES 167

7 THE FERRICENIUM RADICAL CATION 169

7.1 INTRODUCTION 169
7.1.1 The Ground States of Ferrocene and Ferricenium *170*
7.1.2 The Red Transition of the Ferricenium Radical *176*
7.1.3 Assignment of Structure in the Absorption Spectrum *177*
7.1.4 MCD Studies *179*
7.1.5 The Jahn-Teller Effect in Ferricenium *179*
7.2 RESULTS 180

7.2.1 Matrix-isolation Data *180*
7.2.2 Solution Data *185*
7.3 THEORETICAL ASPECTS OF DATA ANALYSIS 187
7.3.1 Molecular Orbitals and Orbital Angular Momenta *188*
7.3.2 Electronic States of Ferricenium *194*
7.3.3 Crystal-field Effects *196*
7.3.4 Jahn-Teller Effects *205*
7.4 DISCUSSION 206
7.4.1 The Importance of Ground-state Crystal-field Effects in $Fe(cp)_2^+/Ar$ *206*
7.4.2 Analysis of Vibrational Structure *208*
7.4.3 The Ground State of Ferricenium *213*
7.4.4 Solution Spectra *216*
7.5 CONCLUSIONS 217
7.6 REFERENCES 220

8 THE CYCLOOCTATETRAENE RADICAL MONOANION 223

8.1 INTRODUCTION 223
8.1.1 The Geometry of COT *223*
8.1.2 Electronic States and Transitions *226*
8.1.3 MCD Studies *228*
8.1.4 Vibronic Structure in the $^2E_{1g} \leftarrow {}^2E_{2u}$ *Transition* *229*
8.2 DISCUSSION 231
8.2.1 A Ground-state Jahn-Teller Effect? *231*
8.2.2 An Alternative Explanation – Herzberg-Teller Coupling *235*
8.2.3 An Excited-state Jahn-Teller Effect? *238*
8.2.4 Reduction of Ground State Orbital Angular Momentum *239*
8.3 CONCLUSION 240
8.4 REFERENCES 242

9 CYCLOPENTADIENYL 243

9.1 INTRODUCTION 243
9.1.1 The Cyclopentadienyl Radical *243*
9.2 RESULTS 247
9.3 DISCUSSION AND CONCLUSION 250
9.4 REFERENCES 252

10 SUMMARY 253

10.1 NOTE 255

10.2 REFERENCES 256

A GROUP THEORETICAL RESULTS FOR SO_3 257

A.1 IRREPS OF SO_3 257

A.2 DIRECT-PRODUCT IRREPS 259

A.3 2JMS AND SOME USEFUL 3JMS IN $SO_3 \supset C_\infty$ 260

A.4 RAISING AND LOWERING OPERATORS 261

A.5 REFERENCES 262

B COMPLETENESS, CLOSURE AND SPECTROSCOPIC STABILITY .. 263

C GROUP THEORETICAL RESULTS FOR D_∞ 265

C.1 2JMS FOR $D_\infty \supset C_\infty$ 265

C.2 3JMS FOR $D_\infty \supset C_\infty$ 265

D GROUP THEORETICAL RESULTS FOR D_5 267

D.1 $D_5 \supset C_5$ 2JMS 267

D.2 $D_5 \supset C_5$ 3JMS 267

E GROUP THEORETICAL RESULTS FOR D_8 269

E.1 $D_8 \supset C_8$ 2JMS 269

E.2 $D_8 \supset C_8$ 3JMS 269

LIST OF FIGURES

Figure 2.1: Subduction schemes for the axial rotational groups.....18

Figure 2.2: Clock representation of the irreps and partners for the $\mathbf{D}_n \supset \mathbf{C}_n$ chain. ...20

Figure 3.1: A view (looking down the z axis) of the relationship between the coordinate systems based on centres o and a in the same x-y plane.....53

Figure 3.2: Two-centre angular momentum about o due to motion of the electron in the plane of the molecule. 53

Figure 3.3: Energy-level diagram for a $^2E_\lambda$ term derived from an e_λ^1 configuration, with a magnetic field at an angle θ with respect to the z axis. 57

Figure 3.4: Top: instantaneous displacements of a pair of orthogonal degenerate bending modes, Q_1 and Q_2, of CO_2. Bottom: the motion represented by the linear combination, Q_+, of Q_1 and Q_2. 66

Figure 4.1: A positive $\mathcal{C}$ term due to excited-state degeneracy. 85

Figure 4.2: MCD terms arising from ground-state degeneracy. 86

Figure 4.3: An axial molecule of a general orientation with respect to the magnet field. 89

Figure 4.4: The Euler angle convention: (a) rotation by ϕ about Z; (b) by θ about ξ, and, (c) by ψ about ζ'.....90

Figure 5.1: A section through the electronic potential energy surfaces for a linear electronic E $\otimes$ e Jahn-Teller effect.....104

Figure 5.2: The electronic potential energy surfaces of a doubly degenerate electronic state as a function of coordinates Q_1 and Q_2.....105

Figure 5.3: A section through the potential surfaces for a linear E $\otimes$ e Jahn-Teller effect after inclusion of spin-orbit coupling.....106

Figure 5.4: A section through the potential surfaces for a quadratic electronic E $\otimes$ e Jahn-Teller effect.....107

Figure 5.5: A section through the potential surfaces for a quadratic E $\otimes$ e Jahn-Teller effect after inclusion of spin-orbit coupling.....109

Figure 5.6: A branch diagram for a linear ($_n$ =1) JT effect for K_1 values between –9/2 and 9/2.....115

Figure 5.7: The eigenvalues for LJT coupling as a function of the dimensionless parameter λ_{JT}, in the absence of SO coupling. 117

Figure 5.8: A branch diagram for an E ⊗ e quadratic ($_n$ =2) Jahn-Teller effect for K_2 values between 0 and 4. 119

Figure 5.9: The eigenvalues for QJT coupling as a function of the dimensionless parameter ϵ_{JT}, in the absence of SO coupling. 121

Figure 5.10: The top two diagrams are respectively absorption and MCD with a linear JT effect in the ground state. 136

Figure 6.1: A signal frequency bandwidth centred at 50 kHz is well removed from most deterministic noise and in a region where flicker noise is insignificant. ..141

Figure 6.2: A schematic diagram of the MOD4 spectrometer with the electromagnet in position. 142

Figure 6.3: Principles of using the PEM 143

Figure 6.4: A schematic diagram of a LIA. 145

Figure 6.5: A schematic diagram showing the mixing that occurs in the PSD 146

Figure 6.6: The electromagnet as used with the helium refrigerator. 149

Figure 6.7: Simplified diagram of the Displex DE-202 expander and vacuum shroud, showing detail of the sample window. 150

Figure 6.8: An overview of the matrix injection system. 153

Figure 6.9: Simplified cross-section of the Spectromag SM4 cryomagnet....154

Figure 6.10: Detail of and around the VTI and needle valve of the SM4 155

Figure 6.11: The top diagram is a schematic of a spilt-pair magnet. 156

Figure 6.12: Schematic cross-section of the matrix-deposition chamber and detail of the sample window and its cooling system. 157

Figure 6.13: Detail of the automated solenoid valve used to control the temperature in the VTI above 4.2 K. 159

Figure 6.14: The circles indicate host molecules while the five-sided figures are the guest species. *a* shows the ideal situation. 161

Figure 6.15: Matrix deposition apparatus. 164

Figure 6.16: Cross section of the continuous-flow cryostat. 165

Figure 7.1: The d-π section of a qualitative MO diagram for the metallocenes assuming $\mathbf{D}_{5d}$ symmetry. 171

Figure 7.2: Spectra for the $^2E_{1u} \leftarrow {}^2E_{1g}$ transition of $Fe(cp)_2^+/Ar$ (with CCl_4 as the electron trap) obtained using the He refrigerator/electromagnet system. 181

Figure 7.3: Absorption spectra for the $^2E_{1u} \leftarrow {}^2E_{1g}$ transition of $Fe(cp)_2^+/Ar$ (with CCl_4 as the electron trap) obtained using the He refrigerator/electromagnet system at $T \approx 16$ K. 182

Figure 7.4: Spectra for the $^2E_{1u} \leftarrow {}^2E_{1g}$ transition of $Fe(cp)_2^+/Ar$ (with CCl_4 as the electron trap) obtained using the SM4/matrix-injection system. 183

Figure 7.5: $\mathbf{M}_0$ for the $^2E_{1u} \leftarrow {}^2E_{1g}$ transition of $Fe(cp)_2^+/Ar$, obtained using the SM4/matrix-injection system, as a function of $\mu_B B$ at various temperatures. . .184

Figure 7.6: $\mathbf{M}_0$ for the $^2E_{1u} \leftarrow {}^2E_{1g}$ transition of $Fe(cp)_2^+/Ar$, obtained using the SM4/matrix-injection system, as a function of $\mu_B B/kT$ for all temperatures. 184

Figure 7.7: Spectra for the $^2E_{1u} \leftarrow {}^2E_{1g}$ transition of $Fe(cp)_2BF_4$ in CH_2Cl_2 solution obtained using the CF1204/electromagnet system at various temperatures. 185

Figure 7.8: Absorption spectra for the $^2E_{1u} \leftarrow {}^2E_{1g}$ transition of $Fe(cp)_2BF_4$ in CH_2Cl_2 solution obtained using the CF1204/electromagnet system at various temperatures.. 186

Figure 7.9: $\mathbf{M}_0/\mathbf{A}_0$ for the $^2E_{1u} \leftarrow {}^2E_{1g}$ transition of $Fe(cp)_2BF_4$ in CH_2Cl_2 solution (three samples) obtained using the CF1204/electromagnet system as a function of $\mu_B B/kT$. 187

Figure 7.10: Molecular coordinate system and qualitative MO energy-level diagram for cyclopentadienyl ($\mathbf{D}_{5h}$ symmetry). 189

Figure 7.11: Molecular and ring-fixed coordinates for biscyclopentadiene. 191

Figure 7.12: Energy level diagram for the SO-CF states of the ground $^2E_{2g}$ ground-state term of $Fe(cp)_2^+$ when the magnetic field is on and off. 198

Figure 7.13: Comparison of an experimental spectrum of $Fe(cp)_2^+/Ar$ obtained at 15 K and 0.6 T with the 'best-fit' spectrum calculated using computer program DYNAMO. 209

Figure 7.14: Graphical representations of equations (7.21) (an ellipse with the principal axis at 45° to the c_d and c_π axes) and (7.27) (a pair of hyperbolas) for the parameters $l_\pi = 0.4$, $\kappa_{cov} = 0.92$ and $S_{e_{2g}} = 0.079$. 213

Figure 7.15: Plots of κ_{JT} as a function of κ_{cov}. 215

Figure 8.1: Some vibrational modes and calculated frequencies for COT^-. Symmetries are given for $\mathbf{D}_{8h}$, with reference coordinates defined in the diagram for the a_{1g} C-C stretching mode. 226

Figure 8.2: Energy level diagram for the π orbitals of COT^- showing the ground-state occupancy and the two lowest-energy orbital excitations. 227

Figure 8.3: Absorption and MCD spectra of COT^-/Ar. 228

Figure 8.4: The dependence of the experimental $\mathbf{M}_0/\mathbf{A}_0$ data for COT^-/Ar on $\mu_B B/kT$. The line is the best linear fit to the data. 229

Figure 8.5: The MCD spectra of the $^2E_{1g} \leftarrow {}^2E_{2u}$ transition of COT^-/Ar. 232

Figure 8.6: The MCD spectra of the $^2E_{1g} \leftarrow {}^2E_{2u}$ transition of COT^-/Ar. 233

Figure 8.7: The MCD spectra of the $^2E_{1g} \leftarrow {}^2E_{2u}$ transition of COT^-/Ar. 238

Figure 9.1: Spectra, prior to baselining, of $C_5H_5^{\bullet}$/Ar obtained on the He refrigerator/electromagnet system at ~12 K and 0.6 T 247

Figure 9.2: Spectra of $C_5H_5^{\bullet}$/Ar obtained at 1 T and the indicated temperatures by using the SM4/matrix-injection system. 248

Figure 9.3: First MCD moments for $C_5H_5^{\bullet}$/Ar plotted as a function of $\mu_B B$ at the indicated temperatures. 249

Figure 9.4: First MCD moments for $C_5H_5^{\bullet}$/Ar plotted as a function of $\mu_B B/kT$. 249

Figure 9.5: Spin-orbit and Zeeman splittings for the $^2A_2''$ and $^2E_1''$ states of $C_5H_5^{\bullet}$. Transitions are indicated with solid lines for left circular polarisation and the dashed lines for right circular polarisation. 251

LIST OF TABLES

Table 2.1: The Mulliken and Butler irrep labelling schemes for axial groups.....19

Table 2.2: Rules for transforming $\mathbf{D}_\infty \supset \mathbf{C}_\infty \rightarrow \mathbf{D}_n \supset \mathbf{C}_n$ using Butler notation.....19

Table 2.3: Direct-product table for irreps of the point groups $\mathbf{D}_n$ and $\mathbf{C}_{nv}$.....21

Table 2.4: Transformation properties of vectors (T) and pseudo vectors (R).....31

Table 3.1: One-electron wavefunctions for a doubly degenerate e_λ orbital.....44

Table 3.2: Two-electron orbital (top) and spin (bottom) wavefunctions for an e_λ^2 configuration.....45

Table 3.3: Anti-symmetrised two-electron spin-orbit wavefunctions for e_λ^2 configuration.....46

Table 3.4: Non-antisymmetrised wavefunctions for a λ^3 configuration.....47

Table 3.5: Anti-symmetrised three-electron spin-orbit wavefunctions for λ^3 configuration.....48

Table 3.6: Transformation properties of the vibrational states $|v, \ell\rangle$ in the $|j\ m\rangle$ basis of $\mathbf{D}_\infty \supset \mathbf{C}_\infty$, $v \leq 5$.....69

Table 3.7: Matrix elements of one-dimensional harmonic oscillator.....71

Table 3.8: Matrix elements for a two-dimensional harmonic oscillator in the $|v, \ell\rangle$ representation.....72

Table 5.1: Allowed quantum numbers for the L_{K_1} branch of an E $\otimes$ e linear Jahn-Teller effect;.....115

Table 5.2: The top left-hand corner of the SO-LJT matrix for the $L^{\Sigma}_{\pm|K_1|}$ branches ...116

Table 5.3: Allowed quantum numbers for the Q_0 ($K_2 = 0$) branch of an E $\otimes$ e quadratic Jahn-Teller effect; $m_2 = 1$.....119

Table 5.4: The top left-hand corner of the QJT-SO matrix for the branch $Q^{\Sigma}_{\pm 0}$.....120

Table 5.5: Allowed quantum number for the Q_{K_2} branch with $|K_2| > 0$ of an E $\otimes$ e quadratic Jahn-Teller effect; $m_2 = |K_2| - 1$.....122

Table 5.6: The top left hand corner of the SO-QJT matrix for the branch $Q^{\Sigma}_{K_2 \neq 0}$.....123

Table 5.7: Non-zero transition moments from the ground state for an axial molecule subject to E ⊗ e JT effect and with molecule with its *z* direction oriented along the laboratory *Z* axis ($\theta = 0$).....128

Table 5.8: Orientationally averaged zeroth absorption and MCD moments, in the linear limit, for individual vibronic transitions within an E⊗e ← E⊗e manifold of an axial molecule.....130

Table 5.9: Orientationally averaged zeroth absorption and MCD moments, in the linear limit, for individual vibronic transitions, E ⊗ e ← E (no ground-state JT effect), of an axial molecule.....131

Table 6.1: Instrumental specifications for the MOD4 spectrometer.....140

Table 6.2: LIA setting used in this work on the Stanford Research Systems Model SR510.....146

Table 7.1: Experimental ESR parameters of ferricenium derivatives. δ is the splitting due to a static low-symmetry effect.....174

Table 7.2: Excited-state frequencies (cm^{-1}), from optical spectroscopy, for various ferricenium salts.....178

Table 7.3: Anti-symmetrised three-electron spin-orbit wavefunctions for e_{2g}^3 and e_{1u}^3 configurations.....195

Table 7.4: The zeroth-order transition-moment matrix-elements between states comprising the $^2E_{1u}$ and $^2E_{2g}$ terms of $Fe(cp)_2^+$.....203

Table 7.5: The first-order transition-moment matrix-elements between states comprising the $^2E_{1u}$ and $^2E_{2g}$ terms of $Fe(cp)_2^+$.....203

Table 7.6: Vibrational frequencies (cm^{-1}) of ferrocene.....210

Table 7.7: Vibrational assignment for the vibronic bands observed in the $^2E_{1u} \leftarrow {}^2E_{2g}$ LMCT transition of $Fe(cp)_2^+/Ar$.....210

Table 8.1: Vibrational frequencies (cm^{-1}), symmetries and assignments for COT^-..225

Table 9.1: Symmetry species of vibrational modes for $C_5H_5^-$ ($\mathbf{D}_{5h}$ symmetry) from $K^+[C_5H_5^-]$ data unless otherwise stated.....245

Table 9.2: Vibrational modes attributed responsibility for JT effects in the $^2E_1''$ ground state of C_5H_5.....246

ABSTRACT

A model has been developed to describe the effects of the Jahn-Teller (JT) effect on the magnetic circular dichroism (MCD) and absorption spectra of axial molecules. It treats spin-orbit and Jahn-Teller coupling on equal footing and, in terms of the latter, allows for both first- (linear) and second-order (quadratic) coupling in both ground and excited states.

Three axial radicals, trapped in solid Ar matrices, were chosen to test the utility of the model. The ferricenium radical cation, $Fe(cp)_2^+$, and the cylcopentadienyl radical, $C_5H_5^{\cdot}$, were generated by photoionisation/photolysis involving a microwave discharge in Ar, then trapped in solid Ar. Their MCD and absorption spectra were then collected on a simultaneous MCD/double-beam absorption spectrometer, MOD4, between temperatures 1.6 and 13 K and magnetic fields of 0 – 5T. The MCD and absorption spectra for the third matrix-isolated radical, the cycloactatetrene radical anion in Ar, COT^-/Ar, were taken from the literature.

The data collected for $C_5H_5^{\cdot}$/Ar were insufficient to allow a useful analysis. The spectra of, $Fe(cp)_2^+$/Ar and COT^-/Ar, on the other hand, show extensive vibrational structure. Quantitative discussion is presented for these two species. JT effects are identified and characterised in the ground ($^2E_{2g}$) and excited ($^2E_{1u}$) states of $Fe(cp)_2^+$, and in the excited ($^2E_{1g}$) state of COT^-. Herzberg-Teller coupling is found to play an important role in the $^2E_{1g} \leftarrow {}^2E_{2u}$ transition of COT^-.

ACKNOWLEDGEMENTS

I would like to thank my supervisor Dr Bryce Williamson without whom I would never have realised my goal of completing a Ph.D. in Chemistry.

I would also like to thank a number of people who have made completing my Ph.D. an easier and more enjoyable experience – Drs Rod Claridge, Craig Tennant, Charles Walsby, Barry Prince, Claire Vallance, Sunny Hu, Brett Cameron, Vaughan Langford and Cara Dunford.

I would also like to thank my parents Irene Lake and Roger Taylor and my partner Matt.

GLOSSARY OF ACRONYMS

AO	atomic orbital
Ar	argon
BO	Born-Oppenhiemer
CD	circular dichroism
CF	crystal field
CF1204	Oxford Instruments continuous-flow cryostat
CFP	coefficients of fractional parentage
CGC	Clebsch-Gordan coefficients
COT^-	cyclooctatetraene mononegative ion
cp	cyclopentadienyl
CSF	configuration state functions
2-MTDF	2-methlytetrhydrofuran
EPR	electron paramagnetic resonance
ESR	electron spin resonance
FC	Frank-Condon
$Fe(cp)_2^+$	ferricenium radical cation
GOT	great orthogonality theorem
HO	harmonic oscillator
HOMO	highest occupied molecular orbital
HSCC	high-symmetry coupling coefficient
HT	Herzberg-Teller
JT	Jahn-Teller
lcp	left circularly polarised
ℓHe	liquid helium
LIA	lock-in amplifier
LOT	little orthogonality theorem
LJT	linear Jahn-Teller
LUMO	lowest unoccupied molecular orbital
MCD	magnetic circular dichroism
MI	matrix isolation
MO	molecular orbital
PEM	photoelectric modulator
QJT	quadratic Jahn-Teller
rcp	right circularly polarised
SO	spin-orbit
SOC	spin-orbit coupling
WET	Wigner-Eckart theorem

1 INTRODUCTION

The main aim of this thesis is to develop methods for determining the nature and magnitude of Jahn-Teller (JT) effects from magnetic circular dichroism (MCD) spectroscopic data. This is achieved by comparison of spectral simulations and theoretical spectroscopic moment expressions with experimental data. The experimental work concerns radicals that have a unique rotation axis of order greater than two, a symmetry condition that is described by saying that the molecules are 'axial'. While the theoretical treatment is not restricted radicals, it is restricted to axial molecules.

The genesis of this research was extensive work on the MCD of metalloporphyrins and their derivatives.[1-5] An excited-state JT effect was invoked to explain the existence of vibrational side bands in the envelopes of E ← A electronic transitions, which have $\mathscr{A}$-term-like dispersion of the opposite sign to that of the origin band. Given the similarity of the expressions for MCD $\mathscr{A}$ and $\mathscr{C}$ terms, our first thought for explaining the existence of oppositely signed $\mathscr{C}$ terms in the spectra presented in the second part of the thesis was an *excited*-state JT effect. In fact, Samet *et al.*[6] interpreted the MCD and absorption spectra of the cyclooctatetrene mononegative radical in exactly these terms. The results of this thesis show that such an interpretation is untenable and that alternating $\mathscr{C}$ terms can only be due to a JT effect if it occurs in the *ground* state. In retrospect, it was unreasonable to have anticipated that an excited state effect could change the sign of a $\mathscr{C}$ term.

This thesis divides naturally into two parts. The first concerns the theoretical aspects of the work. In the second, experimental data and their interpretation are considered for three molecular systems. Introductions are presented at the beginning of each chapter. This general introduction comprises a concise overview of the nature and layout of the thesis.

1.1 Vibronic Coupling and the Jahn-Teller Effect

Vibronic coupling arises from the interaction of nuclear (vibrational) and electronic motion in molecules. Manifestations such couplings including 'unusual' vibrational

structure in electronic spectra,[6-12] reduction of electronic orbital angular momentum and quenching of spin-orbit coupling.[13]

Vibronic mechanisms can generally be classified into four categories. The JT effect occurs in the case of degenerate electronic states of non-linear molecules.[14-19] For linear polyatomics (more than two atoms), there can be no first-order JT effect, but second- or higher-order vibronic couplings, collectively referred to as the Renner-Teller effect[19] can lower any electronic degeneracies. If the electronic degeneracy is 'weakly' removed by an external perturbation of the system, a pseudo-JT effect will ensue.[7,20] And finally, coupling between well-separated mutually non-degenerate electronic states is called the Herzberg-Teller (HT) effect.[5,20]

The most important type of vibronic coupling with regard to this thesis is JT coupling. In 1937, Jahn and Teller[14,15] showed that high-symmetry configurations of nuclear positions in which the (orbital) electronic state of a molecule is degenerate will generally be unstable with respect to displacements along certain asymmetric vibrational coordinates. The exceptions are cases in which the high-symmetry configuration corresponds to all nuclei lying on a straight line (such molecules with more than two atoms are susceptible to Renner-Teller coupling) or when the degeneracy is of a special two-fold kind, due to electronic spin, discussed by Kramer in 1930.[22]

In this thesis, the term *Jahn-Teller effect* is taken to encompass first- and second-order vibronic couplings between the states of an otherwise degenerate manifold of states in non-linear polyatomic molecules. The two types of coupling are distinguished by referring to them as quadratic (QJT) and linear Jahn-Teller (LJT) effects. Rules are presented to determine whether either or both of these effects can occur in a particular state of a given axial molecule.

The first examinations of the spectroscopic consequences of JT coupling in axial molecules were made in the 1950s.[20,23,24] In a series of three papers the physical theory required for interpreting the vibrational and vibronic (vibrational-electronic) absorption and emission spectra of axial molecules with orbitally degenerate states was developed. The most significant of these with regard to this thesis is the second paper[23] – *Studies of the Jahn-Teller effect II. The Dynamical Problem*, published in 1957 in *The Proceedings of the Royal Society A.* – where the authors considered vibronic transitions of the type $E \otimes e \leftrightarrow A$, entailing first-order vibronic coupling of a

degenerate electronic (E) state with a degenerate JT-active (e) mode. Although the authors did not consider spin-orbit or Zeeman interactions (which are of consequence to the work presented here) this paper forms the starting point for the theoretical work in this thesis – many concepts and notations are taken from it.

More recently, calculations have been performed concerning the effects of JT coupling on the magneto-optical spectra of molecules with axial ($\mathbf{D}_{4h}$) symmetry, namely the metalloporphyrins and their derivatives (see Chapter 5 of reference 1 and references therein). However, these calculations suffer from lack of generality.

In this thesis, the JT effect in axial molecules is treated in a general way, by considering E ⊗ e coupling of a hypothetical molecule belonging to the point group $\mathbf{D}_{\infty}$. Earlier this year, Bosnick used operator methods to determine the Hamiltonian matrix elements and eigenvalue spectra for such a problem.[25] While the treatment in this thesis is similar in some respects, it goes very much further. The consequences of simultaneous spin-orbit and JT interactions are considered and the calculations are generalised to allow for ground and/or excited state phenomena. The theoretical section explicitly considers transitions of the type ^{2}E ⊗ e ↔ ^{2}E ⊗ e, but the results are readily adapted to the cases of ^{2}E ⊗ e ↔ ^{2}A/^{2}B or singlet spin systems. The analysis covers JT effects of first and second order (LJT and QJT), but the nomenclature and parameterisation are extendable to any arbitrary higher order of coupling.[i] To deal with real molecules, the methods required for subduction to subgroups of $\mathbf{D}_{\infty}$ are also presented.

1.2 Spectroscopy

The principal experimental techniques of this thesis are matrix isolation (MI) in combination with MCD and absorption spectroscopy.

MI is a technique by which reactive species, including radicals, are trapped in an inert medium, commonly a noble gas, to allow spectroscopic investigations to be performed. In this work, solid argon matrices are used. Even if other solvents could have been employed, MI often leads to simpler spectra by reducing intermolecular

[i] The JT coupling is assumed to be small, and may not be appropriate for systems where the coupling is very large.

interactions. Furthermore, the low-temperatures required to produce rigid matrices also considerable simplify the resulting spectra by ensuring that the molecules are in their lowest electronic and vibrational states (hot bands are eliminated), and the bands will consequently tend to be sharper.

MCD is a longitudinal Zeeman technique that measures the differential absorption of left (*lcp*) and right circularly polarised (*rcp*) light propagating through a sample in the same direction as an externally applied static magnetic field. It provides simultaneous information about the ground and excited electronic-state manifolds of the species under investigation and confers several advantages over more conventional unpolarised or linearly polarised absorption techniques. Whereas the information from the latter is limited to intensities and transition energies (sometimes including vibrational frequencies), MCD provides signed quantities against which assignments can be checked, and gives direct information about the angular momentum (magnetic properties) of the states under investigation. Furthermore, by combining careful experimental studies of magnetic-field and temperature dependencies with an appropriate theoretical formalism, MCD also provides information about spin-orbit (SO), vibronic and crystal-field (CF) effects. In comparison with 'ground-state' techniques such as EPR, the ground-state parameters so obtained are not highly precise. However, MCD can be used to obtain ground-state information for EPR-silent paramagnetic systems such as occurs for ^{2}E systems in the absence of crystal fields.

The interpretation of MCD involves the development of expressions for the electronic Zeeman effect and transition moments, including the influence of the interactions (SO, CF, vibronic *etc.*) of interest. The general principles are covered extensively by Piepho and Schatz in their book *Group Theory in Spectroscopy: With Applications to Magnetic Circular Dichoism.*[26] The expressions presented here are quite general with respect to temperature and the magnetic field strength, in the sense that the so-called linear limit is avoided. However, the linear-limit terminology – $\mathcal{A}$ $\mathcal{B}$ and $\mathcal{C}$ terms, introduced by Stephens and Buckingham[27] – still provide a useful way to describe the MCD

MCD can be used to study JT effects because they involve orbitally degenerate electronic states that carry an orbital magnetic moment. Effects that lead to the reduction of the orbital angular momentum (and SO interactions) of, for example, a

metal-ion complex are well known, and contribute to a so-called orbital-reduction factor. Initially it was considered that orbital reduction was a direct result of delocalisation of the electronic wavefunction because of covalent bonding and the orbital reduction factor was taken as a measure of the importance of covalency. However as was first shown by Ham in 1965,[13] the JT effect may also make an important contribution. In one of the systems considered in this thesis (the ferricenium radical cation), the contributions to the reduction factor from covalency and the JT effect can be disentangled.

1.3 Thesis Layout

The steps required to calculate theoretical MCD and absorption spectra are reflected in the structure of the first five chapters. Although much of the work in the early chapters is not entirely new, it is original in the sense that it gathers together, for the first time and with consistent notation, all the information necessary to perform such calculations.

Chapter 2 presents some relevant, general, group-theoretical results and definitions, as well as some more specific to axial groups, and details some of the quantum-mechanical applications of these concepts. In Chapter 3 the basis functions of axial molecules required for later sections are described and the appropriate electronic and vibrational matrix elements are considered. In Chapter 4, general expressions for the absorption and MCD spectra and moments are presented. Finally in Part 1, Chapter 5 draws on the preceding chapters in the development of the theoretical treatment of the JT interactions and their effects on the MCD and absorption.

A theoretical model is useful only if it reflects and provides insight into experimental results. In Chapters 7-9, the theory developed and discussed in earlier chapters is used in the interpretation of the absorption and MCD spectra of axial radicals. In Chapter 6, details about the experimental apparatus and techniques are summarised. The first chapter on data analysis is Chapter 7, where a comprehensive interpretation is presented for the $^2E_1 \leftarrow {}^2E_2$ transition of the ferricenium radical cation ($\mathbf{D}_{5d}$). In Chapter 8, the theoretical model of Part 1 is compared with previously published data for the $^2E_1 \leftarrow {}^2E_2$ transition of the cyclooctatetrene radical

anion ($\mathbf{D}_{8h}$ symmetry). Vibrational structure, initially attributed to an $E_2 \otimes e_1$ excited-state LJT effect, is shown to be due to the Herzberg-Teller coupling involving a higher-lying $^2E_3$ electronic state. Finally the data obtained for cyclopentadienyl ($\mathbf{D}_{5h}$) are given in Chapter 9. Unfortunately this radical showed insufficient vibrational structure to be suitable for to a detail JT analysis.

1.4 References

(1) Prince, B. J. Ph.D. Dissertation, University of Canterbury, Christchurch, 1999.

(2) Gasyna, Z.; Metcalf, D. H.; Schatz, P. N.; McConnell, C. L.; Willamson, B. E. *J. Phys. Chem.* **1995**, *99*, 5865-5872.

(3) Metcalf, D. H.; VanCott, T. C.; Synder, S. W.; Schatz, P. N.; Williamson, B. E. *J. Phys. Chem.* **1990**, *94*, 2828-2832.

(4) VanCott, T. C.; Koralewski, M.; Metcalf, D. H.; Schatz, P. N.; Williamson, B. E. *J. Phys. Chem.* **1993**, *97*, 7417-7426.

(5) VanCott, T. C.; Rose, J. L.; Williamson, B. E.; Boyle, M. E.; Misener, G. C.; Schimpf, A. E.; Schatz, P. N. E. *J. Phys. Chem.* **1989**, *93*, 2999-3011.

(6) Samet, C.; Rose, J. L.; Piepho, S. B.; Laurito, J.; Andrews, L.; Schatz, P. N. *J. Amer. Chem. Soc.* **1994**, *116*, 11109-11119.

(7) Fulton, R. L.; Gouterman, M. *J. Chem. Phys.* **1961**, *35*, 1059-1071.

(8) Purins, D.; Feeley, H. F. *J. Mol. Struct.* **1973**, *22*, 11-27.

(9) Prins, R. *Chem. Com.* **1970**, 280-281.

(10) Hendrickson, D. N.; Sohn, Y. S.; Gray, H. B. *J. Chem. Phys.* **1974**, *58*, 4666-4675.

(11) Miller, J. H.; Andrews, A.; Lund, P. A.; Schatz, P. N. *J. Chem. Phys.* **1980**, *73*, 4933-4939.

(12) Williamson, B. E.; VanCott, T. C.; Rose, J. L.; Schrimf, A.; Koralewski, M.; Schatz, P. N. *J. Phys. Chem.* **1991**, *95*, 6835-6842.

(13) Ham, F. S. *Phys. Rev.* **1965**, *138*, A1727.

(14) Jahn, H. A. *Proc. Roy. Soc.A* **1938**, *164*, 117.

(15) Jahn, H. A.; Teller, E. *Proc. Roy. Soc.A* **1937**, *161*, 220.

(16) Bersuker, I. B.; Polinger, V. Z. *Vibronic Interactions in Molecules and Crystals*; Springer-Verlag: Berlin, 1989.

(17) Bersuker, I. B. *The Jahn-Teller Effect and Vibronic Interactions in Modern Chemistry*; Plenum Press: New York, 1984.

(18) Englman, R. *The Jahn-Teller Effect in Molecules and Crystals*; Wiley: New York, 1972.

(19) Pople, J. A.; Longuet-Higgins, H. C. *Proc. Roy. Soc. A* **1958**, 373-383.

(20) Öpik, U.; Pryce, M. H. L. *Proc. Roy. Soc. A* **1957**, *238*, 425-447.

(21) Herzberg, G.; Teller, E. *Z. Phys. Chem. B* **1933**, *21*, 410.

(22) Griffith, J. S. *The Theory of Transition-Metal Ions*, 1st ed.; Cambridge University Press: London, 1961.

(23) Longuet-Higgins, H. C.; Öpik, U.; Pryce, M. H. L.; Sack, R. A. *Proc. Roy. Soc. A* **1958**, *244*, 1-16.

(24) Child, M. S.; Longuet-Higgins, H. C. *Phil. Trans. Roy. Soc.* **1961**, *254*, 259-294.

(25) Bosnick, K. A. *Chem. Phys. Lett.* **2000**, *317*, 524-528.

(26) Piepho, S. B.; Schatz, P. N. *Group Theory in Spectroscopy-With Applications to Magnetic Circular Dichroism*; John Wiley & Sons Inc: New York, 1983.

(27) Buckingham, A. D.; Stephens, P. J. *Ann. Rev. Phys. Chem.* **1966**, 17, 399-432.

2 SYMMETRY AND QUANTUM MECHANICS OF AXIAL MOLECULES

The principles of symmetry and the application of group-theoretical techniques are indispensable tools in the interpretation of molecular spectroscopy and the subjects of this chapter. In Section 2.1 some group theoretical results are introduced – more complete and detailed treatments available elsewhere.[1-7] Following this, in Section 2.2, an exploration is made of the deep-rooted relationship between group theory and quantum mechanics as they relate to molecules. This connection is made through angular momenta, firstly in general terms and then specifically for the axial groups. In the final part of 2.2, some quantum-mechanical applications of group theory are presented, in which axial molecules are the focus.

2.1 Group Theory

This section briefly introduces the group-theoretical principles, conventions and definitions that will be used in subsequent sections and chapters. The principal concern is the *representation* theory of spatial symmetry, with no explicit consideration of time reversal. The final part (Section 2.1.3) summarises some group theoretical results for axial molecules.

2.1.1 Definitions

Point groups

The *point group* of a molecule is the complete set of symmetry operations $\{R\}$ that intersect at a single point and leave the molecule apparently unchanged. The number of these operations is called the *order* of the group and is usually designated h.

The group symmetry operations can be divided into *classes*, within which all operations are of the same type (such as n-fold rotation) and are related to each other, pair-wise (A and B), by a third symmetry operation (X) according to

$$B = XAX^{-1} \tag{2.1}$$

Basis functions

A basis is a set of functions $\boldsymbol{f} = \{f_1, f_2, f_3, \ldots f_n\}$ chosen to represent some physical aspect of a molecule. In linear-algebraic terms, the elements of $\boldsymbol{f}$ must be linearly independent (orthogonal) and form a complete set. According to this latter condition, any arbitrary function representing the aspect can be written as a linear combination of the of the basis functions.

Consider two sets of basis functions $\boldsymbol{f}$ and $\boldsymbol{g}$ that can be related by a unitary transformation

$$\boldsymbol{g} = \boldsymbol{f}U \tag{2.2}$$

The columns of U contain the coefficients of basis $\boldsymbol{g}$ in terms of a linear combination of basis $\boldsymbol{f}$. If both basis sets are orthogonal and normalised (othonormal), then U must be unitary.

The basis sets pertaining to a molecule have well-defined transformation properties with respect to the molecular point group. Much of the remainder of this chapter concerns the precise description of those transformation properties.

Representatives, representations and character

The set of n-dimensional square matrices that represent the effect of the point-group symmetry operations on a set of basis functions forms a group, which is isomorphic to (has a multiplication table of the same form as) the point group. Each (transformation) matrix, $D_f^{\Gamma}(R)$, is a *representative* of the corresponding operation R, and the set of all representatives forms a *representation*, Γ_f, of the group. The functions used to construct the representation are said to *span* or *transform as* the representation and are chosen to be mutually orthogonal. The *character* of a representative ($\chi_f(R)$) is the trace (sum of the diagonal elements) of the matrix – it can be shown that the character of operations belonging to the same class are equal.[5]

If two orthonormal bases, $\boldsymbol{g}$ and $\boldsymbol{f}$ are related by the unitary transformation in equation (2.2) then the two representatives of representative R are related by the similarity transformation

$$D_g(R) = UD_f(R)U^{-1} \tag{2.3}$$

Since U is unitary,

$$\chi_g(R) = \chi_f(R) \tag{2.4}$$

In other words, the character of a basis representative for a given symmetry operation (or class) is independent of unitary transformations of the basis.

Irreducible representations

A representation is reducible if a similarity transformation exists that simultaneously converts all of the matrix representatives to the same minimised (irreducible), block-diagonal form. Each block constitutes an irreducible representative of lower dimensionality l

$$D_f^n = D^l \oplus D^{l'} \oplus \ldots \tag{2.5}$$

$l + l' + \ldots = n$ and $\oplus$ indicates a direct sum. Each set of irreducible representatives forms an *irreducible representation*, commonly abbreviated *irrep*, and the original representation is said to be a *direct sum* of those irreps;

$$\Gamma_f = \sum_l a_l \Gamma_l \tag{2.6}$$

where a_l is the number of times irrep Γ_l occurs.

The block-diagonal nature of the representatives that comprise an irrep confers an important property on the basis functions that span that irrep. Specifically, since all other matrix elements in the same rows and columns are zero, the point-group symmetry operations can only transform these basis functions amongst themselves.

In general, the individual elements of a group (symmetry operations or their representations) do not commute with one another. If they do, the group is said to be abelian. All the irreps of an abelian group are one-dimensional with scalar representatives whose values are just the characters under each operation.

Rather than listing all of their constituent representatives, irreps are usually denoted by labels. In this thesis, two types of notation will be used. The Mulliken system is more familiar to chemists, but the Butler system[7] is more closely related to

angular momenta and lends itself more readily to mathematical manipulation. In this thesis Mulliken notation is used to label terms and states but Butler notation is used in most derivations. The labelling schemes as they apply for irreps of axial point groups are presented in the next section, Table 2.1.

Ignoring time-reversal symmetry, the number of irreps of a group is the same as the number of symmetry classes.[5] One of them is always symmetric with respect to all symmetry operations. It is one-dimensional (with characters of unity) and is usually called the *totally symmetric irrep.*

Irrep partners

Irreps with a dimensionality $l > 1$ are said to be degenerate. They represent the simultaneous transformation properties of l symmetry-related basis functions, one for each row of the corresponding irreducible representatives. The basis functions are said to be *partners* and are distinguished by *partner labels.*

The basis functions, that together span a degenerate irrep, are labelled by a common irrep and different partner labels. For example, a function that transforms as the partner γ of irrep Γ is designated in ket form by

$$|\Gamma\gamma\rangle \tag{2.7}$$

Symmetrised bases

The power of group theoretical methods is vastly enhanced if the functions used to describe a system are chosen to transform in the same manner as partners of the irreps of the system. The first step in choosing the correct linear combinations of a set of functions involves the use of projection operators. Obtained using the great orthogonality theorem (see below), projection operator P for the irrep Γ has the form

$$P_\Gamma = \frac{l}{h}\sum_R \chi_\Gamma(R)^* R \tag{2.8}$$

$\chi_\Gamma(R)$ is the character of irrep Γ under symmetry operation R and * means complex conjugation. In the case of degenerate irreps it may then be necessary to carry out further normalisation and orthogonalisation procedures. The resulting linear combinations are said to be *symmetrised* or *symmetry adapted.*

Chains of groups

When an appropriate subset of operations are removed from a group **G**, the remaining operations form a lower-symmetry group $\mathbf{G}_a$, said to be a sub-group of **G**. This can be represented as $\mathbf{G} \supset \mathbf{G}_a$ or $\mathbf{G}_a \subset \mathbf{G}$. Continued application of this principal gives a chain of groups, $\mathbf{G} \supset \mathbf{G}_a \supset \mathbf{G}_b \supset \ldots \supset \mathbf{C}_1$,[7] where the last group contains only the identity operation (E) and is the point group with the lowest possible symmetry. Often a high-symmetry group will be linked to a low-symmetry group *via* a number of different chains; each chain is said to define a basis for the group.

In the chain-of-groups approach, partner labels are determined by tracing the symmetry properties of the basis function of an irrep to an abelian subgroup, each different chain, giving different partner labels. In this thesis, where the axial point groups $\mathbf{D}_n$ are of importance, two types of chains are particularly useful (see Figure 2.1). Basis sets that transform as partners in the chain $\mathbf{D}_n \supset \mathbf{C}_2$ are said to be *complex* (or spherical), while those in the chain $\mathbf{D}_n \supset \ldots \mathbf{D}_p \supset \mathbf{C}_n$, where p is a prime factor of n, are said to *be* real. The nomenclature comes (in part) from the fact that the characters of all except the single-valued irreps of $\mathbf{C}_n$ are complex while all those of $\mathbf{C}_2$ are real. More particularly, the 'real' Cartesian functions x, y, z transform as non-degenerate irreps of $\mathbf{C}_2$ whereas linear combinations of x and y (of the form $x \pm iy$) are required to span irreps of $\mathbf{C}_n$.

In the framework of the chain-of-groups formalism, the transformation properties of a function are specified in the ket form of equation (2.7) by identifying irrep label Γ with the irrep of the highest-symmetry group and the partner label with the irrep of the lowest symmetry group. Although the transformation properties in any intervening groups can have a bearing on the exact description of the partners, they are omitted in the interests of brevity.

The great orthogonality theorem

The great orthogonality theorem (GOT) states that the irreps of a point group are orthogonal to each other, and that all complementary partners (defined by the same chain-of-groups) of an irrep are also mutually orthogonal. Hence, two symmetrised functions that transform as $|\Gamma_A\ \gamma_A\rangle$ and $|\Gamma_B\ \gamma_B\rangle$ can only overlap (mix) if $\Gamma_A = \Gamma_B$ and $\gamma_A = \gamma_B$ – that is, if they transform as the *same* partner of the *same* irrep. Moreover, if

these conditions are met, the value of the overlap integral is independent of the particular partner. This is expressed mathematically as

$$\langle \Gamma_A\ \gamma_A | \Gamma_B\ \gamma_B \rangle = \delta_{\Gamma_A \Gamma_B}\ \delta_{\gamma_A \gamma_B} |A|^{1/2} \langle \Gamma_A \| \Gamma_B \rangle \qquad (2.9)$$

where $\langle \Gamma_A \| \Gamma_B \rangle$ is a reduced overlap integral, independent of γ_A and γ_B and δ is the Kronecker delta.

A weaker form of this theorem, which states that non-zero overlap requires that $\Gamma_A = \Gamma_B$, is called the little (or character[2]) orthogonality theorem (LOT) and can be used to elucidate the coefficients, a_l, in equation (2.6):

$$a_l = \frac{1}{h} \sum_R \chi_l(R)^* \chi_f(R) \qquad (2.10)$$

where the sum is over all the symmetry operations of the group and * means complex conjugate.[i]

Direct products

The products of basis functions $\boldsymbol{g}$, that transform as irrep Γ_g, with $\boldsymbol{f}$, that transform as Γ_f, span a *direct-product* representation Γ_{gf}. This is symbolised by

$$\Gamma_{gf} = \Gamma_g \otimes \Gamma_f \qquad (2.11)$$

where $\otimes$ means the direct product. In general, Γ_{gf} will be reducible according to equation (2.6). This reduction is facilitated by the fact that that the characters of Γ_{gf} are just the products of the corresponding characters of Γ_g and Γ_f:

$$\chi_{gf}(R) = \chi_g(R) \chi_f(R) \qquad (2.12)$$

If both sets of basis functions span the same n-dimensional irrep, Γ, the full set of product functions is

---

[i] This equation can not be used for infinite groups because $h = \infty$. In such cases reduction must be done by inspection following a method like that outlined in Appendix A.2.

$$\{f_1g_1, f_1g_2, \ldots f_2g_1, f_2g_2, \ldots f_ng_n\} \tag{2.13}$$

These can be related by unitary transformations to sums (symmetric products) and differences (anti-symmetric products) of the form

$$\frac{1}{\sqrt{2}}(f_ig_j \pm f_jg_i) \tag{2.14}$$

The point-group symmetry operations will mix the symmetric products only among themselves and likewise for the anti-symmetric products. Thus the symmetric and antisymmetric products transform as different representations. This result is described by the equation,

$$\Gamma \otimes \Gamma = [\Gamma^2] \oplus \{\Gamma^2\} \tag{2.15}$$

where the square brackets indicate the *symmetric square* and the curly brackets the *antisymmetric square*. If $f = g$, the antisymmetric product is identically zero – for example the Cartesian products span only the symmetric product. On the other hand, angular momenta (of the form $l_z = -i\hbar(xp_y - yp_x)$) transform as the anti-symmetric square of the corresponding representation.

2.1.2 Categories of Irreps

When using group theory to simplify quantum mechanical calculations it is useful to classify irreps into three categories according to their behaviour under complex conjugation.[8]

Category-1 irreps

Category-1 irreps are those for which

$$|\Gamma\gamma\rangle^* = |\Gamma\gamma^*\rangle \tag{2.16}$$

Since $\Gamma^* = \Gamma$, the characters of category-1 irreps are always real. Although partners γ and γ^* are not necessarily the same, the basis functions that span a category-1 irrep

can *always* be related by unitary transformation to a set of real functions for which $\gamma = \gamma^*$. In that case

$$|\Gamma\gamma\rangle^* = |\Gamma\gamma\rangle \tag{2.17}$$

For example, in most common molecular point groups the orbital functions ($p_{\pm1}$, p_0) can be rewritten as linear combinations of p_x, p_y and p_z.

Category-2 irreps

In this category also, $\Gamma^* = \Gamma$, so the characters are real and equation (2.16) still applies. However, the basis functions can *never* be rewritten in real form so the equation (2.17) is never valid. Category-2 irreps are spanned by degenerate fermion-like functions such as the spin function the $|s\ m_s\rangle$ basis, $|1/2\ \pm1/2\rangle$. In axial groups these are doubly degenerate and referred to as *Kramers doublets*.

Category 3 irreps

For category-3 irreps, $\Gamma \neq \Gamma^*$ and some of the characters of are complex. Like category-2 irreps, the basis functions can *never* be written in real form, and

$$|\Gamma\gamma\rangle^* = |\Gamma^*\gamma^*\rangle \tag{2.18}$$

Category-three irreps are always non-degenerate (if time reversal is ignored). However, they come in pairs (*Kramers pairs*) that are related by time reversal and so are usually treated as effectively degenerate, *double-valued irreps*. For example the spin functions $|5/2\ 5/2\rangle$ and $|\tilde{5/2}\ 5/2\rangle$ in point groups with five-fold symmetry are not related by any spatial symmetry operations, but are interchanged by time reversal.

Ambivalent and non-ambivalent groups

Ambivalent groups contain only category-1 and -2 irreps. Non-ambivalent groups also contain category-3 irreps. Examples of the latter that have axial symmetry are $\mathbf{C}_n$, $\mathbf{C}_{nh}$, $\mathbf{S}_n$. The $\mathbf{D}_{n(h)}$ point groups with odd n are also ambivalent, each with a single pair of fermion-like category-3 irreps designated $n/2$ and $\tilde{n}/2$ in Butler notation (see Table 2.1).

2.1.3 The Axial Groups

Axial groups, which have a unique n-fold rotation axis ($n > 2$), are of particular interest in this thesis. They include the infinite (or continuous) group $\mathbf{D}_{\infty h}$ and its infinite ($\mathbf{D}_{\infty}$, $\mathbf{C}_{\infty v}$, $\mathbf{C}_{\infty}$ . . .) and finite ($\mathbf{D}_{n(h)}$, $\mathbf{C}_{nv}$, $\mathbf{C}_{n}$, . . .) sub-groups.

$\mathbf{C}_{\infty}$ is the point group of all rotations about the unique (z) axis. $\mathbf{D}_{\infty}$ comprises the operations of $\mathbf{C}_{\infty}$ supplemented by an infinite number of two-fold rotations ($\infty C_2'$) about all axes perpendicular to z. The point group $\mathbf{D}_{\infty h}$ (the point group of a ring) is further supplemented by a horizontal (perpendicular to z) mirror plane (σ_h) and its products with the existing symmetry operations. This doubles the number of symmetry operations ($S_n = C_n\sigma_h$; $\sigma_v = C_2'\sigma_h$) and irreps. The labels for the latter are generated from those of $\mathbf{D}_{\infty}$ by adding subscripts g and u depending on the effect of the inversion operation ($i = S_2$). $\mathbf{C}_{\infty v}$ is isomorphic with $\mathbf{D}_{\infty}$, where $\infty\sigma_v$ replace the $\infty C_2'$.

Subduction of $\mathbf{D}_{\infty}$ through some relevant chains is illustrated in Figure 2.1. $\mathbf{D}_n$ groups consist of the identity operation, E, rotations C_n^k through angle $2\pi k/n$ about an n-fold (z) axis ($k = 1, 2, \ldots n\text{-}1$) and n two-fold rotations about axes perpendicular to z. The C_n^k rotations form $n/2$ classes when n is even or $(n - 1)/2$ classes if n is odd. The two-fold rotations about axes perpendicular to z belong to one class (nC_2') if n is odd but two classes (nC_2' and nC_2'') if n is even. The total number of classes, and hence the total number of irreps in the 'single'[ii] group, is therefore $(n+6)/2$ when n is even and $(n+3)/2$ when n is odd. For the 'double' group, the number of additional irreps is $n/2$ for even n and $(n+3)/2$ for odd n. Hence, the total number of irreps is $(n+3)$.

The irrep-labelling scheme for $\mathbf{D}_n$ is summarised in Table 2.1. Irreps 0 and $\tilde{0}$ (A_1 and A_2) are non-degenerate and belong to category 1; $n/2$ and $\tilde{n}/2$ are also non-degenerate and belong to category 1 (B_1 and B_2) when n is even, but to category 3 (double valued irrep $E_{n/2}$) when n is odd. All other irreps are doubly degenerate and belong to either category 1 (boson-like functions) or category 2 (fermion-like functions). Thus $\mathbf{D}_n$ is ambivalent for even n but non-ambivalent for odd n.

[ii] Single is used to refer to groups containing only boson-like irreps while the double groups contain both boson- and fermion-like irreps.

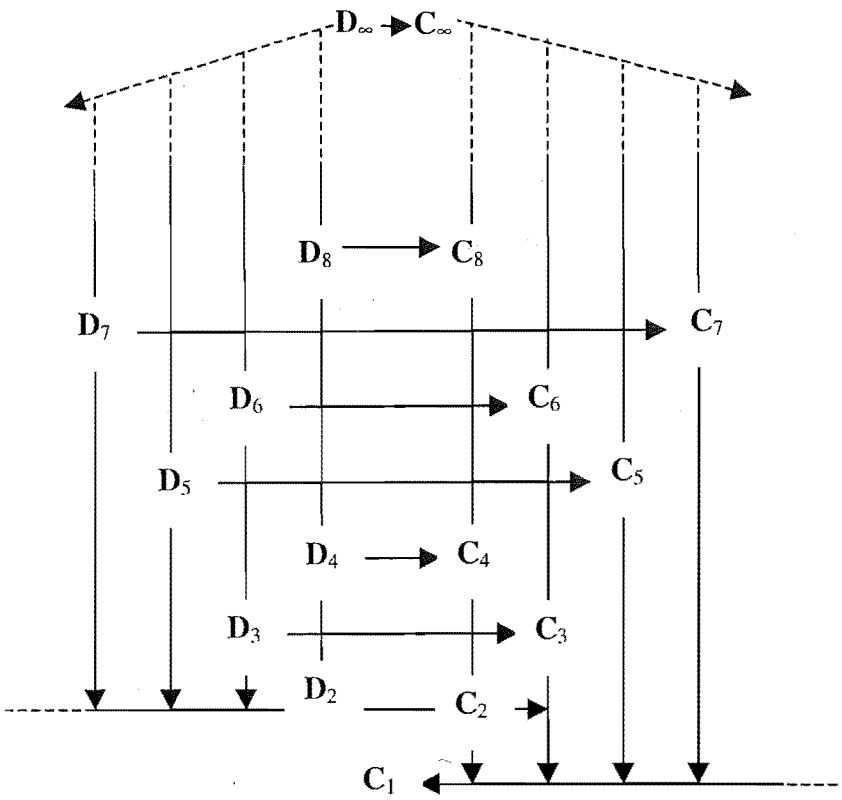

Figure 2.1: Subduction schemes for the axial rotational groups.

The procedure for determining the irreps and partners, $|\Gamma\,\gamma\rangle$, of a function in the chain $\mathbf{D}_n \supset \mathbf{C}_n$ from $|J\ M\rangle$ in the chain $\mathbf{D}_\infty \supset \mathbf{C}_\infty$ can be represented mathematically by modulo (clock) arithmetic. The results are set out, in Butler notation, in Table 2.2

Continuing with the analogy of modulo arithmetic, the $\mathbf{D}_n$ irreps and partners can be conveniently represented on clock diagrams as shown in Figure 2.2. The numerals on the clock are the *partner* labels of degenerate irreps, except at '6 o'clock' and '12 o'clock' where they represent pairs of non-degenerate irreps.

These diagrams can be used as a rapid means to determine direct products, simply by counting around from one irrep in both clockwise and anticlockwise directions by the amount indicated by the second irrep. However, special care must be taken when the $n/2$ and $\tilde{n}\,/2$ irreps are involved – a complete direct product table is given in Table 2.3

Table 2.1: The Mulliken and Butler irrep labelling schemes for axial groups

Degeneracy	Mulliken notation[a]		Butler notation[d]
	finite axial groups	infinite axial groups	
1	A or B[b]	Σ^+ or Σ^- [b]	0 or $\tilde{0}$ $n/2$ or $\tilde{n}/2$
2	$E_{1/2}$	$E_{1/2}$	1/2
2	E_1	Π	1
2	$E_{3/2}$	$E_{3/2}$	3/2
2	E_2	Δ	2
2	$E_{5/2}$	$E_{5/2}$	5/2
2	.	.	.
2	.	.	.
double valued	$E_{n/2}$	$E_{n/2}$	$n/2$ and $\tilde{n}$ /2

[a] For groups with a centre of inversion ($\mathbf{D}_{nh}$ for even n and $\mathbf{D}_{nd}$ for odd n), subscripts g or u are appended to indicate the irrep is symmetric or antisymmetric with respect to that symmetry element.

[b] A one-dimensional irrep is labelled A if it is symmetric with respect to rotation about the highest order axis C_n, or B if it is anti-symmetric. Subscripts 1 or 2 are appended for those irreps that are symmetric or antisymmetric with respect to rotation about a C_2' axis perpendicular to C_n or (in the absence of such an axis) reflection in the σ_v plane. For $\mathbf{D}_{nh}$ where n is odd, ' and " are respectively used to indicate symmetry or antisymmetry with respect to σ_h.

[c] In $\mathbf{D}_{\infty h}$ the + and - superscripts indicate that the irrep that is symmetric or antisymmetric with respect to rotation about the C_2 axis. In $\mathbf{C}_{\infty v}$ they represent the symmetry with respect to the σ_v planes.

[d] $0 \equiv \Sigma^+$ and $\tilde{0} \equiv \Sigma^-$

Table 2.2: Rules for transforming $\mathbf{D}_\infty \supset \mathbf{C}_\infty \rightarrow \mathbf{D}_n \supset \mathbf{C}_n$ using Butler notation

Jmod n	$\mathbf{D}_\infty \supset \mathbf{C}_\infty$		$\mathbf{D}_n \supset \mathbf{C}_n$	
	J	M	Γ	γ
	0 or $\tilde{0}$	0	0	0
$< n/2$	J	$\pm J$	J mod n	$\pm J$ mod n
$n/2$	J	$\pm J$	$n/2 \oplus \tilde{n}$ /2	$n/2$
$> n/2$	J	$\pm J$	n - (J mod n)	$\mp$ (n - (J mod n))
0	J	$\pm J$	$0 \oplus \tilde{0}$	0

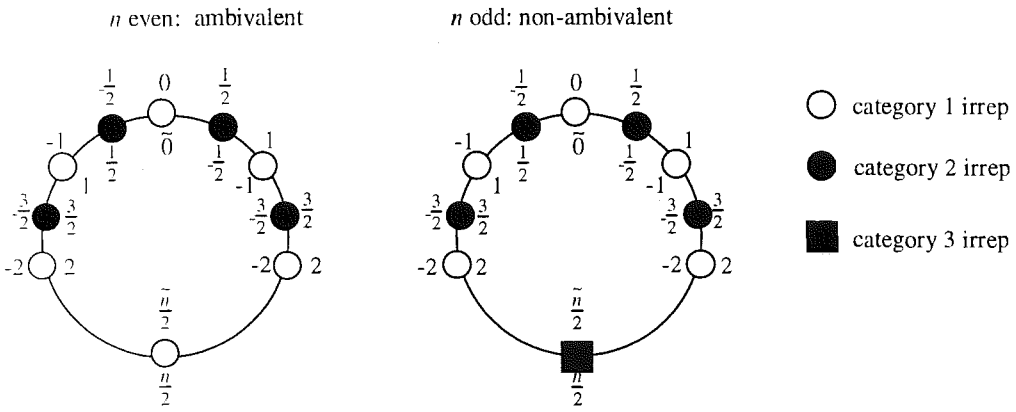

Figure 2.2: Clock representation of the irreps and partners for the $\mathbf{D}_n \supset \mathbf{C}_n$ chain.

2.2 *Quantum-Mechanical Applications of Group Theory*

A basic quantum-mechanical task in theoretical studies of molecules is to solve the time-independent Schrödinger equation

$$\mathcal{H}\psi_n = \varepsilon_n \psi_n \qquad (2.19)$$

This involves determination of the eigenvalues, ε_n, and the corresponding eigenfunctions, ψ_n, for the system under consideration.

In the absence of fields, space is homogeneous and isotropic, and so the Hamiltonian of an isolated system is invariant to translations and rotations of the system as a whole. The conservation principles of linear and angular momenta are direct consequences of this translational and rotational invariance. The latter requires that the total angular momentum operators $\boldsymbol{J}^2$ and J_z commute with the Hamiltonian for an isolated molecule (the so-called molecular Hamiltonian) and share with $\mathcal{H}$ a common, complete set of eigenfunctions.

The molecules considered in this thesis are regarded as fixed, isolated and non-rotating. Under these conditions it is sufficient to consider only the vibronic (vibrational-electronic) part of the molecular Hamiltonian, $\mathcal{H}_{\text{vibronic}}$, without consideration of translations and rotations. If consideration is restricted to $\mathcal{H}_{\text{vibronic}}$, the angular momentum arises from electronic orbital, $\boldsymbol{L}$, and spin, $\boldsymbol{S}$, as well as vibrational, $\boldsymbol{N}$, parts, which combine to give the total angular momentum

Table 2.3: Direct-product table for irreps of the point groups $\mathbf{D}_n$ and $\mathbf{C}_{nv}$*

	category	1	1	1	1	2	2	1	1	3	3
category	⊗	0	$\tilde{0}$	a (integer)	b (integer)	c (1/2-integer)	d (1/2-integer)	$n/2$ (integer)	$\tilde{n}/2$ (integer)	$n/2$ (1/2-integer)	$\tilde{n}/2$ (1/2-integer)
1	0	[0]	$\tilde{0}$	a	b	c	d	$n/2$	$\tilde{n}/2$	$\tilde{n}/2$	$n/2$
1	$\tilde{0}$	$\tilde{0}$	[0]	a	b	c	d	$\tilde{n}/2$	$n/2$	$n/2$	$\tilde{n}/2$
1	a (integer)	a	a	$[0] \oplus \{\tilde{0}\} \oplus \Gamma_{2a}$	$\Gamma_{a+b} \oplus \lvert a-b \rvert$	$\Gamma_{a+c} \oplus \lvert a-c \rvert$	$\Gamma_{a+d} \oplus \lvert a-d \rvert$	$n/2-a$	$n/2-a$	$n/2-a$	$n/2-a$
1	b (integer)	b	b	$\Gamma_{b+a} \oplus \lvert b-a \rvert$	$[0] \oplus \{\tilde{0}\} \oplus \Gamma_{2b}$	$\Gamma_{b+c} \oplus \lvert b-c \rvert$	$\Gamma_{b+d} \oplus \lvert b-d \rvert$	$n/2-b$	$n/2-b$	$n/2-b$	$n/2-b$
2	c (1/2-integer)	c	c	$\Gamma_{c+a} \oplus \lvert c-a \rvert$	$\Gamma_{c+b} \oplus \lvert c-b \rvert$	$\{0\} \oplus [\tilde{0}] \oplus \Gamma_{2c}$	$\Gamma_{c+d} \oplus \lvert c-d \rvert$	$n/2-c$	$n/2-c$	$n/2-c$	$n/2-c$
2	d (1/2-integer)	d	d	$\Gamma_{d+a} \oplus \lvert d-a \rvert$	$\Gamma_{d+b} \oplus \lvert d-b \rvert$	$\Gamma_{d+c} \oplus \lvert d-c \rvert$	$\{0\} \oplus [\tilde{0}] \oplus \Gamma_{2d}$	$n/2-d$	$n/2-d$	$n/2-d$	$n/2-d$
1	$n/2$ (integer)	$n/2$	$\tilde{n}/2$	$n/2-a$	$n/2-b$	$n/2-c$	$n/2-d$	[0]	$\tilde{0}$		
1	$\tilde{n}/2$ (integer)	$\tilde{n}/2$	$n/2$	$n/2-a$	$n/2-b$	$n/2-c$	$n/2-d$	$\tilde{0}$	[0]		
3	$n/2$ (1/2-integer)	$\tilde{n}/2$	$n/2$	$n/2-a$	$n/2-b$	$n/2-c$	$n/2-d$			$\{\tilde{0}\}$	0
3	$\tilde{n}/2$ (1/2-integer)	$n/2$	$\tilde{n}/2$	$n/2-a$	$n/2-b$	$n/2-c$	$n/2-d$			0	$\{\tilde{0}\}$

for $a + b > n/2$, $\Gamma_{a+b} = (a + b)$; for $a + b = n/2$, $\Gamma_{a+b} = n/2 \oplus \tilde{n}/2$; for $a + b < n/2$, $\Gamma_{a+b} = n - (a + b)$

$$\boldsymbol{J} = \boldsymbol{L} + \boldsymbol{S} + \boldsymbol{N} \tag{2.20}$$

The components of these vectors are also additive

$$J_\eta = L_\eta + S_\eta + N_\eta \quad (\eta = x, y, z \text{ or } \pm 1) \tag{2.21}$$

In the absence coupling between these contributions, the operators on the right-hand sides of equations (2.20) and (2.21) individually commute with the Hamiltonian. However in real systems there will be coupling, and the molecular states should then be described in terms of the total angular momentum and its associated quantum numbers. However, the coupled states can be constructed from linear combinations of the complete set of uncoupled basis functions since the latter form a complete set. The solution of the Schrödinger equation then becomes a matter of determining the appropriate combination coefficients. This would appear to be difficult because of the large number of degrees of freedom. However, symmetry and angular momentum can be treated as equivalent concepts,[5,9] so the problem can be immediately simplified by ensuring that the eigenfunctions conform to certain symmetry restrictions.

The molecular Hamiltonian must be invariant to all symmetry operations of the molecular point group. It is therefore a *scalar* operator and must transform as the totally symmetric irrep. This means that the group symmetry operations all commute with $\mathcal{H}$,

$$\mathcal{H}R = R\mathcal{H} \tag{2.22}$$

A significant consequence of this is that the eigenfunctions of $\mathcal{H}$ always belong to the irreps of the molecular point group. This can be shown (*via* equation (2.22)) by application of a point-group operation

$$R\mathcal{H}\psi_i = R\varepsilon_n\psi_i$$

$$\mathcal{H}R\psi_i = \varepsilon_n R\psi_i \tag{2.23}$$

This shows that if ψ_i is an eigenfunction of $\mathcal{H}$, then $R\psi_i$ is also an eigenfunction with the same eigenvalue. The full set of n orthogonal eigenfunctions related to each other by symmetry must therefore form a basis for an n-dimensional irrep.

An important use of group theory occurs when simplifying the matrix elements of quantum mechanical operators. This principally involves determining the non-vanishing matrix elements and relating them to each other, thus reducing the number to be evaluated. Transition moments are matrix elements of particular importance in spectroscopy, although in this work, angular-momentum matrix elements are also of consequence. Although group theory can not be used to actually evaluate such integrals, it can help, for example, in the reduction from many-electron to one-electron form.

The effects of external fields, including the Zeeman and Stark interactions as well as interactions with electromagnetic radiation, are not included in the molecular Hamiltonian. However, these fields have well-defined transformation properties with respect to the molecular point group and so group theory continues to play an important role in dealing with such effects.

In Section 2.2.1, the underlying relation between the rotational transformation properties of a system and its angular momentum are reviewed. The consequences of this relationship for molecules belonging to axial groups are presented in Section 2.2.2, then the transformation properties of some quantum-mechanical operators are discussed in Section 2.2.3. In the final part (Section 2.2.4), some group-theoretical rules are presented for the determination of non-vanishing matrix elements of these operators.

2.2.1 Equivalence of Rotational Symmetry and Angular Momentum

An infinitesimal rotation vector $\delta\boldsymbol{\phi}$ is defined to be of magnitude equal to the angle of the rotation ($\delta\phi$) and in the direction of the axis, ζ, about which the rotation takes place. The change, $\delta\boldsymbol{r}_a$, that occurs in the position vector $\boldsymbol{r}_a$ of particle a in the event of such a rotation is given by

$$\delta\boldsymbol{r}_a = \delta\boldsymbol{\phi} \times \boldsymbol{r}_a \tag{2.24}$$

Consider an arbitrary function ψ that depends on the positions of the particles of system. The change in ψ that occurs on rotation of the system is $\delta\psi$ and

$$\psi + \delta\psi = (1 + \sum_a \delta \boldsymbol{r}_a \cdot \nabla_a)\psi = (1 + \delta\boldsymbol{\phi} \cdot \sum_a \boldsymbol{r}_a \times \nabla_a)\psi \qquad (2.25)$$

where

$$\nabla_a \equiv \partial/\partial \boldsymbol{r}_a \qquad (2.26)$$

In effect, a rotational operator has been defined

$$R_\zeta(\delta\phi) = (1 + \delta\boldsymbol{\phi} \cdot \sum_a (\boldsymbol{r}_a \times \nabla_a)) \qquad (2.27)$$

which rotates ψ by $\delta\phi$ about ζ.

By convention the *infinitesimal rotation operator*, I, is defined as

$$\boldsymbol{I} = -i(\sum_a (\boldsymbol{r}_a \times \nabla_a)) \qquad (2.28)$$

so equation (2.27) can be rewritten as

$$R_\zeta(\delta\phi) = (1 + i\delta\boldsymbol{\phi}.\boldsymbol{I}_\zeta) \qquad (2.29)$$

Rotation by a finite angle ϕ can be considered to be made up of successive infinitesimal rotations $\delta\phi$ (*i.e.* $\phi = n(\delta\phi)$ as $n \to \infty$). The transformation operator for the finite rotation is therefore

$$R_\zeta(\phi) = \lim_{n\to\infty} (R_\zeta(\delta\phi))^n$$

$$= \lim_{\delta\phi\to 0} (1 + i\delta\boldsymbol{\phi}\cdot\boldsymbol{I}_\zeta)^{\frac{\phi}{\delta\phi}}$$

$$= \exp(i\boldsymbol{\phi}\cdot\boldsymbol{I}_\zeta) \qquad (2.30)$$

where the final step uses the fact that $e^y = \lim_{x\to 0}[(1+x)^{y/x}]$. This result can be used to define finite rotational transformations about any arbitrary axis.

It is usually convenient to describe an arbitrary rotation in terms of successive rotations in the x, y and z directions. In general, finite rotations about different axis do not commute; the result of rotation by ϕ_x about x followed by ϕ_y about y, is generally not the same as the result obtained by interchanging the order;

$$R_x(\phi_x)R_y(\phi_y)\psi \neq R_y(\phi_y)R_x(\phi_x)\psi \tag{2.31}$$

Geometric inspection shows that for sufficiently small ϕ_x and ϕ_y (so that the exponents in equation (2.30) can be represented by terms to second-order in the Taylor series expansion), an additional rotation of magnitude $\phi_x\phi_y$ about z is required to reach the same final position.[10] So

$$R_x(\phi_x)\, R_y(\phi_y)\psi = R_z(\phi_x\phi_y)R_y(\phi_y)R_x(\phi_x)\psi \tag{2.32}$$

Substituting equation (2.30) into equation (2.32), expanding as a Taylor series and equating the coefficients of the terms in $\phi_x\phi_y$, gives:

$$I_xI_y - I_yI_x = iI_z \tag{2.33}$$

$$I_yI_z - I_zI_y = iI_x \tag{2.34}$$

$$I_xI_z - I_zI_x = iI_y \tag{2.35}$$

Moreover since the standard angular momentum operator J_ζ is related to I_ζ by[4]

$$J_\zeta = I_\zeta\hbar \tag{2.36}$$

then

$$J_xJ_y - J_yJ_x = iJ_z \tag{2.37}$$

$$J_yJ_z - J_zJ_y = iJ_x \tag{2.38}$$

$$J_xJ_z - J_zJ_x = iJ_y \tag{2.39}$$

Equations (2.37)-(2.39) are the familiar angular momentum commutation relations, which can therefore be considered to be a direct consequence of the geometric properties of composite rotations, along with the invariance of state properties of an isolated system to such transformations.

2.2.2 *Equivalence of Rotational Symmetry and Angular Momentum in Axial Groups*

Irreps of $\mathbf{C}_\infty$

Since successive rotations about the same axis must commute, all irreps of $\mathbf{C}_\infty$ are 1-dimensional, with scalar representatives whose values are just the characters under each operation.

For a normalised basis function $|M\rangle$ that transforms as a general irrep Γ_M of $\mathbf{C}_\infty$

$$R_z(\phi)|M\rangle = \chi_M(\phi)|M\rangle \tag{2.40}$$

Successive rotations through ϕ and ϕ' about *the same axis* must be equivalent to a single rotation by $(\phi + \phi')$, so

$$R_z(\phi')R_z(\phi)|M\rangle = \chi_M(\phi')\chi_M(\phi)|M\rangle$$

$$= \chi_M(\phi'+\phi)|M\rangle \tag{2.41}$$

This requirement can be generally satisfied by an exponential relation of the sort

$$\chi_M(\phi) = e^{iM\phi} \tag{2.42}$$

where $i = \sqrt{-1}$. Substitution of equation (2.42) into equation (2.40) and using equation (2.30) gives

$$\exp(i\phi I_z)|M\rangle = \exp(iM\phi)|M\rangle \tag{2.43}$$

Expanding both sides of the equation and equating terms of the same order, the first-order terms gives

$$I_z|M\rangle = M|M\rangle \tag{2.44}$$

Then since $J_z = I_z\hbar$,

$$J_z|M\rangle = M\hbar|M\rangle \tag{2.45}$$

In other words, the angular momentum of a molecular state $|M\rangle$ is determined entirely by its irrep, and has the value $M\hbar$.

If $|M\rangle$ represents a boson-like state, then it must be invariant to rotations by 2π. Hence

$$R_z(2\pi)|M\rangle = R_z(0)|M\rangle \qquad \text{for bosons} \tag{2.46}$$

When combined with equations (2.41) and (2.42), this requires that M is integral. Thus the boson-like irreps of $\mathbf{C}_\infty$ can be labelled by $M = 0, \pm1, \pm2\ldots$ On the other hand, fermionic functions change sign under rotation by 2π, remaining unchanged by rotation by 4π.

$$R_z(4\pi)\,|M\rangle = R_z(0)|M\rangle = -R_z(2\pi)|M\rangle \qquad \text{for fermions} \tag{2.47}$$

With this requirement and equation (2.41), M must be half-integral. Thus the irreps spanned by fermionic functions can be labelled by $M = \pm1/2, \pm3/2, \pm5/2\ldots$

Irreps of $\boldsymbol{D}_\infty$

The $\mathbf{D}_\infty$ group generators[iii] are $I_z(\phi)$ and $C_2' = R_\perp(\pi)$. Rotations about z by the same angle but in opposite directions, $R_z(\phi)$ and $R_z(-\phi)$, are now related by a similarity transformation involving C_2'

$$R_z(-\phi) = C_2' R_z(\phi) C_2'^{-1} \tag{2.48}$$

[iii] Group generators are the minimum subset of elements from which the entire group can be generated using multiplication tables.

Consequently the basis functions that transform as $|M\rangle$ and $|-M\rangle$ in $\mathbf{C}_\infty$ transform in $\mathbf{D}_\infty$ as partners of a common two-dimensional irrep.

The last point can be seen by taking two basis functions that transform as the irreps $|M_i\rangle$ and $|M_j\rangle$ of $\mathbf{C}_\infty$ but are interchanged by C_2' in $\mathbf{D}_\infty$. The matrix representative of the C_2' operation must be of the form

$$D(C_2') = \begin{pmatrix} 0 & a \\ b & 0 \end{pmatrix} \tag{2.49}$$

where a and b can be +1 or -1 and D is the matrix representative of operation C_2'. From equation (2.42), the matrix representative for $R_z(\phi)$ is

$$D(R_z(\phi)) = \begin{pmatrix} e^{iM_i\phi} & 0 \\ 0 & e^{iM_j\phi} \end{pmatrix} \tag{2.50}$$

and from equation (2.48)

$$R_z(\phi)C_2' = C_2'R_z(-\phi) \tag{2.51}$$

hence

$$D(R_z(\phi))D(C_2')D(R_z(\phi)) = D(C_2') \tag{2.52}$$

The only non-trivial solution of the final equality occurs when $M_i = -M_j$. So when $M \neq 0$, $|M\rangle$ and $|-M\rangle$ simultaneously transform under $R_z(\phi)$ according to

$$D(R_z(\phi)) = \begin{pmatrix} e^{iM\phi} & 0 \\ 0 & e^{-iM\phi} \end{pmatrix} \tag{2.53}$$

and thus form the basis of a two-dimensional irrep labelled $J = |M|$ with partners $M = \pm J$ and character $\chi(R_z(\phi)) = 2\cos(M\phi)$. In angular-momentum parlance, J is the absolute value of the component of orbital angular momentum about the (molecular) z axis, while M is the actual component of the angular momentum in that direction.

In the case where $M = 0$, sum and difference combinations of the basis functions bring $D(C_2')$ into diagonal form, with elements 1 and -1, while leaving $D(R_z(\phi))$

diagonal. In this case the representation is reducible to two one-dimensional irreps, which are labelled Σ^+ (for $\chi(C_2') = 1$) and Σ^- (for $\chi(C_2') = -1$).

2.2.3 *Quantum Mechanical Operators and Group Theory*

In quantum mechanics, for every physical quantity (observable) there corresponds an operator $\mathcal{O}$. In general, these operators act on a function, ψ_A, transforming it into another function ψ_B. For orthonormal functions, the probability amplitude that the transition will occur is given by the integral

$$\int \psi_B^* \mathcal{O} \psi_A \, d\tau \equiv \langle \psi_B | \mathcal{O} | \psi_A \rangle \tag{2.54}$$

$\langle \psi_B |$ is called the bra and $| \psi_A \rangle$ the ket. The transition probability itself is given by

$$P_{B \leftarrow A} = |\langle \psi_B | \mathcal{O} | \psi_A \rangle|^2 \tag{2.55}$$

Integrals of the type in equation (2.54) are called matrix elements because they can be set out in the form of a matrix. This analogy can be carried further to allow quantum-mechanical manipulations to be performed by linear-algebraic methods where states are treated as vectors in a multidimensional (Hilbert) space and operators are treated as transformation matrices.

The expectation value for the observable corresponding to operator $\mathcal{O}$ in a state corresponding to normalised wavefunction ψ_A is given by

$$\langle \mathcal{O} \rangle_A = \langle \psi_A | \mathcal{O} | \psi_A \rangle \tag{2.56}$$

In order for this value to be real, the corresponding operator must be linear and Hermitian. A linear operator has the properties

$$\mathcal{O}(f + g) = \mathcal{O}f + \mathcal{O}g \tag{2.57}$$

and

$$\mathcal{O}(cf) = c\mathcal{O}f \tag{2.58}$$

where f and g are functions and c is a constant. Hermitian operators have the property

$$\langle \psi_A | \mathcal{O} | \psi_B \rangle = \langle \psi_B | \mathcal{O} | \psi_A \rangle^* \tag{2.59}$$

Another point about Hermitian operators is that their eigenfunctions form complete sets. Although this is not a group theoretical result, it lies at the heart of the application of group theory to quantum mechanics.[2]

Hermitian operators can be further classified as *real* or *imaginary* depending on the relationship between the operator and its complex conjugate. For a real operator $\mathcal{R}$

$$\mathcal{R}^* = \mathcal{R} \tag{2.60}$$

whereas for an imaginary operator $\mathcal{I}$

$$\mathcal{I}^* = -\mathcal{I} \tag{2.61}$$

As for wavefunctions, operators have well-defined transformation properties with respect to the molecular point group, which can be specified by irrep and partner labels. However, many operators have additional and quite general transformation properties that are independent of the particular point group but provide valuable information. As discussed above, the molecular Hamiltonian is a scalar operator and will transform as the totally symmetric irrep in any point group. Several others, including those for positions, momenta and dipole moments, have three components, which can be represented as projections onto orthogonal spatial directions. In terms of Cartesian coordinates, a general operator, $\mathcal{V}$, of this type can be represented as

$$\mathcal{V} = (\mathcal{V}_x, \mathcal{V}_y, \mathcal{V}_z) \tag{2.62}$$

Such operators (and the corresponding observables) can be classified as *vector* or *pseudo-vector* operators.

True vectors are anti-symmetric with respect to inversion. They include positions (including vibrational coordinates) and linear momenta, as well as electric dipole moments. Hermitian vector operators are always real and have components that transform as Cartesian displacements, usually designated T_x, T_y, T_z or x, y, z in character tables.

Pseudo-vectors have the transformation properties of rotation about the specified axis and are symmetric with respect to inversion. Examples include angular momenta (including vibrational angular momenta) and quantities derived from them, such as magnetic moments. Hermitian pseudo-vector operators are always complex and have components that transform as rotations about the Cartesian axes, generally designated by R_x, R_y and R_z in character table.

The Cartesian components (defined by the group chain $\mathbf{D}_n \supset \ldots \mathbf{C}_2$) of a (pseudo-) vector are related to complex spherical components (group chain $\mathbf{D}_n \supset \mathbf{C}_n$) by

$$\mathcal{V}_{\pm 1} = \mp\frac{1}{\sqrt{2}}(\mathcal{V}_x, \pm i\,\mathcal{V}_y) \tag{2.63}$$

$$\mathcal{V}_0 = \mathcal{V}_z \tag{2.64}$$

More specific transformation properties are summarised in Table 2.4. Note that if $\mathcal{V}_x$ and $\mathcal{V}_y$ are Hermitian then $\mathcal{V}_{\pm 1}$ are non-Hermitian since,

$$\langle \psi_A | \mathcal{V}_{\pm 1} | \psi_B \rangle = -\langle \psi_A | \mathcal{V}_{\mp 1} | \psi_B \rangle \tag{2.65}$$

Table 2.4: Transformation properties of vectors (***T***) and pseudo vectors (***R***)

(Pseudo-)vector component	Real basis $\mathbf{D}_{n(h)} \supset \ldots \supset \mathbf{C}_2$	Complex basis $\mathbf{D}_{n(h)} \supset \ldots \supset \mathbf{C}_n$
T_x	$\lvert 1_{(u)}\, x\rangle \equiv \lvert E_{1(u)}\, x\rangle$	$(\lvert 1_{(u)}\, -1\rangle - \lvert 1_{(u)}\, 1\rangle)/\sqrt{2}$
T_y	$\lvert 1_{(u)}\, y\rangle \equiv \lvert E_{1(u)}\, y\rangle$	$i(\lvert 1_{(u)}\, -1\rangle + \lvert 1_{(u)}\, 1\rangle)/\sqrt{2}$
$T_z \equiv T_0$	$\lvert \tilde{0}_{(u)}\, x\rangle \equiv \lvert A_{2(u)}\, x\rangle$	$\lvert \tilde{0}_{(u)}\, 0\rangle \equiv \lvert A_{2(u)}\, 0\rangle$
$T_{\pm 1}$	$\mp(\lvert 1_{(u)}\, x\rangle \pm i \lvert 1_{(u)}\, y\rangle)\sqrt{2}$	$\lvert 1_{(u)}\, \pm 1\rangle$
R_x	$\lvert 1_{(g)}\, x\rangle \equiv \lvert E_{1(g)}\, x\rangle$	$(\lvert 1_{(g)}\, -1\rangle - \lvert 1_{(g)}\, 1\rangle)/\sqrt{2}$
R_y	$\lvert 1_{(g)}\, y\rangle \equiv \lvert E_{1(g)}\, y\rangle$	$i(\lvert 1_{(g)}\, -1\rangle + \lvert 1_{(g)}\, 1\rangle)/\sqrt{2}$
$R_z \equiv R_0$	$\lvert \tilde{0}_{(g)}\, z\rangle \equiv \lvert A_{2(g)}\, z\rangle$	$\lvert \tilde{0}_{(g)}\, 0\rangle \equiv \lvert A_{2(g)}\, 0\rangle$
$R_{\pm 1}$	$\mp(\lvert 1_{(g)}\, x\rangle \pm i \lvert 1_{(g)}\, y\rangle)\sqrt{2}$	$\lvert 1_{(g)}\, \pm 1\rangle$

2.2.4 *Coupling Coefficients and Their Applications*

As discussed in Section 2.1.1, direct-product representations are generally reducible. If that is the case, the basis functions for the new irreps are linear combinations of the pair-wise products of basis functions with the coupling coefficients being given by the elements of U of equation (2.2).

The product function $|\Gamma\ \gamma\rangle$ obtained by coupling functions that transform as irreps Γ_A and Γ_B is given by

$$|\Gamma\ \gamma\rangle = \sum_{\gamma_A\ \gamma_B}(\Gamma_A\ \gamma_A\ \ \Gamma_B\ \gamma_B|\Gamma\gamma)|\Gamma_A\ \gamma_A\rangle|\Gamma_B\gamma_B\rangle \tag{2.66}$$

The $(\Gamma_A\ \gamma_A\ \Gamma_B\ \gamma_B|\Gamma\gamma)$ are called Clebsch-Gordan coefficients (CGC), and can be tabulated for each point group.[8] However, in place of CGCs, it is common to use high symmetry coupling coefficients (HSCC),[7] to which they are related by

$$(\Gamma_F\ \gamma_F\ \ \Gamma_B\ \gamma_B|\Gamma_A\ \gamma_A)\ = |\Gamma_A|^{1/2}\begin{pmatrix}\Gamma_A\\ \gamma_A\end{pmatrix}\begin{pmatrix}\Gamma_F\ \Gamma_B\Gamma_A^*\\ \gamma_F\ \gamma_B\ \gamma_A^*\end{pmatrix} \tag{2.67}$$

$|\Gamma_A|$ is the degeneracy of the irrep, $\begin{pmatrix}\Gamma_A\\ \gamma_A\end{pmatrix}$ is a $2jm$ phase which relates the transformation properties of the bra $\langle\Gamma_A\ \gamma_A|$ and the ket $|\Gamma_B\ \gamma_B\rangle$and $\begin{pmatrix}\Gamma_F\ \Gamma_B\Gamma_A^*\\ \gamma_F\ \gamma_B\ \gamma_A^*\end{pmatrix}$ is a $3jm$ coefficient. HSCC have the advantage over CGC that they are easily determined by the methods of Racah algebra and that the $3jm$s in a given point-group chain can be related fairly easily to those in other chains.[2] Some of the $2jm$s and $3jm$s for chains relevant to this work are given in appendices A, B, D and E.

The Wigner-Eckart Theorem

Coupling coefficients are useful not only for determining product functions, as in equation (2.67), but also in the determination of matrix elements using the Wigner-Eckart theorem (WET).

For a matrix element of an operator that transforms as partner $\gamma_\mathcal{O}$ of irrep $\Gamma_\mathcal{O}$,

$$\langle\Gamma_A\ \gamma_A|\Gamma_\mathcal{O}\ \gamma_\mathcal{O}|\Gamma_B\ \gamma_B\rangle \neq 0 \quad \text{iff } \Gamma_A \subset \Gamma_\mathcal{O}\otimes\Gamma_B \tag{2.68}$$

Having demonstrated that non-zero matrix elements are possible, the specific partners that are coupled can then be determined using coupling coefficients. The mathematical expression of this principle is given by the Wigner-Eckart theorem (WET), which, in a form suitable for axial molecules,[iv] using HSCC is

$$\langle \Gamma_A \ \gamma_A | \Gamma_F \ \gamma_F | \Gamma_B \ \gamma_B \rangle = \begin{pmatrix} \Gamma_A \\ \gamma_A \end{pmatrix} \begin{pmatrix} \Gamma_F \ \Gamma_B \Gamma_A^* \\ \gamma_F \ \gamma_B \ \gamma_A^* \end{pmatrix} \langle \Gamma_A || \Gamma_F || \Gamma_B \rangle \qquad (2.69)$$

where $\langle \Gamma_A || \Gamma_F || \Gamma_B \rangle$ is a reduced matrix element whose value is independent of the partners. If the $3jm$ is zero, then the matrix element must vanish. Moreover, all non-zero matrix elements can be related to each other as a coefficient (partner dependent and determined by the product of the $2jm$ and the $3jm$) times a reduced matrix element (partner independent). The utility of this is that only a single reduced matrix element need be evaluated in order to determine a potentially large number of related matrix elements.

It is important to note that while the WET can be used to exclude the possibility of non-zero matrix elements, it does not provide values for the reduced matrix elements. Furthermore, matrix elements that are apparently non-zero according to the WET may still vanish because of other symmetry considerations. Some particularly important cases for *in-state* (or first-order) matrix elements (involving different partners of a degenerate irrep) are given below on the basis of the nature (real or imaginary – Section 2.2.3) of the operator and the irrep category (first or second – Section 2.1.2) of the wavefunctions.

Category-1 irreps

For a real operator $\mathcal{R}_\gamma^\Gamma$

$$\langle \Gamma_1 \ \gamma_\alpha | \ \mathcal{R}_\gamma^\Gamma | \ \Gamma_1 \ \gamma_\beta \rangle \neq 0, \text{ iff } \Gamma \subset [\Gamma_1^2] \qquad (2.70)$$

For an imaginary operator $\mathcal{I}_\gamma^\Gamma$

[iv] In other point groups, this equation must be generalised to take into account repeated representations – see references 2 and 7.

$$\langle \Gamma_1\ \gamma_\alpha |\ \mathcal{S}_\gamma^{\Gamma} |\ \Gamma_1\ \gamma_\beta \rangle \neq 0, \text{ iff } \Gamma \subset \{\Gamma_1^2\} \tag{2.71}$$

Category-2 irreps

$$\langle \Gamma_2\ \gamma_\alpha |\ \mathcal{R}_\gamma^{\Gamma} |\ \Gamma_2\ \gamma_\beta \rangle \neq 0, \text{ iff } \Gamma \subset \{\Gamma_2^2\} \tag{2.72}$$

$$\langle \Gamma_2\ \gamma_\alpha |\ \mathcal{S}_\gamma^{\Gamma} |\ \Gamma_2\ \gamma_\beta \rangle \neq 0, \text{ iff } \Gamma' \subset [\Gamma_2^2] \tag{2.73}$$

2.3 References

(1) Tsukerblat, B. S. *Group Theory in Chemistry and Spectroscopy*; Academic Press INC.: San Diego, 1994.

(2) Piepho, S. B.; Schatz, P. N. *Group Theory in Spectroscopy-With Applications to Magnetic Circular Dichroism*; John Wiley & Sons Inc: New York, 1983.

(3) Davidson, G. *Group Theory for Chemists*, 1st ed.; MacMillan Education Ltd: London, 1991.

(4) Heine, V. *Group Theory in Quantum Mechanics*, 1st ed.; Pergamon Press: London, 1960.

(5) Tinkham, M. *Group Theory and Quantum Mechanics*, 1st ed.; McGraw-Hill Book Company: New York, 1964.

(6) Petrashen, M. I.; Trifonov, E. D. *Applications of Group Theory in Quantum Mechanics*, English ed.; Iliffe Books Ltd: London, 1969.

(7) Butler, P. H. *Point Group Symmetry Applications: Methods and Tables*; Plenum Press: New York, 1981.

(8) Griffith, J. S. *The Theory of Transition-Metal Ions*, 1st ed.; Cambridge University Press: London, 1961.

(9) Landau, L. D.; Lifshitz, E. M. *Quantum Mechanics: Non-Relativistic Theory*, 3rd ed.; Pergamon Press Ltd: London, 1977.

(10) Atkins, P. W.; Friedman, R. S. *Molecular Quantum Mechanics*, 3rd ed.; Oxford University Press Inc.: New York, 1999.

3 ELECTRONIC AND VIBRATIONAL WAVEFUNCTIONS AND MATRIX ELEMENTS OF AXIAL MOLECULES

The molecular Hamiltonian contains kinetic- and potential-energy terms for all nuclei and electrons that make up a molecule. Under appropriate circumstances it can be (at least approximately) separated into two parts; one is a function of both electronic and nuclear coordinates, while the other depends on the nuclear coordinates only. This type of separation is implicit in the picture commonly used to describe molecular structure and dynamics, in which there are taken to exist separate and distinct electronic potential surfaces between which transitions take place, and on which nuclear (vibrational) motions occur.

This type of separation is usually justified on the basis of the Born-Oppenhiemer (BO) approximation. This thesis is principally concerned with cases where this approximation breaks down and hence it is important to understand the approximation so its limitations can be recognised. Furthermore, the completeness theorem means accurate vibronic states can be constructed from linear combinations of BO basis functions from a sufficiently large set even when the approximation is strongly violated, so it is important to know how BO functions are constructed from their electronic and vibrational parts.

3.1 Vibronic Coupling

3.1.1 Nuclear Coordinates

Before considering the vibronic Hamiltonian and the BO approximation, it is useful to briefly consider the nuclear coordinate system that will be used.

For a non-linear molecule of N atoms, six coordinates are required to uniquely specify the centre of mass and the molecular orientation. Changes of these coordinates represent translations and rotations, but do not affect the potential energy of an isolated molecule. Moreover, they do not change the kinetic energy in the reference frame of the molecular coordinates.

Linear combinations of the changes of the remaining $3N$-6 coordinates can be chosen that alter neither the centre of mass nor the orientation, but do change the

positions of the atoms with respect to each other. Such displacements *will* change the potential energy of the molecule and hence be associated with restoring forces, which will cause the system to oscillate. Consequently, they are called vibrational coordinates and are labelled Q_η where $\eta = 1, 2, \ldots 3N\text{-}6$.

3.1.2 Vibronic Hamiltonian

The vibronic Hamiltonian of a molecule can be written

$$\mathcal{H}_{\text{vibronic}}(q,Q) = T_n(Q) + T_e(q) + V(q,Q) \tag{3.1}$$

where Q represents the sum over all nuclear coordinates and q the sum over all electronic coordinates.

$V(q,Q)$ is the sum of electrostatic interactions;

$$V(q,Q) = V_{nn}(Q) + V_{ee}(q) + V_{en}(q,Q) \tag{3.2}$$

where the subscripts indicate interactions between nuclei (n) and/or electrons (e). $T_n(Q)$ and $T_e(q)$ are, respectively, the nuclear and electronic kinetic-energy operators. They are second-derivative operators with respect to the relevant coordinates. For the nuclear coordinates

$$T_n(Q) = \sum_\eta -\frac{\hbar^2}{2\mu_\eta}\frac{\partial^2}{\partial Q_\eta^2} \tag{3.3}$$

where μ_η is an effective (reduced) mass. Alternative coordinate systems include mass-weighted coordinates

$$Q'_\eta = \sqrt{\mu_\eta} Q_\eta \tag{3.4}$$

in which the mass dependence of equation (3.3) is absorbed into Q'_η, and dimensionless coordinates,

$$Q''_\eta = \sqrt{\frac{\omega_\eta \mu_\eta}{\hbar}} Q_\eta \tag{3.5}$$

In terms of the latter

$$T_n(Q'') = \sum_{\eta} \frac{-\hbar\omega}{2} \frac{\partial^2}{\partial Q''^2_{\eta}} \tag{3.6}$$

The vibronic Hamiltonian is commonly rewritten as

$$\mathcal{H}_{\text{vibronic}}(q,Q) = T_n(Q) + \mathcal{H}_{el}(q,Q) \tag{3.7}$$

where $\mathcal{H}_{el}(q,Q)$ is referred to as the electronic Hamiltonian and has the form

$$\mathcal{H}_{el}(q,Q) = T_e(q) + V(q,Q) \tag{3.8}$$

Through $T_e(q)$, $\mathcal{H}_{el}(q,Q)$ involves a differential operator in q space, but also, through $V(q,Q)$, it depends parametrically on Q.

3.1.3 The Born-Oppenheimer Approximation

The Born-Oppenhemier (BO) approximation arises from the notion that (because electrons are very much less massive than nuclei) as the nuclei move the electrons adjust instantaneously to the new nuclear arrangement. Thus, although the electronic dynamics may depend strongly on the position of the nuclei they are essentially independent of nuclear motion. The electronic dynamics of the molecule can therefore be thought of as involving steps between a series of static nuclear configurations (given by Q) each of which has an associated electronic state, $\phi_k(q,Q)$, which is a solution of an *electronic* Shrödinger equation

$$\mathcal{H}_{el}(q,Q)\phi_k(q,Q) = W_k(Q)\phi_k(q,Q) \tag{3.9}$$

By solving this equation for various nuclear configuration, an electronic potential-energy surface $W_k(Q)$ can be mapped out for each electronic wavefunction. By making the steps in Q vanishingly small, the electronic wavefunction and energy are seen to vary continuously and smoothly as a function of Q.

This approach suggests that neither the energy nor the wavefunction is dependent on the rate of change of Q. In mathematical parlance, it implies that since

the eigenfunctions of the electronic Hamiltonian operator depend only parametrically on Q, they commute with the nuclear kinetic-energy operator (see below).

In the BO approximation, the eigenfunctions of $\mathcal{H}_{\text{vibronic}}$ are assumed to have an adiabatic form – they are simple products of electronic and vibrational wavefunctions;

$$\psi_{kv}(q, Q) = \phi_k(q, Q)\varphi_{kv}(Q) \tag{3.10}$$

where v is a vibrational state label. This can be interpreted as indicating that the nuclear motion represented by vibrational function $\varphi_{kv}(Q)$, is confined to a *single* potential-energy surface, $W_k(Q)$. For this to be reasonable it must be possible to derive an independent equation for nuclear motion, which (as suggested above and demonstrated below), in turn, requires that the electronic wavefunction commutes with the nuclear kinetic energy operator according to the relation

$$[T_n(Q), \phi_k(q,Q)] = 0 \tag{3.11}$$

The starting point is the vibronic Shrödinger equation,

$$\mathcal{H}_{\text{vibronic}}(q,Q)\psi_{kv}(q, Q) = \varepsilon_{kv}\psi_{kv}(q, Q) \tag{3.12}$$

with vibronic eigenvalues ε_{kv}. Expanding equation (3.12) according to equations (3.7) and (3.10) gives,

$$[T_n(Q) + \mathcal{H}_{el}(q,Q)]\phi_k(q,Q)\varphi_{kv}(Q) = \varepsilon_{kv}\phi_k(q,Q)\varphi_{kv}(Q) \tag{3.13}$$

By assuming that equation (3.11) is valid, equation (3.13) can be modified in a series of steps (equations (3.14)-(3.17)), the second of which uses equation (3.9).

$$\phi_k(q,Q)T_n(Q)\varphi_{kv}(Q) + \mathcal{H}_{el}(q,Q)\phi_k(q,Q)\varphi_{kv}(Q) = \varepsilon_{kv}\phi_k(q,Q)\varphi_{kv}(Q) \tag{3.14}$$

$$\phi_k(q,Q)T_n(Q)\varphi_{kv}(Q) + W_k(Q)\phi_k(q,Q)\varphi_{kv}(Q) = \varepsilon_{kv}\phi_k(q,Q)\varphi_{kv}(Q) \tag{3.15}$$

$$\phi_k(q,Q)T_n(Q)\varphi_{kv}(Q) + \phi_k(q,Q)W_k(Q)\varphi_{kv}(Q) = \phi_k(q,Q)\varepsilon_{kv}\varphi_{kv}(Q) \tag{3.16}$$

$$\phi_k(q,Q)[T_n(Q) + W_k(Q)]\varphi_{kv}(Q) = \phi_k(q,Q)\varepsilon_{kv}\varphi_{kv}(Q) \qquad (3.17)$$

In equation (3.14) the principle has been used that linear operators commute with scalars (Section 2.2.3). Dividing (3.17) through by $\phi_k(q,Q)$, the independent equation for nuclear motion under the BO approximation is

$$[T_n(Q) + W_k(Q)]\varphi_{kv}(Q) = \varepsilon_{kv}\varphi_{kv}(Q) \qquad (3.18)$$

Thus, nuclear motion can be pictured as being confined to a single potential-energy surface $W_k(Q)$ *only* if the commutation relation (equation (3.11)) is obeyed. In essence equation (3.11) can be regarded as the heart of the BO approximation.

3.2 Electronic States

In this section the electronic parts of the BO products are considered. The basis functions are eigenfunctions of $\mathcal{H}_{el}$, which includes only electrostatic interactions – spin-orbit coupling, and external effects due magnetic or electric fields are considered to be small enough to be determined by perturbation theory and are dealt with in Section 3.3.

3.2.1 Nuclear-coordinate Dependence of Electronic Wavefunctions

Even within the BO approximation the electronic wavefunctions are Q dependent. This can be seen explicitly by expanding V from equation (3.8) as a Taylor's series in each of the coordinates;

$$V(q, Q) = V(q, Q_0) + \sum_{\eta}\left(\frac{\partial V}{\partial Q_\eta}\right)_0 Q_\eta + \frac{1}{2}\sum_{\eta\,\mu}\left(\frac{\partial^2 V}{\partial Q_\eta \partial Q_\mu}\right)_0 Q_\eta Q_\mu \qquad (3.19)$$

where η and μ are vibrational coordinate labels. Inclusion of terms of higher than second order is inconsistent with the BO approximation.[1] The subscript 0 indicates that derivatives are to be evaluated at the equilibrium nuclear coordinates (*i.e.* $Q_\eta = 0$ for all η), denoted by Q_0. The zero-order electronic basis functions are chosen to be eigenfunctions of $\mathcal{H}_{el}(q,Q_0)$, where.

$$\mathcal{H}_{el}(q,Q_0) = T_e(q) + V(q,Q_0) \tag{3.20}$$

$$\mathcal{H}_{el}(q,Q_0)\phi_k(q,Q_0) = W_k^0\phi_k(q,Q_0) \tag{3.21}$$

These $\phi_k(q,Q_0)$ clearly commute with $T_n(Q)$ since they are independent of Q. The full electronic Hamiltonian can now be written

$$\mathcal{H}_{el}(q,Q) = \mathcal{H}_{el}(q,Q_0) + \mathcal{H}_{el}'(q,Q) \tag{3.22}$$

where $\mathcal{H}_{el}'(q,Q)$ represents a perturbation. Comparing equation (3.22) with equations (3.20) and (3.19) gives,

$$\mathcal{H}_{el}'(q,Q) = V(q,Q) - V(q,Q_0) \tag{3.23}$$

and

$$\mathcal{H}_{el}'(q, Q) = \sum_{\eta}\left(\frac{\partial V}{\partial Q_\eta}\right)_0 Q_\eta + \frac{1}{2}\sum_{\eta\mu}\left(\frac{\partial^2 V}{\partial Q_\eta \partial Q_\mu}\right)_0 Q_\eta Q_\mu \tag{3.24}$$

To first order in non-degenerate perturbation theory the eigenvalues are

$$W(Q) = W(Q_0) + \sum_{\eta}\left(\frac{\partial V}{\partial Q_\eta}\right)_0 Q_\eta + \frac{1}{2}\sum_{\eta\mu}\left(\frac{\partial^2 V}{\partial Q_\eta \partial Q_\mu}\right)_0 Q_\eta Q_\mu \tag{3.25}$$

The corresponding eigenfunctions are

$$\phi_k(q, Q) = \phi_k(q, Q_0) + \sum_{j\neq k}\frac{\langle\phi_j(q, Q_0)|\sum_{\eta}\left(\frac{\partial V}{\partial Q_\eta}\right)_0 Q_\eta|\phi_k(q, Q_0)\rangle}{W_k(Q_0)-W_j(Q_0)}\phi_j(q, Q_0) \tag{3.26}$$

In this model, the Q dependence of the electronic wavefunctions comes from vibrationally induced mixing with other electronic states, which is often referred to as Hertzberg-Teller (HT) coupling.[2] Since the magnitude of the coupling is inversely proportional to the energy separation, for well-separated states the wavefunctions vary only slowly with Q and the BO separability holds to a high degree of approximation.

3.2.2 Many-electron Wavefunctions

The electronic states of a molecule generally involve many electrons. The complete set of products of one-electron (1-*e*) functions spans the space of all possible electronic states, but does not commute with $\mathcal{H}_{el}$. The problem of determining the many-electron functions is therefore essentially one of determining the appropriate linear combinations of 1-*e* products by employing the group-theoretical methods outlined in Section 2.2.4. In doing this, care must be taken to ensure anti-symmetry with respect to the exchange of the coordinates of two electrons (as required by the Pauli principle) and commutation with the point-group operators (so that the wavefunctions form the basis of irreps of the group). The results (called configuration state functions) are not *exact* wavefunctions for the system, since configuration interaction will not be taken into account. However, they do have the transformation properties of the exact wavefunctions.

Only the electrons in the unfilled shell need be considered in these constructions, because the contributions from the filled shells will be totally symmetric (contribute no net angular momentum). Since the molecules of concern in this thesis belong subgroups of $\mathbf{D}_{\infty(h)}$, the maximum orbital degeneracy is two. Consequently, a single open shell can contain only one, two or three electrons. Each of these cases is dealt with quite generally below. But first, the designations of these states and the operators that act on them is briefly outlined.

A convention adopted for this and consequent chapters is that many-electron operators, quantum numbers and irrep labels are denoted in upper case (J, L, S, J, M, Λ, M_Λ, A_1, E_1 *etc.*), while those for a single electron are written in lower case (j, l, s, j, m, λ, m_λ, a_1, e_1 *etc.*) unless otherwise stated. The many-electron configuration state functions (for a single open shell) are represented by

$$\phi_{\Lambda S M_\Lambda \Sigma}(q) \equiv | \Gamma_\lambda^{n_e\ 2S+1}\Gamma_\Lambda M_\Lambda \Sigma\rangle \qquad (3.27)$$

Here λ is the irrep label, in Butler notation, of an open-shell orbital containing n_e electrons and Γ_λ is the corresponding label in lower-case Mulliken notation. Λ and M_Λ are the many-electron orbital irrep and partner labels in Butler notation, while Γ_Λ

is the orbital irrep in upper-case Mulliken notation. S is the total electronic-spin quantum number (see Appendix A) and Σ the spin partner label in the appropriate point-group chain (generally $\mathbf{D}_n \supset \mathbf{C}_n$).

One-electron wavefunctions

The 1-*e* states are obtained by coupling spin and orbital parts to give a spin-orbital. The shorthand notation for an electron in the m_λ partner orbital is

$$|m_\lambda^{\pm}\rangle = |\lambda\, m_\lambda\rangle|1/2\ \pm 1/2\rangle \tag{3.28}$$

For a non-degenerate orbital, only two possible spin-orbitals exist, corresponding to spin-up and spin-down states. For a_2 ($\tilde{0}$) and a_1 (0) orbitals, these states are,

$$|\,a_1{}^1\,{}^2A_1\ 0\ \pm 1/2\rangle = |0^{\pm}\rangle \tag{3.29}$$

$$|\,a_2{}^1\,{}^2A_2\ 0\ \pm 1/2\rangle = |\tilde{0}^{\pm}\rangle \tag{3.30}$$

For doubly degenerate e_λ orbitals (with partners $\pm\lambda$) there are four states, which are listed, in terms of their $\mathbf{D}_n \supset \mathbf{C}_n$ transformation properties, in Table 3.1. (The last two columns of Table 3.1 are discussed later in this Chapter, but ε_{SO} and ε_{Zeeman} are SO and Zeeman shift of the states.)

Table 3.1: One-electron wavefunctions for a doubly degenerate e_λ orbital

$\lvert\, \Gamma_\lambda^{n_e}\, {}^{2S+1}\Gamma_\Lambda M_\Lambda\, \Sigma\rangle$	spin-orbital	ε_{SO}	ε_{Zeeman}
$\lvert\, e_\lambda{}^1\, {}^2E_\lambda\ \pm\lambda\ \pm 1/2\rangle$	$\lvert \pm\lambda^{\pm}\rangle$	$-a'_\lambda/2$	$\pm(g_\lambda + g_e)\cos\theta/2$
$\lvert\, e_\lambda{}^1\, {}^2E_\lambda\ \pm\lambda\ \mp 1/2\rangle$	$\lvert \pm\lambda^{\mp}\rangle$	$a'_\lambda/2$	$\pm(g_\lambda - g_e)\cos\theta/2$

Two-electron wavefunctions

The inter-electronic repulsion terms in the molecular Hamiltonian cause the orbital and the spin states of the individual electrons to be coupled. In the point group $\mathbf{D}_n$ only doubly degenerate orbitals need be considered since Γ_λ^2 is a closed shell for a non-degenerate orbital.

Coupling is performed separately in spin and orbital space to produce two-electron (2-*e*) spin and orbital states. According to Table 2.3 (for a category-1 degenerate irrep), the 2-*e* orbital irrep is given by

$$\Lambda = \lambda \otimes \lambda = 0 \oplus \tilde{0} \oplus 2\lambda = A_1 \oplus A_2 \oplus E_{2\lambda} \tag{3.31}$$

The 2-*e* spin quantum numbers can be obtained from the Clebsch-Gordan series (Appendix A).

$$S = |1/2 + 1/2| \ldots |1/2 - 1/2| = 1, 0 \tag{3.32}$$

The direct-product functions obtained separately in orbital and spin space using equation (2.66) and the high-symmetry coupling coefficients in Appendices A and C, are given in Table 3.2.

Table 3.2: Two-electron orbital (top) and spin (bottom) wavefunctions for an e_λ^2 configuration.

2-*e* orbital wavefunctions $\|(\lambda_1\ \lambda_2)\ \Lambda M_\Lambda\rangle$	Sums of 1-*e* products $\sum_{m_{\lambda_1}\ m_{\lambda_2}} (\lambda_1 m_{\lambda_1} \lambda_2 m_{\lambda_2} \| \Lambda M_\Lambda) \|\lambda_1 m_{\lambda_1}\rangle \|\lambda_2 m_{\lambda_2}\rangle$
$\|(\lambda\ \lambda)\ 0\ 0\rangle$	$\frac{1}{\sqrt{2}}(\|\lambda\ -\lambda\rangle\|\lambda\ \lambda\rangle + \|\lambda\ \lambda\rangle\|\lambda\ -\lambda\rangle)$
$\|(\lambda\ \lambda)\ \tilde{0}\ 0\rangle$	$\frac{1}{\sqrt{2}}(\|\lambda\ -\lambda\rangle\|\lambda\ \lambda\rangle - \|\lambda\ \lambda\rangle\|\lambda\ -\lambda\rangle)$
$\|(\lambda\ \lambda)\ 2\Lambda\ -2\Lambda\rangle$	$\|\lambda\ \lambda\rangle\|\lambda\ \lambda\rangle$
$\|(\lambda\ \lambda)\ 2\Lambda\ 2\Lambda\rangle$	$\|\lambda\ -\lambda\rangle\|\lambda\ -\lambda\rangle$
2-*e* spin wavefunctions $\|(\sigma_1\ \sigma_2)\ S\ \Sigma\rangle$	Sums of 1-*e* spin products $\sum_{\sigma_1\sigma_2} (s_1\ \sigma_1 s_2\ \sigma_2 \| S\ \Sigma) \|s_1\ \sigma_1\rangle \|s_1\ \sigma_2\rangle$
$\|(1/2\ 1/2)\ 0\ 0\rangle$	$\frac{1}{\sqrt{2}}(\|1/2\ 1/2\rangle\|1/2\ -1/2\rangle - \|1/2\ -1/2\rangle\|1/2\ 1/2\rangle)$
$\|(1/2\ 1/2)\ 1\ 1\rangle$	$\|1/2\ 1/2\rangle\|1/2\ 1/2\rangle$
$\|(1/2\ 1/2)\ 1\ 0\rangle$	$\frac{1}{\sqrt{2}}(\|1/2\ 1/2\rangle\|1/2\ -1/2\rangle + \|1/2\ -1/2\rangle\|1/2\ 1/2\rangle)$
$\|(1/2\ 1/2)\ 1\ -1\rangle$	$\|1/2\ -1/2\rangle\|1/2\ -1/2\rangle$

Next, products of the spin and orbital wavefunctions are taken. In the case of an e_λ^2 configuration, the combining of symmetric spin functions *only* with antisymmetric spatial functions, and *vice versa*, automatically gives states that conform to the Pauli principle. The results are presented in Table 3.3 in terms of normalised Slater determinants using the definition

$$|a\ b\rangle = \frac{1}{\sqrt{2}}(|a\rangle|\ b\rangle - |\ b\rangle|a\rangle) \tag{3.33}$$

Table 3.3: Anti-symmetrised two-electron spin-orbit wavefunctions for e_λ^2 configuration

$\lvert \Gamma_\lambda^{n_e\ 2S+1}\Gamma_\Lambda\ M_\Lambda\ \Sigma\rangle$	Normalised Slater determinants
$\lvert e_\lambda^{2\ 1}A_1\ 0\ 0\rangle$	$\frac{1}{\sqrt{2}}(\lvert -\lambda^+\lambda^-\rangle - \lvert\lambda^- -\lambda^+\rangle)$
$\lvert e_\lambda^{2\ 3}A_2\ 0\ 1\rangle$	$\lvert -\lambda^+\ \lambda^+\rangle$
$\lvert e_\lambda^{2\ 3}A_2\ 0\ 0\rangle$	$\frac{1}{\sqrt{2}}(\lvert -\lambda^+\lambda^-\rangle + \lvert\lambda^- -\lambda^+\rangle)$
$\lvert e_\lambda^{2\ 3}A_2\ 0\ -1\rangle$	$\lvert -\lambda^-\ \lambda^-\rangle$
$\lvert e_\lambda^{2\ 1}E_{2\lambda}\ -2\lambda\ 0\rangle$	$\lvert\lambda^+\ \lambda^-\rangle$
$\lvert e_\lambda^{2\ 1}E_{2\lambda}\ 2\lambda\ 0\rangle$	$\lvert\lambda^+\ -\lambda^-\rangle$

3.2.2.1 Three-electron wavefunctions

Again, only doubly degenerate orbitals need be considered. The spin and orbital angular momenta of the third electron couple with the totals from the first two. If this coupling is done without regard to the fermionic nature of the electrons, the six 2-*e* functions of Table 3.2 give 24 coupled 3-*e* functions. On the other hand, the hole-particle formalism shows that, for a e_λ^3 configuration, there is only a single spin-doublet term, with $\Lambda = \lambda$, which comprises only four states. This contradiction can be reconciled by recognising that half of the directly coupled states violate the Pauli principle and therefore must vanish. The only direct-product wavefunctions that can contribute to the correctly antisymmetrised final states are the twelve, summarised in Table 3.4, that transform as $^2E_\lambda$.

Table 3.4: Non-antisymmetrised wavefunctions for a λ^3 configuration

$\|(\Gamma_\lambda^{n_e-1}(S_1\ \Lambda_1), \Gamma_\lambda^1))\Gamma_\lambda^{n_e\ 2S+1}\Gamma_\Lambda M_\Lambda\ \Sigma\rangle$	Non-anti-symmetrised combinations of products
$\|(e_\lambda^2\ (0\ 0), e_\lambda^1)\ e_\lambda^3\ ^2E_\lambda \pm\lambda\ -½\rangle$	$\frac{1}{\sqrt{2}}(\|-\lambda^+\lambda^-\rangle\|\pm\lambda^-\rangle - \|\lambda^--\lambda^+\rangle\|\pm\lambda^-\rangle)$
$\|(e_\lambda^2\ (0\ 0), e_\lambda^1)\ e_\lambda^3\ ^2E_\lambda \pm\lambda 1/2\ \rangle$	$\frac{1}{\sqrt{2}}(\|-\lambda^+\lambda^-\rangle\|\pm\lambda^+\rangle - \|\lambda^--\lambda^+\rangle\|\pm\lambda^+\rangle)$
$\|(e_\lambda^2\ (0\ 2\lambda), e_\lambda^1)\ e_\lambda^3\ ^2E_\lambda \pm\lambda\text{-}1/2\ \rangle$	$\|\pm\lambda^+ \pm \lambda^-\rangle\|\mp\lambda^-\rangle$
$\|(e_\lambda^2\ (0\ 2\lambda), e_\lambda^1)\ e_\lambda^3\ ^2E_\lambda \pm\lambda 1/2\ \rangle$	$\|\pm\lambda^+ \pm\lambda^-\|\mp\lambda^+\rangle$
$\|(e_\lambda^2\ (1\ \tilde{0}), e_\lambda^1)\ e_\lambda^3\ ^2E_\lambda \pm\lambda\ 1/2\rangle$	$\mp\frac{1}{\sqrt{6}}(\|-\lambda^+\lambda^-\rangle\|\pm\lambda^+\rangle + \|-\lambda^-\lambda^+\rangle\|\pm\lambda^+\rangle - 2\|-\lambda^+\lambda^+\rangle\|\pm\lambda^-\rangle)$
$\|(e_\lambda^2\ (1\ \tilde{0}\ ), e_\lambda^1)\ e_\lambda^3\ ^2E_\lambda \pm\lambda\ 1/2\rangle$	$\pm\frac{1}{\sqrt{6}}(\|-\lambda^+\lambda^-\rangle\|\pm\lambda^-\rangle+\|-\lambda^-\lambda^+\rangle\|\pm\lambda^-\rangle - 2\|-\lambda^-\lambda^-\rangle\|\pm\lambda^+\rangle)$

In this case, antisymmetrisation must be imposed by choosing four appropriate linear combinations of the twelve *parent* functions. The generalised relationship is

$$|e_\lambda^3\ ^2E_\lambda M_\Lambda\ \Sigma\rangle = \sum_{S_1\ \Lambda_1} (e_\lambda^2\ S_1\ \Lambda_1, e_\lambda^1|e_\lambda^3\ \Sigma\ \Lambda)|(e_\lambda^2\ (S_1\ \Lambda_1), e_\lambda^1)\ e_\lambda^3\ ^2E_\lambda M_\Lambda\ \Sigma\rangle \quad (3.34)$$

where S_1 and Λ_1 refer to the two-electron wavefunctions. The $(e_\lambda^2\ \Sigma_1\ \Lambda_1, e_\lambda^1|e_\lambda^3\ \Sigma\ \Lambda)$ are known as *coefficients of fractional parentage* (CFP) because they specify the contributions of the "parent" functions $|(\Gamma_\lambda^{n_e-1}\ (S_1\ \Lambda_1), \Gamma_\lambda^1)\Gamma_\lambda^{n_e\ 2S+1}\Gamma_\Lambda\ M_\Lambda\ \Sigma\rangle$ of Table 3.4 to the properly antisymmetrised $|\Gamma_\lambda^{n_e\ 2S+1}\Gamma_\Lambda M_\Lambda\ \Sigma\rangle$ wavefunctions. Quite generally

$$|e_\lambda^3\ ^2E_\lambda M_\Lambda\ \Sigma\rangle = c_0|(e_\lambda^2\ (0\ 0), e_\lambda^1)e_\lambda^3\ ^2E_\lambda M_\Lambda\ \Sigma\rangle + c_{2\lambda}|(e_\lambda^2\ (0\ 2\lambda), e_\lambda^1)e_\lambda^3\ ^2E_\lambda\ \Lambda\ \Sigma\rangle$$

$$+c_{\tilde{0}}|(e_\lambda^2\ (1\ \tilde{0}), e_\lambda^1))^2E_\lambda M_\Lambda\ \Sigma\rangle \quad (3.35)$$

where the cs are the CFP. For the state with $M_\Lambda = \lambda$ and $\Sigma = -1/2$,

$$|e_\lambda^3\ ^2E_\lambda\ \lambda\ -1/2\rangle = \frac{c_0}{\sqrt{2}}\{|-\lambda^+\lambda^-\rangle|\lambda^-\rangle - |\lambda^--\lambda^+\rangle|\lambda^-\rangle\} + c_{2\lambda}|\lambda^+\lambda^-\rangle|-\lambda\rangle$$

$$+\frac{c_0^{\sim}}{\sqrt{6}}\{|-\lambda^+\lambda^-\rangle|\lambda^-\rangle + |-\lambda^-\lambda^+\rangle|\lambda^-\rangle - 2|-\lambda^-\lambda^-\rangle|\lambda^+\rangle\} \qquad (3.36)$$

According to Pauli's exclusion principle no two electrons can exist in the same spin-orbital state. Therefore, the term in $|\lambda^+\ \lambda^-\rangle|\lambda^-\rangle$ must vanish, which requires $c_0^{\sim} = -\sqrt{3}c_0$. Substituting this into equation (3.36), using the fact that permutations of the 2-*e* determinants causes a change in sign, gives

$$|e_\lambda^3\ ^2E_\lambda\ \lambda\ -1/2\rangle = -c_{2\lambda}|\lambda^-\lambda^+\rangle|-\lambda^-\rangle - \sqrt{2}c_0|-\lambda^-\lambda^+\rangle|\ \lambda^-\rangle + \sqrt{2}c_0|-\lambda^-\lambda^-\rangle|\lambda^+\rangle \qquad (3.37)$$

Finally, to put the wavefunction into normalised determinantal form requires $c_{2\lambda} = -1/\sqrt{3}$, $c_0 = 1/\sqrt{6}$ and hence $c_0^{\sim} = -1/\sqrt{2}$ to give

$$|e_\lambda^3\ ^2E_\lambda\ \lambda\ -1/2\rangle = \frac{1}{\sqrt{3}}(|-\lambda^-\rangle|\lambda^-\lambda^+\rangle - |\lambda^-\rangle|-\lambda^-\lambda^+\rangle + |-\lambda^-\lambda^-\rangle|\lambda^+\rangle) \equiv |-\lambda^-\lambda^-\lambda^+\rangle \qquad (3.38)$$

Using the same coefficients in the expressions for the other states gives the results in Table 3.5

Table 3.5: Anti-symmetrised three-electron spin-orbit wavefunctions for λ^3 configuration

$\lvert \Gamma_\lambda^{n_e\ 2S+1}\Gamma_\Lambda M_\Lambda\ \Sigma\rangle$	Normalised Slater determinant	ε_{SO}	$\varepsilon_{Zeeman}/\mu_B B$
$\lvert e_\lambda^3\ ^2E_\lambda\ \lambda\ 1/2\rangle$	$\lvert -\lambda^+\ \lambda^-\ \lambda^+\rangle$	$-a'_\lambda/2$	$(g_\lambda + g_e)\cos\theta/2$
$\lvert e_\lambda^3\ ^2E_\lambda\ -\lambda\ -1/2\rangle$	$\lvert -\lambda^-\ -\lambda^+\ \lambda^-\rangle$	$-a'_\lambda/2$	$-(g_\lambda + g_e)\cos\theta/2$
$\lvert e_\lambda^3\ ^2E_\lambda\ \lambda\ -1/2\rangle$	$\lvert -\lambda^-\ \lambda^-\ \lambda^+\rangle$	$a'_\lambda/2$	$(g_\lambda - g_e)\cos\theta/2$
$\lvert e_\lambda^3\ ^2E_\lambda\ -\lambda\ 1/2\rangle$	$\lvert -\lambda^-\ -\lambda^+\ \lambda^+\rangle$	$a'_\lambda/2$	$-(g_\lambda - g_e)\cos\theta/2$

3.3 Electronic Matrix Elements

In this Section, general methods are presented for determining spin-orbit, electric-dipole and Zeeman matrix elements using the wavefunctions determined in the previous section are considered. In cases where the resulting matrix is diagonal, the energy of the states due to the relevant interaction is determined by inspection. The effects of static vibronic interaction are considered in Chapter 5 .

3.3.1 Reduction to One-electron Form

The reduction of many-electron matrix elements to one-electron form can be simplified using the Slater-Condon rules. These apply to determinantal wavefunctions and can be used for any operator that is the sum of one-electron operators of the form

$$F = \sum_i f(i) \tag{3.39}$$

The first step is to permute the spin-orbitals in one determinant to achieve maximal coincidence with the order in the other. This introduces a factor $(-1)^{n_p}$ where n_p is the number of permutations required. The rules for a one-electron operator are then as follows:

If the determinants are identical, then

$$\langle \phi_1 \phi_2 \phi_3 \ldots \phi_N | F | \phi_1 \phi_2 \phi_3 \ldots \phi_N \rangle = \sum_i \langle \phi_i | f(i) | \phi_i \rangle \tag{3.40}$$

If they differ by only one spin-orbital ($\phi_k \neq \phi_j$), then

$$\langle \phi_1 \phi_2 \phi_3 \ldots \phi_j \ldots \phi_N | F | \phi_1 \phi_2 \phi_3 \ldots \phi_k \ldots \phi_N \rangle = \langle \phi_j | f(i) | \phi_k \rangle \tag{3.41}$$

Finally, if the determinants differ by more than one spin-orbital, the matrix element is zero.

3.3.2 Electronic Angular Momenta

There are two reasons for calculating electronic angular momenta. Firstly, they contribute magnetic moments that are manifest in the Zeeman effect, and secondly, they are involved in spin-orbit interactions.

Electron spin

The many-electron spin operator is a sum of 1-*e* contributions:

$$\boldsymbol{S} = \sum_k \boldsymbol{s}_k \tag{3.42}$$

$\boldsymbol{S}$ and $\boldsymbol{s}$ are pseudo-vector operators with projections onto axis η (x, y, z) that are related by

$$S_\eta = \sum_k (s_\eta)_k \tag{3.43}$$

The complex-basis ($\mathbf{D}_n \supset \mathbf{C}_n$) operators are

$$S_{\pm 1} = \mp \frac{1}{\sqrt{2}} (S_x \pm i S_y) \tag{3.44}$$

$\boldsymbol{S}$ and its components are imaginary in the sense described by equation (2.61), so the non-zero first-order matrix elements of functions that transform as degenerate irreps can be determined using the rules at the end of Section 2.2.4.

In $\mathbf{D}_n \supset \mathbf{C}_n$, S_z (and s_z) transforms as $|\widetilde{0}\ 0\rangle$, which belongs to the antisymmetric square for a basis of degenerate bosonic (category-1) functions and the symmetric square of degenerate fermionic (category-2) functions. Thus for all spin bases, the only non-zero matrix elements are (in units of $\hbar$)

$$\langle S\ \Sigma | S_z | S\ \Sigma \rangle = \Sigma \tag{3.45}$$

$S_{\pm 1}$ transform as $|1\ \pm 1\rangle$, and can be related to the annihilation and creation operators $s^{\pm}$ according to Appendix A.4. Considering only the basis $|1/2\ \pm 1/2\rangle$ (which is relevant to this work), the non-zero matrix elements are

$$\langle 1/2\ \pm 1/2\ |S_{\pm 1}|1/2\ \mp 1/2\rangle = \mp 1/\sqrt{2} \tag{3.46}$$

Or in terms of the Cartesian components,

$$\langle 1/2\ \pm 1/2\ |S_x|1/2\ \mp 1/2\rangle = 1/2 \tag{3.47}$$

$$\langle 1/2\ \pm 1/2|S_y|1/2\ \mp 1/2\rangle = \mp i/2 \tag{3.48}$$

Electronic orbital angular momenta

The many-electron operator for the orbital angular momentum about a given centre is again a sum of 1-*e* terms:

$$\boldsymbol{L} = \sum_k \boldsymbol{l}_k \tag{3.49}$$

where

$$\boldsymbol{l}_k = -i\hbar(\boldsymbol{r}_k \times \boldsymbol{p}_k) \tag{3.50}$$

$\boldsymbol{r}_k$ and $\boldsymbol{p}_k$ being the vector operators pertaining to the position and conjugate linear momentum of electron k with respect to that centre. The determination of the orbital angular momentum is therefore a matter of reducing the many-electron matrix elements to 1-*e* form using the Slater-Condon rules, then evaluating the latter.

$\boldsymbol{L}$ and $\boldsymbol{l}$ are imaginary (pseudo-vector) operators with the same transformation properties as those described for $\boldsymbol{S}$ above. All orbital functions are bosonic (category-1) so the only non-zero first-order matrix elements are those of the z component operators $l_z = -i\hbar(x\partial/\partial y - y\partial/\partial x)$ and L_z, which, in the chain $\mathbf{D}_n \supset \mathbf{C}_n$ transform as $|\tilde{0}\ 0\rangle$.

Using the WET, the non-zero first-order matrix elements of L_z are of the form (in units of $\hbar$)

$$\langle \Lambda\ \pm\Lambda\,|\,L_z\,|\,\Lambda\ \pm\Lambda\rangle \equiv \pm g_\Lambda/2 \tag{3.51}$$

For the 1-e wavefunctions, the matrix elements have the explicit form

$$\langle \lambda \pm\lambda | l_z | \lambda \pm\lambda \rangle \equiv \pm g_\lambda/2 \tag{3.52}$$

where g_λ is the orbital g value for an electron in an e_λ orbital. For systems with $\mathbf{D}_\infty$ symmetry,

$$g_\lambda = 2\lambda \tag{3.53}$$

In lower symmetries, the g_λ generally has a smaller value:

$$g_\lambda = 2\kappa\lambda \quad \text{in } \mathbf{D}_n \tag{3.54}$$

The parameter κ, called the orbital reduction factor, can be due to a number of causes including covalent bonding interactions, vibronic coupling and crystal-field effects.

In the following sections it will be necessary to determine the components of orbital angular momentum with respect to several centres. To determine the contribution of the Zeeman effect it is necessary to determine the matrix elements relative to the centre of the molecule. But to determine the SO interaction, the orbital angular momenta about each of the nuclei of the molecule are required.

The molecules examined in this thesis are planar molecules with delocalised π molecular orbitals that encircle the z-axis and are composed of linear combinations of p_z atomic orbitals (AOs). The components of angular momentum due to electronic motions in a localised AO about the nucleus of an atom are readily determined. However, to calculate the values about other points – namely the molecular centre or another nucleus – a transformation of the operator l_z to the new point of reference is required.

Consider an orbital p_a localised on atom a. The operator that relates the z component of angular momentum operator about a, l_z^a, to the operator l_z^o about centre o, is

$$l_z^o = l_z^a - i\hbar D_{oa}(\sin\gamma\partial/\partial y_a + \cos\gamma\partial/\partial x_a) \tag{3.55}$$

Here, the x and y coordinates in the two reference frames (x_a, y_a and x_o, y_o) are taken to be parallel but displaced, D_{oa} is the distance between centres o and a, and γ is the angle defined in Figure 3.1.

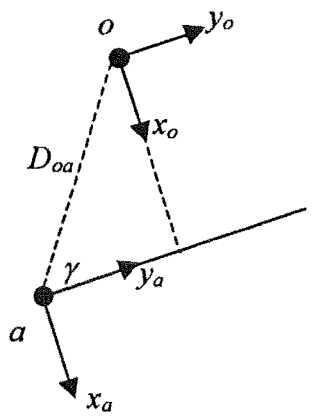

Figure 3.1: A view (looking down the z axis) of the relationship between the coordinate systems based on centres o and a in the same x-y plane.

If p_a is a p_z orbital then $\hat{l}_z^o|p_a\rangle = 0$, and the first term of the operator in equation (3.25) does not contribute to the orbital angular momentum. Furthermore, if the electron is confined to p_a, a change of reference coordinates will not alter the situation, because a localised p_z orbital still contributes no net angular momentum in the z direction. Thus,

$$\langle p_a|\hat{l}_z^o|p_a\rangle = 0 \tag{3.56}$$

Another possibility (in a delocalised system) is that the electron moves from p_a on atom a to p_b on atom b (Figure 3.2). The appropriate matrix element in this case is

$$\langle p_b|\,\hat{l}_z^o\,|p_a\rangle = \langle p_b|\,-i\hbar D_{oa}(\sin\gamma\partial/\partial y_a + \cos\gamma\partial/\partial x_a)\,|p_a\rangle \tag{3.57}$$

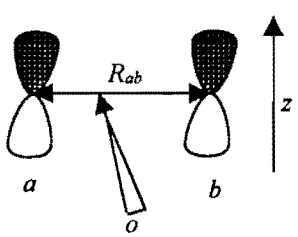

Figure 3.2: Two-centre angular momentum about o due to motion of the electron in the plane of the molecule.

This matrix element can be evaluated by transforming to confocal elliptical coordinates with a and b at the focii. Using Slater-type atomic orbitals of the form

$$|p_a\rangle = \left(\frac{k^5}{\pi}\right)^{1/2} z e^{-kr_a} \tag{3.58}$$

where k is a shielding constant and r_a is the distance of the electron from the nucleus of atom a, the result is (in units of $\hbar$)[3-5]

$$\langle p_b|l_z^o|p_a\rangle = iD_{oa}k^2R_{ab}e^{-kR_{ab}}\sin\gamma_{oab}[1 + kR_{ab} + (kR_{ab})^2/3]/5 \tag{3.59}$$

where R_{ab} is the distance between a and b and γ_{oab} is the angle between the vector connecting two atoms a and b and another vector connecting a to the centre about which the orbital angular momentum is being calculated.

A number of useful, general results derive directly from equation (3.59). Firstly, since $R_{aa} = 0$, $\langle p_a|l_z^o|p_a\rangle$ vanishes, as anticipated in equation (3.56). Secondly, if the centre about which that angular momentum is being evaluated is moved to one of the atoms in question (*i.e.* $o = a$), then, since $D_{aa} = 0$,

$$\langle p_b|l_z^a|p_a\rangle = 0 \tag{3.60}$$

and

$$\langle p_a|l_z^a|p_b\rangle = \langle p_b|l_z^a|p_a\rangle^* = 0 \tag{3.61}$$

In a classical sense, these last two results are hardly surprising since they represent cases where the (average) path of the electron is in a direct line between the two atoms. They have significant consequences for SO coupling in planar delocalised π systems since the lowest-order non-vanishing components of orbital angular momentum around any nucleus are therefore three-centre terms of the type

$$\langle p_b|l_z^c|p_a\rangle = iD_{oa}k^2R_{ab}e^{-kR_{ab}}\sin\gamma_{cab}[1 + kR_{ab} + (kR_{ab})^2/3]/5 \tag{3.62}$$

This represents the component of angular momentum about a third nucleus, *c*, as the electron moves from atom *a* to atom *b*. Because the distances between nuclei are large in comparison with the separation of an electron from the nucleus in an atom, the magnitude of SO coupling in planar π delocalised molecules is therefore very weak.[6]

3.3.3 Spin-orbit Coupling

Spin-orbit (SO) coupling comes about because of the interaction between an electrons intrinsic, relativistic electric dipole (due to spin) and the internal electric fields of the molecule. In principle, all charged centres, including other electrons, should be considered, but to avoid the complications that this would entail (including the fact that the corresponding operator would not be a sum of one-electron terms), the electrons are regarded as shielding each other from the nuclei. A screening constant is introduced and the charges are taken to have effective values and to be at the positions of the nuclei. With these approximations, the effect can be treated as equivalent to an interaction between the spin magnetic moment and a magnetic field generated by the component of the electron's orbital angular momentum about a nucleus. Hence the name spin-orbit coupling.

For a single electron, *k*, orbiting a single nucleus, *i*, the SO Hamiltonian is

$$\mathcal{H}_{so}(i,k) = \xi_{ik}\, \boldsymbol{l}_k^i \cdot \boldsymbol{s}_k \tag{3.63}$$

where $\boldsymbol{l}_k^i$ is the component of angular momentum about the nucleus and ξ_{ik} is the corresponding spin-orbit coupling constant. For a molecule

$$\mathcal{H}_{so} = \sum_k \sum_i \mathcal{H}_{so}(i,k) = \sum_k \sum_i \xi_{ik}\, \boldsymbol{l}_k^i \cdot \boldsymbol{s}_k \tag{3.64}$$

where the sums are over all nuclei and unpaired electrons (the contribution from pairs of electrons in the same orbitals with opposite spin cancel). Note that although the individual operators $\boldsymbol{l}$ and $\boldsymbol{s}$ are pseudo-vector operators, $\mathcal{H}_{so}$ is a scalar operator that transforms as the totally symmetric irrep of the molecular point group.

In order for a state to exhibit SO splitting it must involve both orbital and spin degeneracies. Thus, the only states of Table 3.1 and Table 3.5 that need be considered are those belonging to $^2E_\Lambda$ terms from e_λ^1 or e_λ^3 configurations. For these states, the only non-zero matrix elements of $\mathcal{H}_{SO}$ involve $l_z s_z$ because (as discussed in Section 3.3.2) the only non-zero orbital-angular-momentum matrix elements are those of l_z. Thus, these wavefunctions are diagonal in the SO effect, with non-zero first-order matrix elements given by

$$\langle {}^2E_\Lambda M_\Lambda \Sigma | \mathcal{H}_{so} | {}^2E_\Lambda M_\Lambda \Sigma \rangle = -M_\Lambda \Sigma A'_\Lambda / \Lambda \qquad (3.65)$$

where A'_Λ is an empirical SO coupling parameter.[i] Using the Slater-Condon rule in equation (3.40) the matrix elements for the two SO levels can be written in one-electron form:

$$\langle {}^2E_\Lambda \pm\Lambda \mp 1/2 | \mathcal{H}_{so} | {}^2E_\Lambda \pm\Lambda \mp 1/2 \rangle = (-1)^{(n_e-1)/2} \langle \lambda\lambda | \sum_i \xi_i l'_k | \lambda\lambda \rangle /2 \equiv (-1)^{(n_e-1)/2} a'_\lambda /2 \quad (3.66)$$

$$\langle {}^2E_\Lambda \pm\Lambda \pm 1/2 | \mathcal{H}_{so} | {}^2E_\Lambda \pm\Lambda \pm 1/2 \rangle = -(-1)^{(n_e-1)/2} \langle \lambda\lambda | \sum_i \xi_k l'_k | \lambda\lambda \rangle /2 \equiv -(-1)^{(n_e-1)/2} a'_\lambda /2 \quad (3.67)$$

Parameter a'_λ is the spin-orbit coupling parameter for an e_λ electron, and the phase factor $(-1)^{(n_e-1)/2}$ accounts for the regular and inverted splittings for e_λ^1 and e_λ^3 configurations, respectively. Thus, each $^2E_\lambda$ term splits into two doubly degenerate SO levels with a separation of $\Delta\varepsilon_{SO} = |A'_\Lambda| = |a'_\lambda|$ (Figure 3.3).

---

[i] Parameters A'_Λ and a'_λ are related to A_Λ and a_λ used by Herzberg[2, 10] by $A'_\Lambda = \Lambda A_\Lambda$ and $A_\Lambda a'_\lambda = \lambda a_\lambda$

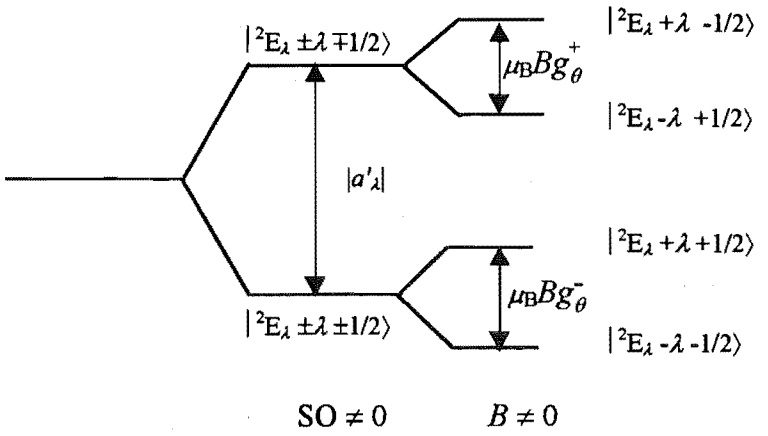

Figure 3.3: Energy-level diagram for a $^2E_\lambda$ term derived from an e_λ^1 configuration, with a magnetic field at an angle θ with respect to the z axis. For an e_λ^3 configuration the spin-orbit levels would be inverted.

3.3.4 The Zeeman Effect

The interaction between an external magnetic field, with inductance $\boldsymbol{B}$, and the magnetic dipole, μ, of a molecule gives rise to the Zeeman effect, for which the Hamiltonian is

$$\mathcal{H}_{\text{Zeeman}} = -\boldsymbol{\mu}\cdot\boldsymbol{B} \tag{3.68}$$

The strong magnetic dipoles due to the spin and orbital dynamics of electrons are responsible for the *electronic* Zeeman effect. Since the total spin and orbital angular momenta can be written as sums of the contributions from each electron, the electronic magnetic moment operator is

$$\boldsymbol{\mu} = -\mu_B(\boldsymbol{L} + g_e\boldsymbol{S}) = -\mu_B\sum_k(\boldsymbol{l}_k + g_e\boldsymbol{s}_k) \tag{3.69}$$

where μ_B is the Bohr magneton, g_e is the free-electron g value and the orbital angular momenta are referenced to the molecular centre of symmetry.

A consequence of the Zeeman effect is that all spin degeneracies are removed by the application of an external magnetic field (Kramers theorem[7]). Thus, each of the doubly degenerate SO levels determined in Section 3.3.3 is split by an amount that depends on the projection of the magnetic field onto the molecular reference coordinates. This Zeeman splitting is quantified by a "g" matrix, whose principal

components are labelled g_η where $\eta = x, y, z$. For a field along the molecular η direction,

$$\Delta\varepsilon_{\text{Zeeman}} = g_\eta \mu_B B \tag{3.70}$$

For n-fold axial systems with $n > 2$, the x and y directions are equivalent and there are only two independent principal g values for each pair of degenerate states. These are named "g-parallel" ($g_\parallel$) and "g-perpendicular" ($g_\perp$) where

$$g_\parallel = g_z \tag{3.71}$$

$$g_\perp = g_x = g_y \tag{3.72}$$

These g values are determined by matrix elements of the relevant components of $\boldsymbol{L}+g_e\boldsymbol{S}$. For the $^2E_\Lambda$ states, the first-order matrix elements are

$$\langle {}^2\mathrm{E}_\Lambda M_\Lambda' \Sigma' | \boldsymbol{L}+g_e\boldsymbol{S} | {}^2\mathrm{E}_\Lambda M_\Lambda \Sigma\rangle = \langle {}^2\mathrm{E}_\Lambda M_\Lambda' | \boldsymbol{L} | {}^2\mathrm{E}_\Lambda M_\Lambda\rangle \delta_{\Sigma'\Sigma} + \langle \Sigma' | g_e\boldsymbol{S} | \Sigma\rangle \delta_{M_\Lambda' M_\Lambda} \tag{3.73}$$

Following Section 3.3.2, the only non-zero matrix elements are those of the component operators S_x, S_y, S_z and L_z, corresponding to $\Delta\Sigma = \pm 1$ or 0, and $\Delta M_\Lambda = 0$. Using equations (3.45), (3.48), (3.49) and (3.51),

$$\langle {}^2\mathrm{E}_\Lambda M_\Lambda \pm 1/2 | L_z + g_e S_z | {}^2\mathrm{E}_\Lambda M_\Lambda \pm 1/2\rangle = \frac{M_\Lambda g_\Lambda}{\Lambda\ 2} \pm \frac{g_e}{2} \tag{3.74}$$

$$\langle {}^2\mathrm{E}_\Lambda M_\Lambda' \pm 1/2 | L_x + g_e S_x | {}^2\mathrm{E}_\Lambda M_\Lambda \mp 1/2\rangle = \frac{g_e}{2} \delta_{M_\Lambda' M_\Lambda} \tag{3.75}$$

$$\langle {}^2\mathrm{E}_\Lambda M_\Lambda' \pm 1/2 | L_y + g_e S_y | {}^2\mathrm{E}_\Lambda M_\Lambda \mp 1/2\rangle = \mp i\frac{g_e}{2} \delta_{M_\Lambda' M_\Lambda} \tag{3.76}$$

Equation (3.74) immediately shows that the wavefunctions of both degenerate SO levels are diagonal in the z component of the magnetic dipole operator. (The explicit values of the Zeeman shifts for the states are listed in terms of the one-electron g values in Table 3.1 and Table 3.5.) For these states

$$g_{\|} = \frac{M_\Lambda}{\Lambda} g_\Lambda + g_e \tag{3.77}$$

From equations (3.75) and (3.76), $g_\perp = 0$ for these states – since no degenerate (at zero-field) pair of SO levels share the same values of M_Λ, the $\delta_{M_\Lambda', M_\Lambda}$ factor cause all first-order matrix elements to vanish. This remains true even when magnetic interactions between different SO levels from the same term are accounted for – these cause (small) shifts of both states of an SO level in the same direction. However, as will be demonstrated in Chapter 6, $g_\perp$ may become non-zero when the molecule is influenced by symmetry-lowering perturbations, such as crystal fields.

If the angle between $\boldsymbol{B}$ and the molecular symmetry axis is θ, then the Zeeman splittings of the SO levels of a $^2E_\Lambda$ term are

$$\Delta\varepsilon_{\text{Zeeman}} = \overset{\pm}{g}_\theta \mu_B B \tag{3.78}$$

where g_θ is an effective g value, the superscripts + or – respectively indicating the upper or lower SO levels. In the absence of external crystal-field perturbations (when $g_\perp = 0$),

$$g_\theta = g_{\|} \cos\theta \tag{3.79}$$

as shown in Figure 3.3. Explicit values of Zeeman shifts are listed earlier in Table 3.1 and Table 3.5.

3.3.5 Electronic Transition Moments

The molecular electronic transitions considered in this thesis are induced by interactions between molecular electric dipoles and the electric field of the radiation. In the absence of significant SO mixing between terms, these change only the orbital states, so the spin selection rules are $\Delta S = 0$ and, for an axial molecule, $\Delta\Sigma = 0$. Furthermore, since a photon is a vector boson, the orbital selection rules for axial molecules are $\Delta\Lambda = 0, \pm 1$ and $u \leftrightarrow g$.

The electric dipole operator is

$$\boldsymbol{m} = \sum_i \boldsymbol{m}_i \tag{3.80}$$

where the sum is over all the electrons. With the electronic wavefunctions of the form of equation (3.26) the electric-dipole transition moments are

$$\langle\chi_m|\langle\phi_m(q, Q)|\boldsymbol{m}|\phi_k(q, Q)\rangle|\chi_k\rangle = \langle\phi_m(q, Q_0)|\boldsymbol{m}|\phi_k(q, Q_0)\rangle\langle\varphi_m|\varphi_k\rangle$$

$$+\sum_\eta \Big[\sum_{m \neq j} \frac{\langle\phi_m(q,Q_0)|\left(\frac{\partial V}{\partial Q_\eta}\right)_0|\phi_j(q,Q_0)\rangle}{W_j(Q_0)-W_m(Q_0)}\langle\phi_j(q,Q_0)|\boldsymbol{m}|\phi_k(q,Q_0)\rangle$$

$$+ \sum_{j \neq k}\langle\phi_m(q, Q_0)|\boldsymbol{m}|\phi_j(q, Q_0)\rangle\frac{\langle\phi_j(q,Q_0)|\left(\frac{\partial V}{\partial Q_\eta}\right)_0|\phi_k(q,Q_0)\rangle}{W_k(Q_0)-W_j(Q_0)}\Big]\langle\varphi_m|Q_\eta|\varphi_k\rangle \tag{3.81}$$

In the Franck-Condon (FC) approximation, the electronic functions are assumed to be sufficiently slowly varying functions of Q that they are well approximated by their value at Q_0, and only the first term of equation (3.81) need be evaluated. The selection rules for vibronic transitions within the envelope of an allowed electronic transition are then determined by the $\langle\varphi_m|\varphi_j\rangle$, the FC vibrational overlap factors. In group-theoretical terms, assuming that the ground state and excited states have the same symmetry group, the orthogonality theorems of Section 2.1.1 require that φ_m and φ_j transform as the same irrep. As will be seen in Section 3.4 Δv can take any value for a totally symmetric vibrational mode. Thus, in the FC approximation, only progressions in totally symmetric vibrational modes are permitted with intensities determined by the magnitude of the displacement between the two potential energy surfaces. For all other modes the selection rules are $\Delta v = 0, \pm 2, \pm 4, \ldots$ but unless there is a large change in geometry only the transitions with $\Delta v = 0$ are important. Evaluation of the square of the FC factor allows determination of the intensity of the vibronic transition. If the potential surfaces have the same shape and are not displaced relative to one another, the overlap function reduces to a delta function

The FC approximation is not very rigorous, and its breakdown may be generally anticipated. Consideration of the second, Herzberg-Teller (HT), term in equation (3.81) has especially significant consequences with regard to formally forbidden or

weakly allowed spectroscopic processes, as will be seen for the cyclooctatetraene radical anion in Chapter 8. In particular the terms $\langle\varphi_m|Q_\eta|\varphi_j\rangle$ permits the existence of other (false) origins on which progressions can be built. The determination of these matrix elements is covered in the next section.

Of particular importance in this thesis are the transition moments involving the complex components $m_{\pm1}$ related to the Cartesian components according to equation (2.63)

$$m_{\pm1} = \mp\frac{1}{\sqrt{2}}(m_x \pm i m_y) \tag{3.82}$$

These interact with circularly polarised radiation that has a component of propagation along the molecular symmetry axis, and are responsible for transitions with $\Delta\Lambda = \pm1$. In the chain $\mathbf{D}_n \supset \mathbf{C}_n$, these transform as $|1\ \pm1\rangle$.

For transitions between ^{2}E states of an axial molecule, the matrix elements of these operators can be related to each other by employing the WET:

$$\langle {}^2\mathrm{E}_{\Lambda+1}\ \mp(\Lambda+1)\ \Sigma|m_{\mp1}|{}^2E_\Lambda\ \mp\Lambda\ \Sigma\rangle = \frac{1}{\sqrt{2}}\langle {}^2\mathrm{E}_{\Lambda+1}||m||{}^2\mathrm{E}_{\Lambda+1}\rangle \equiv \mathfrak{M}_{\mp1} \tag{3.83}$$

and

$$\langle {}^2\mathrm{E}_{\Lambda-1}\ \mp(\Lambda-1)\ \Sigma|\,m_{\pm1}\,|\,{}^2\mathrm{E}_\Lambda\ \mp\Lambda\ \Sigma\rangle = \frac{1}{\sqrt{2}}\langle {}^2\mathrm{E}_{\Lambda-1}||m||{}^2\mathrm{E}_\Lambda\rangle \equiv \mathfrak{M}_{\pm1} \tag{3.84}$$

For both of these cases,

$$|\mathfrak{M}_{+1}| = |\mathfrak{M}_{-1}| \equiv |\mathfrak{M}| \tag{3.85}$$

but the ±1 subscripts are retained to keep track of the transition polarisations for calculation of MCD (Chapter 4).

3.4 Vibrational States

In this section the wavefunctions for the vibrational states of axial molecules are considered. These are solutions of the vibrational Hamiltonian

$$\mathcal{H}_{\text{vib}} = T_{\text{n}}(Q) + W(Q) \tag{3.86}$$

$W(Q)$ is given in equation (3.25) and can be considered as an effective potential for vibrational motion. It represents a multidimensional paraboloid surface, and the system will undergo harmonic oscillations. For a pure vibrational problem $W(Q_0)$ is normally set to zero and, since the equilibrium position is a minimum, all first derivatives at Q_0 are equal to zero. Under the assumption of such conditions, the harmonic-oscillator (HO) approximation

$$W(Q) = \frac{1}{2}\sum_{\eta\mu} k_{\eta\mu} Q_\eta Q_\mu \tag{3.87}$$

where

$$k_{\eta\mu} = \left(\frac{\partial^2 W(Q)}{\partial Q_\eta \partial Q_\mu}\right)_0 \tag{3.88}$$

measures the restoring force and is called a force constant.

Normal coordinates are linear combinations of the vibrational coordinates that simultaneously bring the kinetic and potential energy terms of the vibrational Hamiltonian into diagonal form. In a normal-coordinate basis, the non-zero force constants are also diagonal, with values

$$k_\eta \equiv k_{\eta\eta} = \left(\frac{\partial^2 W}{\partial Q_\eta^{\,2}}\right)_0 \tag{3.89}$$

In the HO approximation, the kinetic and potential energy operators for a general normal coordinate are given by[ii]

$$T_n(Q_\eta) = \frac{\omega_\eta^2}{2k_\eta} P_\eta^2 \tag{3.90}$$

$$W(Q_\eta) = \frac{1}{2} k_\eta Q_\eta^2 \tag{3.91}$$

$\omega_\eta = 2\pi\nu_\eta$ is the 'circular' frequency of vibration along coordinate Q_η and P_η is the conjugate momentum operator;

$$P_\eta = -i\hbar \frac{\partial}{\partial Q_\eta} \tag{3.92}$$

Although the HO approximation might seem drastic, in practice, under most circumstances it is reasonable for low-energy vibrational levels. Furthermore, the complete set of HO functions (and their products) spans the space of all vibrational functions, and so forms a valid basis for more complicated cases.

3.4.1 Non-degenerate Vibrations

Since the vibrational Hamiltonian is diagonal in terms of normal coordinates, the eigenvalues for a single non-degenerate coordinate are

$$\varepsilon_v = (v + 1/2)\hbar\omega \tag{3.93}$$

where $v = 0, 1, 2, \ldots$ is a vibrational quantum number. The corresponding eigenfunctions, denoted $|v\rangle$ for brevity, have the form

$$|v\rangle = N_v H_v(y)\, e^{-y^2/2} \tag{3.94}$$

[ii] For non-mass-weighted coordinates, $k = \mu\omega^2$; for mass-weighted coordinates, $k = \omega^2$ and for dimensionless coordinates, $k = \hbar\omega$

N_v is a normalisation coefficient and $H_v(y)$ is a Hermite polynomial:

$$y = Q/\alpha \tag{3.95}$$

$$\alpha = \left(\frac{\hbar^2}{\mu k}\right)^{1/4} \tag{3.96}$$

and μ is the reduced mass. $|0\rangle$ is called the zero-point level while $|1\rangle$, with a single quantum of vibrational excitation, is called a *fundamental* level. Excitation of two or more quanta gives *overtone* levels.

Since a non-degenerate vibrational mode cannot be fundamentally changed by a molecular symmetry operation, the corresponding group-theoretical representation will comprise scalar representatives whose values are just the character, $\chi_Q(R) = \pm 1$, under each symmetry operation. The explicit forms of the Hermite polynomials, show that the wavefunction for non-degenerate harmonic-oscillator states with even v involve even powers of Q while those odd v involve odd powers of Q. Thus for state $|v\rangle$ of a non-degenerate vibrational mode,

$$RQ^v = \chi_Q(R)Q^v \quad \text{for odd } v \tag{3.97}$$

whereas

$$RQ^v = Q^v \quad \text{for even } v \tag{3.98}$$

It follows, therefore, that all even overtones belong to the totally symmetric irrep while all odd overtone levels belong to the same irrep as Q.

The total wavefunction for a number of non-degenerate normal coordinates is a product of vibrational functions

$$|v_1, v_2, \ldots\rangle = \prod_\eta |v_\eta\rangle \tag{3.99}$$

This *combination* state will be non-degenerate with transformation properties determined by the direct product of the appropriate one-dimensional irreps. The corresponding total energy is

$$\varepsilon_{\text{vib}} = \sum_{\eta} (v_\eta + 1/2)\hbar\omega_\eta \tag{3.100}$$

3.4.2 Doubly Degenerate Vibrations

The vibrational state pertaining to a pair of degenerate vibrational coordinates, Q_1 and Q_2, can be designated $|v_1\ v_2\rangle$. However, any pair of orthonormal linear combinations of these coordinates also provides a valid basis for the vibrations. An important pair is formed by the complex coordinates

$$Q_\pm = \frac{1}{\sqrt{2}}(Q_1 \pm iQ_2) \tag{3.101}$$

with conjugate momenta

$$P_\pm = \frac{1}{\sqrt{2}}(P_1 \pm iP_2) \tag{3.102}$$

Using these momenta, equation (3.90) gives

$$T_n(Q_1) + T_n(Q_2) = \frac{\omega^2}{2k}(P_1^2 + P_2^2) = \frac{\omega^2}{k}P_+ P_- \tag{3.103}$$

In the $\mathbf{D}_\infty \supset \mathbf{C}_\infty$ chain, $Q_\pm$ transform as partners $m = \pm j$ of a doubly degenerate irrep, j, and therefore entail *vibrational angular momentum* $m\hbar$ about the symmetry axis. Q_+ represents rotation in the positive sense, as illustrated in Figure 3.4 for the degenerate bending modes of a linear triatomic molecule, and transforms as $|j\ j\rangle$. Q_- represents rotation in the negative sense and transforms as $|j\ -j\rangle$.

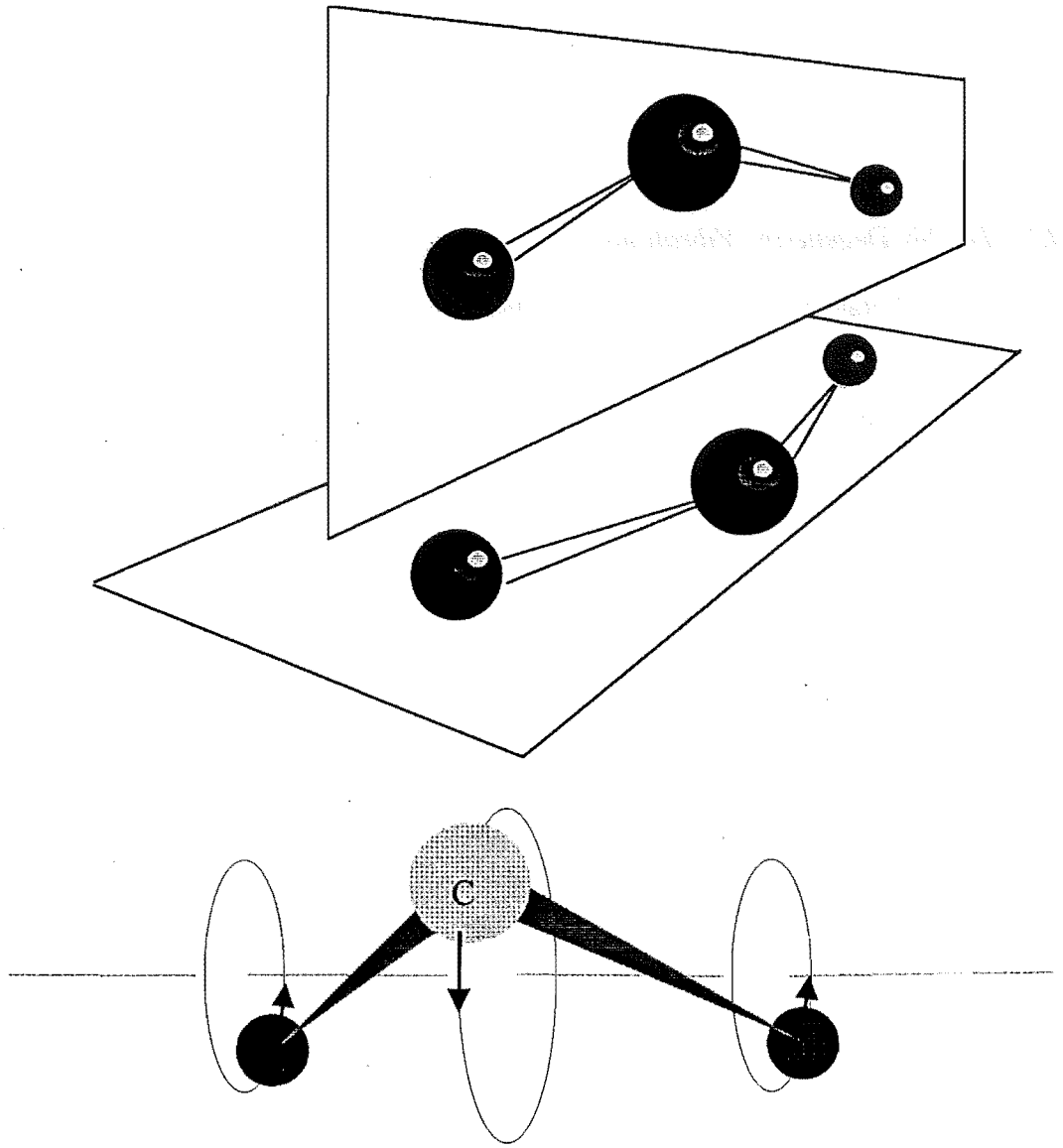

Figure 3.4: Top: instantaneous displacements of a pair of orthogonal degenerate bending modes, Q_1 and Q_2, of CO_2. Bottom: the motion represented by the linear combination, Q_+, of Q_1 and Q_2

In the complex basis, the total wavefunctions can be denoted $|v_+ v_-\rangle$. However, it is often useful to write them as $|v\ \ell\rangle$ where

$$v = v_+ + v_- \tag{3.104}$$

$$\ell = v_+ - v_- = v, v\text{-}2, \ldots -v \tag{3.105}$$

there being v+1 values of ℓ for every v.[iii] Quantum number v gives the total number of vibrational quanta and defines the vibrational energy

$$\varepsilon_v = (v+1)\hbar\omega \tag{3.106}$$

while ℓ gives a measure of the net component of vibrational angular momentum along molecular (z) axis – in units of $\hbar$

$$N_\ell = \ell j \tag{3.107}$$

The transformation properties of the states comprising an overtone level can be determined by successive coupling of single quanta into the $|0\ 0\rangle$ state, using vector coupling coefficients. However, vibrational coordinates are boson-like, and the resulting wavefunctions must therefore be symmetric with respect to exchange of vibrational coordinates. Consequently, antisymmetric wavefunctions disappear, and many of the irreps determined by direct vector coupling are redundant. To avoid unnecessary work, an equation can be derived that gives the characters of that part of representative spanned by the symmetric wavefunctions.[8, 9]

For each point-group symmetry operation, R, there is a linear combination of Q_1 and Q_2 for which the matrix representative $D(R)$ is diagonal with elements d_1 and d_2. The character under R is therefore

$$\chi(R) = d_1 + d_2 \tag{3.108}$$

which is independent of the choice of the particular linear combination. For an overtone level involving v quanta of these modes, the vibrational degeneracy is v+1. The corresponding wavefunctions, using the $|v_1\ v_2\rangle$ scheme and omitting invariant terms, have the form

$$|v_1{=}v\ \ v_2{=}0\rangle \sim H_v(Q_1)$$

[iii] For an n-fold degenerate vibration, the number of states comprising the overtone level with quantum number v is $(v + n - 1)!/(v(n - 1))!$[11]

$$|v_1=v\text{-}1 \;\; v_2=1\rangle \sim H_{v-1}(Q_1)H_1(Q_2)$$

$$|v_1=v\text{-}i \;\; v_2=i\rangle \sim H_{v-i}(Q_1)H_i(Q_2)$$

$$|v_1=0 \;\; v_2=v\rangle \sim H_v(Q_2) \qquad (3.109)$$

Each Hermite polynomial $H_{v-i}(Q_\eta)$ in equation (3.109) contains terms up to order v-i (i = 0, 1 ... v-1) in the coordinate Q_η. Since the symmetry transformations are linear operators, they mixed only terms of the same order amongst themselves. Hence, it is only necessary to determine the transformation properties of the highest-order terms, those in Q_1^v, $Q_1^{v-1}Q_2, \ldots Q_1^{v-i}Q_2^i, \ldots Q_2^v$, to determine the representations of the wavefunctions.

Since the functions in equation (3.109), and the discussion that precedes it, are a complete set of degenerate basis functions they must form a representation whose character under R is given by

$$\chi_v(R) = d_1^v + d_1^{v-1}d_2 + \ldots + d_1^1 d_2^{v-1} + d_2^v \qquad (3.110)$$

Determination of the ds would be tedious, but the characters can be obtained more simply by using a recursion formula. For the immediately lower overtone, the character is

$$\chi_{v-1}(R) = d_1^{v-1} + d_1^{v-2}d_2^1 + \ldots + d_2^{v-1} \qquad (3.111)$$

And from equation (3.108) the character for an operation consisting of R applied v times is

$$\chi(R^v) = d_1^v + d_2^v \qquad (3.112)$$

These give the result,

$$\chi_v(R) = \frac{1}{2}[\chi(R^v) + \chi_{v-1}(R)\chi_1(R)] \qquad (3.113)$$

The fact, noted above, that the antisymmetric products vanish, can be explicitly represented by rewriting equation (3.113) as

$$\chi_\nu(R) = \chi_{\nu-1}(R)\chi_1(R) - [\chi_{\nu-1}(R)\chi_1(R) - \chi(R^\nu)]/2 \qquad (3.114)$$

The first term gives the character of the direct-product representation without regard to the symmetry with respect to transposition of coordinates, while the second term removes those contributions due to antisymmetric functions.

Having determined the character of the representative in the above manner for each symmetry operation, the irreps are determined by reducing the representation as described in footnote i of Chapter 2 . The results for the states of doubly degenerate vibrational modes that transform as $j > 0$ in $\mathbf{D}_\infty$ are

$$\Gamma_v = 0 \oplus 2j \oplus \ldots vj \quad \text{for even } v \qquad (3.115)$$

$$\Gamma_v = j \oplus 3j \oplus \ldots vj \quad \text{for odd } v \qquad (3.116)$$

The corresponding vibrational angular momentum quantum numbers are

$$\ell = 0, \pm 2j, \ldots \pm v \quad \text{for even } v \qquad (3.117)$$

$$\ell = \pm 1, \pm 3, \ldots \pm v \quad \text{for odd } v \qquad (3.118)$$

These results are set out in tabular form for $v = 0$ to 5 in Table 3.6

Table 3.6: Transformation properties of the vibrational states $|v, \ell\rangle$ in the $|j\ m\rangle$ basis of $\mathbf{D}_\infty \supset \mathbf{C}_\infty$, $v \le 5$

$\mathbf{D}_\infty \supset \mathbf{C}_\infty$ label $\|j\ m\rangle$	$\|5j\ 5j\rangle$	$\|4j\ 4j\rangle$	$\|3j\ 3j\rangle$	$\|2j\ 2j\rangle$	$\|j\ j\rangle$	$\|0\ 0\rangle$	$\|j\ -j\rangle$	$\|2j\ -2j\rangle$	$\|3j\ -3j\rangle$	$\|4\ -4j\rangle$	$\|5\ -5j\rangle$
v											
5	$\|5\ 5\rangle$		$\|5\ 3\rangle$		$\|5\ 1\rangle$		$\|5\ -1\rangle$		$\|5\ -3\rangle$		$\|5\ -5\rangle$
4		$\|4\ 4\rangle$		$\|4\ 2\rangle$		$\|4\ 0\rangle$		$\|4\ -2\rangle$		$\|4\ -4\rangle$	
3			$\|3\ 3\rangle$		$\|3\ 1\rangle$		$\|3\ -1\rangle$		$\|3\ -3\rangle$		
2				$\|2\ 2\rangle$		$\|2\ 0\rangle$		$\|2\ -2\rangle$			
1					$\|1\ 1\rangle$		$\|1\ -1\rangle$				
0						$\|0\ 0\rangle$					

The $|\Gamma_{v\ell}\ \gamma_{v\ell}\rangle$ in $\mathbf{D}_n \supset \mathbf{C}_n$ can be obtained by subduction from $|j\ m_j\rangle$ by using the rules in Table 2.2.

3.5 Vibrational Matrix Elements

3.5.1 Non-degenerate Vibrations

To determine matrix elements of a 1-dimensional coordinate, Q_η, and its conjugate momentum, P_η, operators $a^\dagger$ and a are defined, which, respectively, create and destroy one quantum of the vibrations associated with Q_η (to convert to mass-weighted or dimensionless form, see footnote ii of this section)

$$a_\eta = \left(\frac{k}{2\hbar\omega}\right)^{1/2} Q_\eta + i\left(\frac{\omega}{2\hbar k}\right)^{1/2} P_\eta \tag{3.119}$$

$$a_\eta^\dagger = \left(\frac{k}{2\hbar\omega}\right)^{1/2} Q_\eta - i\left(\frac{\omega}{2\hbar k}\right)^{1/2} P_\eta \tag{3.120}$$

where

$$a_\eta|v\rangle = \sqrt{v}\,|v\text{-}1\rangle \tag{3.121}$$

$$a_\eta^\dagger|v\rangle = \sqrt{v+1}\,|v\text{+}1\rangle \tag{3.122}$$

Rearranging gives

$$Q_\eta = \left(\frac{\hbar\omega}{2k}\right)^{1/2} (a_\eta + a_\eta^\dagger) \tag{3.123}$$

$$P_\eta = i\left(\frac{k\hbar}{2\omega}\right)^{1/2} (a_\eta^\dagger - a_\eta) \tag{3.124}$$

These equations allow the generation of the vibrational matrix elements for a non-degenerate coordinate and its conjugate momentum. The results are given in Table 3.7

Table 3.7: Matrix elements of one-dimensional harmonic oscillator[8, 9]

$\langle v+1 \mid Q \mid v \rangle = \sqrt{\frac{\hbar\omega}{2k}}\sqrt{v+1}$	$\langle v+1 \mid P \mid v \rangle = i\sqrt{\frac{\hbar k}{2\omega}}\sqrt{v+1}$
$\langle v-1 \mid Q \mid v \rangle = \sqrt{\frac{\hbar\omega}{2k}}\sqrt{v}$	$\langle v-1 \mid P \mid v \rangle = -i\sqrt{\frac{\hbar k}{2\omega}}\sqrt{v}$
$\langle v-2 \mid Q^2 \mid v \rangle = \frac{\hbar\omega}{2k}\sqrt{v(v-1)}$	$\langle v-2 \mid P^2 \mid v \rangle = -\frac{\hbar k}{2\omega}\sqrt{v(v-1)}$
$\langle v \mid Q^2 \mid v \rangle = \frac{\hbar\omega}{2k}(2v+1)$	$\langle v \mid P^2 \mid v \rangle = \frac{\hbar k}{2\omega}(2v+1)$
$\langle v-2 \mid Q^2 \mid v \rangle = \frac{\hbar\omega}{2k}\sqrt{(v+2)(v+1)}$	$\langle v+2 \mid P^2 \mid v \rangle = -\frac{\hbar k}{2\omega}\sqrt{(v+1)(v+2)}$

3.5.2 Doubly Degenerate Vibrations

To determine matrix elements of $Q_\pm$ and their conjugate momenta, operators $a_\pm^\dagger$ and $a_\pm$ operators are defined, which, respectively, create and destroy one quantum of the vibrations associated with $Q_\pm$:[9]

$$a_\pm^\dagger = \frac{1}{\sqrt{2}}(a_1^\dagger \pm i a_2^\dagger) \tag{3.125}$$

$$a_\pm = \frac{1}{\sqrt{2}}(a_1 \mp i a_2) \tag{3.126}$$

In terms of the $|v\ \ell\rangle$ basis

$$a_\pm |v\ \ell\rangle = \sqrt{\frac{v\pm\ell}{2}}\,|v\text{-}1\ \ell\mp 1\rangle \tag{3.127}$$

$$a_\pm^\dagger |v\ \ell\rangle = \sqrt{\frac{v\pm\ell+1}{2}}\,|v\text{+}1\ \ell\pm 1\rangle \tag{3.128}$$

Rearranging equations (3.119) and (3.120), the coordinate and momentum operators can be rewritten as

$$Q_\pm = \left(\frac{\hbar\omega}{2k}\right)^{1/2}(a_\mp + a_\pm^\dagger) \tag{3.129}$$

$$P_{\pm} = i\left(\frac{k\hbar}{2\omega}\right)^{1/2}(a_{\pm}^{\dagger} - a_{\mp}) \qquad (3.130)$$

The matrix elements of these operators, determined using equations (3.123), (3.124), (3.129), and (3.130), are listed in Table 3.8.

Table 3.8: Matrix elements for a two-dimensional harmonic oscillator in the $|v, \ell\rangle$ representation

$\langle v, \ell \lvert Q_{\pm} \rvert v+1, \ell \mp 1\rangle = \sqrt{\frac{h\omega}{2k}}\sqrt{(v \mp \ell + 2)/2}$	$\langle v, \ell \lvert P_{\pm} \rvert v+1, \ell \mp 1\rangle = -i\sqrt{\frac{k\hbar}{2\omega}}\sqrt{(v \mp \ell + 2)/2}$
$\langle v, \ell \lvert Q_{\pm} \rvert v-1, \ell \mp 1\rangle = \sqrt{\frac{h\omega}{2k}}\sqrt{(v \pm \ell)/2}$	$\langle v, \ell \lvert P_{\pm} \rvert v-1, \ell \mp 1\rangle = i\sqrt{\frac{k\hbar}{2\omega}}\sqrt{(v \pm \ell)/2}$
$\langle v, \ell \lvert Q_{\pm}Q_{\mp} \rvert v+2, \ell\rangle = \frac{1}{2}\left(\frac{h\omega}{2k}\right)\sqrt{(v+\ell+2)(v-\ell+2)}$	$\langle v, \ell \lvert P_{\pm}P_{\mp} \rvert v+2, \ell\rangle = -\frac{1}{2}\left(\frac{k\hbar}{2\omega}\right)\sqrt{(v+\ell+2)(v-\ell+2)}$
$\langle v, \ell \lvert Q_{\pm}Q_{\mp} \rvert v, \ell\rangle = \left(\frac{h\omega}{2k}\right)\sqrt{(v+1)}$	$\langle v, \ell \lvert P_{\pm}P_{\mp} \rvert v, \ell\rangle = \left(\frac{k\hbar}{2\omega}\right)\sqrt{(v+1)}$
$\langle v, \ell \lvert Q_{\pm}Q_{\mp} \rvert v-2, \ell\rangle = \frac{1}{2}\left(\frac{h\omega}{2k}\right)\sqrt{(v^2-\ell^2)}$	$\langle v, \ell \lvert P_{\pm}P_{\mp} \rvert v-2, \ell\rangle = -\frac{1}{2}\left(\frac{k\hbar}{2\omega}\right)\sqrt{(v^2-\ell^2)}$
$\langle v, \ell \lvert Q_{\pm}^2 \rvert v+2, \ell \mp 2\rangle = \frac{1}{2}\left(\frac{h\omega}{2k}\right)\sqrt{(v \mp \ell + 4)(v \mp \ell + 2)}$	$\langle v, \ell \lvert P_{\pm}^2 \rvert v+2, \ell \mp 2\rangle = -\frac{1}{2}\left(\frac{k\hbar}{2\omega}\right)\sqrt{(v \mp \ell + 4)(v \mp \ell + 2)}$
$\langle v, \ell \lvert Q_{\pm}^2 \rvert v, \ell \mp 2\rangle = \left(\frac{h\omega}{2k}\right)\sqrt{(v \mp \ell + 2)(v \pm \ell)}$	$\langle v, \ell \lvert P_{\pm}^2 \rvert v, \ell \mp 2\rangle = \left(\frac{k\hbar}{2\omega}\right)\sqrt{(v \mp \ell + 2)(v \pm \ell)}$
$\langle v, \ell \lvert Q_{\pm}^2 \rvert v-2, \ell \mp 2\rangle = \frac{1}{2}\left(\frac{h\omega}{2k}\right)\sqrt{(v \pm \ell - 2)(v \pm \ell)}$	$\langle v, \ell \lvert P_{\pm}^2 \rvert v-2, \ell \mp 2\rangle = -\frac{1}{2}\left(\frac{k\hbar}{2\omega}\right)\sqrt{(v \pm \ell - 2)(v \pm \ell)}$

3.6 Vibronic Basis Functions in the Born-Oppenheimer Approximation

If a system has both electronic orbital and vibrational angular momenta these will couple to give vibronic states. The normal starting point for tackling such problems is to generate a basis of Born-Oppenhiemer states – simple products obtained by coupling individual electronic $|{}^{2S+1}\Gamma_{\Lambda} M_{\Lambda} \Sigma\rangle$ and vibrational $|v\ \ell\rangle$ functions.

$$|e_{\lambda}^{3}\ {}^{2}E_{\lambda}\ \lambda\ 1/2\rangle|v\ \ell\rangle$$

$$|e_{\lambda}^{3}\ {}^{2}E_{\lambda}\ -\lambda\ -1/2\rangle|v\ \ell\rangle$$

$$|e_{\lambda}^{3}\ {}^{2}E_{\lambda}\ \lambda\ -1/2\rangle|v\ \ell\rangle$$

$$|e_{\lambda}^{3}\ {}^{2}E_{\lambda}\ -\lambda\ 1/2\rangle|v\ \ell\rangle$$

3.7 References

(1) Ballhausen, C. J.; Hansen, A. E. *Ann. Rev. Phys. Chem.* **1972**, *23*, 15.

(2) Herzberg, G. *Molecular Spectra and Molecular Structure*, 2nd ed.; Krieger Publishing Company: Malabar, 1991; Vol. 3 – Electronic spectra and electronic structure of polyatomic molecules.

(3) Bishop, D. M.; Dingle, T. W. *J. Chem. Phys* **1968**, *48*, 541.

(4) Synder, P. A.; Lund, P. A.; Schatz, P. N.; Rowe, E. M. *Chem. Phys. Lett.* **1981**, *82*, 546-551.

(5) McHugh, A. J.; Gouterman, M.; Weiss, C. *Theoret. Chim. Acta.* **1971**, *24*.

(6) McClure, D. S. *J. Chem. Phys* **1952**, *20*, 682-686.

(7) Griffith, J. S. *The Theory of Transition-Metal Ions*, 1st ed.; Cambridge University Press: London, 1961.

(8) Wilson, E. B.; Decuis, J. C.; Cross, P. C. *Molecular Vibrations. The Theory of Infrared and Raman Vibrational Spectra*; McGraw-Hill Book Company, Inc.: New York, 1955.

(9) Messiah, A. *Quantum Mechanics*; North Holland Publishing Company: Amsterdam, 1958; Vol. 1.

(10) Herzberg, G. *Molecular Spectra and Molecular Structure*, 2nd ed.; Robert E. Krieger Publishing CO., Inc.: Malabar, 1989; Vol. 1 – Spectra of Diatomic Molecules.

(11) Tinkham, M. *Group Theory and Quantum Mechanics*, 1st ed.; McGraw-Hill Book Company: New York, 1964.

4 MAGNETO-OPTICAL SPECTROSCOPY

Magnetic circular dichroism (MCD) is a manifestation of the Zeeman effect (the interaction of atoms and molecules with an external magnetic field), involving electromagnetic-radiation-induced transitions between Zeeman levels in *different* electronic-state manifolds.

Although MCD is ubiquitous (due to higher-order inter-state Zeeman interactions), it is most powerful in the study of species with degenerate electronic states where the first-order Zeeman effects are dominant. Like conventional Zeeman spectroscopy, MCD provides information on the Zeeman splittings. The former technique gives this information directly, but can only be used when the transition bandwidths are smaller than the Zeeman shifts. Hence, although readily applied to atoms, for molecules, the Zeeman splittings remains unresolved due to broad bands. MCD reveals this information through the use of modulated circular polarisation, which enables the low-intensity difference signal to be extracted from the noise by phase-sensitive detection using a lock-in amplifier (see Chapter 6).

In the mid 1960s A. D. Buckingham and P. J. Stephens[1-3] developed a theoretical formalism of MCD that allowed useful parameters to be extracted from the experimental spectra. This involved deconvoluting the spectra into contributions from $\mathcal{A}$, $\mathcal{B}$ and $\mathcal{C}$ terms arising, respectively, from the first-order splittings, second-order field-induced mixing of the states, and the populations of Zeeman levels within the ground-state manifold. The magnitudes of these terms are quantified by the corresponding Faraday parameters. For the purposes of the work presented in this thesis, the information implicit in these parameters is too limited, however the formalism remains a useful way of introducing the concepts and terminology of MCD.

4.1 The Origin of MCD

When linearly polarised light passes through a substance with natural or magnetically induced optically activity, the emerging light can be considered to have been affected in two ways. The polarisation develops a degree of ellipticity (θ) and the principal

axis is rotated (by angle ϕ) with respect to the original plane of polarisation. These effects can be understood by regarding plane-polarised light as an equal superposition of left (-) and right (+) circularly polarised (*lcp* and *rcp*) components with an electric vector of the form

$$E = \frac{1}{\sqrt{2}}(E_+ + E_-) \tag{4.1}$$

The ellipticity comes about due to the differential absorption of the circularly polarised components and is called circular dichroism (CD), while the rotation results from the components having different velocities through the medium (circular birefringence).[4] These effects can be simultaneously specified by a *complex* optical rotation $\hat{\phi}$ given by

$$\hat{\phi} = \phi - i\theta = \frac{\pi\omega l}{2c}(\hat{n}_- - \hat{n}_+) \tag{4.2}$$

where l is the distance the electromagnetic field propagates through the medium, c is the speed of light, ω is the radiation frequency and

$$\hat{n}_\pm = n_\pm - ik_\pm \tag{4.3}$$

are the *complex* refractive indices for circularly polarised light, $n_\pm$ being the normal refractive indices and $k_\pm$ the corresponding absorption coefficients. It follows that ϕ is proportional to $n_- - n_+$ while θ is proportional to $k_- - k_+$.

The quantity of interest in this thesis is the component of θ induced by the presence of a longitudinal (with respect to the direction of propagation of light) magnetic field – referred to as magnetic circular dichroism (MCD).

4.2 The Absorption Coefficient

The experimentally observed value of θ is a bulk property of an optically active sample. To compare it with theory, the absorption coefficients, $k_\pm$, are related to parameters that reflect the molecular properties – the transition moment integrals.

The intensity of light is the energy passing per unit time through a unit area normal to the propagation direction. For circularly polarised light propagating along the laboratory Z axis

$$I_{\pm} = |\langle \frac{c}{4\pi}(\Re_e \boldsymbol{E}_{\pm} \times \Re_e \boldsymbol{B}_{\pm})\rangle| = \frac{c}{8\pi}|\boldsymbol{E}_0|^2 e^{-2\omega k_{\pm} Z/c} = I_0 e^{-2\omega k_{\pm} Z/c} \tag{4.4}$$

where $\boldsymbol{B}_{\pm}$ is the magnetic-field vector of the electromagnetic field and I_0 is the intensity in the *absence* of absorption and $\Re_e$ specifies the real part of the following expression. $\boldsymbol{E}_0$ is the *vector* amplitude of the electric field and is defined by

$$\boldsymbol{E}_0 = \pi_{\pm} E_0 \tag{4.5}$$

where E_0 is the scalar amplitude and $\pi_{\pm}$ is a vector that describes the polarisation of circularly polarised light. Explicitly

$$\pi_{\pm} = \frac{1}{\sqrt{2}}(e_X \pm i e_Y) \tag{4.6}$$

where e_X and e_Y are unit vectors in the laboratory X and Y directions.

From equation (4.4) $k_{\pm}$ has the effect of attenuating the light intensity and therefore acts as an absorption coefficient. Expressions for $k_{\pm}$ are obtained by rewriting equation (4.4) in differential form and rearranging

$$k_{\pm} = -\frac{4\pi}{\omega|E_0|^2}\frac{\partial I_{\pm}}{\partial Z} \tag{4.7}$$

where the assumption is made that the wavelength at optical frequencies ($\lambda \sim$ (2-10) $\times$ 10^3 Å) are much larger than the size of the molecule (~1-10 Å). The partial differential represents the diminution of intensity over distance. If the exponential part of $\boldsymbol{E}_{\pm}$, $e^{-\omega k_{\pm} Z/c}$ is assumed to be approximately equal to the first term in a Taylor's expansion, then equation (4.7) can be rewritten as

$$k_{\pm} = -\frac{4\pi}{\omega|E_0|^2}\frac{\partial I_{\pm}}{\partial Z} \tag{4.8}$$

Ignoring emission, it is determined by the transition probabilities of the absorbing species in the volume through which the light passes

$$-\frac{\partial I_{\pm}}{\partial Z} = \sum_{aj} \frac{h\omega}{2\pi} N_a (P_{j\leftarrow a})_{\pm} \tag{4.9}$$

where $(P_{j\leftarrow a})_{\pm}$ is the probability that a species, initially in stationary state $|a\rangle$, will absorb radiation with energy $\varepsilon = \hbar\omega$ and undergo a transition to stationary state $|j\rangle$. The sum is over all the states in the absorbing species and N_a is the number of absorbing species per unit volume in state $|a\rangle$. Substitution of equation (4.9) into equation (4.7) gives

$$k_{\pm} = \sum_{aj} \frac{2h}{|E_0|^2} N_a (P_{j\leftarrow a})_{\pm} \tag{4.10}$$

The expectation value, at time t, for the energy of a quantum mechanical system under in the influence of a time-dependent perturbation is[5]

$$\langle \varepsilon \rangle = \sum_{j} |\mathcal{W}_j(t)|^2 \varepsilon_j \tag{4.11}$$

where the sum is over all stationary states (unperturbed eigenfunctions of the time-independent molecular Hamiltonian) and $\mathcal{W}_j(t)$ are the time-dependent coefficients of the perturbed wavefunction expressed as linear combinations of stationary states. Comparison with the standard statistical formula for the expectation value[5] indicates that the probability of finding the system in state j with energy ε_j at time t is $|\mathcal{W}_j(t)|^2$. Thus the transition probability per unit time is

$$(P_{j\leftarrow a})_{\pm} = |\mathcal{W}_j(t)|^2 / t \tag{4.12}$$

Semi-classical radiation theory, where the atoms are treated quantum-mechanically and the electromagnetic radiation is treated as a classical perturbation, gives[6,7]

$$\mathcal{W}_j(t) = \frac{1}{i\hbar}\int_0^t \langle j|\mathcal{H}_T'|a\rangle e^{-i\omega_{ja}t}\,dt \tag{4.13}$$

where $\mathcal{H}_T'$, is the time dependent perturbation Hamiltonian due to the radiation and ω_{ja} is the circular frequency corresponding to the energy difference between $|a\rangle$ and $|j\rangle$.

In the following only electronic transitions are considered, so terms representing the interaction with nuclei are ignored. Moreover, only the electric-dipole interactions are considered so equation (4.13) becomes

$$\mathcal{W}_j(t) = \sum_i \frac{1}{2}\left[\frac{\alpha}{\sqrt{n_\pm}}\langle j|\boldsymbol{E}_0^*\cdot\boldsymbol{m}_i|a\rangle\right]\left[\frac{1-e^{i(\omega_{ja}-\omega)t}}{\hbar(\omega_{ja}-\omega)}\right]\delta\omega\omega_{ja} \tag{4.14}$$

where $\boldsymbol{m}_i$ is the electric dipole operator associated with electron i and α is an effective-field correction that allows, for example, for the dielectric effects of surrounding solvent molecules. Substitution of equation (4.14) into (4.12) and assuming that $n_\pm = n$ is independent of circular polarisation and magnetic field gives

$$(P_{j\leftarrow a})_\pm = \frac{1}{4t}\left|\frac{\alpha}{\sqrt{n}}\langle j|\boldsymbol{E}_0^*\cdot\boldsymbol{m}|a\rangle\right|^2 \times \left|\frac{1-e^{i(\omega_{ja}-\omega)t}}{\hbar(\omega_{ja}-\omega)}\right|^2 \delta\omega\omega_{ja} \tag{4.15}$$

This expresses the probability, per unit time, of a system under the influence of *perfectly* monochromatic radiation of circular frequency ω undergoing a transition $j\leftarrow a$. But in practice, it is better to consider $P_{j\leftarrow a}$ to be a probability *density* function, which, when integrated over a range of frequencies in the vicinity of ω_{ja} gives,

$$(P_{j\leftarrow a})_\pm = \frac{\pi^2}{h^2}\left|\frac{\alpha}{\sqrt{n}}\langle j|\boldsymbol{E}^{0*}\cdot\boldsymbol{m}|a\rangle\right|^2 \tag{4.16}$$

Replacing $\boldsymbol{E}_0$ with $\pi_\pm E_0$ according to equation (4.5) gives

$$(P_{j\leftarrow a})_\pm = \frac{\pi^2}{h^2}|E_0|^2\left|\frac{\alpha}{\sqrt{n}}\langle j|\,\pi_\pm^*\cdot\boldsymbol{m}|a\rangle\right|^2 \tag{4.17}$$

According to equation (4.6),

$$\pi_{\pm}^{*} = \pi_{\mp} \tag{4.18}$$

so

$$\pi_{\pm}^{*} \cdot \boldsymbol{m} = \pi_{\mp} \cdot \boldsymbol{m} \equiv m_{\mp} \tag{4.19}$$

But from this point (for group-theoretical reasons) it is convenient to express the circularly polarised dipole moment components in the form $m_{\pm 1}$, (Section 2.2.3)

$$m_{\pm 1} = \mp m_{\pm} \tag{4.20}$$

so

$$(P_{j \leftarrow a})_{\pm} = \frac{\pi^2}{h^2} |E_0|^2 \left| \frac{\alpha}{\sqrt{n}} \langle j | m_{\mp 1} | a \rangle \right|^2 \tag{4.21}$$

The treatment outlined so far does not allow for finite transition bandwidths. Although the effects of lifetime (and Doppler) broadening for an ensemble of truly isolated molecules can be calculated *a priori*, in condensed phases it is easier and more convenient to use an *ad hoc* normalised line-shape function f_{ja} such that

$$\int_0^{\infty} f_{ja}(\varepsilon) \mathrm{d}\varepsilon = 1 \tag{4.22}$$

Substitution of (4.21) and (4.22) into (4.10) gives $k_{\pm}$ in terms of transition probabilities;

$$k_{\pm} = \sum_{aj} \frac{2\pi^2}{h} N_a \left| \frac{\alpha}{\sqrt{n}} \langle j | m_{\mp 1} | a \rangle \right|^2 f_{ja}(\varepsilon) \tag{4.23}$$

4.3 Absorption and MCD

MCD is defined to be the difference between the absorbance of *lcp* light (A_-) and *rcp* light (A_+)

$$\Delta A' = (A_- - A_+) \tag{4.24}$$

where the primes denote magnetic-field dependent quantities. The absorbance is taken to be the average value at zero magnetic field

$$A = (A_- + A_+)/2 \tag{4.25}$$

The absorbances of the individual circularly polarised components are related to the absorption coefficients $k_\pm$ through the Beer-Lambert law

$$A_\pm = \mathfrak{E}_\pm Cl \tag{4.26}$$

where $\mathfrak{E}_\pm = (2\omega k_\pm/Cc)\log_{10}e$ is the *molar extinction coefficient*, C is the concentration (in mol L^{-1}) of absorbing species and l is the path length of the radiation through the sample. The absorbance of *lcp* and *rcp* is given by

$$\frac{A_\pm}{\varepsilon} = Cl\gamma \sum_{aj} P_a |\langle j | m_{\mp 1} | a \rangle|^2 f_{ja}(\varepsilon) \tag{4.27}$$

where $\gamma = 2N_0\pi^3\alpha^2\log_{10}(e)/h^2cn$, $P_a = N_a/N$ is the fractional population of state $|a\rangle$ and N_0 is Avogadro's number. Thus the MCD and absorption are given by

$$\Delta A'/\varepsilon = Cl\gamma \sum_{aj} P_a'(|\langle j|m_{+1}|a\rangle'|^2 - |\langle j|m_{-1}|a\rangle'|^2) f'_{ja}(\varepsilon) \tag{4.28}$$

$$A/\varepsilon = \frac{Cl\gamma}{2} \sum_{aj} P_a(|\langle j|m_{+1}|a\rangle|^2 + |\langle j|m_{-1}|a\rangle|^2) f_{ja}(\varepsilon) \tag{4.29}$$

4.4 MCD Magnetic-field and Temperature Dependence

In the rest of this chapter, only pure electronic transitions will be considered. It will later be necessary to introduce vibronic interactions, but that is deferred to later chapters.

The eigenfunctions of the molecular electronic Hamiltonian are here abbreviated $|J\,\lambda\rangle$ where J and λ are electronic irrep and partner labels. For a magnetic field along the laboratory Z axis, the electronic Zeeman Hamiltonian is given by equation (3.68) where in this case the coordinates refer to the laboratory system (which is defined in Section 4.5). For states diagonal in μ_Z the energy of state $|J\,\lambda\rangle$ to the first order in perturbation theory (linear in B), is

$$\varepsilon'_{J\lambda} = \varepsilon_{J\lambda} - B\langle J\lambda|\mu_Z|J\lambda\rangle \tag{4.30}$$

The first term is the zero-field energy and the second is the Zeeman shift.

As well as this first-order energy shift, the magnetic field mixes states giving first-order wavefunctions, of the form

$$|J\,\lambda\,\rangle' = |J\,\lambda\rangle' - B\sum_{K\neq J,\kappa}\frac{\langle K\kappa|\mu_Z|J\lambda\rangle}{\varepsilon_J - \varepsilon_K}|K\,\kappa\,\rangle \tag{4.31}$$

For a transition $|J\,\lambda\rangle\leftarrow|A\,\alpha\rangle$, the matrix elements of the electric dipole operator are

$$\langle J\lambda|m_{\pm1}|A\,\alpha\,\rangle' = \langle J\lambda|m_{\pm1}|A\,\alpha\,\rangle - B\sum_{K\neq J,\kappa}\frac{\langle J\,\lambda|\mu_Z|K\,\kappa\rangle\langle K\,\kappa|m_{\pm1}|A\,\alpha\rangle}{\varepsilon_J - \varepsilon_K}$$

$$-B\sum_{K\neq A,\kappa}\frac{\langle K\,\kappa|\mu_Z|A\,\alpha\rangle\langle J\,\lambda|m_{\pm1}|K\,\kappa\rangle}{\varepsilon_A - \varepsilon_K} \tag{4.32}$$

Assuming that the populations of the Zeeman levels within the ground-state manifold can be described by the Boltzmann distribution, the fractional population of the initial state is

$$P'_{A\alpha} = \frac{\exp\{-\varepsilon'_{A\alpha}/kT\}}{\sum_{\alpha} \exp\{-\varepsilon'_{A\alpha}/kT\}}$$

$$= \frac{\exp\{-\varepsilon'_{A\alpha}/kT\}\exp(\langle A\alpha|\mu_Z|A\alpha\rangle B/kT)}{\sum_{\alpha} \exp\{-\varepsilon'_{A\alpha}/kT\}}$$

$$= \frac{1}{|A|}\exp(\langle A\alpha|\mu_z|A\alpha\rangle B/kT) \qquad (4.33)$$

where k is Boltzmann's constant and $|A|$ is the ground-state degeneracy.

At sufficiently high temperatures and low magnetic fields the Zeeman energies are small compared to kT and the exponential in equation (4.33) can be approximated as the first few terms of an exponential series. To the term linear in B this is

$$P'_{A\alpha} \approx \frac{1}{|A|}(1 + \langle A\alpha|\mu_Z|A\alpha\rangle B/kT) \qquad (4.34)$$

Since the fractional population in equation (4.34) depends linearly on the field, this approximation is called the *linear limit*. As will be seen below, it predicts a linear dependence of $\mathcal{C}$-term intensity on B/T.

The lineshape function, $f'_{A\alpha J\lambda}(\varepsilon)$ is also magnetic field dependent. It is commonly assumed that the Zeeman shifts occur without change of line shapes (the *rigid-shift* approximation). Defining this to be

$$\delta\varepsilon_{A\alpha J\lambda} = (\varepsilon'_{J\lambda} - \varepsilon'_{A\alpha}) - (\varepsilon_J - \varepsilon_A) = (\langle J\lambda|\mu_Z|J\lambda\rangle - \langle A\alpha|\mu_Z|A\alpha\rangle)B \qquad (4.35)$$

then

$$f'_{A\alpha J\lambda}(\varepsilon) = f_{AJ}(\varepsilon - \delta\varepsilon_{A\alpha J\lambda}) \qquad (4.36)$$

Provided the zero-field energy is much greater than the Zeeman shift then equation (4.36) can be approximated by the first few terms of a Taylor series in f. To first order

$$f'_{A\alpha J\lambda}(\varepsilon) = f_{AJ}(\varepsilon) - \delta\varepsilon_\alpha \frac{\partial f_{AJ}(\varepsilon)}{\partial \varepsilon}$$

$$= f_{AJ}(\varepsilon) + B(\langle J\lambda|\mu_Z|J\lambda\rangle - \langle A\alpha|\mu_Z|A\alpha\rangle)\frac{\partial f_{AJ}(\varepsilon)}{\partial \varepsilon} \qquad (4.37)$$

4.4.1 Faraday Terms and Parameters

Under circumstances where the approximations of the immediately preceding discussion are valid, an MCD spectrum can be deconvoluted into three types of line shape, referred to as Faraday terms and quantified by Faraday parameters.[1-3]

In this section expressions for the Faraday parameters are derived and qualitative features of the corresponding MCD terms are discussed. For the parameters to be valid descriptors, the first-order Zeeman shifts must be small compared with both kT and the transition bandwidth – that is, the linear limit and rigid-shift approximations must be valid. Working in the linear limit effects a great simplification of the interpretation of MCD, but also leads to a loss of valuable information. It will prove useful late in this thesis to go beyond this formalism.[8]

The result of substituting equations (4.32), (4.34) and (4.37) into equations (4.28) and (4.29), ignoring contributions from natural CD and keeping only those terms that are linear in the magnetic field, is

$$\frac{\Delta A'}{\varepsilon} = \gamma C l \mu_B B[\mathcal{A}_1(-\partial f_{AJ}(\varepsilon)/\partial\varepsilon) + (\mathcal{B}_0 + \mathcal{C}_0/kT) f_{AJ}(\varepsilon)] \qquad (4.38)$$

where $\mathcal{A}_1$, $\mathcal{B}_0$ and $\mathcal{C}_0$ are the Faraday parameters. Referenced to the laboratory axes, they are given by

$$\mathcal{A}_1 = -\frac{1}{|A|}\sum_{\alpha,\lambda}(\langle J\lambda|L_Z + g_e S_Z|J\lambda\rangle - \langle A\alpha|L_Z + g_e S_Z|A\alpha\rangle)$$

$$\times(|\langle J\,\lambda|m_{+1}|A\,\alpha\rangle|^2 - |\langle J\,\lambda|m_{-1}|A\,\alpha\rangle|^2) \qquad (4.39)$$

$$\mathcal{B}_0 = \frac{-2\Re_e}{|A|}\sum_{\alpha,\lambda}\Big[\sum_{K\neq J,\kappa}\frac{\langle J\,\lambda|L_Z + g_e S_Z|K\,\kappa\rangle}{\varepsilon_J - \varepsilon_K}$$

$$\times(\langle K\,\kappa|m_{+1}|A\,\alpha\rangle\langle A\,\alpha|m_{-1}|J\,\lambda\rangle - \langle K\,\kappa|m_{-1}|A\,\alpha\rangle\langle A\,\alpha|m_{+1}|J\,\lambda\rangle)$$

$$+ \sum_{K\neq A,\kappa}\frac{\langle K\,\kappa|L_Z + g_e S_Z|A\,\alpha\rangle}{\varepsilon_K - \varepsilon_A}$$

$$\times(\langle J\,\lambda|m_{+1}|K\,\kappa\rangle\langle A\,\alpha|m_{-1}|J\,\lambda\rangle - \langle J\,\lambda|m_{-1}|K\,\kappa\rangle\langle A\,\alpha|m_{+1}|J\,\lambda\rangle)\Big] \qquad (4.40)$$

$$\mathcal{C}_0 = \frac{-1}{|A|}\sum_{\alpha,\lambda}(\langle A\,\alpha|L_Z + g_e S_Z|A\,\alpha\rangle(|\langle J\,\lambda|m_{+1}|A\,\alpha\rangle|^2 - |\langle J\,\lambda|m_{-1}|A\,\alpha\rangle|^2) \qquad (4.41)$$

From equation (4.39) the appearance of an $\mathcal{A}$ term requires that either or both of the ground and excited states are degenerate and that their Zeeman splittings are different. This leads to field-induced shifts of the *lcp* and *rcp* transitions, so $\mathcal{A}$ terms have a dispersion that is the derivative of the band-shape function. They can be either positive (positive lobe at the higher energy) or negative (negative lobe at the higher energy), and are temperature independent.

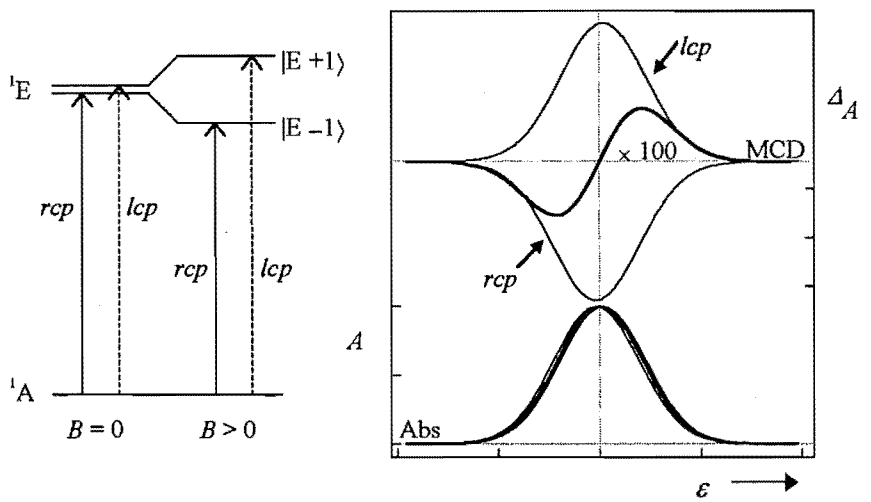

Figure 4.1: A positive $\mathcal{A}$ term due to excited-state degeneracy. The *lcp* transition terminates in the higher Zeeman level of the excited state, so the higher-energy lobe is positive. The resultant MCD is amplified by a factor of 100.

$\mathfrak{B}$ terms arise because of field-induced mixing of the zero-field wavefunctions and are ubiquitous, even in systems of low symmetry (no degenerate states). Since their magnitude is inversely proportional to the energy separation of the mixed states, $\mathfrak{B}$ term contributions are generally weak unless they involve interactions between states from the same term manifold. $\mathfrak{B}$ terms have an absorption-like dispersion of either sign and are temperature-independent.

The occurrence of $\mathfrak{C}$ terms requires that the ground-state manifold is degenerate (in the absence of a magnetic field). They come about because of differences between the Boltzmann populations of the Zeeman states in the ground-state manifold. Thus, their intensities are temperature dependent showing (in the linear limit) inverse dependence on temperature. They have single-signed absorption-like dispersion, and their sign depends on the polarisation of the transition from the lowest (and therefore most populated) Zeeman state. $\mathfrak{C}$ terms will always coincide with $\mathfrak{A}$ terms, but in the vast majority of cases, especially at low temperatures, the $\mathfrak{C}$ terms will dominate.

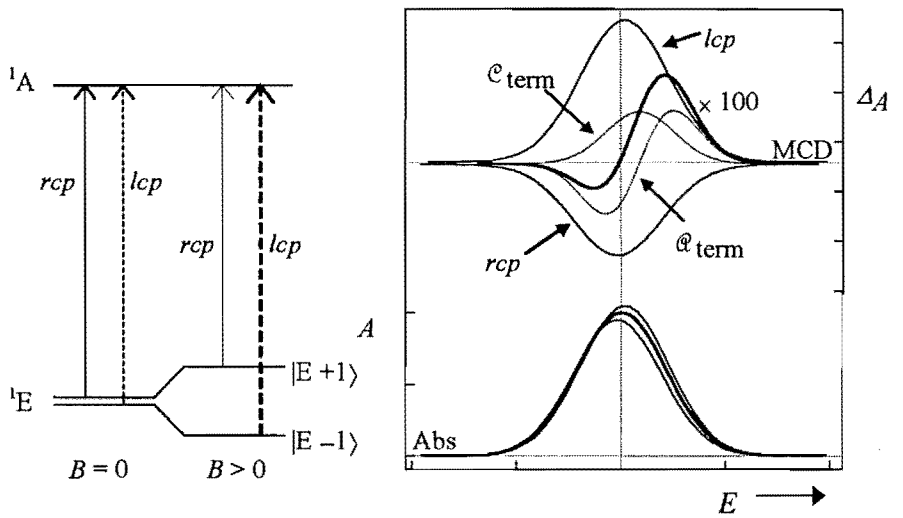

Figure 4.2: MCD terms arising from ground-state degeneracy. The MCD (dark curve at the top) is amplified by 100. It can be deconvoluted into an $\mathfrak{A}$ and a $\mathfrak{C}$ term which (in this case) are positive since the *lcp* transition arises from the most lowest, and therefore most populated Zeeman level.

Strictly, the absorption should be measured at zero magnetic field. However, if the bandwidth is very much greater than the Zeeman splitting, the field dependence of the absorption is negligible. In either case

$$\frac{A}{\varepsilon} = Cl\gamma\mathcal{D}_0 f_{A,J}(\varepsilon) \tag{4.42}$$

where $\mathcal{D}_0$ is the dipole strength, given by

$$\mathcal{D}_0 = \frac{1}{2|A|}\sum_{\alpha,\lambda}\left(|\langle J\ \lambda|m_{+1}|A\ \alpha\rangle|^2 + |\langle J\ \lambda|m_{-1}|A\ \alpha\rangle|^2\right) \tag{4.43}$$

4.4.2 Extraction of Molecular Parameters from Experimental Data

There are two common ways of extracting theoretical information from experimental spectra. One is to use spectral simulation or band fitting assuming *ad hoc* analytical band-shape functions. This can sometimes prove difficult and time consuming, and decisions about the number of overlapping bands, their intensities and bandwidths can be very subjective. It is best employed when the theoretical basis of the fit is well defined and the experimental data show well-separated bands. This technique is used in Chapters 7 and 8 in the analysis of the experimental spectra of ferricenium and cyclooctatetrane radicals.

An alternative is to employ the method of moments. *Moments* measure average deviations of a set of data about a reference point.[9] They can be taken to orders from zero to infinity[i] and quantify the shape of a distribution in terms of characteristics like the average value, variance, skewness and peakedness. The formula for the nth moment for the function $\alpha(\varepsilon)$ about ε^0 is

$$\langle\alpha(\varepsilon)\rangle_n^{\varepsilon^0} = \int \alpha(\varepsilon)(\varepsilon - \varepsilon^0)^n d\varepsilon \tag{4.44}$$

The equations for the moments of the MCD and absorption spectra are determined by putting (4.28) and (4.29) into equation (4.44). In principle the range of integration should be infinite, but when considering lower moments it is sufficient to limit the range to points beyond which the MCD or absorption is *effectively* zero. (For this reason, any theory with which the method is used should account for integration over the whole range of well-separated bands). The reference point is

---

[i] To uniquely identify a function using moments it would be necessary to determine all the moments.

taken to be the average energy of the absorption band $\bar{\varepsilon}$ (the absorption barycentre) defined so that $\langle A/\varepsilon \rangle_1^{\bar{\varepsilon}} = 0$. Thus

$$\bar{\varepsilon} = \frac{\langle A/\varepsilon \rangle_1^0}{\langle A/\varepsilon \rangle_0} \tag{4.45}$$

Since the only energy-dependent parts of (4.28) and (4.29) are the line-shape functions, the nth absorption are given by

$$\mathbf{A}_n \equiv \langle A/\varepsilon \rangle_n^{\bar{\varepsilon}} = Cl\gamma\mathcal{D}_0 \int f_{J,A}(\varepsilon)(\varepsilon - \bar{\varepsilon})^n \mathrm{d}\varepsilon \tag{4.46}$$

Only the zeroth absorption moments are important in this work. From equation (4.22), they are given by

$$\mathbf{A}_0 = Cl\gamma\mathcal{D}_0 \tag{4.47}$$

The MCD moments are

$$\mathbf{M}_n \equiv \langle \Delta A'/\varepsilon \rangle_n^{\bar{\varepsilon}} = Cl\gamma\mu_B B[-\mathcal{A}_1 \int \frac{\mathrm{d}f_{J,A}}{\mathrm{d}\varepsilon}(\varepsilon - \bar{\varepsilon})^n \mathrm{d}\varepsilon + (\mathcal{B}_0 + \mathcal{C}_0/kT) \int f_{J,A}(\varepsilon)(\varepsilon - \bar{\varepsilon})^n \mathrm{d}\varepsilon] \tag{4.48}$$

Thus, in the linear limit, the first MCD moment is proportional to the magnitude of the $\mathcal{A}$ term and the zeroth moment gives the sum of the magnitude of the $\mathcal{B}$ and $\mathcal{C}$ terms;

$$\mathbf{M}_1 = \gamma Cl\mu_B B\mathcal{A}_1 \tag{4.49}$$

$$\mathbf{M}_0 = \gamma Cl\mu_B B(\mathcal{B}_0 + \mathcal{C}_0/kT) \tag{4.50}$$

These equations show why subscripts 0 or 1 are used with the Faraday parameters. The first MCD moment gives $\mathcal{A}_1$, which measures the magnitude of an $\mathcal{A}$ term. The zeroth MCD moment gives the magnitudes of the $\mathcal{B}$ and $\mathcal{C}$ terms – a plot of $\mathbf{M}_0$ against

$\mu_B B/kT$ will be linear (in the linear limit) with a slope proportional to $\mathcal{C}_0$ and a y-intercept proportional to $\mathcal{B}_0$.

Molecular information is most readily determined from the MCD or its moments when the corresponding absorption data are also available. For example, by dividing the MCD moments by $\mathbf{A}_0$, a number of factors that are unknown or difficult to determine – including the transition moments, sample concentrations, effective-field corrections *etc* – will cancel.

Even in cases where the conditions make equations (4.49) and (4.50) invalid, moment analysis can still be applied. That is the approach taken in this thesis since a great deal of the experimental information pertains to conditions outside the linear limit. Here, moment analysis is done numerically using a QuickBasic computer programme called MOMENT (written by members of this group).

4.5 Molecule Fixed Operators and Orientational Averaging

In the expressions thus far presented, the operators μ_Z and $m_{\pm 1}$ refer to laboratory (X, Y, Z) coordinates, with the Z axis is defined by the coincident directions of the propagation of light and the magnetic field.

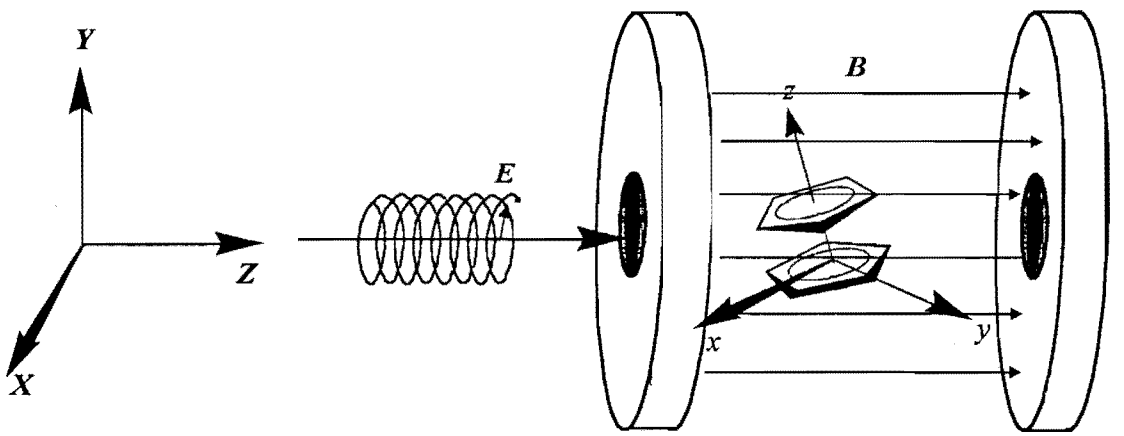

Figure 4.3: An axial molecule of a general orientation with respect to the magnet field

To relate the spectroscopic parameters (including moments) to molecular properties, it is necessary to re-express these operators in terms of the molecular coordinate system.

If (as is the case in this thesis) the samples consist of a large number of molecules at random orientations, it also is necessary to average over all molecular orientations

The rotation of a vector (or pseudo-vector) operator $\mathcal{O}$ from laboratory (X, Y, Z) coordinates into the molecular (x, y, z) coordinate system is represented by[10]

$$\begin{pmatrix} \mathcal{O}_x \\ \mathcal{O}_y \\ \mathcal{O}_z \end{pmatrix} = \mathcal{R} \begin{pmatrix} \mathcal{O}_X \\ \mathcal{O}_Y \\ \mathcal{O}_Z \end{pmatrix} \tag{4.51}$$

where $\mathcal{R}$ is determined by the successive Euler rotations about Z by ϕ, ξ by θ, and ζ' by ψ as represented in Figure 4.4.[10]

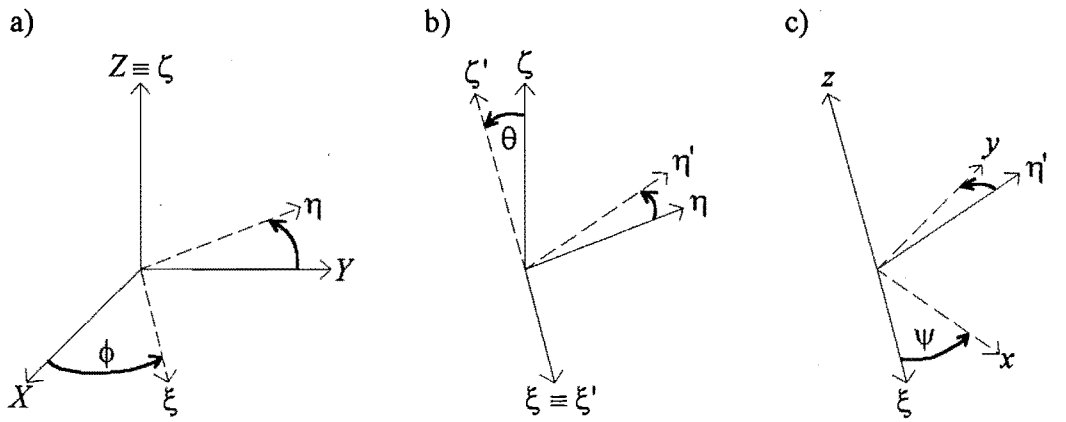

Figure 4.4: The Euler angle convention: (a) rotation by ϕ about Z; (b) by θ about ξ, and, (c) by ψ about ζ'

Thus $\mathcal{R}$ is

$$\mathcal{R} = \begin{pmatrix} \cos\psi\cos\phi - \sin\psi\cos\theta\sin\phi & \cos\psi\sin\phi + \sin\psi\cos\theta\cos\phi & \sin\psi\sin\theta \\ -\sin\psi\cos\phi - \cos\psi\cos\theta\sin\phi & -\sin\psi\sin\phi + \cos\psi\cos\theta\cos\phi & \cos\psi\sin\theta \\ \sin\theta\sin\phi & -\sin\theta\cos\phi & \cos\theta \end{pmatrix} \tag{4.52}$$

Since $\mathcal{R}$ is orthogonal, a vector (or pseudo-vector) operator $\mathcal{O}$, originally given in the laboratory coordinate system, can be in given in terms of molecular coordinates by

$$\begin{pmatrix} \mathcal{O}_X \\ \mathcal{O}_Y \\ \mathcal{O}_Z \end{pmatrix} = \mathcal{R}^{\mathrm{T}} \begin{pmatrix} \mathcal{O}_x \\ \mathcal{O}_y \\ \mathcal{O}_z \end{pmatrix} \tag{4.53}$$

Expanding this out gives

$$\mathcal{O}_X = \mathcal{R}_{11}\mathcal{O}_x + \mathcal{R}_{21}\mathcal{O}_y + \mathcal{R}_{31}\mathcal{O}_z$$

$$\mathcal{O}_Y = \mathcal{R}_{12}\mathcal{O}_x + \mathcal{R}_{22}\mathcal{O}_y + \mathcal{R}_{32}\mathcal{O}_z$$

$$\mathcal{O}_Z = \mathcal{R}_{13}\mathcal{O}_x + \mathcal{R}_{23}\mathcal{O}_y + \mathcal{R}_{33}\mathcal{O}_z \qquad (4.54)$$

These expressions can be substituted into equations (4.28) and (4.29) (or any derivatives thereof) giving equations for the MCD and absorption an ensemble of molecules with the same orientations (θ, ϕ, ψ) with respect to the laboratory coordinate system.

The average value $\bar{\mathcal{O}}$ of the observable, determined by operator $\mathcal{O}$, for a large number of randomly oriented species is given by

$$\bar{\mathcal{O}} = \frac{\int_0^{2\pi}\int_0^{2\pi}\int_0^{\pi} \mathcal{P}(\theta, \phi, \psi) O(\theta, \phi, \psi) \mathrm{d}\theta \mathrm{d}\phi \mathrm{d}\psi}{\int_0^{2\pi}\int_0^{2\pi}\int_0^{\pi} \mathcal{P}(\theta, \phi, \psi) \mathrm{d}\theta \mathrm{d}\phi \mathrm{d}\psi} \qquad (4.55)$$

where $\mathcal{P}(\theta, \phi, \psi)$ is the probability density for a molecule having the indicated orientation and the denominator acts as a normaliser. All values (0-2π) of angles ϕ and ψ are equally likely so averaging over these gives

$$\mathcal{O}(\theta) = \frac{\int_0^{2\pi}\int_0^{2\pi} O(\theta,\phi,\psi)\mathrm{d}\phi\mathrm{d}\psi}{\int_0^{2\pi}\int_0^{2\pi}\mathrm{d}\phi\mathrm{d}\psi} = \frac{\int_0^{2\pi}\int_0^{2\pi} O(\theta,\phi,\psi)\mathrm{d}\phi\mathrm{d}\psi}{4\pi^2} \qquad (4.56)$$

Now consider an axial molecule (x and y directions are equivalent) and transitions $J \leftarrow A$ that are x-y polarised (so that $\langle J\lambda | m_z | A\alpha \rangle = 0$). After averaging over all ϕ for a given angle θ the MCD and absorption expressions are

$$\frac{\Delta A'(\theta)}{\varepsilon} = \cos\theta C l\gamma \sum_{\alpha\lambda} P'_{\alpha}(|\langle J\,\lambda|m_{+1}|A\,\alpha\rangle|^2 - |\langle J\,\lambda|m_{-1}|A\,\alpha\rangle|^2) f'_{A\alpha J\lambda}(\varepsilon) \quad (4.57)$$

$$\frac{A(\theta)}{\varepsilon} = \frac{Cl\gamma}{|A|}\frac{(\cos^2\theta + 1)}{4}\sum_{\alpha\lambda}(|\langle J\,\lambda|m_{+1}|A\,\alpha\rangle|^2 + |\langle J\,\lambda|m_{-1}|A\,\alpha\rangle|^2) f_{A,J}(\varepsilon) \quad (4.58)$$

Angle θ is weighted as $\sin\theta/2$ over the integrating range 0 to π, so

$$\bar{\mathcal{C}} = \frac{\int_0^{\pi} \mathcal{C}(\theta)\sin\theta \mathrm{d}\theta}{\int_0^{\pi} \sin\theta \mathrm{d}\theta} = \frac{1}{2}\int_{-1}^{1} \mathcal{C}(\theta)\mathrm{d}\cos\theta \quad (4.59)$$

and equations (4.57) and (4.58) become

$$\frac{\Delta\bar{A}'}{\varepsilon} = \frac{Cl\gamma}{2}\sum_{\alpha\lambda}[(|\langle J\,\lambda|m_{+1}|A\,\alpha\rangle|^2 - |\langle J\,\lambda|m_{-1}|A\,\alpha\rangle|^2) f'_{A\alpha J\lambda}(\varepsilon)\int_{-1}^{1} P'_{\alpha}\cos\theta \mathrm{d}\cos\theta] \quad (4.60)$$

$$\frac{\bar{A}}{\varepsilon} = \frac{Cl\gamma}{3|A|}\sum_{\alpha\lambda}(|\langle J\,\lambda|\,m_{+1}\,|A\,\alpha\rangle|^2 + |\langle J\,\lambda|m_{-1}|A\,\alpha\rangle|^2) f_{A,J}(\varepsilon) \quad (4.61)$$

Appropriate moment expressions can be derived from this starting point without recourse to the linear-limit approximation, but the Faraday parameters (though still descriptively useful) lose much of their meaning.

4.6 Saturation of $\mathcal{C}$ terms

As the temperature decreases or the magnetic field increases sufficiently so that the ground-state Zeeman splitting is no longer very much smaller than kT, the linear-limit approximation is no longer valid. The magnitude of the $\mathcal{C}$ terms will still increase with field, but with a decreasing rate tending to a constant asymptotic limit. The $\mathcal{C}$ term is said to be undergoing (magnetisation) saturation. This behaviour can be

qualitatively understood by remembering, from Section 4.4.1, that $\mathcal{C}$ term intensity is due to different populations of the Zeeman levels within the ground-state manifold. If the magnetic field is sufficiently large or the temperature sufficiently small, essentially all the molecules will reside in their lowest Zeeman state and the $\mathcal{C}$-term intensity will be maximised. Data were collected for this thesis under conditions of low temperatures (~1.4 K) and high magnetic fields (~5 T), well outside the linear limit.

Consider a doubly degenerate ground state whose upper (α = +1) and lower (α = -1) Zeeman levels gives rise to *rcp* and *lcp* transitions, respectively. If the Zeeman splitting is $g\mu_B B$, then the population difference of these levels is

$$P'_{-1} - P'_{+1} = \frac{\exp(+g\mu_B B/2kT) - \exp(-g\mu_B B/2kT)}{\exp(g\mu_B B/2kT) + \exp(-g\mu_B B/2kT)} \tag{4.62}$$

The transition moments will be of the form

$$|\langle J\,\lambda|m_{\pm 1}|A\,+1\rangle| = |\langle J\,-\lambda|m_{\mp 1}|A\,-1\rangle| \tag{4.63}$$

whence the $\mathcal{C}$-term-like part of equation (4.28) gives

$$\frac{\Delta A'}{\varepsilon} = Cl\tanh\left(\frac{g\mu_B B}{2kT}\right)\left(|\langle J\lambda|\,m_{+1}\,|A\alpha\rangle|^2 - |\langle J\lambda|\,m_{-1}\,|A\alpha\rangle|^2\right) f_{J\lambda A\alpha}(\varepsilon) \tag{4.64}$$

In other words, the field dependence has the form of a hyperbolic tangent function, with saturation at larger values of $g\mu_B B/2kT$. At low values, with $|A| = 2$ and $\tanh(x) \approx x$ for small x, it is readily seen that it reduces to the same approximately linear form as the second term in equation (4.38).

The saturation phenomenon adds to the complexity of the MCD analysis, but (as noted above) it also provides more information. For example, it confers the advantage of allowing the ground-state Zeeman splitting (and hence its g value) to be determined from the curvature of the $\mathcal{C}$-term intensity behaviour, as a function of $\mu_B B/kT$, without the absorption data. (Essentially, the transition moments, concentrations and effective field corrections, enter as an arbitrary scaling factor.) This is particularly useful when the absorption spectrum is unmeasurable or unreliable – such cases will be presented in later chapters.[11]

4.7 References

(1) Stephens, P. J. *J. Chem. Phys.* **1969**, *52*, 3489-3516.

(2) Buckingham, A. D.; Stephens, P. J. *Ann. Rev. Phys. Chem.* **1966**, 17, 399-432.

(3) Stephens, P. J. In *Advances in Chemical Physics*; Prigogine, I.; Rice, S. A., Eds.; John Wiley and Sons: New York, 1974; Vol. 35, pp. 197-264.

(4) Saito, Y. *Inorganic Molecular Dissymmetry*, 1st ed.; Springer-Verlag: Berlin, 1979.

(5) Levine, I. N. *Quantum Chemistry*; Allyn and Bacon, Inc.: Boston, 1970; Vol. 2.

(6) Eyring, H.; Walter, J.; Kimball, G. *Quantum Chemistry*, 1st ed.; John Wiley & Sons, Inc.: New York, 1994.

(7) Atkins, P. W.; Friedman, R. S. *Molecular Quantum Mechanics*, 3rd ed.; Oxford University Press Inc.: New York, 1997.

(8) Piepho, S. B.; Schatz, P. N. *Group Theory in Spectroscopy: With Applications to Magnetic Circular Dichroism*; John Wiley & Sons Inc: New York, 1983.

(9) Harnett, D. L. *Introduction to Statistical Methods*, 1st ed.; Addison-Wesley Publishing Company: Reading, 1970.

(10) Goldstein, H. *Classical Mechanics*; Addison-Wesley: Reading, 1950.

(11) Schatz, P. N.; Mowery, R. L.; Krausz, E. R. *Mol. Phys.* **1978**, *35*, 1537-1557.

5 THE JAHN-TELLER EFFECT

5.1 Introduction

Molecules that have degenerate electronic states can exhibit an effect, caused by coupling of the electronic states with certain vibrations, whereby the electronic degeneracy is lowered at all nuclear configurations away from the highest-symmetry point. Jahn and Teller[1] showed that such lifting of the degeneracy occurs along at least one vibrational coordinate, called a Jahn-Teller-active mode, for all *orbitally* degenerate systems of non-linear molecules. The only type of *electronic* degeneracy that is immune to such effects is spin (Kramers) degeneracy. Note that although the electronic degeneracy is removed, it is replaced by a vibronic (vibrational-electronic) degeneracy.

One of the consequences of this Jahn-Teller (JT) effect is the existence of lower-symmetry configurations corresponding to potential-energy minima. However, despite this an isolated molecule subject to a JT effect will not be trapped in one of these minima and have the correspondingly lower symmetry. There exist a number of symmetry-related minima, and the geometry of an isolated molecule will be a (weighted) superposition of all these possibilities. To the extent that the surfaces provide a valid description, the vibronic degeneracy can be explained by these superpositions. Note that in any real condensed-phase system, external perturbations (e.g. crystal-fields) may exist which may stabilise one minimum producing a "trapped" JT effect. The larger the JT effect the more susceptible will be the system to such perturbation. However, it is not uncommon for the energy barrier between minima to be smaller than the zero-point energy, so the molecule will retain the original higher symmetry anyway.

For these reasons the wavefunctions used in considering the JT problem should be classified according to the irreps of the higher symmetry point group, although the classification must be *via* vibronic functions rather than electronic functions.

5.1.1 Breakdown of the Born-Oppenhiemer Approximation

The BO approximation (Section 3.1.3) is generally valid for well-separated, non-degenerate orbital states. But for orbitally degenerate states it fails because of

potential-energy terms in $\mathcal{H}_{el}$ (equation (3.8)), which couple the electronic partner states of a degenerate manifold. This coupling is a function the nuclear coordinates and is therefore mediated by molecular vibrations. Two result of this are: first, that the electronic degeneracy is removed at all values of the nuclear coordinates away from the non-perturbed equilibrium configuration, Q_0; and second, that the new electronic eigenfunctions are functions of the nuclear coordinates, and therefore do not commute with $T_n(Q)$. Ultimately the existence of JT coupling means that nuclear motion is no longer confined to a single potential energy surface. In fact, the very idea of separate electronic potential surfaces loses a good deal of its meaning.

5.1.2 The Vibronic (Dynamic) Jahn-Teller Problem

The vibronic Hamiltonian introduced in Section 3.1.2, is here used in the vibronic Schrödinger equation:

$$\mathcal{H}_{\text{vibronic}} \Psi'_{k\kappa i} = [T_n(Q) + \mathcal{H}_{el}(q,Q)] \Psi'_{k\kappa i} = \varepsilon_{k\kappa i} \Psi'_{k\kappa i} \qquad (5.1)$$

where $\varepsilon_{k\kappa i}$ is a vibronic eigenvalue, which contains both electronic potential-energy *and* nuclear kinetic-energy contributions. To solve this equation, the corresponding matrix, generated using an appropriate set of basis functions is diagonalised. This procedure allows complete flexibility in the choice of the basis functions, as long as they form a complete set – it proves convenient to chose the BO products introduced in Chapter 2. The *non-adiabatic* eigenfunctions of equation (5.1) are then written as linear combinations of the adiabatic functions in the form

$$\psi'_{k\kappa i} = \sum_{\rho} \sum_{j} c_{\kappa i,\rho j} \phi_{k\rho}(q,Q) \varphi_{kj}(Q) \qquad (5.2)$$

where the cs are mixing coefficients. These have the advantage that the electronic parts ($\phi_{k\rho}$) of each basis function commute with the nuclear kinetic energy operator.

The non-adiabatic form of the wavefunction has important consequences for the appearance of molecular spectra. Even within the Franck-Condon approximation, as the BO approximation breaks down progressions and hot bands involving JT-active modes gain intensity at the expense of the origin band. Furthermore, progressions of totally symmetric modes can be built on each of these bands.

Another consequence is a reduction of the magnitude of some electronic properties, such as to orbital angular momenta and spin-orbit coupling parameters. This is due to the Ham effect[2] and is caused by reduced (from unity) overlap of the vibration functions associated with the non-degenerate electronic functions.

At this point it is useful to introduce a JT Hamiltonian defined by

$$\mathcal{H}_{\mathrm{JT}} = T_{\mathrm{n}}(Q) + \mathcal{H}_{\mathrm{el}}(q,Q)' = T_{\mathrm{n}}(Q) + \sum_{\eta}\left(\frac{\partial V}{\partial Q_\eta}\right)_0 Q_\eta + \frac{1}{2}\sum_{\eta}\sum_{\mu}\left(\frac{\partial^2 V}{\partial Q_\eta \partial Q_\mu}\right)_0 Q_\eta Q_\mu \quad (5.3)$$

The expansion as a Taylor series implies that the effect of higher-order terms will be less than lower order ones. This means that the treatment may be invalid for large JT effects. $\mathcal{H}_{\mathrm{vibronic}}$ is then rewritten

$$\mathcal{H}_{\mathrm{vibronic}} = \mathcal{H}_{\mathrm{el}}(q\ Q_0) + \mathcal{H}_{\mathrm{JT}} \quad (5.4)$$

The matrix elements of $\mathcal{H}_{\mathrm{JT}}$ have the form

$$[\mathcal{H}_{\mathrm{JT}}]_{\kappa j,\lambda i} = \sum_{\eta}\langle\varphi_{kj}|T_{\mathrm{n}}(Q)|\varphi_{kj}\rangle\delta_{\kappa\rho} + \sum_{\eta} V^{\eta}_{\kappa\rho}\langle\varphi_{kj}|Q_\eta|\varphi_{ki}\rangle + \frac{1}{2}\sum_{\eta} V^{\eta\eta}_{\kappa\rho}\langle\varphi_{kj}|Q_\eta^2|\varphi_{ki}\rangle\delta_{\kappa\rho}$$

$$+\frac{1}{2}\sum_{\eta}\sum_{\mu\neq\eta} V^{\eta\mu}_{\kappa\rho}\langle\varphi_{kj}|Q_\eta Q_\mu|\varphi_{ki}\rangle \quad (5.5)$$

where $V^{\eta}_{\kappa\rho}$ and $V^{\eta\mu}_{\kappa\rho}$ are electronic matrix elements given by

$$V^{\eta}_{\kappa\rho} = \langle\phi_{k\kappa}|(\partial V/\partial Q_\eta)_0|\phi_{k\rho}\rangle \quad (5.6)$$

$$V^{\eta\mu}_{\kappa\rho} = \langle\phi_{k\kappa}|(\partial^2 V/\partial Q_\eta \partial Q_\mu)_0|\phi_{k\rho}\rangle \quad (5.7)$$

The diagonal elements $V^{\eta\eta}_{\kappa\kappa}$ give the force-constants for the normal coordinates Q_η. Non-zero off-diagonal matrix elements in the $V^{\eta}_{\kappa\rho}$ give rise to linear (first-order) JT effects with respect to the normal coordinate Q_η, while those in $V^{\eta\mu}_{\kappa\rho}$ give rise to quadratic (second-order) effects.

5.1.3 The Electronic (Static) Jahn-Teller

A purely electronic treatment of the JT effect, which ignores vibrational dynamics (hence the alternative title of the static JT effect[i]) is insufficient for the interpretation of the spectroscopic data be presented later in this thesis. However, this analysis is useful because it allows electronic potential surfaces upon which nuclear motion occurs to be defined. Although such surfaces provide a valid description of the system only when the BO approximation holds, if care is taken with their interpretation, they serve as useful tools for understanding some of the consequences of a JT effect.

In Section 3.2.1, the electronic problem was solved by assuming that each electronic state could be treated in isolation except for Herzberg-Teller (HT) coupling with states from other electronic manifolds. This is a limited scenario that only occurs in the case of non-degenerate electronic states. In this section the case of formally degenerate states and the consequences of JT activity will be treated by the application of degenerate perturbation theory.

The relevant form of the electronic Schrödinger equation is

$$\mathcal{H}_{el}\phi'_{k\rho} = W_{k\rho}\phi'_{k\rho} \tag{5.8}$$

where the ϕ' differ from the ϕ of equation (3.26) in that they include the effects of interactions between states within a formally degenerate manifold – ρ labels one of the resultant eigenstates from within an n-fold manifold k. Since the basis states, ϕ, form a complete set, these eigenfunctions can be written in the form

$$\phi'_{k\rho} = \sum_{\kappa=1}^{n} c_{\rho\kappa}\phi_{k\kappa} \tag{5.9}$$

The eigenvector coefficients $c_{\rho\kappa}$, and eigenvalues (electronic potential-energy surfaces) $W_{k\rho}$, are obtained by diagonalising the Hamiltonian matrix whose elements are of the form

---

[i] In some cases 'static' is used to describe a system trapped in a JT minimum – but that is not the meaning intended here.

$$[\mathcal{H}_{el}]_{\kappa\rho} = W_k^0\delta_{\kappa\rho} + \sum_{\eta} V_{\kappa\rho}^{\eta} Q_\eta + \frac{1}{2}\sum_{\eta\mu} V_{\kappa\rho}^{\eta\mu} Q_\eta Q_\mu \qquad (5.10)$$

Here W_k^0 is the zeroth-order electronic energy – the energy mimimum at Q_0 of the degenerate electronic states before the JT effect is considered. Since Q_η and Q_μ appear in equation (5.10), the coefficients $c_{\rho\kappa}$, and hence the eigenfunctions $\phi_{k\rho}'$ are inherently dependent on the JT coordinate(s). Consequently, they do not commute with $T_n(Q)$, and the BO approximation fails.

5.2 E ⊗ e Jahn-Teller Coupling

The JT effect for axial molecules can be treated in a general way by considering a hypothetical system belonging to the $\mathbf{D}_\infty$ point group. Molecules belonging to subgroups can then be treated by subduction, as described in Section 2.1.3.[3]

In $\mathbf{D}_\infty$, all electronic and vibrational states are two-dimensional, except those with 0 and $\tilde{0}$ (A_1 and A_2) symmetry, which cannot exhibit JT activity. As discussed in Section 2.1.3, 'E' is used to label the irrep of a generalised doubly degenerate electronic state, while 'e' is a generic label used for a two-dimensional vibration. The problem is therefore known as E ⊗ e JT coupling.

Following Section 5.1.2, the non-zero vibronic matrix elements for an E ⊗ e system are (dropping the label k from equation (5.5))

$$[\mathcal{H}_{JT}]_{\kappa j,\rho i} = \langle\varphi_j|T_n(Q_1)+T_n(Q_2)|\varphi_i\rangle\delta_{\kappa\rho} + \langle\varphi_j|Q_1|\varphi_i\rangle\langle\phi_\kappa|\left(\frac{\partial V}{\partial Q_1}\right)_0|\phi_\rho\rangle$$

$$+ \langle\varphi_j|Q_2|\varphi_i\rangle\langle\phi_\kappa|\left(\frac{\partial V}{\partial Q_2}\right)_0|\phi_\rho\rangle + \frac{1}{2}\langle\varphi_j|{Q_1}^2|\varphi_i\rangle\langle\phi_\kappa|\left(\frac{\partial V}{\partial {Q_1}^2}\right)_0|\phi_\rho\rangle$$

$$+\frac{1}{2}\langle\varphi_j|{Q_2}^2|\varphi_i\rangle\langle\phi_\kappa|\left(\frac{\partial V}{\partial {Q_2}^2}\right)_0|\phi_\rho\rangle + \frac{1}{2}\langle\varphi_j|Q_1Q_2|\varphi_i\rangle\langle\phi_\kappa|\left(\frac{\partial^2 V}{\partial Q_1\partial Q_2}\right)_0|\phi_\rho\rangle] \qquad (5.11)$$

In terms of the 'real' coordinates Q_1 and Q_2 of a two-dimensional vibration, the vibrational states would be represented as $|v_1\ v_2\rangle$ in equation (5.11). However, it is

more convenient to use the coordinates $Q_{\pm}$, defined by equation (3.101), for which the vibrational wavefunctions can be written using the $|v, \ell\rangle$ representation. Using the kinetic energy operator in the form given in equation (3.103) gives JT matrix elements

$$[\mathcal{H}_{JT}]_{\kappa j,\rho i} = \langle\varphi_j|\frac{\omega^2}{k}P_+P_-|\varphi_i\rangle\delta_{\kappa\rho} + \langle\varphi_j|(f^+_{\kappa\rho}Q_+ + f^-_{\kappa\rho}Q_-|\varphi_i\rangle$$

$$+\frac{1}{2}\langle\varphi_j|g^+_{\kappa\rho}Q_+^2 + g^-_{\kappa\rho}Q_-^2 + 2\,k_{\kappa\rho}Q_+Q_-|\varphi_i\rangle \qquad (5.12)$$

where the electronic matrix elements are

$$f^{\pm}_{\kappa\rho} = \langle\phi_\kappa|\left(\frac{\partial V}{\partial Q_\pm}\right)_0|\phi_\rho\rangle \qquad (5.13)$$

$$g^{\pm}_{\kappa\rho} = \langle\phi_\kappa|\left(\frac{\partial^2 V}{\partial Q_\pm^2}\right)_0|\phi_\rho\rangle \qquad (5.14)$$

$$k_{\kappa\rho} = \langle\phi_\kappa|\left(\frac{\partial^2 V}{\partial Q_+\partial Q_-}\right)_0|\phi_\rho\rangle \qquad (5.15)$$

$f^{\pm}_{\kappa\rho}$ is represents the linear JT coupling of electronic states ϕ_κ and ϕ_ρ, whereas $g^{\pm}_{\kappa\rho}$ represents quadratic coupling.

5.2.1 The Electronic (Static) Jahn-Teller Effect

Despite the fact that the JT operators are one-electron operators, evaluation of the electronic matrix elements in equations (5.13) to (5.15) is difficult. However, using the WET (Section 2.2.4) it is possible to determine the independent elements, which can then be treated as parameters. The relevant operators have the form

$$\left(\frac{\partial^{n+m}V}{\partial Q_\eta^n \partial Q_\mu^m}\right)_0 Q_\eta^n Q_\mu^m \qquad (5.16)$$

and must transform as the totally symmetric irrep since they form part of a molecular Hamiltonian. Thus, the differential operator transforms as the *adjoint* of the coordinate product

$$\left(\frac{\partial^{n+m}V}{\partial Q_\eta^n\,\partial Q_\mu^m}\right)_0 \sim (Q_\eta^n Q_\mu^m)^\dagger \tag{5.17}$$

If the vibrational modes $Q_\pm$ transform as $|j\ \pm j\rangle$ in $\mathbf{D}_\infty$ (Section 3.4.2) then the transformation properties of the linear differential operators are given by

$$\partial V/\partial Q_\pm \sim |j\ \pm j\rangle^\dagger \sim |j\ \mp j\rangle \tag{5.18}$$

The transformation properties of the quadratic coordinate products are obtained (using the fact that the vibrations are bosonic in character) from the symmetric square of j

$$[j^2] = 0 \oplus 2j \tag{5.19}$$

According to equation (2.66) and the tables in Appendix C, the specific combinations of products are

$$|(j\,j)\ 0\ 0\rangle = \frac{1}{\sqrt{2}}[|j\ {-j}\rangle|j\ j\rangle + |j\ j\rangle|j\ {-j}\rangle] \tag{5.20}$$

$$|(j\,j)\ 2j\ \pm 2j\rangle = |j\ \pm j\rangle|j\ \pm j\rangle \tag{5.21}$$

So it can be induced that

$$Q_+Q_- \sim |0\ 0\rangle \tag{5.22}$$

$$Q_\pm^2 \sim |2j\ \pm 2j\rangle \tag{5.23}$$

And therefore, using equation (5.17)

$$\partial^2 V/\partial Q_\pm^2 \sim |2j \mp 2j\rangle \tag{5.24}$$

$$\partial^2 V/\partial Q_+ \partial Q_- \sim |0\ 0\rangle \tag{5.25}$$

Since $\partial^2 V/\partial Q_+ \partial Q_-$ is totally symmetric, it can couple only states of the same symmetry (angular momentum) and will henceforth be referred to as a diagonal operator. On the other hand $\partial^2 V/\partial Q_\pm^2$ couple states that differ by two units of angular momentum and will be referred to as quadratic operators.

For the systems of interest in this thesis, the general electronic wavefunctions used above are replaced by (Section 3.2.2)

$$|\phi_\kappa\rangle = |^{2S+1}\mathrm{E}_\Lambda M_\Lambda\, \Sigma\rangle \tag{5.26}$$

The vibronic operators couple only the orbital parts. Since the operators transform as category-1 irreps, a linear JT effect in a mode that transforms as irrep Γ_L requires (in Butler notation)

$$[\Lambda^2] \supset \Gamma_\mathrm{L} \quad \text{or} \quad \Gamma_\mathrm{L} = 2\Lambda \tag{5.27}$$

A quadratic effect in the same state requires modes that transform as Γ_Q where

$$[\Lambda^2] \supset 2\Gamma_\mathrm{Q} \quad \text{or} \quad \Gamma_\mathrm{Q} = \Lambda \tag{5.28}$$

Consequently, in $\mathbf{D}_\infty$ a vibration can be either linearly or quadratically JT active with respect to a given electronic state, but not both. This last principle will be extended to the finite subgroups of $\mathbf{D}_\infty$ in a later section.

5.2.1.1 The Linear Jahn-Teller Effect

A linear Jahn-Teller (LJT) effect for an orbital state $|\mathrm{E}_\Lambda M_\Lambda\rangle$ requires modes, $Q_\pm$, that transform as $|2\Lambda \pm 2\Lambda\rangle$. According to equation (5.17), $\partial V/\partial \mathrm{Q}_\pm \sim |2\Lambda \pm 2\Lambda\rangle^\dagger \sim |2\Lambda \mp 2\Lambda\rangle$ and the non-zero off-diagonal electronic matrix elements are, using the WET and Appendix B:

$$\langle \mathrm{E}_\Lambda \mp \Lambda | \left(\frac{\partial V}{\partial Q_\pm} \right)_0 | \mathrm{E}_\Lambda \pm \Lambda \rangle = \frac{1}{\sqrt{2}} \langle \mathrm{E}_\Lambda \| 2\Lambda \| \mathrm{E}_\Lambda \rangle \equiv F \tag{5.29}$$

The diagonal electronic matrix elements are

$$\langle \mathrm{E}_\Lambda \, \Lambda | W^0 + 2Q_+Q_-k | \mathrm{E}_\Lambda \, \Lambda \rangle = W^0 + kQ_+Q_- \tag{5.30}$$

The Hamiltonian matrix constructed for the linear electronic (static) JT effect is

$\mathcal{H}_{\mathrm{el(L)}}$	$\lvert \mathrm{E}_\Lambda - \Lambda \rangle$	$\lvert \mathrm{E}_\Lambda + \Lambda \rangle$
$\langle \mathrm{E}_\Lambda - \Lambda \rvert$	$W^0 + kQ_+Q_-$	FQ_+
$\langle \mathrm{E}_\Lambda + \Lambda \rvert$	FQ_-	$W^0 + kQ_+Q_-$

(5.31)

where L indicates a linear JT effect. The eigenvalues for this matrix are

$$V_{\mathrm{L}\pm}(Q_+, Q_-) = W^0 + kQ_+Q_- \pm \sqrt{F^2Q_+Q_-} \tag{5.32}$$

So the linear electronic JT effect splits the potential energy into two surfaces, which, by expanding Q_+Q_- according to equation (3.101), can be seen to intersect only when Q_1 and Q_2 are zero.

It is instructive to rewrite equation (5.32) in plane polar coordinates (r θ). Parameter r measures the *magnitude* of displacement from the high-symmetry nuclear configuration (Q_0) and is given by

$$r = \sqrt{Q_1^2 + Q_2^2} = \sqrt{2Q_+Q_-} \tag{5.33}$$

while $\theta = \tan^{-1}(Q_2/Q_1)$. This allows equation (5.32) to be rewritten as

$$V_{\mathrm{L}\pm}(r) = W^0 + \frac{1}{2}kr^2 \pm \frac{1}{\sqrt{2}}Fr \tag{5.34}$$

Since this is independent of θ, the potential surfaces are cylindrically symmetric about Q_0. The minimum potential energy value is

$$V_{\mathrm{L}}^{\,0} = W^0 - F^2/4k \tag{5.35}$$

which occurs at JT displacements

$$r_0 = \mp F/k\sqrt{2} \tag{5.36}$$

the two distinct (±) values indicating that the surfaces are *not* degenerate at the minimum. The JT stabilisation energy is

$$\varepsilon_{JT} = W^0 - V^0 = F^2/4k \tag{5.37}$$

Figure 5.1 shows a section through the potential surfaces (r dependence).

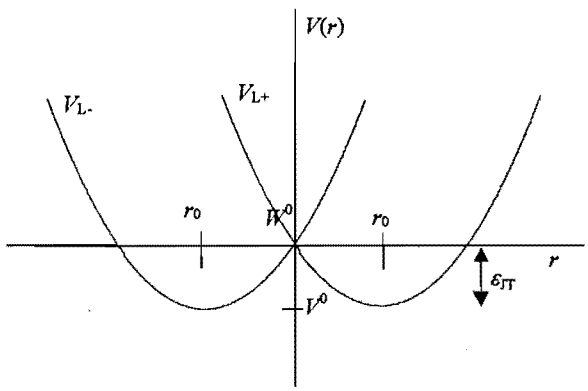

Figure 5.1: A section through the electronic potential energy surfaces for a linear electronic E ⊗ e Jahn-Teller effect. Parameters are defined in the text.

It is conventional to define a dimensionless linear JT displacement parameter λ, in terms of dimensionless coordinates defined by equation (3.5). This gives

$$\lambda_{JT} = \left(\frac{k}{\hbar\omega}\right)^{1/2} |r_0| = \frac{F}{\sqrt{2k\hbar\omega}} \tag{5.38}$$

which in turn gives the JT stabilisation energy as

$$\varepsilon_{JT} = \frac{\hbar\omega\lambda_{JT}^2}{2} \tag{5.39}$$

Equation (5.34) can be converted to dimensionless form by putting Q_1 and Q_2 in dimensionless form and setting $k = \hbar\omega$ (see footnote ii from Chapter 2). This gives

$$V_{L\pm}(r) = W^0 + \hbar\omega[\frac{r^2}{2} \pm \lambda_{JT} r] \tag{5.40}$$

The 'Mexican-hat' potential surfaces described by these equations are plotted in the top diagram of Figure 5.2. At the high-symmetry nuclear configuration (Q_0), the electronic states are degenerate but the potential energy is *not* minimised. The system will therefore distort to lower symmetry. However, since the minimum is cylindrically symmetric, the molecule will perform pseudo-rotations and will retain the time-averaged higher symmetry of Q_0.

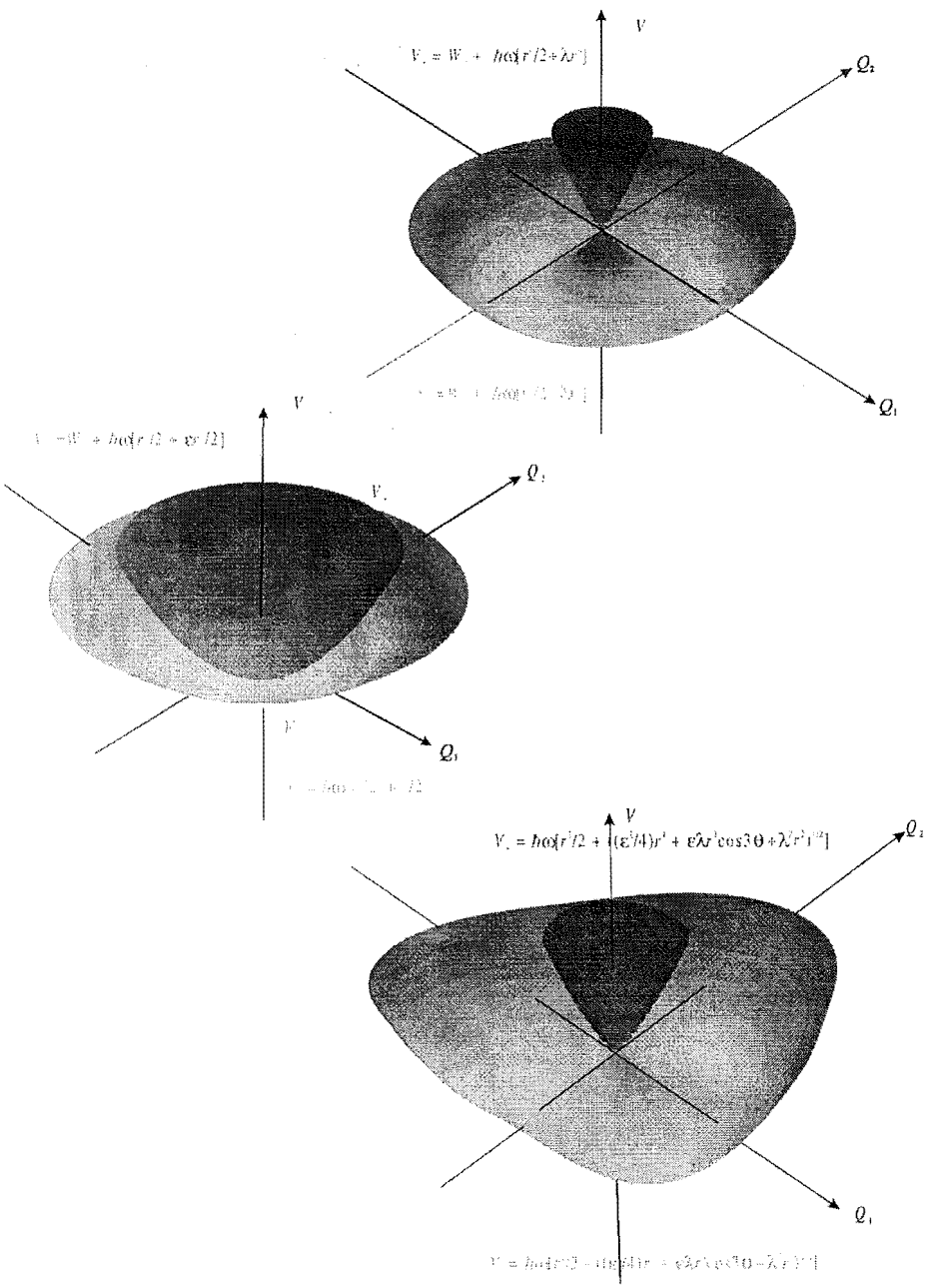

Figure 5.2: The electronic potential energy surfaces of a doubly degenerate electronic state as a function of coordinates Q_1 and Q_2. From top to bottom, the Jahn-Teller-active mode is linearly, quadratically and both linearly and quadratically active.

Inclusion of Spin

The states that are of interest in this thesis derive from ^{2}E terms with configurations e^1 and e^3. These can undergo SO splitting, which is diagonal in the $|^2E_\Lambda M_\Lambda \Sigma\rangle$ basis, with matrix elements given by equation (3.65) where, according to equations (3.66) and (3.67),

$$A'_\Lambda = (-1)^{(ne-1)} a'_\lambda \tag{5.41}$$

The corresponding four-dimensional electronic LJT-SO matrix is therefore block-diagonal, according to spin, with two sub matrices given by

$$\begin{array}{c|cc} \mathcal{H}_{el(L)} + \mathcal{H}_{SO} & \left|{}^2E_\Lambda \pm\Lambda \pm 1/2\right\rangle & \left|{}^2E_\Lambda \mp\Lambda \pm 1/2\right\rangle \\ \hline \left\langle {}^2E_\Lambda \pm\Lambda \pm 1/2\right| & W^0 + kQ_+Q_- - A'_\Lambda/2 & FQ_+ \\ \left\langle {}^2E_\Lambda \mp\Lambda \pm 1/2\right| & FQ_- & W^0 + kQ_+Q_- + A'_\Lambda/2 \end{array} \tag{5.42}$$

The eigenvalues of this matrix are (using dimensionless polar coordinates)

$$V_{L\pm}(r) = W^0 + \frac{1}{2}kr^2 \pm \sqrt{\frac{F^2r^2 + A'^2_\Lambda}{2}} \tag{5.43}$$

Thus, the four potential energy surfaces are split into two doubly degenerate LJT-SO surfaces, which are again cylindrically symmetric. A section through these is shown in Figure 5.3

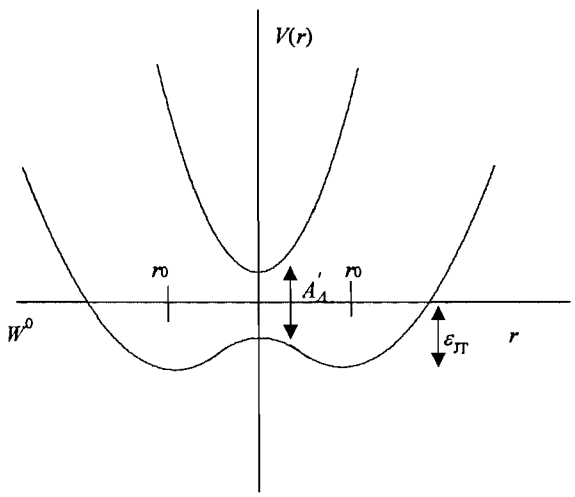

Figure 5.3: A section through the potential surfaces for a linear E ⊗ e Jahn-Teller effect after inclusion of spin-orbit coupling.

5.2.1.2 The Quadratic Jahn-Teller Effect

Non-zero quadratic Jahn-Teller effect (QJT) in an $|E_\Lambda M_\Lambda\rangle$ state require modes $Q_\pm$ that transform as $|\Lambda \pm\Lambda\rangle$. For such modes, $\partial^2 V/\partial Q_\pm^2 \sim |2\Lambda \pm 2\Lambda\rangle^\dagger \sim |2\Lambda \mp 2\Lambda\rangle$. Therefore, using the WET, the non-zero off-diagonal electronic matrix elements are:

$$\langle E_\Lambda \mp\Lambda|\left(\frac{\partial^2 V}{\partial Q_\pm^2}\right)_0|E_\Lambda \pm\Lambda\rangle = \frac{1}{\sqrt{2}}\langle\Lambda\|2\Lambda\|\Lambda\rangle \equiv G \tag{5.44}$$

The diagonal matrix elements are given by equation (5.30), so the Hamiltonian matrix for the quadratic electronic JT effect is

$\mathcal{H}_{el(Q)}$	$\lvert E_\Lambda -\Lambda\rangle$	$\lvert E_\Lambda +\Lambda\rangle$
$\langle E_\Lambda -\Lambda\rvert$	$W^0 + kQ_+Q_-$	$GQ_+^2/2$
$\langle E_\Lambda +\Lambda\rvert$	$GQ_-^2/2$	$W^0 + kQ_+Q_-$

(5.45)

with eigenvalues

$$V_{Q\pm}(Q_+, Q_-) = W^0 + kQ_+Q_- \pm \frac{G}{2}Q_+Q_- = W^0 + \frac{k}{4}r^2 \pm \frac{G}{2}r^2 \tag{5.46}$$

Again, the absence of θ from this expression indicates that the resulting surfaces are cylindrically symmetric and non-degenerate at all values of Q_1 and Q_2 except those giving $r = 0$. In fact, they are paraboloids with stationary points at $r = 0$. Figure 5.4 below shows a section through the potential surfaces (r dependence at a particular θ).

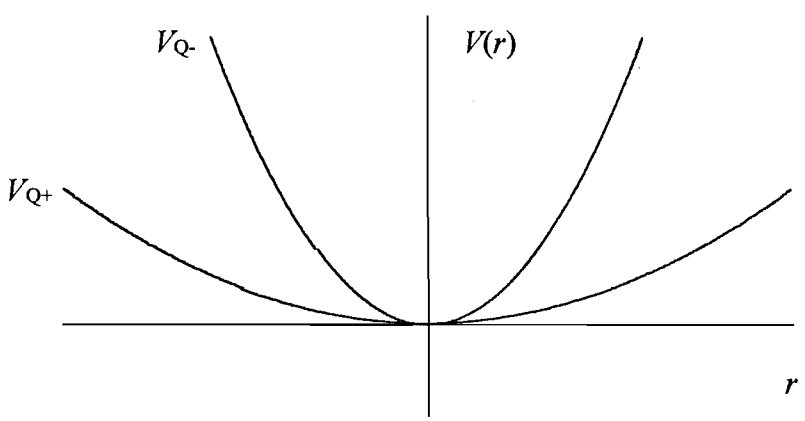

Figure 5.4: A section through the potential surfaces for a quadratic electronic E ⊗ e Jahn-Teller effect. Parameters are defined in the text.

In terms of dimensionless vibrational coordinates

$$V_{Q\pm}(r) = W^0 + \frac{1}{2}\hbar\omega(1 \pm \epsilon_{JT})r^2 \tag{5.47}$$

where ϵ_{JT} is a dimensionless QJT parameter defined by[4]

$$\epsilon_{JT} = \frac{G}{2k} \tag{5.48}$$

The potential surfaces described by these equations are plotted in the middle diagram of Figure 5.2. The lack of low-symmetry minima means that the quadratic effect cannot alone reduce the symmetry of a molecule.

Inclusion of spin

Proceeding in the same way as for the LJT effect in Section 5.2.1.1, the matrices electronic QJT-SO effect for a $^2E_\Lambda$ manifold are given by

$\mathcal{H}_{el(Q)} + \mathcal{H}_{SO}$	$\left\|{}^2E_\Lambda\ \pm\Lambda\ \pm 1/2\right\rangle$	$\left\|{}^2E_\Lambda\ \mp\Lambda\ \pm 1/2\right\rangle$
$\left\langle{}^2E_\Lambda\ \pm\Lambda\ \pm 1/2\right\|$	$W^0 + kQ_+Q_- - A'_\Lambda/2$	$GQ_-^2/2$
$\left\langle{}^2E_\Lambda\ \mp\Lambda\ \pm 1/2\right\|$	$GQ_+^2/2$	$W^0 + kQ_+Q_- + A'_\Lambda/2$

(5.49)

with eigenvalues

$$V_{Q\pm}(r) = W^0 + \frac{1}{2}kr^2 \pm \sqrt{\left(\frac{Gr^2}{4}\right)^2 + \left(\frac{A'_\Lambda}{2}\right)^2} \tag{5.50}$$

So the combined QJT and SO effects coupling splits the four states to give two doubly degenerate QJT-SO surfaces.

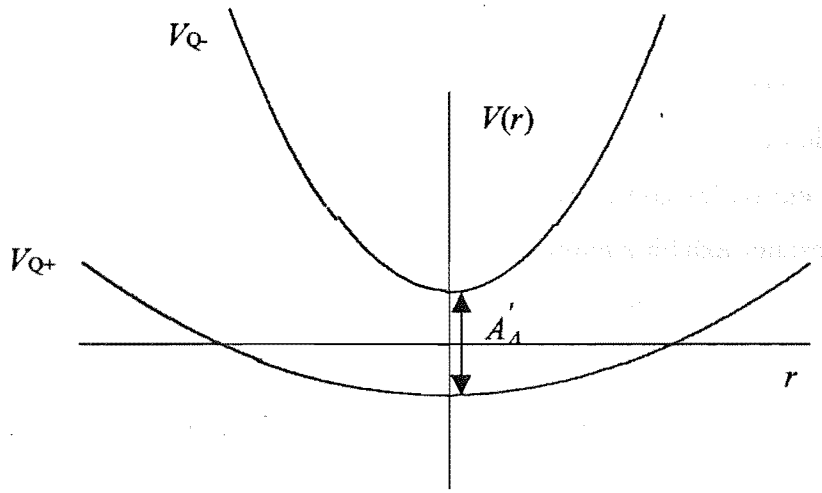

Figure 5.5: A section through the potential surfaces for a quadratic E ⊗ e Jahn-Teller effect after inclusion of spin-orbit coupling.

5.2.1.3 Simultaneous Linear and Quadratic Jahn-Teller Effects

As stated above, an electronic state of a system with $\mathbf{D}_\infty$ symmetry is not simultaneously susceptible to LJT and QJT effects in the same modes. However, in some subgroups of $\mathbf{D}_\infty$, simultaneous activity is possible. This matter was briefly discussed by Engelking and Lineberger,[5] but since their proof is rather terse and the results seem not to be a familiar part of the literature, they are reiterated here.

Consider a pair of orbital states that transform in point group $\mathbf{D}_n$ as E_Λ where $0 < \Lambda < n/2$. From equation (5.28) quadratic activity requires (in Butler notation)

$$\Gamma_Q = \Lambda \tag{5.51}$$

Linear activity requires $\Gamma_L \subset [\Lambda^2]$ (excluding the totally symmetric irrep). If $2\Lambda \leq n/2$ then $\Gamma_L = 2\Lambda$ and simultaneous QJT and LJT effects in the same mode are forbidden. However, if $2\Lambda > n/2$, then

$$\Gamma_L = n - 2\Lambda \tag{5.52}$$

In this case simultaneous activity ($\Gamma_Q = \Gamma_L$) requires

$$\Lambda = n/3 \tag{5.53}$$

and, since Λ must be an integer, n must be a multiple of 3. The only axial molecules with this property must have a principal axis C_3, C_6 ... Moreover, for such molecules, these conditions only exist for the case of $E_{n/3} \otimes e_{n/3}$ coupling.

The molecules considered in this thesis have five- or eight-fold symmetry and therefore cannot exhibit simultaneous LJT and QJT effects. But for completeness the hypothetical electronic case is briefly considered here.

The appropriate Hamiltonian matrix is given by the common diagonals and the sums of the off-diagonals given in equations (5.31) and (5.45)[ii]

$$\begin{array}{c|cc} \mathcal{H}_{\mathrm{el(L\&Q)}} & |\mathrm{E}_\Lambda - \Lambda\rangle & |\mathrm{E}_\Lambda + \Lambda\rangle \\ \hline \langle \mathrm{E}_\Lambda - \Lambda| & W^0 + kQ_+Q_- & FQ_- + GQ_+^2/2 \\ \langle \mathrm{E}_\Lambda + \Lambda| & FQ_+ + GQ_-^2/2 & W^0 + kQ_+Q_- \end{array} \qquad (5.54)$$

The eigenvalues, in polar coordinates, are

$$V_\pm(r\ \theta) = W^0 + \frac{1}{2}kr^2 \pm \frac{r}{2}\sqrt{(Gr/2)^2 + \sqrt{2}GFr\cos 3\theta + 2F^2} \qquad (5.55)$$

or, in dimensionless form,

$$V_\pm = W^0 + \hbar\omega\left[\frac{r^2}{2} \pm \sqrt{\epsilon_{\mathrm{JT}}^2 r^4/4 + \epsilon_{\mathrm{JT}}\lambda_{\mathrm{JT}} r^3 \cos 3\theta + \lambda_{\mathrm{JT}}^2 r^2}\right] \qquad (5.56)$$

The $\cos(3\theta)$ dependence indicates that the resulting potential surfaces will have three-fold symmetry about $r = 0$. The bottom diagram in Figure 5.2 shows that the lower surface has three symmetry-related minima away from the high-symmetry configuration. However, an isolated molecule will exist in a superposition of configurations with retention of the higher symmetry.

[ii] In a group $\mathbf{D}_n$, for a single vibrational mode to be both linearly and quadratically active, the requirement of equation (5.52) means that the subscripts ± for Q in the off-diagonal matrix elements must have the opposite sign for the linear effect and quadratic effects.

5.2.2 The Vibronic Jahn-Teller Effect

To solve the vibronic JT problem, the vibrational matrix elements of equation (5.12) must be determined using the results in Table 3.8. Since the operators of the type described in equation (5.16) cannot act on the spin part of the electronic wavefunction, the only non-zero JT matrix elements are those between basis states with the same values of Σ.

The diagonal matrix elements involve only the operators $Q_{\pm}Q_{\mp}$ and $P_{\pm}P_{\mp}$, and are

$$[\mathcal{H}_{JT}]_{\pm\Lambda v\ell,\pm\Lambda v\ell} = \langle v\ \ell|\frac{\omega^2}{k}P_+P_-|v\ \ell\rangle + \langle v\ \ell|kQ_+Q_-|v\ \ell\rangle = \hbar\omega(v+1) \qquad (5.57)$$

The non-zero off-diagonal elements require $M_\Lambda' = M_\Lambda \pm 2\Lambda$ (see section 5.2.1). They are of the form

$$[\mathcal{H}_{JT}]_{\mp\Lambda v\ell,\pm\Lambda,v'\ell'} = \langle v\ \ell|FQ_\pm + \frac{G}{2}Q_\pm^2|v'\ \ell'\rangle \qquad (5.58)$$

As discussed above in Section 5.2.1.3, for the molecules of interest in this thesis (which do not have three-fold symmetry axes) the matrix elements of only one of the operators on the right-hand side of equation (5.58) can be non-zero for a given vibration in a given electronic state. It is therefore convenient to consider the LJT and QJT effects separately.

The work required to determine the non-zero matrix elements of the types given in equation (5.58) is greatly reduced by noting that $\mathcal{H}_{JT}$ can only connect states with the same total vibronic angular momentum. For an axial molecule, this amounts to conservation of the sum of electronic and vibrational angular momenta in the direction of the molecular symmetry (z) axis. If the vibronic matrix elements are written in the general form;

$$\langle v\ \ell|\langle^2\mathrm{E}_\Lambda M_\Lambda\ \Sigma|\mathcal{H}_{JT}|^2\mathrm{E}_\Lambda M_\Lambda'\ \Sigma'\rangle|v'\ \ell'\rangle \qquad (5.59)$$

then

$$M_\Lambda + \Sigma + j\ell = M_\Lambda' + \Sigma' + j\ell' \tag{5.60}$$

where $j\ell$ gives the component of vibrational angular momentum in the z direction (Section 3.4.2). Furthermore, since $\Sigma = \Sigma'$ then

$$M_\Lambda + j\ell = M_\Lambda' + j\ell' \tag{5.61}$$

According to equations (5.27) and (5.28), LJT coupling requires $j = 2\Lambda$ while QJT coupling requires $j = \Lambda$. These results can be generalised for coupling of order n as

$$j = 2\Lambda/n \tag{5.62}$$

When combined with equation (5.60), the principle of conservation of vibronic angular moment can be re-couched in terms of conservation of a vibronic angular-momentum quantum number K_n defined by

$$K_n = \ell + nM_\Lambda/2\Lambda \tag{5.63}$$

Since $\ell = 0, \pm1, \pm2, \ldots$ and $M_\Lambda/\Lambda = \pm1$, then $K_2 = 0, \pm1, \pm2, \ldots$ for a QJT effect and $K_1 = \pm1/2, \pm3/2, \ldots$ for an LJT effect.[iii]

The problem defined by the value of n can be separated into independent sub-problems (branches) according to the value K_n. The first step in the construction of the matrices for each sub-problem is to determine the values of ℓ, v and M_Λ that must be considered for the given branch.

Since there are two values of M_Λ ($\pm\Lambda$), each branch must involve two values of ℓ. By rearranging equation (5.63) these are

$$\ell = K_n - nM_\Lambda/2\Lambda = K_n \mp n/2 \tag{5.64}$$

To determine the allowed values of v, it is useful to define a vibrational quantum number, m_n, giving the lowest possible value of v within the K_n branch. Since the lowest value of v for a given ℓ is (Section 3.4.2)

$$v_{\min} = |\ell| \tag{5.65}$$

then from equation (5.64)

$$m_n = |K_n \mp n/2|_{\min} = ||K_n| - n/2| \tag{5.66}$$

In terms of m_n the allowed values of v are then

$$v = m_n, m_n + n, m_n + 2n, \ldots \tag{5.67}$$

The allowed values of ℓ can also be expressed in terms of m_n:

for $K_n = 0$: $$\ell = \mp n/2 \tag{5.68}$$

for $K_n \neq 0$: $$\ell = m_n K_n/|K_n| \quad \text{and} \quad (m_n + n)K_n/|K_n| \tag{5.69}$$

It now remains to find the values of M_Λ that go with each ℓ. From equation (5.63),

$$M_\Lambda = (K_n - \ell)2\Lambda/n \tag{5.70}$$

Then from equations (5.68),

for $K_n = 0$: $$M_\Lambda = \pm\Lambda \tag{5.71}$$

[iii] $K_1 = m$ from reference 7 and $K_2 = K$ from reference 3.

whereas, from equations (5.66) and (5.69)

for $K_n \neq 0$: $M_\Lambda = (K_n - m_n K_n/|K_n|))2\Lambda/n$ and $(K_n - (m_n + n) K_n/|K_n|)2\Lambda/n$

$$= \Lambda K_n/|K_n| \quad \text{and} \quad -\Lambda K_n/|K_n| \tag{5.72}$$

5.2.2.1 Linear Jahn-Teller Effect

For LJT coupling the possible values of K_1 are

$$K_1 = \pm 1/2, \pm 3/2, \pm 5/2, \ldots \tag{5.73}$$

and K_1 can never be zero. The corresponding m_1 values are

$$m_1 = 0, 1, 2, \ldots \tag{5.74}$$

where for each m_1,

$$v = m_1, m_1 + 1, m_1 + 2, \ldots \tag{5.75}$$

Since $\ell = v, v\text{-}2, \ldots -v$, only one of the two values of ℓ permitted by equation (5.69) occurs for each v. The value of M_Λ is determined by comparison of equations (5.69) and (5.72).

It proves useful (especially for the writing of computer software) to arrange the basis states for a given branch (denoted hereafter for the LJT effect by L_{K_1}) in an order denoted by positive integers $i = 1, 2, 3 \ldots$, which, for the LJT effect increases with v. The quantum numbers for the basis states, so arranged, are listed in Table 5.1.

Table 5.1: Allowed quantum numbers for the L_{K_l} branch of an E ⊗ e linear Jahn-Teller effect;

$m_l = |K_l| - 1/2$ [a]

i	1	2	3	4	5	6	...	
v	m_l	m_l+1	m_l+2	m_l+3	m_l+4	m_l+5	...	m_l+i-1
ℓ	$\pm m_l$	$\pm(m_l+1)$	$\pm m_l$	$\pm(m_l+1)$	$\pm m_l$	$\pm(m_l+1)$	...	$\pm\left(m_l+\frac{(1+(-1)^i)}{2}\right)$
M_A	$\pm\Lambda$	$\mp\Lambda$	$\pm\Lambda$	$\mp\Lambda$	$\pm\Lambda$	$\mp\Lambda$	...	$\pm(-1)^i\Lambda$

[a] Prefixes ± or ∓ refer to $K_l/|K_l| = \pm 1$.

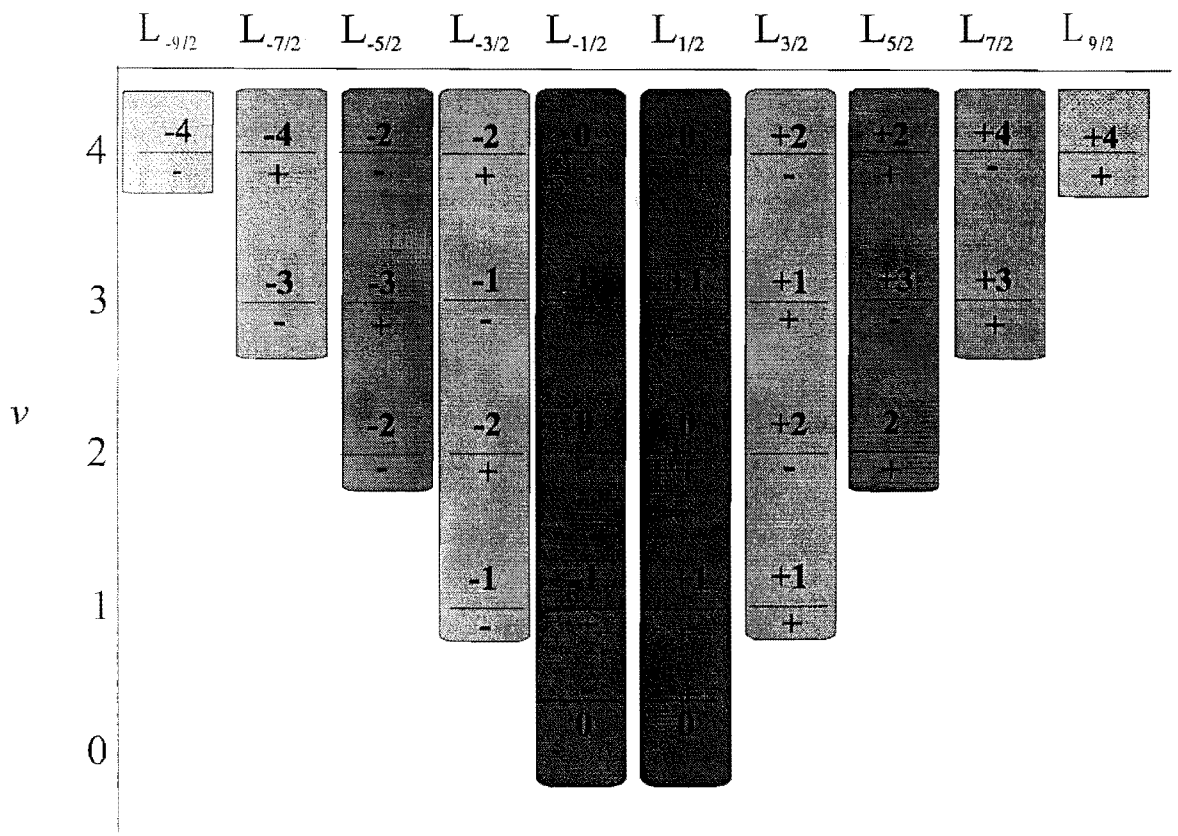

Figure 5.6: A branch diagram for a linear (n =1) JT effect for K_l values between –9/2 and 9/2. The Born-Oppenheimer basis states are labelled by v (on the "y-axis") and $\ell/\pm$, where ± indicates $M_A = \pm\Lambda$. Each vertical block labelled L_{K_l} is called a branch – the LJT effect mixes only those basis states within a branch.

The non-zero matrix elements (equation (5.12)) can now be determined in terms of m_1 and i. The diagonal elements are

$$[\mathcal{H}_{\mathrm{LJT}}]_{i,i} = \hbar\omega(m_1 + i) \tag{5.76}$$

The off-diagonals are slightly more complicated. Using the vibrational integrals from Table 3.8, they are (in terms of the dimensionless LJT parameter λ_{JT} defined by equation (5.38))

$$\text{for } i = 1, 3, 5, \ldots: \quad [\mathcal{H}_{\mathrm{LJT}}]_{i,i+1} = [\mathcal{H}_{\mathrm{LJT}}]_{i+1,i} = \lambda_{\mathrm{JT}}\hbar\omega\sqrt{m_1 + (i+1)/2} \tag{5.77}$$

$$\text{for } i = 2, 4, 6, \ldots: \quad [\mathcal{H}_{\mathrm{LJT}}]_{i,i+1} = [\mathcal{H}_{\mathrm{LJT}}]_{i+1,i} = \lambda_{\mathrm{JT}}\hbar\omega\sqrt{i/2} \tag{5.78}$$

When spin is included, each of the L_{K_1} branches so far considered splits into two, according to the value of Σ and denoted $L^{\Sigma}_{K_1}$, which do not intermix. Within each of these spin branches, SO interactions must be considered. This is easily achieved because $\mathcal{H}_{\mathrm{SO}}$ is diagonal in this LJT basis with (following equation (3.25)) elements

$$[\mathcal{H}_{\mathrm{so}}]_{i,i} = (-1)^{i}\Sigma A'_{\Lambda} K_1/|K_1| \tag{5.79}$$

The first few elements of the LJT-SO matrix for the $L^{\Sigma}_{\pm|K_1|}$ branches are set out in Table 5.2.

Table 5.2: The top left-hand corner of the SO-LJT matrix for the $L^{\Sigma}_{\pm|K_1|}$ branches [a]

$\mathcal{H}_{\mathrm{SO}} + \mathcal{H}_{\mathrm{LJT}}/\hbar\omega$	$\lvert^2E_A \pm\Lambda\ \Sigma\rangle$ $\lvert m_1, \pm m_1\rangle$	$\lvert^2E_A \pm\Lambda\ \Sigma\rangle$ $\lvert m_1+1, \pm(m_1\pm1)\rangle$	$\lvert^2E_A \pm\Lambda\ \Sigma\rangle$ $\lvert m_1+2, \pm m_1\rangle$	$\lvert^2E_A \pm\Lambda\ \Sigma\rangle$ $\lvert m_1+3, \pm(m_1\pm1)\rangle$	$\lvert^2E_A \pm\Lambda\ \Sigma\rangle$ $\lvert m_1+4, \pm m_1\rangle$
$\langle m_1, \pm m_1 \rvert\langle^2E_A \pm\Lambda\ \Sigma\rvert$	$\mp\Sigma A'_{\Lambda} + (m_1+1)$	$\lambda\sqrt{m_1+1}$			
$\langle m_1+1, \pm(m_1\pm1) \rvert\langle^2E_A \pm\Lambda\ \Sigma\rvert$	$\lambda\sqrt{m_1+1}$	$\pm\Sigma A'_{\Lambda} + (m_1+2)$	$\lambda\sqrt{1}$		
$\langle m_1+2, \pm m_1 \rvert\langle^2E_A \pm\Lambda\ \Sigma\rvert$		$\lambda\sqrt{1}$	$\mp\Sigma A'_{\Lambda} + (m_1+3)$	$\lambda\sqrt{m_1+2}$	
$\langle m_1+3, \pm(m_1\pm1) \rvert\langle^2E_A \pm\Lambda\ \Sigma\rvert$			$\lambda\sqrt{m_1+2}$	$\pm\Sigma A'_{\Lambda} + (m_1+4)$	$\lambda\sqrt{2}$
$\langle m_1+4, \pm m_1 \rvert\langle^2E_A \pm\Lambda\ \Sigma\rvert$				$\lambda\sqrt{2}$	$\mp\Sigma A'_{\Lambda} + (m_1+5)$

[a] Prefixes $\pm$ or $\mp$ refer to $K_1/|K_1| = \pm1$.

The eigenfunctions and eigenvalues of matrix can be determined by numerical diagonalisation. Although the matrix is of infinite dimension, in practice it can be truncated to a reasonable size determined by convergence of the results to the point where the lowest 80 states are invariant to the basis size. The LJT energies ($A_A' = 0$), which are independent of the sign of K_1 are plotted in Figure 5.7

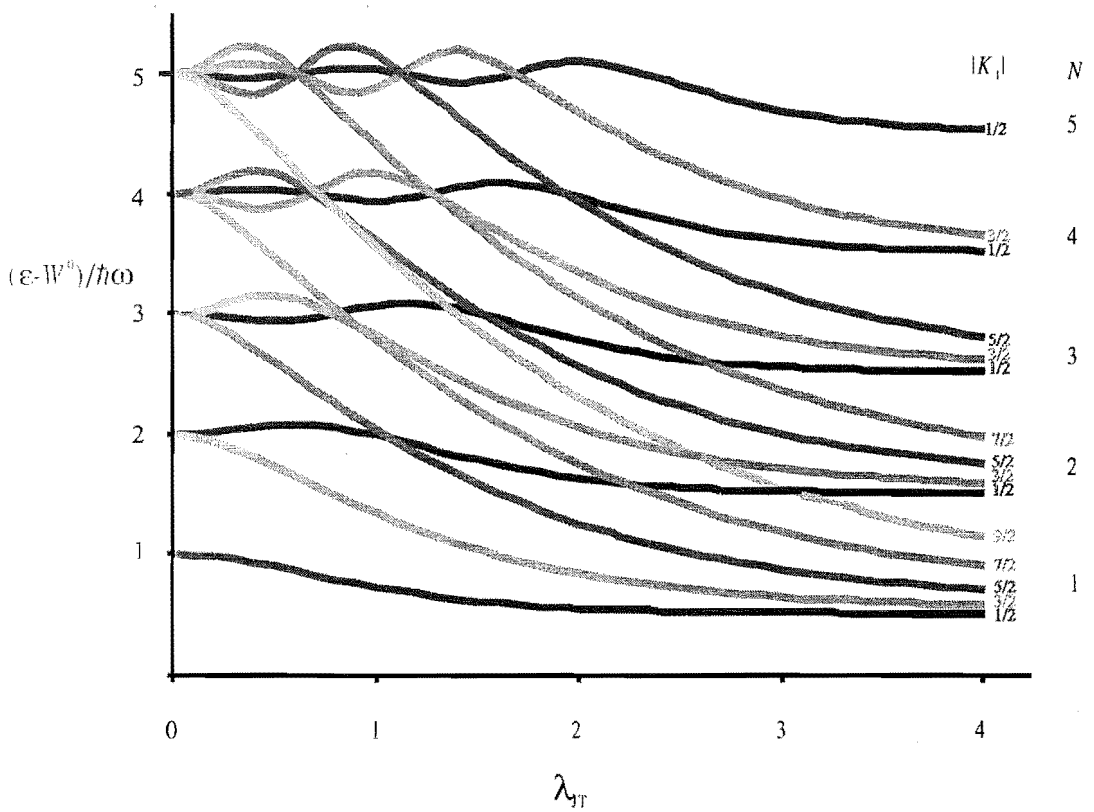

Figure 5.7: The eigenvalues for LJT coupling as a function of the dimensionless parameter λ_{JT}, in the absence of SO coupling. The shading of the lines are correlated with Figure 5.6 and indicate the L_{K_1} branch to which the state belongs.

The LJT-SO wavefunctions that result from the diagonalisation of the matrix are indexed by $N = 1, 2, 3, \ldots$, chosen so that, in the absence of SO coupling, it increases with ascending energy. To ensure that the $N = 1$ state is lowest, independent of the presence or sign (regular or inverted) of SO splitting, a spin parameter σ is introduced where

$$\sigma = (-1)^{(n_e+1)}\Sigma \qquad (5.80)$$

Thus $\sigma = -\Sigma$ for a regular SO system (e_λ^1 configuration) and $\sigma = \Sigma$ for an inverted system (e_λ^3 configuration). The eigenstates for the $L_{K_1}^{\Sigma}$ branch are then denoted $|L_{K_1}^{\Sigma} N\rangle$, and have the general form

$$|L_{\mp|K_1|}^{\mp\sigma}, N\rangle = \sum_{i=1,3,5\ldots} c^{-}_{|K_1|,i,N} |^2E_\Lambda \mp\Lambda \mp\sigma\rangle|m+i-1, \mp m\rangle$$

$$+ \sum_{i=2,4,6\ldots} c^{-}_{|K_1|,i,N} |^2E_\Lambda \pm\Lambda \mp\sigma\rangle|m+i-1, \mp(m+1)\rangle \qquad (5.81)$$

$$|L_{\pm|K_1|}^{\mp\sigma}, N\rangle = \sum_{i=1,3,5\ldots} c^{+}_{|K_1|,i,N} |^2E_\Lambda \pm\Lambda \mp\sigma\rangle|m+i-1, \pm m\rangle$$

$$+ \sum_{i=2,4,6\ldots} c^{+}_{|K_1|,i,N} |^2E_\Lambda \mp\Lambda \mp\sigma\rangle|m+i-1, \mp(m+1)\rangle \qquad (5.82)$$

Here the $c^{\pm}_{|K_1|,i,N}$ are coefficients determined by the diagonalisation procedure. In the absence of SO coupling, $c^{+}_{|K_1|,i,N} = c^{-}_{|K_1|,i,N}$, but this is generally not the case.

5.2.2.2 Quadratic Jahn-Teller Effect

The QJT branches are denoted Q_{K_2}, where

$$K_2 = 0, \pm1, \pm2, \pm3, \pm4, \ldots$$

The corresponding m_2 values are:

$$m_2 = 1, 0, 1, 2, 3, \ldots$$

where for each m_2,

$$v = m_2, m_2 + 2, m_2 + 4, \ldots$$

There now exists a $K_2 = 0$ branch, which is most easily treated separately from the other possibilities.

$K_2 = 0$

The Q_0 branch is represented by the central 'column' of Figure 5.8. The eigenvalues that result from diagonalisation of this matrix are shown in the central column of Figure 5.9.

Table 5.3: Allowed quantum numbers for the Q_0 ($K_2 = 0$) branch of an E ⊗ e quadratic Jahn-Teller effect; $m_2 = 1$

i	1	2	3	4	5	6	...	odd i	even i
v	1	1	3	3	5	5	...	i	i-1
ℓ	-1	1	-1	1	-1	1	...	-1	1
M_Λ	Λ	$-\Lambda$	Λ	$-\Lambda$	Λ	$-\Lambda$	...	Λ	$-\Lambda$

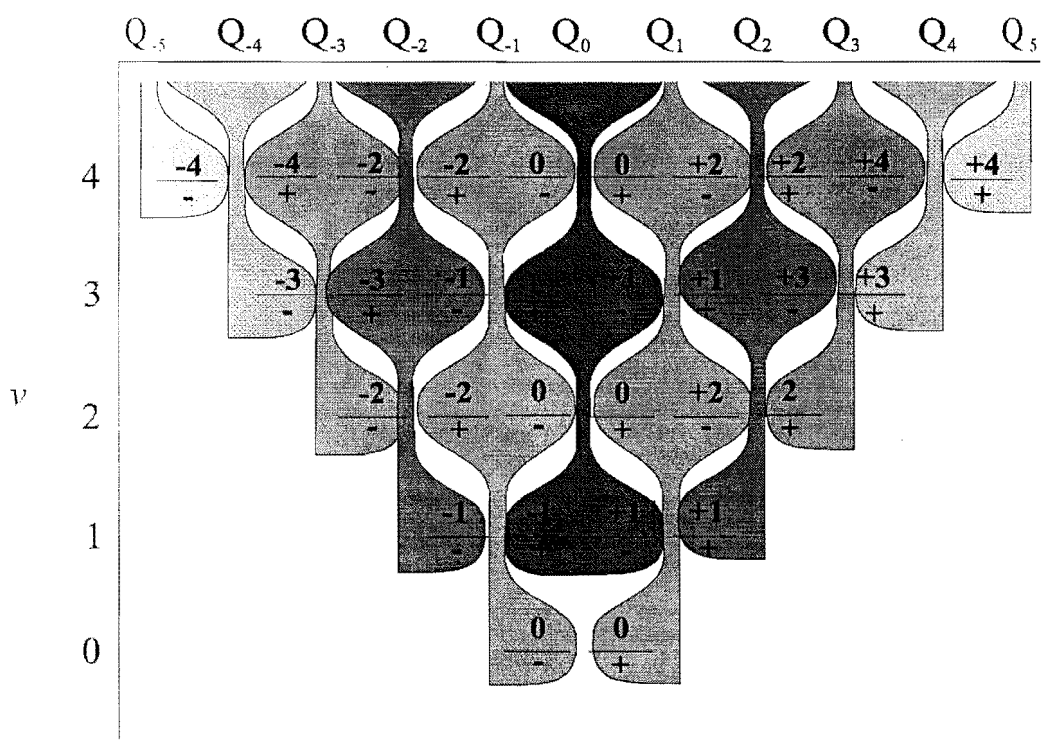

Figure 5.8: A branch diagram for an E ⊗ e quadratic (n =2) Jahn-Teller effect for K_2 values between 0 and 4. The Born-Oppenheimer basis states are labelled by v (on the "y-axis") and $\ell/\pm$, where ± indicates $M_\Lambda = \pm\Lambda$. Each vertical block labelled Q_{K_2} is called a *branch* – the QJT effect mixes only those basis states within a branch.

Again using equation (5.12) and Table 3.8, the non-zero matrix elements are (in terms of the dimensionless QJT parameter ϵ_{JT}, defined by equation (5.48).

for $i = 1, 3, 5, \ldots$:

$$[\mathcal{H}_{QJT}(0)]_{i,i} = \hbar\omega(i+1) \tag{5.83}$$

$$[\mathcal{H}_{QJT}(0)]_{i,i+1} = [\mathcal{H}_{QJT}(0)]_{i+1,i} = \epsilon_{JT}\hbar\omega(i+1)/2 \tag{5.84}$$

$$[\mathcal{H}_{QJT}(0)]_{i,i+3} = [\mathcal{H}_{QJT}(0)]_{i+3,i} = \epsilon_{JT}\hbar\omega\sqrt{(i+1)(i+3)}/4 \tag{5.85}$$

for $i = 2, 4, 6, \ldots$:

$$[\mathcal{H}_{QJT}(0)]_{i,i} = \hbar\omega i \tag{5.86}$$

$$[\mathcal{H}_{QJT}(0)]_{i,i+1} = [\mathcal{H}_{QJT}(0)]_{i+1,i} = \epsilon_{JT}\hbar\omega\sqrt{(i)(i+2)}/4 \tag{5.87}$$

For $K_2 = 0$, there are only two QJT-SO branches. However, it will be useful to treat this case as if there were four, labelled $Q_{\pm 0}^{\mp\sigma}$, where σ was defined in equation (5.80) (in fact $Q_{+0}^{\mp\sigma} = Q_{-0}^{\mp\sigma} \equiv Q_{0}^{\mp\sigma}$) . The top left corner of the corresponding QJT-SO matrix is given in Table 5.4

Table 5.4: The top left-hand corner of the QJT-SO matrix for the branch $Q_{\pm 0}^{\Sigma}$

$\mathcal{H}_{SO} + \mathcal{H}_{QJT}(0)/\hbar\omega$	$\|^2E_A\,\Lambda\,\Sigma\rangle\|1, -1\rangle$	$\|^2E_A\,-\Lambda\,\Sigma\rangle\|1, 1\rangle$	$\|^2E_A\,\Lambda\,\Sigma\rangle\|3, -1\rangle$	$\|^2E_A\,-\Lambda\,\Sigma\rangle\|3, 1\rangle$	$\|^2E_A\,\Lambda\,\Sigma\rangle\|5, -1\rangle$
$\langle 1, -1\|\langle^2E_A\,\Lambda\,\Sigma\|$	$-\Sigma A_\Lambda' + 2$	ϵ_{JT}		$\epsilon_{JT}\sqrt{1/2}$	
$\langle 1, 1\|\langle^2E_A\,-\Lambda\,\Sigma\|$	ϵ_{JT}	$\Sigma A_\Lambda' + 2$	$\epsilon_{JT}\sqrt{1/2}$		
$\langle 3, -1\|\langle^2E_A\,\Lambda\,\Sigma\|$		$\epsilon_{JT}\sqrt{1/2}$	$-\Sigma A_\Lambda' + 4$	$2\epsilon_{JT}$	
$\langle 3, 1\|\langle^2E_A\,-\Lambda\,\Sigma\|$	$\epsilon_{JT}\sqrt{1/2}$		$2\epsilon_{JT}$	$\Sigma A_\Lambda' + 4$	$\epsilon_{JT}\sqrt{3/2}$
$\langle 5, -1\|\langle^2E_A\,\Lambda\,\Sigma\|$				$\epsilon_{JT}\sqrt{3/2}$	$-\Sigma A_\Lambda' + 6$

The general forms for the eigenfunctions are in this case

$$|Q_{\pm 0}^{\mp\sigma}, N\rangle = \sum_{i=1,3,5\ldots} c_{0,i,N}^{+} |^2E_A \mp\Lambda \mp\sigma\rangle|\, i, \mp 1\rangle + \sum_{i=2,4,6\ldots} c_{0,i,N}^{+} |^2E_A \pm\Lambda \mp\sigma\rangle|i\text{-}1, \pm 1)\rangle \tag{5.88}$$

$$|Q_{\mp 0}^{\mp\sigma}, N\rangle = \sum_{i=1,3,5\ldots} c_{0,i,N}^{-} |^2E_A \mp\Lambda \mp\sigma\rangle|i, \pm 1\rangle + \sum_{i=2,4,6\ldots} c_{0,i,N}^{-} |^2E_A \pm\Lambda \mp\sigma\rangle|\, i\text{-}1, \mp 1)\rangle \tag{5.89}$$

Note that $|Q_{\pm 0}^{\mp\sigma}, N\rangle$ and $|Q_{\mp 0}^{\mp\sigma}, N\rangle$ are the same, differing only in the *i*-order of the states. The corresponding eigenvalues are plotted as a function of the dimensionless parameterϵ_{JT} in Figure 5.9.

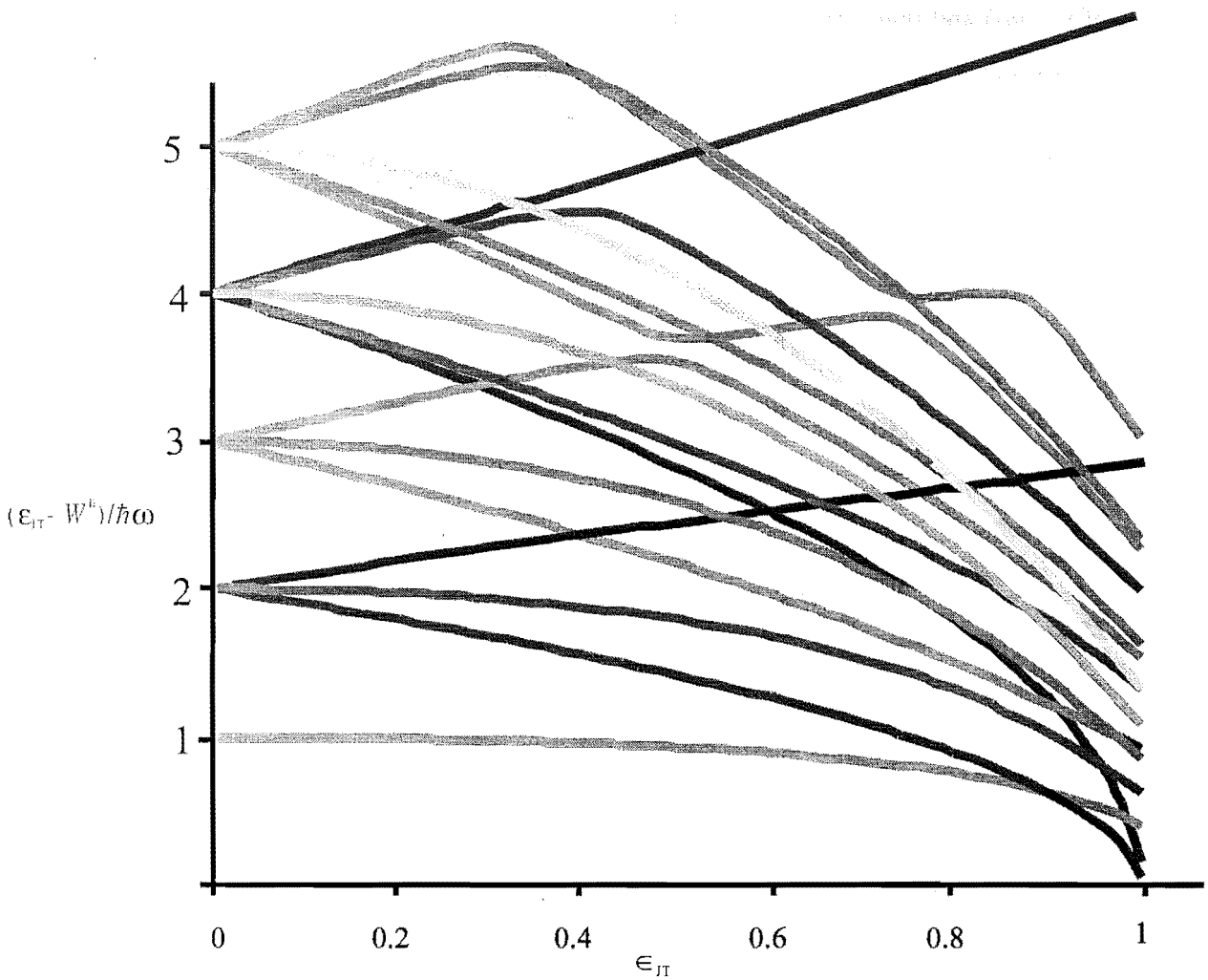

Figure 5.9: The eigenvalues for QJT coupling as a function of the dimensionless parameter ϵ_{JT}, in the absence of SO coupling. The shading of the lines are correlated with Figure 5.8 and indicate the Q_{K_2} branch to which the state belongs. As ϵ_{JT} gets large the energy of the eigenfunctions tends towards zero. This is an artefact of the of the model which assumes that the electronic potential takes the form of a Taylor's expansion.

$K_2 \neq 0$

The $Q_{K_2 \neq 0}$ branches form pairs, with the same value of $|K_2|$, mirrored around the Q_0 branch of Figure 5.8. As required for software development, the allowed quantum numbers are given in Table 5.5, with i increasing with increasing v (from a minimum of $v = m_2$) and then with decreasing $|\ell|$. The values of $v > m_2$ occur twice (once with each ℓ and M_Λ value) in steps of two, but $v = m_2$ occurs only once.

Table 5.5: Allowed quantum number for the Q_{K_2} branch with $|K_2| > 0$ of an E ⊗ e quadratic Jahn-Teller effect; $m_2 = |K_2| - 1$[a]

i	1	2	3	4	5	6	...	odd i	even i
v	m_2	m_2+2	m_2+2	m_2+4	m_2+4	m_2+6	...	m_2+i-1	m_2+i
ℓ	$\pm m_2$	$\pm(m_2+2)$	$\pm m_2$	$\pm(m_2+2)$	$\pm m_2$	$\pm(m_2+2)$	...	$\pm m_2$	$\pm(m_2+2)$
M_Λ	$\pm\Lambda$	$\mp\Lambda$	$\pm\Lambda$	$\mp\Lambda$	$\pm\Lambda$	$\mp\Lambda$	...	$\pm\Lambda$	$\mp\Lambda$

[a] Prefixes ± or ∓ refer to $K_1/|K_1| = \pm 1$.

The non-zero QJT matrix elements are

for $i = 1, 3, 5, \ldots$: $$[\mathcal{H}_{QJT}]_{i,i} = \hbar\omega(m_2+i) \tag{5.90}$$

$$[\mathcal{H}_{QJT}]_{i,i+1} = [\mathcal{H}_{QJT}]_{i+1,i} = \epsilon_{JT}\hbar\omega\sqrt{(2m_2+i+1)(2m_2+i+3)}/4 \tag{5.91}$$

for $i = 2, 4, 6, \ldots$: $$[\mathcal{H}_{QJT}]_{i,i} = \hbar\omega(m_2+i+1) \tag{5.92}$$

$$[\mathcal{H}_{QJT}]_{i,i+1} = [\mathcal{H}_{QJT}]_{i+1,i} = \epsilon_{JT}\hbar\omega\sqrt{i(2m_2+i+2)}/2 \tag{5.93}$$

$$[\mathcal{H}_{QJT}]_{i,i+3} = [\mathcal{H}_{QJT}]_{i+3,i} = \epsilon_{JT}\hbar\omega\sqrt{i(i+2)}/4 \tag{5.94}$$

The top left corner of the QJT-SO matrix for the $Q_{K_2 \neq 0}$ branch is given in Table 5.6

Table 5.6: The top left-hand corner of the SO-QJT matrix for the branch $Q^{\Sigma}_{K_2\neq 0}$

$\mathcal{H}_{SO} + \mathcal{H}_{QJT}/\hbar\omega$	$\|^2E_A \pm\Lambda\ \Sigma\rangle$ $\|m_2, \pm m_2\rangle$	$\|^2E_A \mp\Lambda\ \Sigma\rangle$ $\|m_2+2, \pm(m_2+2)\rangle$	$\|^2E_A \pm\Lambda\ \Sigma\rangle$ $\|m_2+2, \pm m_2\rangle$	$\|^2E_A \mp\Lambda\ \Sigma\rangle$ $\|m_2+4, \pm(m_2+2)\rangle$	$\|^2E_A \pm\Lambda\ \Sigma\rangle$ $\|m_2+4, \pm m_2\rangle$
$\langle m_2, \pm m_2 \|\langle^2E_A \pm\Lambda\ \Sigma\|$	$\mp\Sigma A'_{\Lambda} + (m_2+1)$	$\varepsilon\sqrt{m_2^2+3m_2+2}/2$			
$\langle m_2+2, \pm(m_2+2) \|\langle^2E_A \mp\Lambda\ \Sigma\|$	$\varepsilon\sqrt{m_2^2+3m_2+2}/2$	$\Sigma A'_{\Lambda} + (m_2+3)$	$\varepsilon\sqrt{m_2+2}$	$\varepsilon\sqrt{1/2}$	
$\langle m_2+2, \pm m_2 \|\langle^2E_A \pm\Lambda\ \Sigma\|$		$\varepsilon\sqrt{m_2+2}$	$\mp\Sigma A'_{\Lambda} + (m_2+3)$	$\varepsilon\sqrt{m_2^2+5m_2+6}/2$	
$\langle m_2+4, \pm(m_2+2) \|\langle^2E_A \mp\Lambda\ \Sigma\|$		$\varepsilon\sqrt{1/2}$	$\varepsilon\sqrt{m_2^2+5m_2+6}/2$	$\Sigma A'_{\Lambda} + (m_2+5)$	$\varepsilon\sqrt{2m_2+6}$
$\langle m_2+4, \pm m_2 \|\langle^2E_A \pm\Lambda\ \Sigma\|$				$\varepsilon\sqrt{2m_2+6}$	$\mp\Sigma A'_{\Lambda} + (m_2+5)$

The QJT wavefunctions that result are denoted by index N and are of the general form

$$|Q^{\mp\sigma}_{\mp|K_2|}, N\rangle = \sum_{i=1,3,5\ldots} \mathcal{C}^{-}_{|K_2|,i,N} |^2E_A \mp\Lambda\ \mp\sigma\rangle |m_2+i-1, \mp m_2\rangle$$

$$+ \sum_{i=2,4,6\ldots} \mathcal{C}^{-}_{|K_2|,i,N} |^2E_A \pm\Lambda\ \mp\sigma\rangle |m_2+i, \mp(m_2+2)\rangle \qquad (5.95)$$

$$|Q^{\mp\sigma}_{\pm|K_2|}, N\rangle = \sum_{i=1,3,5\ldots} \mathcal{C}^{+}_{|K_2|,i,N} |^2E_A \pm\Lambda\ \mp\sigma\rangle |m_2+i-1, \pm m_2\rangle$$

$$+ \sum_{i=2,4,6\ldots} \mathcal{C}^{+}_{|K_2|,i,N} |^2E_A \mp\Lambda\ \mp\sigma\rangle |m_2+i, \pm(m_2+2)\rangle \qquad (5.96)$$

The corresponding eigenvalues are plotted against ε_{JT} in Figure 5.9.

5.3 Zeeman Matrix Elements

The SO-JT wavefunctions given in equations (5.81), (5.82), (5.95) and (5.96) can be generalised

$$|\psi^{\mp\sigma}_{\mp|K_n|}, N\rangle = \sum_{i=1,3,5\ldots} \mathcal{C}^{-}_{|K_n|,i,N} |^2E_A \mp\Lambda\ \mp\sigma\rangle |v_i, \ell_i\rangle + \sum_{i=2,4,6\ldots} \mathcal{C}^{-}_{|K_n|,i,N} |^2E_A \pm\Lambda\ \mp\sigma\rangle |v_i, \ell_i\rangle \quad (5.97)$$

$$|\psi^{\mp\sigma}_{\pm|K_n|}, N\rangle = \sum_{i=1,3,5\ldots} c^{+}_{|K_n|,i,N} |{}^2\mathrm{E}_\Lambda \pm\Lambda \mp\sigma\rangle|v_i, -\ell_i\rangle + \sum_{i=2,4,6\ldots} c^{+}_{|K_n|,i,N} |{}^2\mathrm{E}_\Lambda \mp\Lambda \mp\sigma\rangle| v_i, \ell_i\rangle \quad (5.98)$$

where in equations (5.97) and (5.98):

for $\psi = \mathrm{L}$, $n = 1, v_i = m_1 + i - 1$, $\ell_{i=1,3,5\ldots} = \mp m_1$ and $\ell_{i=2,4,6\ldots} = \mp(m_1+1)$.

for $\psi = \mathrm{Q}$, $n = 2$, $v_{i=1,3,5\ldots} = m_2 + i - 1$, $v_{i=2,4,6\ldots} = m_2 + i$, $\ell_{i=1,3,5\ldots} = \mp m_2$ and $\ell_{i=2,4,6\ldots} = \mp(m_2+2)$.

The following treatment relates to axial molecules without three-fold symmetry axes, so that a mode can be either LJT or QJT active in one state, but not both. The electronic angular momentum matrix elements required for Zeeman interactions within a vibronic manifold are

$$\langle \psi^{\sigma'}_{K_n'}, N' | L_\eta + g_e S_\eta | \psi^{\sigma}_{K_n}, N\rangle \quad (\eta = x, y, z) \quad (5.99)$$

The non-zero electronic parts can be determined using equations (3.74) and (3.75). However, vibrational orthogonality must also be considered, giving

$$\langle v'\ \ell'|\langle {}^2\mathrm{E}_\Lambda M_\Lambda'\ \Sigma'|L_z + g_e S_z|{}^2\mathrm{E}_\Lambda M_\Lambda\ \Sigma\rangle|v\ \ell\rangle$$

$$= (g_\Lambda M_\Lambda/2\Lambda + g_e\Sigma)\delta_{\Sigma',\Sigma}\delta_{M_\Lambda',M_\Lambda}\delta_{v',v}\delta_{\ell',\ell} \quad (5.100)$$

$$\langle v'\ \ell'|\langle {}^2\mathrm{E}_\Lambda M_\Lambda'\ \Sigma'|L_x + g_e S_x|{}^2\mathrm{E}_\Lambda M_\Lambda\ \Sigma\rangle|v\ \ell\rangle = \frac{g_e}{2}\delta_{\Sigma',\Sigma}\delta_{M_\Lambda',M_\Lambda}\delta_{v',v}\delta_{\ell',\ell} \quad (5.101)$$

The vibrational delta functions mean that Zeeman coupling between two BO basis functions will only occur if they belong to the same JT branch – that is, they ha ve the same value of K_n. The non-zero z-component matrix elements of the $\psi^{\mp\sigma}_{\mp|K_n|}$ JT-SO branches (which contains the lowest energy vibronic state, $|\psi^{\mp\sigma}_{\mp|K_n|}, 1\rangle$) can therefore be rewritten:

$$\langle \psi^{\mp\sigma}_{\mp|K_s|}, N'|L_z + g_e S_z|\psi^{\mp\sigma}_{\mp|K_s|}, N\rangle = \mp\Big(\sum_{i=1,3,5\ldots} c^{-*}_{|K_s|,i,N'} c^{-}_{|K_s|,i,N} - \sum_{i=2,4,6\ldots} c^{-*}_{|K_s|,i,n'} c^{-}_{|K1|,i,N}\Big)g_\Lambda$$

$$\mp \sum_i c^{-*}_{|K_s|,i,N} c^{-}_{|K_s|,i,N} \sigma g_e \qquad (5.102)$$

Recognising that the spin coefficient is a delta function, this becomes

$$\langle \psi^{\mp\sigma}_{\mp|K_s|}, N'|L_z + g_e S_z|\psi^{\mp\sigma}_{\mp|K_s|}, N\rangle$$

$$= \mp\Big(\sum_{i=1,3,5\ldots} c^{-*}_{|K_s|,i,N} c^{-}_{|K_s|,i,N} - \sum_{i=2,4,6\ldots} c^{-*}_{|K_s|,i,N} c^{-}_{|K_s|,i,N}\Big)g_\Lambda \mp \sigma g_e \delta_{NN'} \qquad (5.103)$$

Using the same approach the non-zero z-component matrix elements of the $\psi^{\mp\sigma}_{\pm|K_s|}$ JT-SO branches are of the form

$$\langle \psi^{\mp\sigma}_{\pm|K_s|}, N'|L_z + g_e S_z|\psi^{\mp\sigma}_{\pm|K_s|}, N\rangle$$

$$= \pm\Big(\sum_{i=1,3,5\ldots} c^{+*}_{|K_s|,i,N'} c^{+}_{|K_s|,i,N} - \sum_{i=2,4,6\ldots} c^{+*}_{|K_s|,i,N'} c^{+}_{|K_s|,i,N}\Big)g_\Lambda \mp \sigma g_e \delta_{NN'} \qquad (5.104)$$

The non-zero x-component matrix-elements link states with the same K_n but opposite values of Σ. They are of the form

$$\langle \psi^{\pm\sigma}_{\mp|K_s|}, N'|L_x + g_e S_x \psi^{\mp\sigma}_{\mp|K_s|}, N\rangle = \sum_i c^{-*}_{|K_s|,i,N'} c^{+}_{|K_s|,i,N} g_e/2 \qquad (5.105)$$

5.3.1 g Values

The g values are given by the first-order matrix elements of $\boldsymbol{L}+g_e\boldsymbol{S}$ – those that connect states that would be degenerate in the absence of an external magnetic field. The degenerate pairs of JT-SO states are encompassed within either $|\psi^{\mp\sigma}_{\mp|K_s|}, N\rangle$ or

$|\psi^{\mp\sigma}_{\pm|K_s|}, N\rangle$. All are diagonal in $L_z+g_eS_z$, which, from equations (3.77) and (5.104) gives

$$g_{\parallel}(\psi^{\mp\sigma}_{\mp|K_s|}) = 2\sigma g_e + \kappa^{-}_{|K_s|,N} g_A \tag{5.106}$$

$$g_{\parallel}(\psi^{\mp\sigma}_{\pm|K_s|}) = 2\sigma g_e - \kappa^{+}_{|K_s|,N} g_A \tag{5.107}$$

where

$$\kappa^{\pm}_{|K_s|,N} = \Big(\sum_{i=1,3,5\ldots} C^{\pm *}_{|K_s|,i,N} C^{\pm}_{|K_s|,i,N} - \sum_{i=2,4,6\ldots} C^{\pm *}_{|K_s|,i,N} C^{\pm}_{|K_s|,i,N}\Big) \tag{5.108}$$

are reduction factors (Section 3.3.2), which measure the reduction of orbital angular momentum due to the dynamic JT effect.

In both cases, as a consequence of vibrational (branch) orthogonality of the states within each SO-JT level, there are no non-zero matrix elements of the operator $L_x + g_eS_x$ and so

$$g_{\perp}(\psi^{\Sigma}_{\mp|K_s|}) = 0 \tag{5.109}$$

Having established that $g_{\perp}(\psi^{\Sigma}_{\mp|K_s|})$ vanishes, the Zeeman splitting of a SO-JT state is given by

$$\Delta\varepsilon_{\text{Zeeman}} = g_{\parallel}\mu_B B\cos\theta \equiv g_{\theta}\mu_B B \tag{5.110}$$

where θ is the angle between the magnetic field and the molecular z axis.

5.4 *Low-temperature Spectroscopy*

At low temperatures, only the lowest-energy vibronic level of the lower SO manifold will be appreciably populated. This level will be the $N = 1$ states of the $L^{\mp\sigma}_{\mp 1/2}$ branches for a LJT effect or the $Q^{\mp\sigma}_{\mp 1}$ branches for QJT effect. The wavefunctions for these states are, respectively

$$|L^{\mp\sigma}_{\mp 1/2},\ 1\rangle = \sum_{i=1,3,5\ldots} \mathcal{C}^{-}_{1/2,\,i,\,1}|^2E_\Lambda \mp\Lambda\ \mp\sigma\rangle|i\text{-}1,\ 0\rangle + \sum_{i=2,4,6\ldots} \mathcal{C}^{-}_{1/2,\,i,\,1}|^2E_\Lambda \pm\Lambda\ \mp\sigma\rangle|i\text{-}1,\ \mp 1\rangle \quad (5.111)$$

$$|Q^{\mp\sigma}_{\mp 1},\ 1\rangle = \sum_{i\,=\,1,3,5\ldots.} \mathcal{C}^{-}_{1,\,i,\,1}|^2E_\Lambda \mp\Lambda\ \mp\sigma\rangle|i\text{-}1,\ 0\rangle + \sum_{i\,=\,2,4,6\ldots} \mathcal{C}^{-}_{1,\,i,\,1}|^2E_\Lambda \pm\Lambda\ \mp\sigma\rangle|i,\ \mp 2\rangle \quad (5.112)$$

5.4.1 Non-zero Transition Moments from the Ground State

As mentioned previously, for the systems under consideration, a vibrational mode cannot be simultaneously linearly and quadratically JT active in the same electronic state. Going further, for the transitions of interest in this thesis, the ground and excited states cannot be susceptible to JT effects of the same order in the same mode. If the ground state has a LJT effect then there *may* be a quadratic effect in the excited state, but there is definitely not a linear effect. Conversely, in the case of a QJT effect in the ground state, the excited state may be subject to a LJT but not to a QJT effect.

With reference to Section 3.3.5 the transition moments between the basis functions of a $^2E_\Lambda' \leftarrow {}^2E_\Lambda$ transition are

$$\langle v\ell|\langle {}^2E_\Lambda' M_\Lambda' \Sigma|\boldsymbol{m}|{}^2E_\Lambda' M_\Lambda' \Sigma'\rangle|v'\ell'\rangle = \langle {}^2E_\Lambda' M_\Lambda'|\boldsymbol{m}|{}^2E_\Lambda' M_\Lambda'\rangle \delta_{\Sigma,\Sigma'}\,\delta_{v,v'}\,\delta_{\ell,\ell'}$$

$$= \mathfrak{M}_{\pm 1}\delta_{\Sigma,\Sigma'}\,\delta_{v,v'}\,\delta_{\ell,\ell'} \quad (5.113)$$

where, as outlined in Section 3.3.5 $\mathfrak{M}_{+1} = \mathfrak{M}_{-1}$, but the ± 1 subscripts are used to keep track of the transition polarisations, which are needed to determine the MCD expressions. Comparison of Figures 5.6 and 5.8 indicates the branches with which the initial states will show non-zero vibrational overlap factors – *viz* $|L^{\mp\sigma}_{\mp 1/2},\ 1\rangle$ overlaps with $|Q^{\mp\sigma}_{\mp 0},\ N\rangle$ and $|Q^{\mp\sigma}_{\mp 1},\ N\rangle$, while $|Q^{\mp\sigma}_{\mp 1/2},\ 1\rangle$ overlaps with $|L^{\mp\sigma}_{\mp 1/2},\ N\rangle$ and $|L^{\mp\sigma}_{\mp 3/2},\ N\rangle$. Thus an effective vibronic selection rule for Q $\leftrightarrow$ L is

$$\Delta K = K_n' - K_n = \pm 1/2 \quad (5.114)$$

The non-zero transition moments for a molecule with its z direction oriented along the laboratory Z axis ($\theta = 0$) are summarised in Table 5.7 for the cases $\Delta\Lambda = \pm 1$.

Table 5.7: Non-zero transition moments from the ground state for an axial molecule subject to E ⊗ e JT effect and with molecule with its z direction oriented along the laboratory Z axis ($\theta = 0$).

$\Delta\Lambda$	Transition moment	value
1	$\langle Q^{\mp\sigma}_{\mp1}, N \vert m_{\mp1} \vert L^{\mp\sigma}_{\mp1/2}, 1\rangle$	$\mathfrak{M}_{\mp1} \sum_{i=1,3,5\ldots} (\mathcal{C}^{-}_{1,i,N})^{*}\mathcal{C}^{-}_{1/2,i,1}$
	$\langle Q^{\mp\sigma}_{\mp0}, N \vert m_{\pm1} \vert L^{\mp\sigma}_{\mp1/2}, 1\rangle$	$\mathfrak{M}_{\pm1} \sum_{i=2,4,6\ldots} (\mathcal{C}^{-}_{0,i,N})^{*}\mathcal{C}^{-}_{1/2,i,1}$
	$\langle L^{\mp\sigma}_{\mp3/2}, N \vert m_{\pm1} \vert Q^{\mp\sigma}_{\mp1}, 1\rangle$	$\mathfrak{M}_{\pm1} \sum_{i=2,4,6\ldots} (\mathcal{C}^{-}_{3/2,i,N})^{*}\mathcal{C}^{-}_{1,i,1}$
	$\langle L^{\mp\sigma}_{\mp1/2}, N \vert m_{\mp1} \vert Q^{\mp\sigma}_{\mp1}, 1\rangle$	$\mathfrak{M}_{\mp1} \sum_{i=1,3,5\ldots} (\mathcal{C}^{-}_{1/2,i,N})^{*}\mathcal{C}^{-}_{1,i,1}$
-1	$\langle Q^{\mp\sigma}_{\mp1}, N \vert m_{\pm1} \vert L^{\mp\sigma}_{\mp1/2}, 1\rangle$	$\mathfrak{M}_{\pm1} \sum_{i=1,3,5\ldots} (\mathcal{C}^{-}_{1,i,N})^{*}\mathcal{C}^{-}_{1/2,i,1}$
	$\langle Q^{\mp\sigma}_{\mp0}, N \vert m_{\mp1} \vert L^{\mp\sigma}_{\mp1/2}, 1\rangle$	$\mathfrak{M}_{\mp1} \sum_{i=2,4,6\ldots} (\mathcal{C}^{-}_{0,i,N})^{*}\mathcal{C}^{-}_{1/2,i,1}$
	$\langle L^{\mp\sigma}_{\mp3/2}, N \vert m_{\mp1} \vert Q^{\mp\sigma}_{\mp1}, 1\rangle$	$\mathfrak{M}_{\mp1} \sum_{i=2,4,6\ldots} (\mathcal{C}^{-}_{3/2,i,N})^{*}\mathcal{C}^{-}_{1,i,1}$
	$\langle L^{\mp\sigma}_{\mp1/2}, N \vert m_{\pm1} \vert Q^{\mp\sigma}_{\mp1}, 1\rangle$	$\mathfrak{M}_{\pm1} \sum_{i=1,3,5\ldots} (\mathcal{C}^{-}_{1/2,i,N})^{*}\mathcal{C}^{-}_{1,i,1}$

5.4.1.1 Zeroth Absorption and MCD Moments of Individual Bands

In this section, the Zeeman matrix elements of equation (5.104) and transition moments given in Table 5.7 are used to derive expressions for the zeroth MCD and absorption moments for the individual vibronic transitions originating from the ground vibronic state.

The states of lowest-energy vibronic level are generalised as $\psi^{\mp\sigma}_{\mp n/2}$ (either $L^{\mp\sigma}_{\mp1/2}$ or $Q^{\mp\sigma}_{\mp1}$) and the zero-field energy of this level is defined to be zero. For a general transition $\langle \psi^{\mp\sigma}_{K'} N \vert \leftarrow \langle \psi^{\mp\sigma}_{\mp n/2}\ 1 \vert$, expressions for these moments are obtained using equation (4.44). In anticipation of Chapter 8 the effects of field induced mixing of states (that is, $\mathfrak{B}$ terms) are ignored and the descriptors of Section 4.4.2 is used. For a general orientation, where the molecular symmetry axis makes angle θ with respect to the optical and magnetic-field direction

$$\mathbf{A}_0^{\theta} = \frac{(Cl\gamma\cos^2\theta + 1)}{4} |\mathfrak{M}|^2 |\Sigma|^2 (P^{-\sigma}_{-n/2} + P^{+\sigma}_{+n/2}) \qquad (5.115)$$

$$\mathbf{M}_0^{\theta} = \mathbb{S}Cl\gamma\cos\theta\,|\mathfrak{M}|^2\Delta\Lambda|\Sigma|^2(P_{-n/2}^{-\sigma}-P_{+n/2}^{+\sigma}) \qquad (5.116)$$

The factors $\mathbb{S}$ take values ±1, according to Table 5.8, while explicit form of the functions $|\Sigma|^2$ for particular transitions can be obtained from the right-hand column of Table 5.7. Note that the MCD changes sign according to $\Delta\Lambda$, as required by the principle of conversion of angular momentum. The fractional Boltzmann populations (as defined in equation 4.33) of the ground-level Zeeman states are

$$P_{\mp n/2}^{\mp\sigma} = \frac{1}{\mathcal{Q}}\exp(\pm g_{\theta}(\psi_{\mp n/2}^{\mp\sigma})\mu_B B/2kT) \qquad (5.117)$$

where $\mathcal{Q}$ is the partition function. If the temperature is low enough that only the lowest JT-SO level is significantly occupied, then equations (5.115) and (5.116) can be rewritten

$$\mathbf{A}_0^{\theta} = \frac{Cl\gamma(\cos^2\theta+1)}{4}\,|\mathfrak{M}|^2\,|\Sigma|^2 \qquad (5.118)$$

$$\mathbf{M}_0^{\theta} = \mathbb{S}Cl\gamma\cos\theta\,\Delta\Lambda\,|\mathfrak{M}|^2\,|\Sigma|^2\tanh(g_{\theta}(\psi_{\mp n/2}^{\mp\sigma})\mu_B B/2kT) \qquad (5.119)$$

Averaging over all orientations then gives

$$\mathbf{A}_0 = \frac{Cl\gamma}{3}\,|\mathfrak{M}|^2\,|\Sigma|^2 \qquad (5.120)$$

$$\mathbf{M}_0 = \frac{\mathbb{S}Cl\gamma\Delta\Lambda|\mathfrak{M}|^2|\Sigma|^2}{2}\int_{-1}^{1}\cos\theta\tanh\left(\frac{g_{\parallel}(\psi_{\mp n/2}^{\mp\sigma})\cos\theta\mu_B B}{2kT}\right)\mathrm{d}\cos\theta \qquad (5.121)$$

In the linear limit

$$\tanh\left(\frac{g_{\parallel}(\psi_{\mp n/2}^{\mp\sigma})\cos\theta\mu_B B}{2kT}\right) \approx \frac{g_{\parallel}(\psi_{\mp n/2}^{\mp\sigma})\cos\theta\mu_B B}{2kT} \qquad (5.122)$$

so

$$(\mathbf{M}_0)_{\text{lin lim}} = \mathcal{S}\Delta\Lambda Cl\gamma|\mathcal{M}|^2|\Sigma|^2\frac{g_{\parallel}(\psi^{\mp\sigma}_{\mp n/2})\mu_B B}{4kT}\int_{-1}^{1}\cos^2\theta \mathrm{d}\cos\theta$$

$$= \mathcal{S}\Delta\Lambda Cl\gamma|\mathcal{M}|^2|\Sigma|^2\frac{g_{\parallel}(\psi^{\mp\sigma}_{\mp n/2})\mu_B B}{6kT} \qquad (5.123)$$

and

$$\left(\frac{\mathbf{M}_0}{\mathbf{A}_0}\right)_{\text{lin lim}} = \frac{\mathcal{S}\Delta\Lambda g_{\parallel}(\psi^{\mp\sigma}_{\mp n/2})\mu_B B}{2kT} \qquad (5.124)$$

The linear-limit results are summarised in Table 5.8. The important thing to note about this information is the sign of the MCD, which does not change when the linear-limit condition is relaxed. For Q ← L and L ← Q there are MCD bands of both signs. In particular, the origin band is either $\langle Q^{\mp\sigma}_{\mp 1}, 1| \leftarrow \langle L^{\mp\sigma}_{\mp 1/2}, 1|$ (first row of Table 5.8) or $\langle L^{\mp\sigma}_{\mp 1/2}| \leftarrow \langle Q^{\mp\sigma}_{\mp 1}, 1|$ (third row) and has an MCD sign determined by $-\Delta\Lambda$. In contrast, the first vibronic side band involving the JT mode is either $\langle Q^{\mp\sigma}_{\mp 0}, 1| \leftarrow \langle L^{\mp\sigma}_{\mp 1/2}, 1|$ (second row) or $\langle L^{\mp\sigma}_{\mp 3/2}| \leftarrow \langle Q^{\mp\sigma}_{\mp 1}, 1|$ (fourth row), with sign determined by $\Delta\Lambda$. So in both cases the first overtone is predicted to have MCD of the *opposite* sign to that of the origin.

Table 5.8: Orientationally averaged zeroth absorption and MCD moments, in the linear limit, for individual vibronic transitions within an E⊗e ← E⊗e manifold of an axial molecule

transition	$\mathcal{S}$	$\mathbf{A}_0$	$(\mathbf{M}_0/\mathbf{A}_0)_{\text{lin lim}}$
$\langle Q^{\mp\sigma}_{\mp 1}, N\| \leftarrow \langle L^{\mp\sigma}_{\mp 1/2}, 1\|$	-1	$\frac{Cl\gamma\|\mathcal{M}\|^2}{3}\left\|\sum_{i=1,3,5\ldots}(\mathcal{C}^{-}_{1,i,N})^*\mathcal{C}^{-}_{1/2,i,1}\right\|^2$	$\frac{-\Delta\Lambda\, g_{\parallel}(L^{\mp\sigma}_{\mp 1/2})\mu_B B}{2kT}$
$\langle Q^{\mp\sigma}_{\mp 0}, N\| \leftarrow \langle L^{\mp\sigma}_{\mp 1/2}, 1\|$	1	$\frac{Cl\gamma\|\mathcal{M}\|^2}{3}\left\|\sum_{i=2,4,6\ldots}(\mathcal{C}^{-}_{0,i,N})^*\mathcal{C}^{-}_{1/2,i,1}\right\|^2$	$\frac{\Delta\Lambda\, g_{\parallel}(L^{\mp\sigma}_{\mp 1/2})\mu_B B}{2kT}$
$\langle L^{\mp\sigma}_{\mp 1/2}, N\| \leftarrow \langle Q^{\mp\sigma}_{\mp 1}, 1\|$	-1	$\frac{Cl\gamma\|\mathcal{M}\|^2}{3}\left\|\sum_{i=1,3,5\ldots}(\mathcal{C}^{-}_{1/2,i,N})^*\mathcal{C}^{-}_{1,i,1}\right\|^2$	$\frac{-\Delta\Lambda\, g_{\parallel}(Q^{\mp\sigma}_{\mp 1})\mu_B B}{2kT}$
$\langle L^{\mp\sigma}_{\mp 3/2}, N\| \leftarrow \langle Q^{\mp\sigma}_{\mp 1}, 1\|$	1	$\frac{Cl\gamma\|\mathcal{M}\|^2}{3}\left\|\sum_{i=2,4,6\ldots}(\mathcal{C}^{-}_{3/2,i,N})^*\mathcal{C}^{-}_{1,i,1}\right\|^2$	$\frac{\Delta\Lambda\, g_{\parallel}(Q^{\mp\sigma}_{\mp 1})\mu_B B}{2kT}$

5.4.2 Absence of a Ground-State Jahn-Teller Effect

In the absence of a ground-state JT effect, the lowest energy wavefunctions can be written

$$|\psi^{\mp\sigma}_{\mp n/2}\ ,\ 1\rangle = |^2\mathrm{E}_\Lambda \mp\Lambda\ \mp\sigma\rangle|0,\ 0\rangle \qquad (5.125)$$

which corresponds to equation (5.111) or (5.112) with $\mathcal{C}^{-}_{n/2,i,1} = \delta_{i1}$. Using this result, Table 5.8 reduces to Table 5.9.

Table 5.9: Orientationally averaged zeroth absorption and MCD moments, in the linear limit, for individual vibronic transitions, $\mathrm{E}\otimes\mathrm{e} \leftarrow \mathrm{E}$ (no ground-state JT effect), of an axial molecule

transition	$\mathbf{A}_0$	$(\mathbf{M}_0/\mathbf{A}_0)_{\text{lin lim}}$
$\langle \mathrm{Q}^{\mp\sigma}_{\mp1},\ N\vert \leftarrow \langle \mathrm{L}^{\mp\sigma}_{\mp1/2},\ 1\vert$	$\frac{Cl\gamma\vert\mathfrak{M}\vert^2}{3}\vert\mathcal{C}^{-}_{1,\,1,\,N}\vert^2$	$\frac{-\Delta\Lambda\, g_{\parallel}(\mathrm{L}^{\mp\sigma}_{\mp1/2})\mu_{\mathrm{B}}B}{2kT}$
$\langle \mathrm{Q}^{\mp\sigma}_{\mp0},\ N\vert \leftarrow \langle \mathrm{L}^{\mp\sigma}_{\mp1/2},\ 1\vert$	0	-
$\langle \mathrm{L}^{\mp\sigma}_{\mp3/2},\ N\vert \leftarrow \langle \mathrm{Q}^{\mp\sigma}_{\mp1},\ 1\vert$	0	-
$\langle \mathrm{L}^{\mp\sigma}_{\mp1/2},\ N\vert \leftarrow \langle \mathrm{Q}^{\mp\sigma}_{\mp1},\ 1\vert$	$\frac{Cl\gamma\vert\mathfrak{M}\vert^2}{3}\vert\mathcal{C}^{-}_{1/2,i,\,N}\vert^2$	$\frac{-\Delta\Lambda\, g_{\parallel}(\mathrm{L}^{\mp\sigma}_{\mp1/2})\mu_{\mathrm{B}}B}{2kT}$

Thus, in the absence of a ground-state JT effect, all MCD overtones must have the *same* sign. So the presence of bands in a spectrum of *opposite* sign to the origin is indicative of either a *ground*-state JT effect or some entirely different (non-JT) mechanism.

5.4.3 Absorption and MCD Moments over all Bands

Applying the principle of spectroscopic stability, the sum of all transition intensities (at low temperature) is given by

$$\sum_{K'N'} |\langle \psi^{\mp\sigma}_{K'} N' | m_{\pm1} | \psi^{\mp\sigma}_{\mp n/2}\ 1\rangle|^2 = \sum_{M_\Lambda'\Sigma' v'\ell'} |\langle v'\ell'|\langle {}^2\mathrm{E}_{\Lambda'} M_{\Lambda'}\Sigma' | m_{\pm1} | \psi^{\mp\sigma}_{\mp n/2}\ 1\rangle|v,\ \ell\rangle|^2$$

$$= \sum_{i=1,3,5\ldots} |\bar{c}_{n/2,i,N}\langle {}^2E_\Lambda' \mp\Lambda'|m_{\pm1}|{}^2E_\Lambda \mp\Lambda\rangle|^2 + \sum_{i=2,4,6\ldots} |\bar{c}_{n/2,i,N}\langle {}^2E_\Lambda' \pm\Lambda'|m_{\pm1}|{}^2E_\Lambda \pm\Lambda\rangle|^2 \qquad (5.126)$$

where the last step invokes spin and vibrational orthogonality. After using the WET according to Appendix C, the moments for the molecule oriented at angle θ are

$$(A_0^\theta)_{\text{whole band}} = \frac{Cl\gamma(\cos\theta+1)}{4}|\Re|^2 \sum_i |\bar{c}_{n/2,i,N}|^2\{P(^{-\sigma}_{-n/2}) + P(^{+\sigma}_{+n/2})\}$$

$$= \frac{Cl\gamma(\cos\theta+1)}{4}|\Re|^2 \qquad (5.127)$$

$$(M_0^\theta)_{\text{whole band}} = -\Delta\Lambda Cl\gamma\cos\theta\,|\Re|^2\Big(\sum_{i=1,3,5\ldots}|\bar{c}_{n/2,i,N}|^2 - \sum_{i=2,4,6\ldots}|\bar{c}_{n/2,i,N}|^2\Big)\{P(^{-\sigma}_{-n/2}) - P(^{+\sigma}_{+n/2})\}$$

$$= -\Delta\Lambda Cl\gamma\cos\theta|\Re|^2\bar{\kappa}_{n/2,1}\tanh\left(\frac{g_\parallel(\psi^{\mp\sigma}_{\mp n/2})\cos\theta\mu_B B}{2kT}\right) \qquad (5.128)$$

where $\bar{\kappa}_{n/2,1}$ is the orbital reduction factor defined by equation (5.108). Averaging over all orientations gives

$$(A_0)_{\text{whole band}} = \frac{Cl\gamma|\Re|^2}{3} \qquad (5.129)$$

$$(M_0)_{\text{whole band}} = -\Delta\Lambda Cl\gamma\,|\Re|^2\bar{\kappa}_{n/2,1}\int_0^1 \cos\theta\tanh\left(\frac{g_\parallel(\psi^{\mp\sigma}_{\mp n/2})\cos\theta\mu_B B}{2kT}\right)d\cos\theta \qquad (5.130)$$

and gives for the moment ratios

$$\left(\frac{M_0}{A_0}\right)_{\text{whole band}} = -3\Delta\Lambda\bar{\kappa}_{n/2,1}\int_0^1 \cos\theta\tanh\left(\frac{g_\parallel(\psi^{\mp\sigma}_{\mp n/2})\cos\theta\mu_B B}{2kT}\right)d\cos\theta \qquad (5.131)$$

In the linear limit

$$(\mathbf{M}_0)_{\substack{\text{whole band}\\ \text{linear limit}}} = -\Delta\Lambda C l\gamma\,|\mathfrak{M}|^2 \kappa^{-}_{n/2,1} \frac{g_{\parallel}(\psi^{\mp\sigma}_{\mp n/2})\mu_B B}{6kT} \tag{5.132}$$

and

$$\left(\frac{\mathbf{M}_0}{\mathbf{A}_0}\right)_{\substack{\text{whole band}\\ \text{linear limit}}} = -\Delta\Lambda\, \kappa^{-}_{n/2,1} \frac{g_{\parallel}(\psi^{\mp\sigma}_{\mp n/2})\mu_B B}{2kT} \tag{5.133}$$

The ratios for the origin band only are given by

$$\left(\frac{\mathbf{M}_0}{\mathbf{A}_0}\right)_{\text{origin}} = -3\Delta\Lambda \int_0^1 \cos\theta \tanh\left(\frac{g_{\parallel}(\psi^{\mp\sigma}_{\mp n/2})\cos\theta\mu_B B}{2kT}\right) d\cos\theta \tag{5.134}$$

$$\left(\frac{\mathbf{M}_0}{\mathbf{A}_0}\right)_{\substack{\text{origin}\\ \text{linear limit}}} = -\Delta\Lambda \frac{g_{\parallel}(\psi^{\mp\sigma}_{\mp n/2})\mu_B B}{2kT} \tag{5.135}$$

Consequently, the ratio

$$\frac{(\mathbf{M}_0/\mathbf{A}_0)_{\text{whole band}}}{(\mathbf{M}_0/\mathbf{A}_0)_{\text{origin}}} = \kappa^{-}_{n/2,1} \tag{5.136}$$

provides a measure of the reduction factor, independent of the temperature and magnetic-field conditions under which the spectra are run.

5.5 Spectral Simulation Programme: DYNAMO

DYNAMO is a computer program, written as part of the work done for this thesis, that simulates the low-temperature absorption and MCD spectra of an E ⊗ e ← E ⊗ e transition of an axial molecule and compares them with experimental data. It allows two possible cases for a system without three-fold symmetry: one where the JT mode is simultaneously linearly active in the ground state and quadratically active in the excited state (Q ← L); the other where the activity is quadratic in the ground state and

linear in the excited state (L ← Q). It also permits FC progressions in as many as three totally symmetric vibrations

Input data required for the simulation include $\Delta\Lambda$ (±1) and the zeroth-order energy difference (in cm^{-1}) between the two electronic states. Also required are the energy of the vibrational modes (in cm^{-1} and assumed to be the same in both states), the dimensionless ground- and excited-state JT coupling parameters (λ_{JT} and ϵ_{JT}), and the SO splitting parameters (cm^{-1}) for each states. The temperature (K) and magnetic field (T) and the displacement parameters ($\mathfrak{L}$) for any totally symmetric modes also form part of the input data. The line-shapes are assumed to be Gaussian and the bandwidth is also input data.

From the entered data, the matrices described in Sections 5.2.2.1 and 5.2.2.2 are constructed up to a specified dimension – typically to $i \approx 80$ for the work done in this thesis. For an LJT effect in the ground state (Q ← L), it is necessary to consider the $L^{-\sigma}_{\pm 1/2}$ and $Q^{-\sigma}_{\pm 1}$ and $Q^{-\sigma}_{\pm 0}$ branches. For a QJT effect in the ground state (L ← Q), $Q^{-\sigma}_{\pm 1}$ and $L^{-\sigma}_{\pm 1/2}$ and $L^{-\sigma}_{\pm 3/2}$ must be considered.

DYNAMO uses a numerical (Jacobian) diagonalisation to obtain the eigenvalues and eigenvectors. These are sorted into order of ascending energy for each branch. The g value of the lowest ground-state level is determined using the appropriate eigenvector coefficients, according to equations (5.106) and (5.107). The g value is, in turn, used with the magnetic field strength and temperature to determine the Zeeman shifts (equation (5.110)) and populations of each of the lowest-energy Zeeman states (equation (5.117)). These calculations assume 'Z-oriented' molecules ($\theta = 0$) – a factor for random orientation is introduced into the expressions for absorption and MCD later.

The program next determines the relative transition moments for individual transitions, in left and right circular polarisation, from the eigenfunction coefficients, according to Table 5.7. These moments are squared and weighted by the initial-state populations to obtain the relative transition intensities.

Spectral bands

The intensity of each band of the three possible totally symmetric progressions is calculated by taking the square of the overlap factor of the overtone with the origin. The overlap factors are given by[6]

$$\langle 0 | v \rangle = (1/v!)^{1/2}(-\mathfrak{L}/\sqrt{2})^{v} e^{-\mathfrak{L}^2/2} \qquad (5.137)$$

where $\mathfrak{L}$ is the displacement of the equilibrium positions of the ground and excited state surfaces with respect to the ground state.

Next, the energy (position) and the intensity of the combination (of totally symmetric and JT progressions) bands are calculated. Only the first ten or so members of the progression due to each mode needs to be considered (depending on the range of the calculated spectra). The energy of the band is calculated by summing the eigenvalues of all the members of the relevant progressions. The intensity of the combination band ($\mathfrak{I}$) is calculated by multiplying together the transition intensities of all the members of the progressions.

Each $\mathfrak{I}$ is used to define a Gaussian band of the specified bandwidth at the energy specified by the difference between the eigenvalues of the final and initial states. The Gaussians are added directly to give the absorption. For the MCD, those bands corresponding to *rcp* transitions are subtracted from those corresponding to *lcp*. The result is multiplied by ΔA and then 1/2 to account for randomised orientation in the linear limit.

The spectra are then plotted on the screen, where they can be compared with experimental data. DYNAMO can used to generate a number of useful diagrams. Figure 5.10 shows four sets of calculated MCD and absorption spectra. Each set consists of spectra with a linear *or* quadratic JT effect in the ground state. Within each set the JT parameter λ_{JT} or ϵ_{JT} are varied.

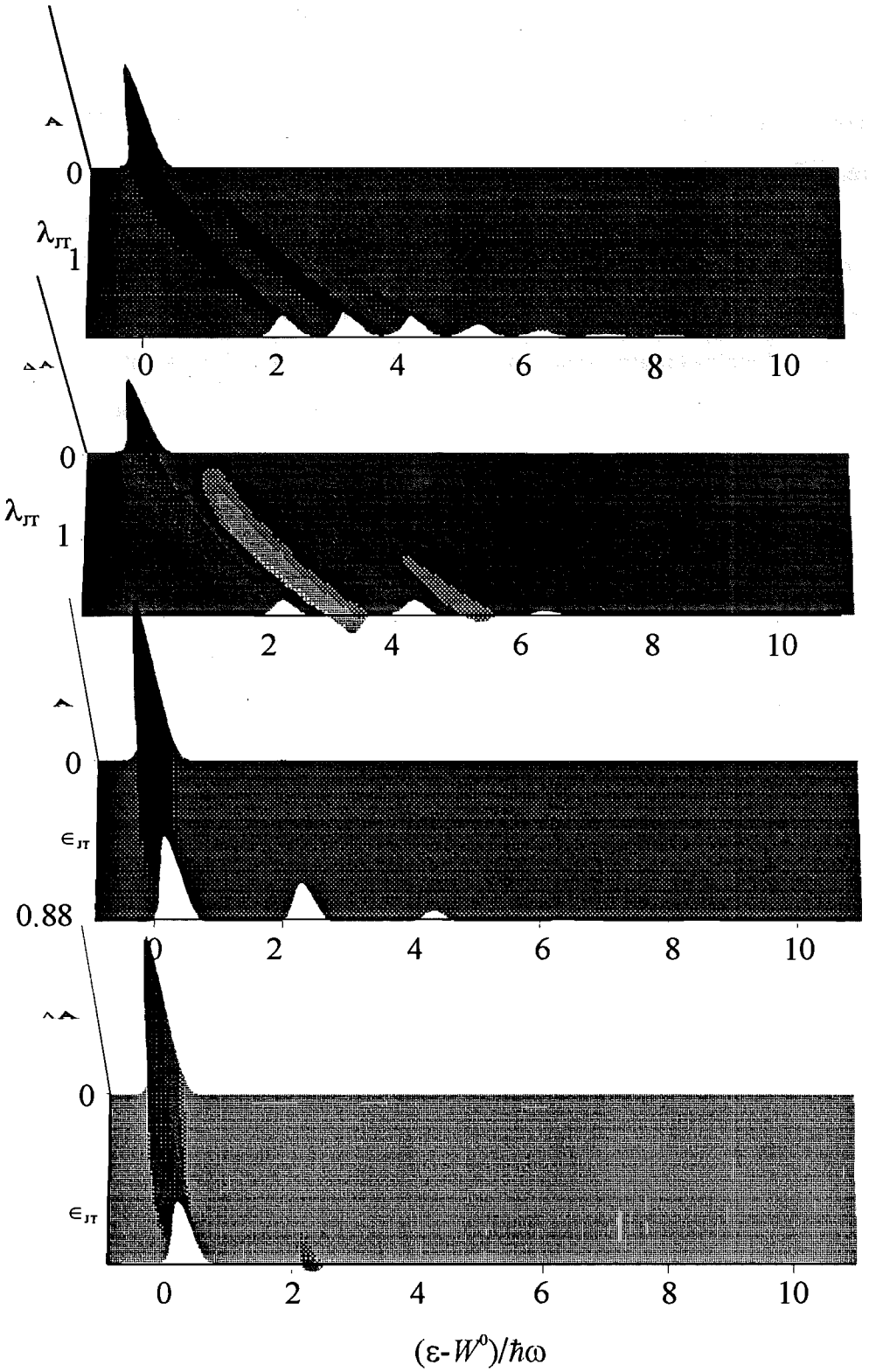

Figure 5.10: The top two diagrams are respectively absorption and MCD with a linear JT effect in the ground state. In both cases λ varies from 0 to 2. The bottom two diagrams are also absorption and MCD but with a quadratic JT effect in the ground state. In these cases ε varies from 0 to 0.88.

5.6 References

(1) Jahn, H. A.; Teller, E. *Proc. Roy. Soc. A* **1937**, *161*, 220.

(2) Ham, F. S. *Phys. Rev.* **1965**, *138*, A1727.

(3) Longuet-Higgins, H. C.; Öpik, U.; Pryce, M. H. L.; Sack, R. A. *Proc. Roy. Soc. A* **1958**, *244*, 1-16.

(4) Herzberg, G. *Molecular Spectra and Molecular Structure*, 2nd ed.; Krieger Publishing Company: Malabar, 1991; Vol. 3 – Elecronic spectra and electronic structure of polyatomic molecules.

(5) Engelking, P. C.; Lineberger, W. C. *J. Chem. Phys* **1977**, *67*, 1412-1417.

(6) Fulton, R. L.; Gouterman, M. *J. Chem. Phys* **1961**, *35*, 1059-1071.

(7) Pople, J. A.; Longuet-Higgins, H. C. *Proc. Roy. Soc.* **1958**, 373-383.

6 EXPERIMENTAL APPARATUS AND PROCEDURES

This chapter is divided into four sections. The first describes the spectrometer that was used to make most spectral measurements for this project. The second describes two experimental systems that enable spectroscopic investigations of matrix-isolated samples to be carried out over a range of magnetic field strengths and (low) temperatures. Thirdly the method of preparing samples of matrix-isolated free radicals is described. Finally the equipment used make low-temperature spectroscopic measurements on solutions is described

6.1 The Spectrometer: MOD4

Most of the spectroscopic measurements considered in this thesis were performed on MOD4,[i] a simultaneous MCD/double-beam absorption spectrometer, constructed by Vaughan Langford as a major part of his Ph.D. research project.[1] His thesis describes the spectrometer in detail, including the electronics, computer interfacing and operation, and instrument specifications. In this work, I will only outline the workings of the important components. The instrumental parameters used in this project are recorded in Table 6.1.

Until the early 1970s absorption and (M)CD spectra were measured on different spectrometers or, at best, on the same spectrometer using different optical paths. For this reason, the spectra could never be collected under entirely identical conditions – different spectrometers will generally have different wavelength calibrations and optical bandwidths, while some samples (such as matrix-isolated ones) may not be invariant in either space or time. Since the absorption data are an almost indispensable aid in the analysis of the corresponding MCD, the use of these early instruments led to the possibility of errors of interpretation.

---

[i] MOD4 is the fourth in a series of related simultaneous MCD/double-beam absorption spectrometers. MOD1 and MOD2 were designed and built at the University of Virginia by members of Prof. Paul Schatz's group. MOD3, now decommissioned, was built at the University of Canterbury.[24]

Table 6.1: Instrumental specifications for the MOD4 spectrometer

component	Specification
lamp	300-W Xe-arc
monochromator	1-m Czerny-Turner grating
filters	Esco RG-395 for $395 < \lambda < 800$ nm Corning 7-54 for $\lambda < 395$ nm
linear polariser	Glan-Turner polariser
PEM	Hinds International Inc. PEM-80
PMT	Hamamatsu R-376
LIA	Stanford Research Systems Model SR510
computer	PC 486SX with 14-bit Advantech PCL-814B interface card

Problems like these led Collingwood *et al*, in 1974, to develop the first simultaneous MCD/absorption spectrometer.[2] Other features of their instrument that have been employed in most subsequent systems (including the MOD1–4 series) are double-beam measurement of the absorption and phase-sensitive detection of the MCD.

Double-beam absorption offers a number of advantages over single-beam operation. Because the effects of fluctuations, drift and the variable wavelength response of the optical components can be minimised, the absorbance values can be reliably obtained.[3]

Measurement of MCD presents an inherent problem of low signal intensity (typically $\Delta A/A << 1$). However the differential nature of the technique allows phase-sensitive detection to be employed. Modern systems (including MOD4) combine the use of a photoelastic modulator and a lock-in-amplifier to extract very small CD signals from background noise that may be many orders of magnitude more intense. Sampling, in MOD4, occurs at ~50 kHz because the amount of noise at that frequency is small compared to that at lower sampling rates. As shown in Figure 6.1 *flicker* noise has a frequency-dependent power spectrum of the form $P \propto 1/f^n$. At 50 kHz,

the noise spectrum is completely dominated by *white* noise, which has a frequency-*in*dependent spectrum and therefore cannot be reduced by choice of frequency.[ii] Also, 50 kHz is well away from most sources of *deterministic* noise, such as the power-line hum at 50 Hz and the harmonics thereof.

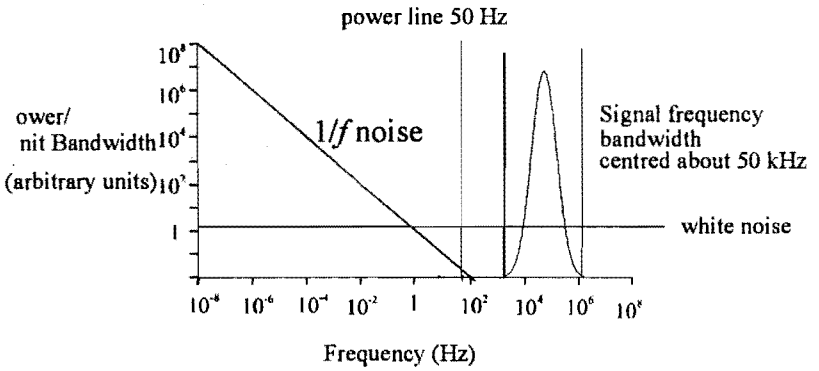

Figure 6.1: A signal frequency bandwidth centred at 50 kHz is well removed from most deterministic noise and in a region where flicker noise is insignificant.

6.1.1 Optical Layout

The optical layout of the MOD4 spectrometer is illustrated in Figure 6.2. The main parts of the light path are enclosed by a (non-magnetic) wooden box, which prevents light, other than that from the monochromator, from reaching the sample or the detector. A "C"-shaped section of the optical table has been removed to accommodate the cryostats and magnets described in Section 6.2.

The light source is an ILC Technology LX300UV Xe-arc lamp, which produces 300 W of output at a current of 20 A. An aluminium hood is used to protect the user from the UV light that is produced. The ozone produced by the photolysis of oxygen ($\lambda > 190$ nm) is drawn away by a fan and exhausted to the outside of the building. A second fan blows air through the hood to cool the lamp. The double-beam nature of MOD4 means that variations in the intensity of lamps due to an inherent flicker, is intrinsically corrected for.

[ii] The origin of flicker noise is generally unknown. White noise consists of *Johnson* or thermal noise caused by the random motion of thermally agitated electron in resistive materials and *shot* noise caused by the random arrival of electrons at electrodes *etc.*

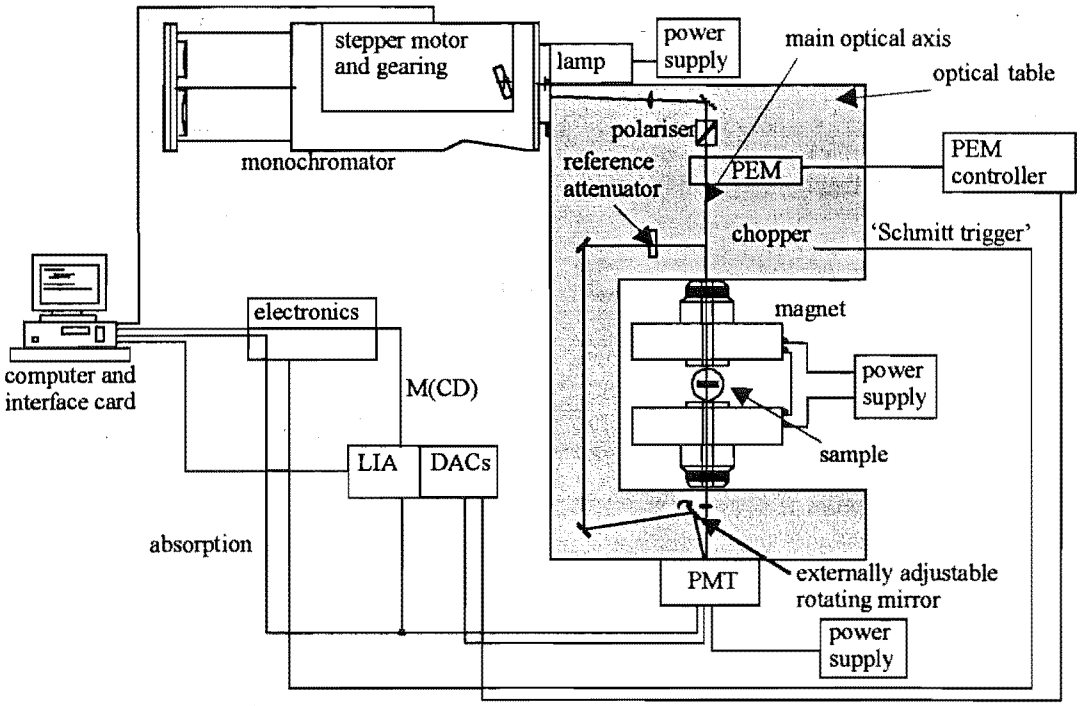

Figure 6.2: A schematic diagram of the MOD4 spectrometer (adapted from reference 1), shown with the electromagnet (Section 6.2.2) in position.

The light produced by the lamp is dispersed by a Jarrell-Ash 78-463 single-grating Czerny-Turner monochromator with a focal length of 1 m. The grating used for the work reported in this thesis was 110 mm square with 1180 grooves/mm and was blazed for a wavelength of 300 nm, giving a reciprocal dispersion of 0.82 nm/mm.[4] The entrance and exit slits are simultaneously adjustable between 0 and 400 μm. Wavelength calibrations for this grating were performed using emission lines from a low-pressure mercury lamp.

A convex lens collimates the light exiting the monochromator, which is then reflected along the main optical axis of the spectrometer. A colour-glass cut-off filter removes higher orders of diffracted light, and the remaining (first-order) light is polarised by a combination of a Glan-Taylor prism and a photoelastic modulator (Section 6.1.2). An 11-Hz mechanical chopper then splits the light into two beams that alternately pass through the sample (*sample* beam) or around the sample (*reference* beam), both terminating at the photomultiplier tube (PMT) (Section 6.1.3). Twice every chopper cycle the detector *dark* current is measured by completely blocking the optical path to the detector. This signal is subtracted from both the sample and reference signals.

6.1.2 Circular Polarisation Modulation

The Glan-Turner polariser used in MOD4 is oriented to transmit the vertically polarised component of the light while the horizontal component undergoes total internal reflection and is removed from the optical path.

The photoelastic modulator (PEM) converts the polarisation to give an output that is modulated between left and right circular polarisation at a frequency of ~50 kHz. This is achieved by passing the light through a transparent optical element, which exhibits the photoelastic effect – when mechanically stressed, it splits the light into two components with orthogonal linear polarisations that propagate at different speeds. The magnitude of this induced birefringence is proportional to strain the element experiences.

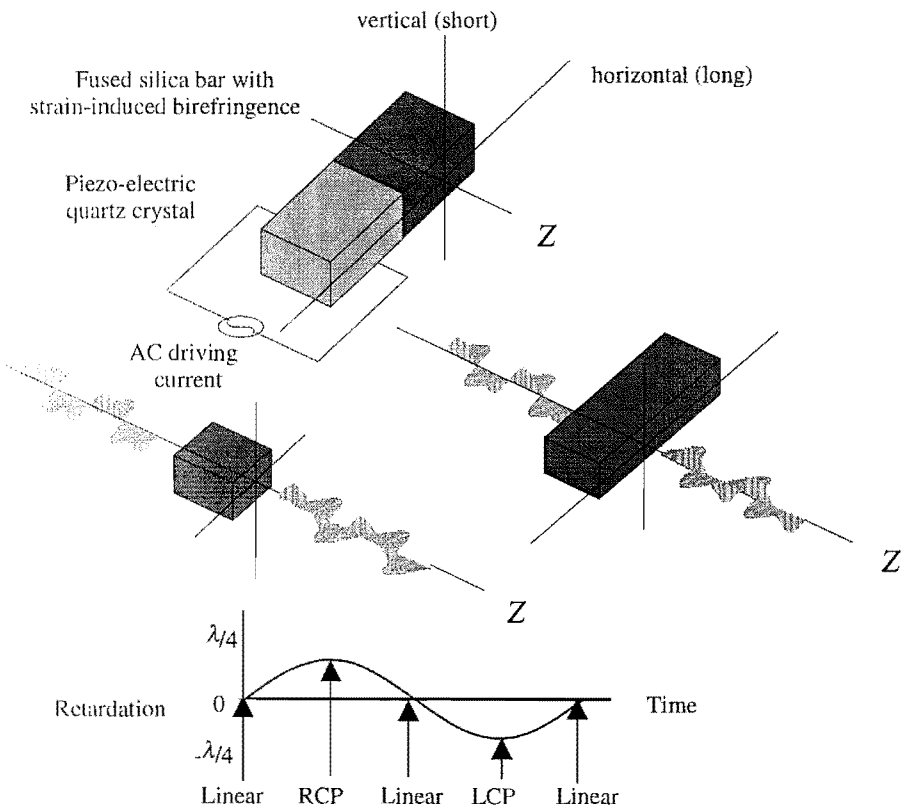

Figure 6.3: Principles of using the PEM to create modulated circularly polarised light. The top diagram shows the compressions and expansions of the fused silica bar causing the orthogonally polarised components of light to travel at different speeds. The bottom diagram shows the polarisation of the emerging light throughout one vibrational cycle of the silica bar.

The optical element of the Hinds International PEM-80 used in MOD4 is a bar of fused silica with a natural vibrational frequency of ~50 kHz.[iii] The mechanical strain is induced by a resonance-matched quartz-crystal piezoelectric transducer, which is driven by an AC voltage of the appropriate frequency. The strain (long and short) axes of the optical element are oriented at 45° to the vertical, so the vertically polarised light from the Glan-Taylor prism is split into two equal intensity rays. The AC voltage is chosen so that the vibrational extrema correspond to the condition where these components are exactly $\lambda/4$ out of phase. Interference between the beams leaving the PEM therefore gives light that oscillates between right and left circular polarisation (*rcp* and *lcp*) at 50 kHz.

6.1.3 The Detector

The Hamamatsu R-376 PMT used in this work is an end-on tube with a semi-transparent multialkali photocathode, which has a peak radiant sensitivity (current per unit of incident light power) at 420 nm and a usable wavelength range of 160 - 850 nm. μ–metal shields surrounding the PMT are used to reduce the effects of the magnet field.

A preamplifier with a current-to-voltage gain of $\sim 5\times10^5$ V/A is built into the PMT housing to produce a signal voltage, which consists of a DC component representing the average light level, as well as a much weaker AC component due to the circular dichroism of the sample.

6.1.4 Signal Processing

6.1.4.1 Absorbance

The absorbance of a sample at a given wavelength according to the Beer-Lambert law is

$$A = -\log_{10}(I/I_0) \qquad (6.1)$$

where I_0 is the intensity of the incident light on the sample and I is the transmitted intensity. In MOD4, A is determined from the DC preamplifier voltages read into the

---

[iii] The natural frequency is determined by the length of the bar and the speed of longitudinal sound waves propagating through it.

computer *via* analogue-to-digital (A/D) conversion by a PCL-814B interface card. A signal from the chopper (the 'Schmitt trigger' in Figure 6.2) synchronises the computer with the periods in which the sample, reference and dark signals are measured. The absorbance is calculated digitally according to the relationship

$$A_{measured} = -\log_{10}((V_{sample} - V_{dark})/(V_{reference} - V_{dark})) \qquad (6.2)$$

6.1.4.2 Circular dichroism

The AC signal from the PMT preamplifier is extracted from the noise using a Stanford Research Systems Model SR510 lock-in amplifier (LIA), a schematic diagram of which is shown in Figure 6.4.

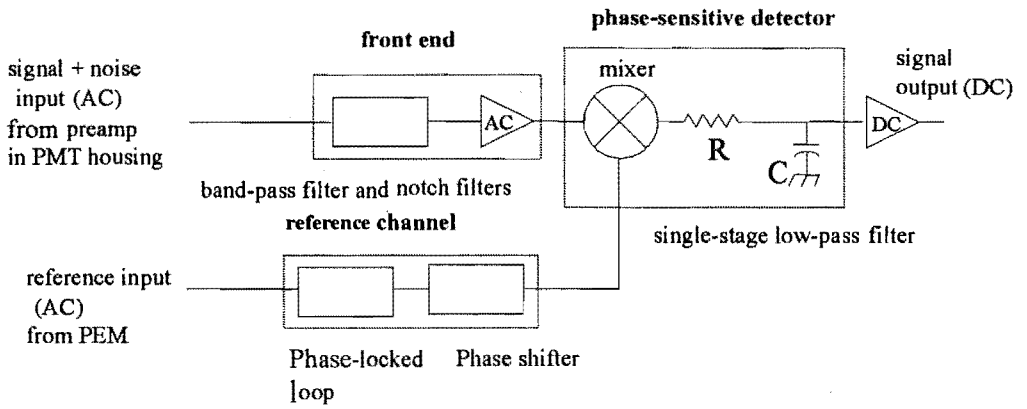

Figure 6.4: A schematic diagram of a LIA.

The input signal is first amplified, then filtered (front-end filtering) using a *band-pass* filter, which allows only a narrow range of frequencies around the desired signal to pass into the phase-sensitive detector (PSD). The reference signal (peak-to-peak amplitude of 6 V) originates from the PEM itself and has a frequency corresponding to the modulation of circular polarisation. A *phase-locked loop* converts this reference to a square wave, and the *shifter* matches the reference phase to that of the signal.

The square reference wave is multiplied with the input containing the signal and all unfiltered noise. The result is a superposition of two signals – an AC sum at twice the reference frequency and a DC difference proportional to the amplitude of the

signal.[iv] This is represented schematically in Figure 6.5 and further discussion of the details can be found in references 5 and 6. A low-pass filter removes the AC components while the DC passes through unattenuated. The signal emerging from the PSD is passed through two single-section low-pass filters.[7] Finally a DC amplifier amplifies the output signal.

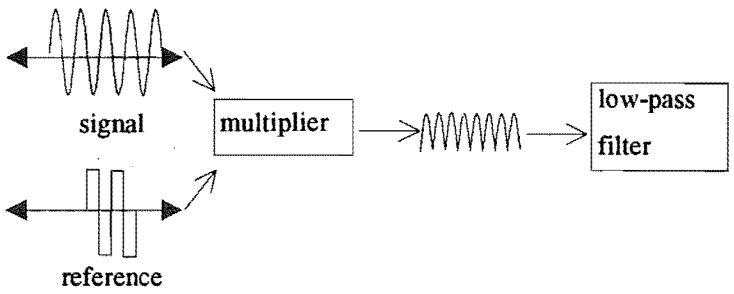

Figure 6.5: A schematic diagram showing the mixing that occurs in the PSD of a LIA

The sensitivity (L = 1 nV to 500 mV, full scale) sets the overall gain of the LIA for full-scale output of ±10 V. The apportioning of this gain between the AC (front-end) and DC (back-end) amplifiers is determined by the dynamic reserve – the ratio of the overload level (peak value of noise that will *just* cause the LIA to overload) to the peak value of a full-scale signal. The lower the dynamic reserve, the more gain is apportioned to the AC amplifier at the expense of the DC amplifier, and *vice versa*. Greater AC amplifier gain is preferable because it produces better signal stability. With very noisy signals, however, it may be necessary to reduce the AC gain to avoid overloading. The LIA settings employed in this work are given in Table 6.2.

Table 6.2: LIA setting used in this work on the Stanford Research Systems Model SR510

instrumental parameter	range	commonly used setting
band-pass of front-end filter		1% of reference frequency
full scale output	±10 V	
sensitivity	1 nV to 500 mV	10 nV
dynamic reserve	low/norm/high	low
time constant for low-pass (back-end) filter	1 ms –100 s	1 ms

[iv] Since the reference is a square wave, it actually comprises the sum of all odd harmonics of the signal frequency, but noise and unwanted signals at these frequencies will have been strongly attenuated by the front-end filter.

6.1.4.3 Calculation of MCD

The MCD electronics perform two major tasks. Firstly, they *gate* the input to the LIA, cutting out the *reference* and *dark* signals and leaving only the signal obtained during the *sample* period, which contains the MCD. Secondly, they integrate the LIA output over the sample period to further improve the signal-to-noise ratio.

Once the MCD signal has undergone analogue-to-digital (A/D) conversion by a PCL-814B interface card, it must be corrected (normalised) to take into account the sample beam intensity and the LIA sensitivity. The signal is also multiplied by an empirical calibration factor f, determined for a LIA sensitivity of 10 mV. Thus, the final signal that is calculated and stored by the computer is

$$\theta = \frac{S_{MCD} L f}{(V_{sample} - V_{dark}) \times 10\ mV} \tag{6.3}$$

S_{MCD} is the integrated MCD signal and θ is the corrected MCD in units of ellipticity (millidegrees, mdeg). To convert to absorbance units,[8]

$$\Delta A = \frac{\theta}{3298.2\ mdeg} \tag{6.4}$$

The factor f is determined using enantiomerically pure solutions of *d*-$[Co(en)_3]Cl[tartrate].5H_2O$ of various concentrations. The digital CD signal, S_{MCD} at λ = 493 nm was compared with the 'true' ellipticity calculated from the absorbance maximum (at λ = 469 nm) and the previously determined relationship,[9]

$$\theta_{493\ nm}/A_{469\ nm} = 742.1\ mdeg \tag{6.5}$$

Different detectors have different responses therefore require independent calibration. For quick checks between more careful calibration, seven to ten bands of varying intensities (between θ = 0 and 2000 mdeg) over the wavelength range 495 - 545 nm of a standardised crystal of $Na_3[Nd(ODA)_3].2NaClO_4.6H_2O$ (abbreviated Nd(ODA where ODA = $^-OOCCH_2\text{-}OCH_2COO^-$) was used.[10]

6.2 Matrix-Isolation/Cryomagnet Systems

Two experimental systems were used for sample preparation and to provide the magnetic fields and low temperatures required for the matrix-isolation MCD and absorption studies presented in this work.

There are a number of similarities between the two systems. Each is designed for use in conjunction with MOD4 and therefore fits neatly into the section of the optical table removed for this purpose. Both contain a vacuum chamber that interfaces to the matrix-deposition apparatus described in Section 6.3. Pfeiffer Balzers TSH172 170-L s^{-1} and/or TPU170 170 L s^{-1} turbo-molecular pumps are used to evacuate these chambers to ~2×10^{-5} Torr (as monitored by a cold-cathode Penning gauge) before the deposition window is cooled and sample preparation can commence.

6.2.1 Deposition Windows

The window onto which the matrix is deposited and through which spectra are measured, is cut, with faces at right angles to the crystal *c* axis, from an artificial sapphire. Sapphire is an appropriate window material for low-temperature experiments where accurate thermometry is required because it has a thermal conductivity about five orders of magnitude greater than quartz in the temperature range 10 to 20 K. It has the additional advantages of being hard and transparent over the entire visible region. However, it is optically anisotropic, showing linear birefringence for light with a component of propagation perpendicular to the *c* axis. To minimise the potential effects of window misalignment (or imperfections) the light is made to pass through the matrix before traversing the window. Depolarisation of the circularly polarised condition of the light by the crystal *after* it has passed through the sample will have no bearing on the *intensity* detected by the PMT. However, the (M)CD can be drastically reduced if the light is depolarised before it passes through the sample.

6.2.2 Helium Refrigerator/Electromagnet System

This apparatus comprises a closed-cycle helium refrigerator and vacuum chamber mounted between the poles of the electromagnet. It is intended for measurement of

temperature independent MCD spectra (no $\mathcal{C}$ terms) because it does not permit very low temperatures or high magnetic fields to be achieved. Furthermore, it does not allow the temperature of the sample be determined accurately (as discussed below). However, it has the advantages of being simple and cheap to operate (it does not use liquid He (ℓHe)) and also allows multiple over-depositions of the sample to be made within a single run, with spectroscopic measurements in between. For these reasons, even when studying MCD spectra with substantial $\mathcal{C}$ terms, this system is very useful for refining matrix-preparation techniques to obtain samples with good transmission properties and acceptable radical yield. Also the sample turn-around period is only several hours, permitting two entirely separate experiments to be completed in a day.

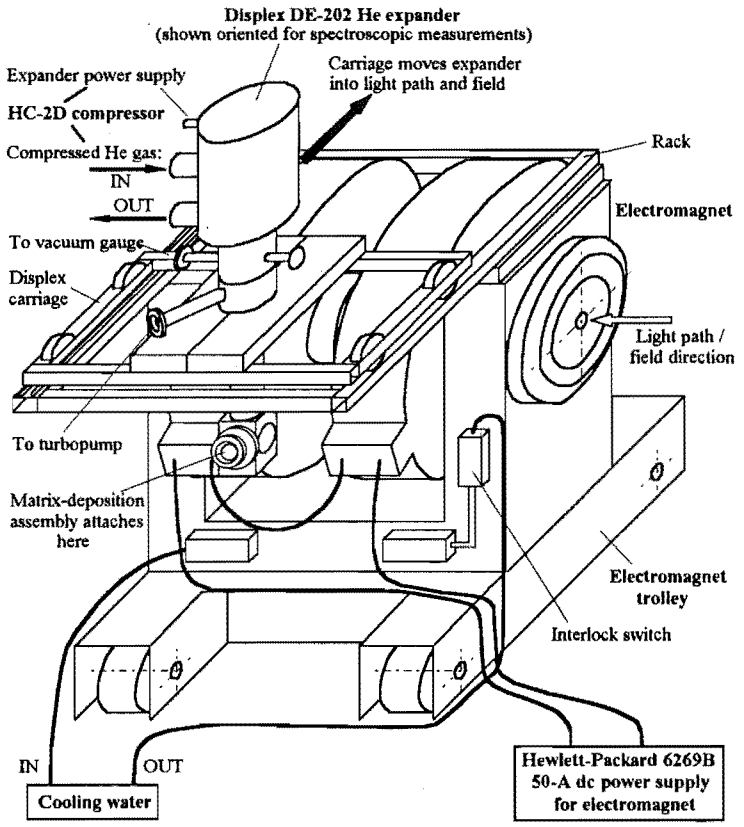

Figure 6.6: The electromagnet as used in combination with the helium refrigerator (adapted from reference 1).

The electromagnet is an Alpha Magnetic Inc. 4800 U-frame system with the pole caps removed to allow longitudinal (relative to the magnetic field) optical access through the poles. Power is supplied by a Hewlett-Packard 6269B 50-A, 40-V DC power supply. With the pole gap of ~6 cm required to accommodate the refrigerator, the maximum current of 50 A produces a field of 0.7 T at the sample window.

Cooling is provided by an APD Cryogenics Inc. closed-cycle He refrigerator (Figure 6.7), comprising an HC-2D compressor and a Displex DE-202 expander operating on a Gifford-McMahon refrigeration cycle.[11] The window is mounted with indium gaskets in a copper block attached to the colder (T_{min} ~12 K) of the two expander stages. The second-stage regenerator and sample window are shielded from ambient IR radiation by a chrome-plated Cu radiation shield, which is held at ~80 K by the first stage regenerator. After evacuation, the system requires approximately an hour to cool to its lowest possible (base) temperature.

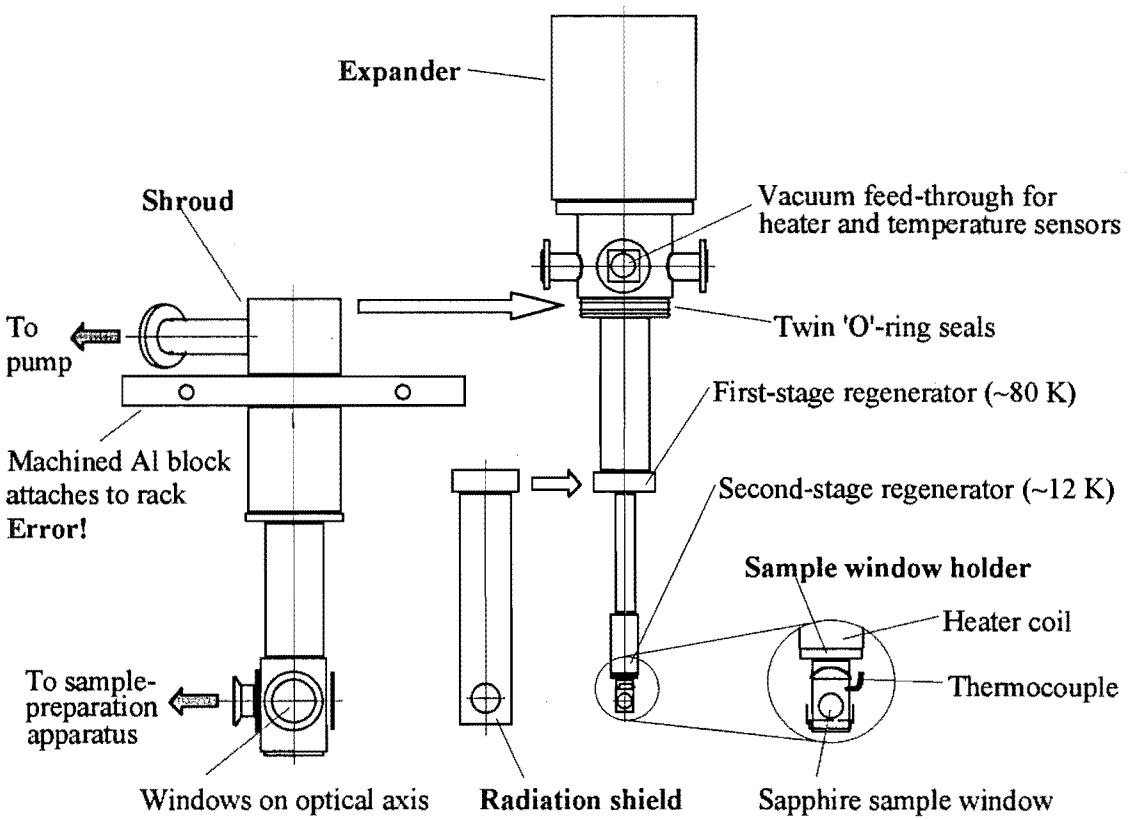

Figure 6.7: Simplified diagram of the Displex DE-202 expander and vacuum shroud, showing detail of the sample window.

The expander unit is inserted into a shroud that is fixed between the magnet poles and can be evacuated *via* a KW-25 port. The optical path of the spectrometer passes through two quartz windows on opposite sides of the shroud. Twin O-rings permit the expander to be rotated so that the deposition ('front') surface of the window faces either the incident light from the spectrometer or the matrix deposition apparatus.

The temperature sensor is an Au/.07%-Fe thermocouple used in conjunction with an Oxford Instrument ITC4 'intelligent' temperature control unit. The thermocouple junction is pressed, with 'crycon' grease, into a hole in the window holder located as close as possible to the window itself. The ITC4 displays the temperature in K according to a programmed calibration determined from the freezing point of water (273.15 K) and the boiling point of liquid N_2 (77.3 K). This instrument can also control the sample temperature at a *set point* above the refrigerator base temperature by adjusting the power through a ~37-Ω nichrome-wire heater wound around the second stage regenerator.

The main problem with this apparatus is the existence of temperature gradients between different parts of the system that result from having the sample in a vacuum. Heat transfer to and from the sample, which occurs almost entirely by conduction *via* the matrix itself, the window, the indium gasket and the copper sample holder, is much less efficient than it would be in the presence of a bath of exchange fluid. Consequently the sample never reaches the same temperature as the second-stage regenerator (the coldest part of the expander unit). But perhaps more importantly, a thermal gradient inevitably exists between the sample and the temperature sensor so accurate measurement of the sample temperature is not possible.

6.2.3 SM4/Matrix Injection System

In magneto-optical experiments the dominant temperature-dependent part of the MCD varies as $1/T$ ($\mathcal{C}$ terms) and the ability to separate this from the non-temperature dependent part ($\mathcal{A}$ and $\mathcal{B}$) requires that $1/T$ be varied over a considerable range. In argon matrix samples, one is usually limited to temperatures below 20 K to avoid irreversible diffusion effect and changes in the transmission characteristics. The ability to cool the sample to 4 K or below is crucial.

When matrix-isolation and MCD were first combined, the experimental set-up employed a super-conducting solenoid in the tail of a liquid-helium bath cryostat. The sample window was mounted, in vacuum, at the centre of the solenoid bore and cooled conductively by the same cryogenic fluid.[12,13] The cryostat tail was mounted in rotating housing, and after deposition of the sample, could be rotated by 90° into the optical path of the spectrometer in the same manner as described above for the electromagnet/refrigerator system.

While this type of set-up has a number of advantages over the system described in Section 6.2.2 – namely higher magnet fields (typically up to ~5 T), compactness, and the potential to cool the sample to near ℓHe temperature – many of the major problems remain. Most significantly, it is still impossible to accurately measure the temperature of the sample. Moreover, this type of system is costly (due to consumption of ℓHe) and time-consuming to operate. If an unsuitable matrix is produced, the system must be warmed to room temperature with time and money being wasted.

In response to these problems a 'top-loading' experimental technique called *matrix injection* was invented at Oxford Instruments under contract for the University of Virginia.[14] This method satisfies the requirements of having the window under vacuum during matrix deposition, while allowing the sample to be bathed in a cryogenic fluid (liquid or gas) to enable accurate thermometry at temperatures as low as ~1.4 K during spectroscopic measurements. It also has the additional advantages of requiring very little ℓHe for sample preparation, and having a relatively fast turn-around – if a matrix is unsuitable or another sample is to be measured, the deposition window can be withdrawn, warmed to room temperature (without need to warm the entire system) and cleaned, with a new matrix being deposited within an hour or two.

A similar but superior system has been established at the University of Canterbury.[15-17] It has the advantage over the one at Virginia in that the sample is actively cooled during the injection procedure (described below), significantly reducing the risk of losing the sample during this busy and complicated operation. The following is a general description of the system and its operation. For further details the reader is referred elsewhere.[15,16]

The University of Canterbury *matrix-injection* system comprises the three major components shown in Figure 6.8; an Oxford Instruments *SpectroMag* SM4 magneto-cryostat, a matrix-preparation chamber and a long, 'injectable' siphon rod on the tip of which is mounted the window holder and matrix-deposition window. The matrix-preparation chamber is interlocked to the top of the SM4 *via* a gate valve. The sample rod is top-loaded into the deposition chamber through a sliding seal and can be injected into or retracted from the sample chamber of the SM4 when the gate valve is open.

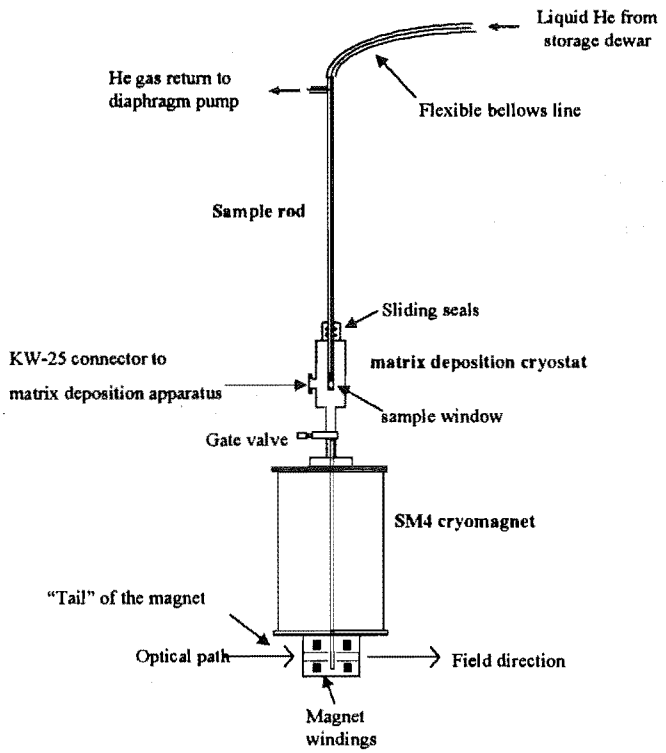

Figure 6.8: An overview of the matrix injection system (reproduced from reference 15).

The main volume of the Spectromag SM4 is a super-insulated ℓHe bath cryostat (model MD 10) surrounded by a liquid-nitrogen-cooled radiation shield. Bolted to the bottom of the cryostat (with indium sealing gaskets) is a demountable tail section in which is housed a 6-T split-coil NbTi superconducting magnet. Vertically, through the centre of the cryostat, extends a cylindrical sample chamber, which ends in a variable-temperature insert (VTI) positioned in the centre of the magnet (Figure 6.10).

A vertical length of NbTi wire, through which a current pulse is passed every ~100 s, is used to monitor the ℓHe level in the bath cryostat. The portion of the wire below the surface of the ℓHe is super-conducting, so the measured voltage is proportional to amount of wire in the resistive (non-super-conducting) state. The voltage is electronically converted to a ℓHe level before being displayed on an Oxford Instruments helium-level meter

The ℓHe serves to cool not only the magnet but also the VTI and its contents. The VTI is connected to the main ℓHe reservoir *via* a stainless-steel capillary. A needle valve, which can be adjusted from the top of the cryostat assembly, controls the siphoning of cryogenic fluid (liquid or gaseous He) from the reservoir into the

VTI. A radiation shield between the VTI and the ℓHe reservoir acts to minimise boil off in the reservoir when the VTI is operated at higher (than ℓHe) temperatures.

Optical access to the VTI is available from five (below and four horizontal) directions between the 'splits' of the magnet coil and through fused-quartz windows set with strain-free mounts into the outer tail section, the nitrogen-cooled vacuum shield and the VTI walls. The spectrometer light path passes through two of the horizontal sets of these windows.

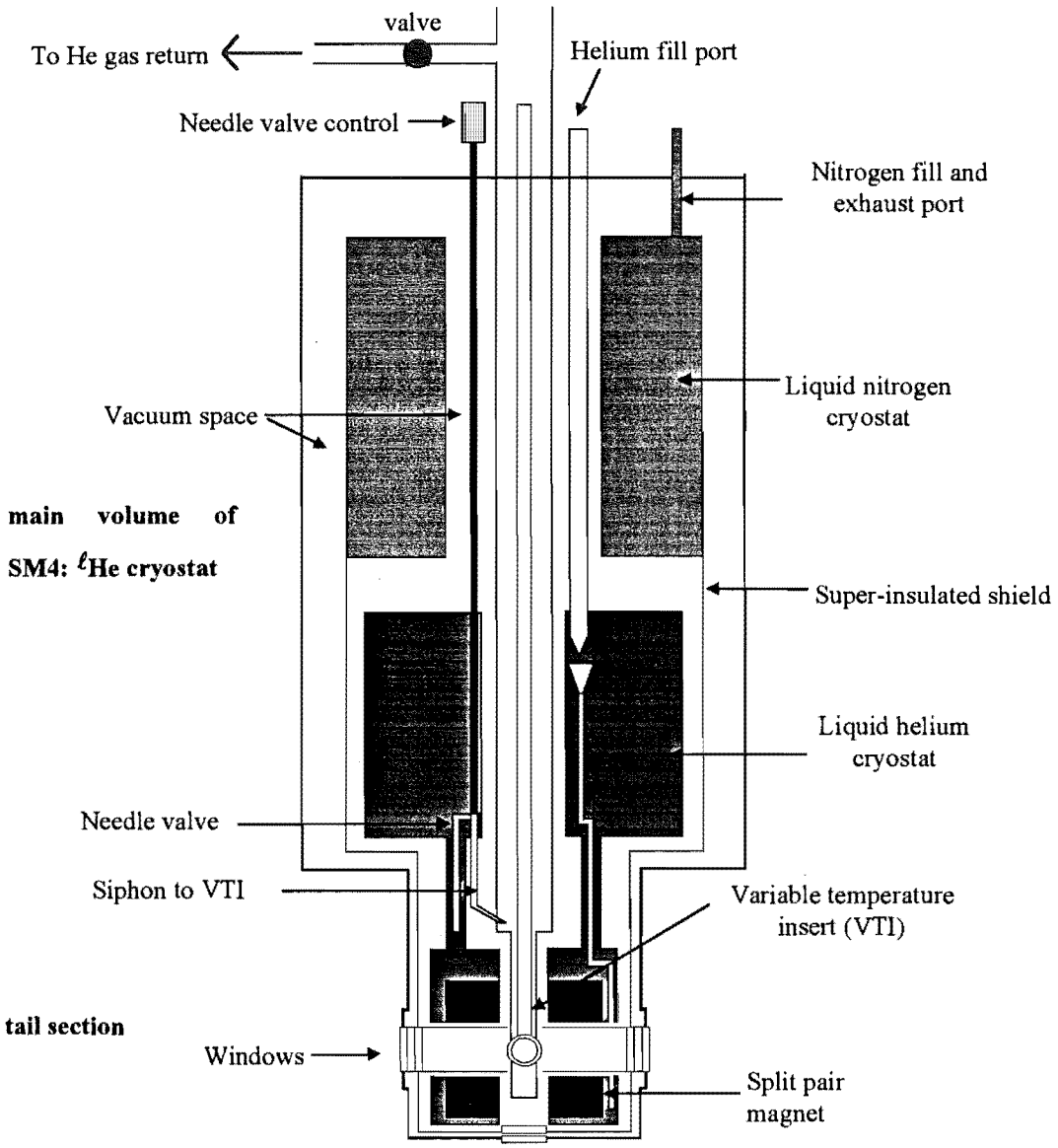

Figure 6.9: Simplified cross-section of the Spectromag SM4 cryomagnet

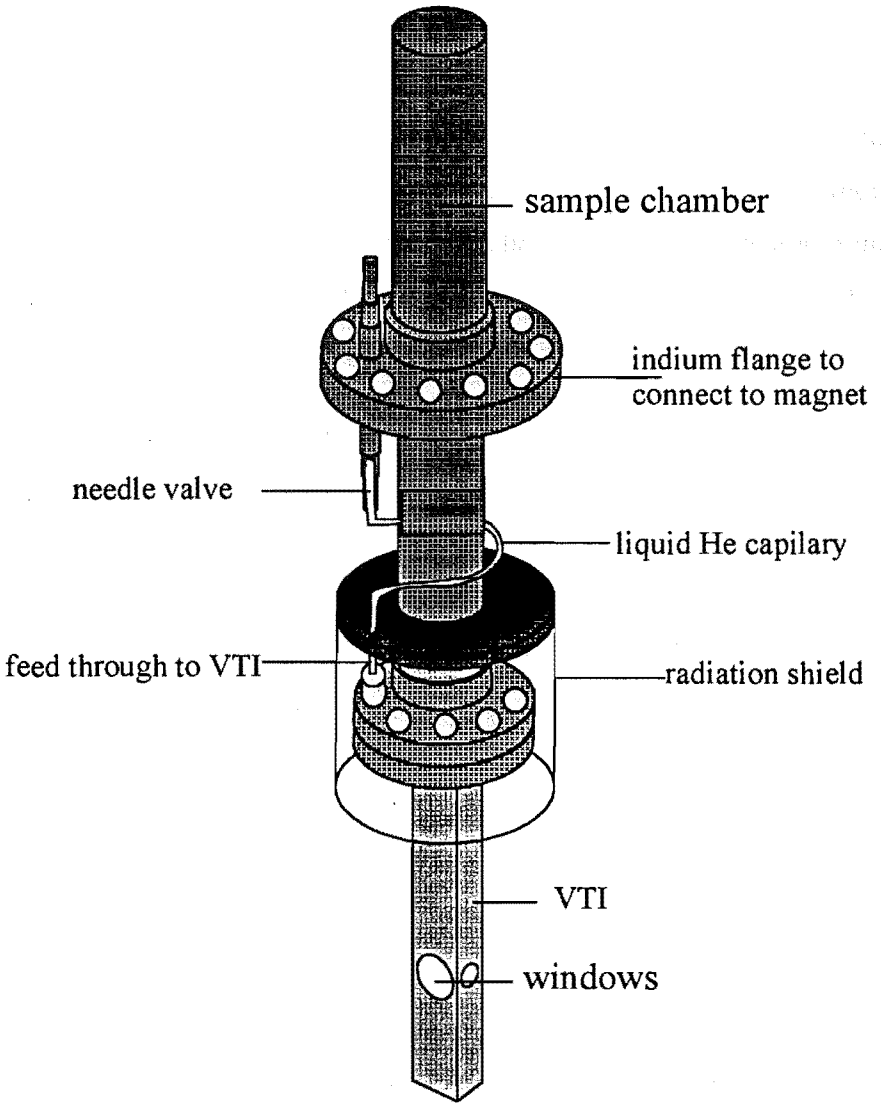

Figure 6.10: Detail of and around the VTI and needle valve of the SM4

The magnet is energised by using a 'switch' (Figure 6.11) consisting of a resistive wire (switch heater) wound non-inductively around a length of super-conducting wire that loops out from the main solenoid. When current is passed through the switch heater, the temperature of the loop rises above the critical point, putting it into a resistive (non-super-conducting) condition. In this state, current from the copper leads will flow through the super-conducting coils in preference to the switch. By adjusting the current (using an Oxford Instruments PS 75 Mk III power supply ramped by an SG3 sweep generator), the field generated by the coil can be controlled. When the desired field is reached, the switch heater is turned off, so the switch returns to the super-conducting condition. Now the voltage across the switch

must be zero (since it has zero resistance) and therefore the net current across the switch must also be zero. This condition can be considered as resulting from the sum of two counter-propagating currents – one passes through the leads without passing through the solenoid while the other, of the same magnitude but opposite sense, passes through the solenoid only. The second is said to be the *persistent* current of the closed super-conducting circuit since it persists in the absence of a voltage. According to Faraday's laws of induction, it will resist any changes in the magnetic flux and will continue even after the current in the leads has been withdrawn.

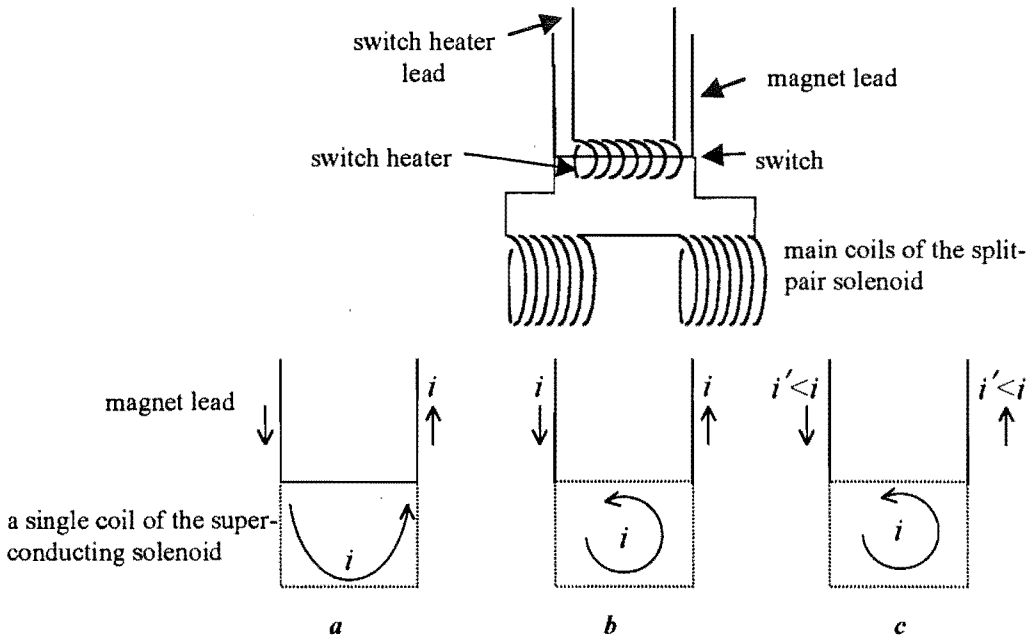

Figure 6.11: The top diagram is a schematic of a split pair magnet. The bottom diagrams show how the current in the magnet is changed. In ***a*** the switch is in a resistive state (on). In this arrangement the current *i* that passes through the magnet's lead in to the main solenoid can be increased or decreased. In ***b*** the switch is in a super-conducting state (off) and two opposing current loops are operating. As shown in ***c*** as the current in the magnet's leads is reduced to zero, the current in the solenoid remains constant due to Faraday's law of induction

6.2.3.1 Matrix Preparation and Injection

The matrix-preparation chamber (Figure 6.12) is a cylindrical vacuum vessel containing a radiation shield that encloses the sample rod, and onto which the matrix-deposition equipment is connected. Since the sample rod cannot be rotated, the deposition apparatus is aligned parallel to the optical path aiming towards the front surface of the sample window so that the matrix forms on the correct side of this window (Section 6.2). During matrix preparation, the sample rod is retracted into the

deposition chamber, the gate valve is closed and the chamber is evacuated by a Pfeiffer Balzers TSH172 170 L s^{-1} turbo-molecular pump. During deposition, the matrix can be viewed through a quartz window directly opposite to the deposition apparatus.

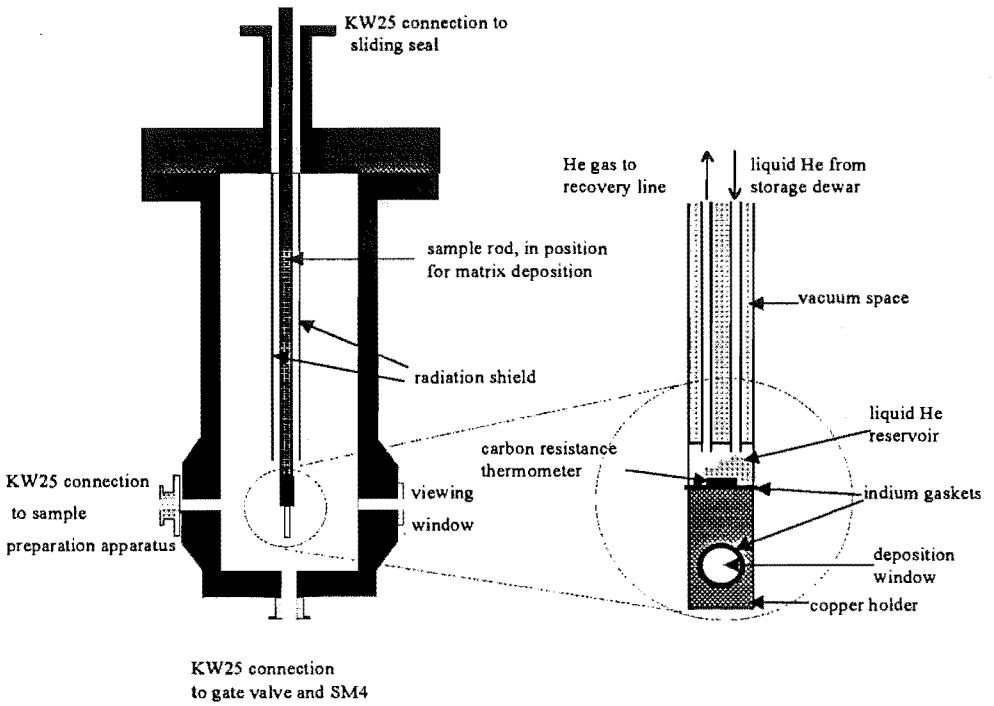

Figure 6.12: Schematic cross-section of the matrix-deposition chamber (left) and detail of the sample window and its cooling system (right).

The sample rod is constructed from an evacuated 1.7 m-long, 12 mm-diameter thin-walled stainless steel tube, which houses two stainless-steel capillary tubes. During deposition, ℓHe is drawn through one capillary from a storage dewar to a small reservoir in the tip of the sample rod. The sample window is cooled by the reservoir fluid *via* conduction through the copper window holder. An indium metal gasket between the window and its holder facilitates conduction. The second capillary, which provides the return path for the waste gas, is connected to a Compton D/189 diaphragm pump and an Oxford instruments flow-control console that together provide a controlled flow of cryogen. The window is held at ~20 K by controlling the helium flow rate (typically ~2 L hr^{-1}). The approximate temperature of the window is monitored by measuring the resistance of a 1/8-W Allen-Bradley carbon resistor

thermometer mounted in the ℓHe reservoir which has a resistance of 100 Ω at room temperature (RT) and ~230 Ω at 20 K.

Once the matrix has been prepared, it can be injected through the gate valve and SM4 sample chamber into the VTI until the sample window is situated in the optical path of the spectrometer. Before this occurs, the VTI is pre-cooled to ~10 K (VTI carbon resistance thermometer reading of ~100 Ω) by introducing cold He gas from the main SM4 reservoir *via* the needle valve shown in Figure 6.10 while the gate valve is shut. The needle valve is then closed and the sample chamber is evacuated to avoid destruction of the matrix by warmer He near the neck of the cryostat. When the pressure is low enough, the gate valve is opened so that the SM4 sample chamber and matrix-preparation chamber form a single space, the vacuum of which can be maintained by a single pump. The pump previously used to maintain the deposition-chamber vacuum is then recommitted to pumping the small vacuum space between two O-rings in the sliding seal while the sample rod is slowly injected. To avoid air passing into the sample chamber the pressure in the sliding seal should not be allowed to exceed ~10^{-4} Torr.

Once the sample has been injected and deemed suitable for further spectroscopic investigation, the sample chamber is isolated from the vacuum pump, and the needle valve to the main SM4 reservoir is reopened, allowing cold He gas to flood into the VTI. When the sample chamber reaches ambient pressure, a valve is opened to allowing excess gas to escape from the SM4 sample chamber into a return line. The flow of ℓHe through the sample rod is halted and the temperature of the matrix is henceforth controlled by the cryogenic fluid in the VTI.

6.2.3.2 Temperature Control of the Injected Sample

After injection, the sample is bathed in highly conductive exchange fluid (cold gaseous or liquid He) and rapidly reaches thermal equilibrium with the nearby temperature sensors in the sample rod and VTI, permitting accurate and precise thermometry.

Temperatures above the boiling point of ℓHe (> 4.2 K) are obtained by bathing the sample in expanding He gas, which flows into the VTI through the needle valve and has a cooling power (in a fixed volume) proportional to its flow rate.[16] This rate is controlled by throttling the gas return line from the sample chamber. The

temperature is monitored by two carbon resistors mentioned previously – one (~100 Ω at RT) is situated immediately above the sample in the He reservoir of the sample rod, while the other (~270 Ω at RT) is in the VTI a few mm from the sample. The resistance of the latter is read and displayed on an Oxford Instruments model 3400 DC resistance meter, which also outputs an error signal proportional to the difference between the measured resistance and a set-point value.

An innovation used for the first time during the work conducted in this project, is the use of the resistance-meter error output to control a mechanical valve in the He gas return line. If the temperature is too high, the valve opens, allowing a flow of gas, which cools the sample. If the temperature is too low, the valve closes, stemming the flow and allowing the sample to warm. In this way the temperature of a sample can be *automatically* maintained at temperatures above 4.2 K to within ~ 0.2 K of the set point for indefinite periods.[18] This set-up not only relieves the operator from long hours of tedious, manual control of the flow rate, but it also enables samples to be left overnight with out the risk of the temperature rising to the point where the sample was lost.

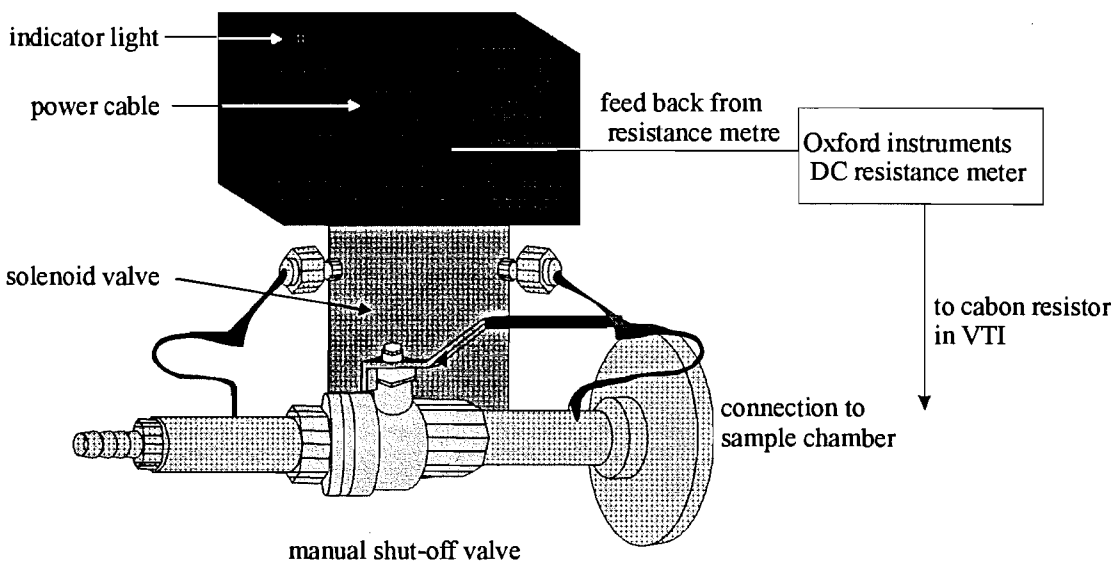

Figure 6.13: Detail of the automated solenoid valve used to control the temperature in the VTI above 4.2 K.

Sample temperatures below ~ 4.2 K (to ~ 1.4 K) are obtained by filling the VTI with ℓHe then pumping the headspace of the sample chamber with a rotary vane

pump. To fill the VTI, the needle valve is fully opened and liquid is siphoned into the VTI until frost begins to form on the exterior top of the sample chamber. (If the ℓHe level in the main reservoir is low, the He return line from the reservoir can be shut – as liquid evaporates the increase of pressure forces liquid into the VTI.) The relationship between the vapour pressure over ℓHe and the temperature of the liquid is well established.[19] Thus, the liquid can be cooled to a known temperature by reducing the vapour pressure to a particular value. Once the desired pressure, as measured by a 1000-Torr MKS Baratron capacitance manometer (type 622A13TAE) is achieved, it is controlled by an Oxford Instruments MNT manostat, a simple device that operates by comparing the vapour pressure in the VTI with a chosen reference pressure.[16] This device works extremely well maintaining the pressure at the set point to within 1 Torr (~0.01 K) for as long as ~3 hrs, *ie* until the liquid in the VTI runs out.

6.2.3.3 Sample Suitability

One disadvantage of the present matrix-injection system is that the suitability of samples for spectroscopic investigation (involving assessment of the optical properties and guest concentration of the matrix) cannot be gauged before injection, except by visual inspection through the quartz viewing window of the deposition chamber. If the sample is unsuitable, the sample rod must be retracted, which inevitably leads to loss of the matrix, then the whole preparation procedure must be repeated. (For this reason, the matrix preparation techniques must be optimised using the electromagnet/refrigerator system before the more-expensive injection system is used.) To rectify this situation, a system using an optical guide will be installed to enable absorption measurement of the matrix to be made while it is still in the deposition chamber.

6.3 Sample Preparation: Isolation of Radicals in Argon Matrices

Matrix-isolation (MI) involves trapping the species to be studied (the *guest*) in an excess of an inert *host* material on a cold surface. Often, as in this thesis, the species under consideration are too reactive to be studied by other methods. By trapping them at low concentration and low temperature in an inert matrix, they are well isolated

from one another (minimising intermolecular interactions) and are unable to diffuse together to undergo reactions.

If the host material is well chosen, complications due to guest-host interactions will be weak. Ideally, perturbations of the molecular structure of the guest and shifts in its transition frequencies will be minimal, so the spectral line positions will be similar to those in the gas phase. Also, variations in guest-host interaction due to different guest sites will be small, so spectral lines will be sharp and vibrational structure may be resolved. In fact, matrix-isolation tends to give the sharpest lines of any condensed phase except single crystals.

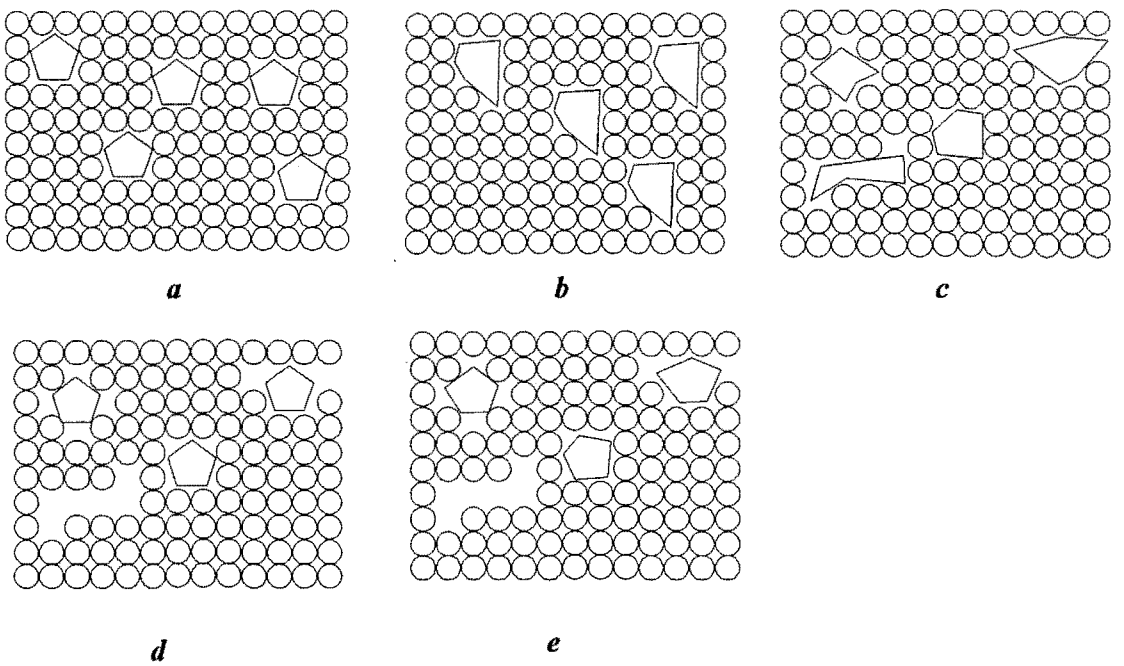

Figure 6.14: The circles indicate host molecules while the five-sided figures are the guest species. ***a*** shows the ideal situation; the matrix has a negligible effect on the electronic or vibrational structure of the guest molecule. In ***b*** the crystal fields set up by the host molecules distort the guest and the spectroscopic bands would be shifted compared to ***a***. In ***c***, as well as strongly distorting the guests, the added complication of multiple sites exists. Band shifting, broadening and (in the extreme) splitting would be expected. In case ***d*** multiple sites exist but guest-host interactions are so weak there is little effect of the spectra. Case ***e*** is the most likely scenario – different guest environments exist but, since guest host interactions are weak and perturbations are small, leading only to slight line broadening.

Matrix-isolation always carries the risk of introducing complicating factors. The existence of a number of different matrix environments (sites; Figure 6.14) can lead to band broadening and the appearance of multiple bands (site structure). Aggregation effects, due to guest-guest interactions ranging from loose Van der

Waals association through to complex (or adduct) formation, can also cause similar effects.

In any solid sample there will always be centres present (for example, crystallites), which can scatter and/or depolarise light. The potential for a matrix to scatter and/or depolarise the light, and its effect on MCD spectroscopy, has been considered by Graham and Grinter.[20] They showed that scattering does not affect the measured MCD whereas depolarisation causes reduction of the measured value. However, provided the latter effect is not too large it can be readily and quantitatively corrected for. The extent of depolarisation is assessed by passing the light emerging from the sample through a naturally optically active sample of known CD. The difference between the true and measured CD (in the absence of a magnetic field) is used to determine the *degree of depolarisation*, which can then be used to calculate the true MCD. For the experiments described in this thesis, an optically active single crystal of Nd(ODA) was used to show that the degree of depolarisation was negligible.

Annealing can be used to improve the resolution of the measured spectra. This involves warming the matrix to the point where it softens, allowing the guest species to reorient and the strain due to the arrangements of neighbouring host atoms to relax. Generally this reduces the number of different sites and therefore decreases the inhomogeneous spectral bandwidths.

The species considered in this project are free radicals. Since they are prepared *in situ* there is the possibility that many species may be formed and incorporated into the matrix. It is usually possible to identify some of the species created using IR and Raman spectroscopy in combination with photolysis and isotope substitution.[11] However, in this work existing data for gas-, solution- and solid-phase radicals have been used to determine the parts of the spectra pertaining to species of interest.

The host is a solidified gas whose concentrations is hundreds to thousands of times greater than that of the guest. Its most obvious requirement is that it is essentially chemically inert with respect to the guest species and for that reason it is common to use noble gases. This choice confers a number of additional advantages. Noble gases form isotropic matrices with weak (but non-zero) host-guest interactions. They also form films of high optical quality, that don't significantly scatter or depolarise light and are highly transparent over a broad spectral range from the UV to

the mid-IR. A disadvantage is that temperatures below that of liquid nitrogen are required for rigid matrices.

The host used in this work was argon (Matheson U.H.P. >99.999% purity), which forms rigid matrices below ~35 K. While xenon and krypton remain rigid at higher temperatures, they interact more strongly with the guest species (observed as shifting and broadening of bands), are more expensive and tend to give matrices of poorer optical quality. Neon gives the sharpest bands (weakest guest-host interaction) but its matrices are not rigid above ~6 K.

For matrix preparation, the deposition chamber must be maintained under a moderate vacuum ($<1\times10^{-5}$ Torr) for two principal reasons – to remove contaminants (air), which would otherwise be incorporated into the matrix, and to prevent heat conduction enabling the necessary low temperature to be achieved.

Matrices were deposited using the 'spray-on' technique,[11] in which the matrix components, the flows of which are controlled by needle valves, are deposited on the window at the lowest achievable temperature: ~12 K for the He refrigerator and ~20 K in the SM4 matrix deposition chamber.

The matrix components are delivered through concentric quartz tubes of 6 and 12 mm diameter (Figure 6.15), which terminate ~30 mm in front of the deposition window and are sealed to the vacuum chamber *via* a 1/2″ Cajon-to-KW-25 connector. The outer tube carries the guest species as well as Ar, sometimes pre-mixed with a small amount of an electron trapping species. The flow through is tube is ~1 mmol h^{-1}. Pure Ar is introduced from a 1-L stainless-steel reservoir *via* a stop valve, a stainless-steel needle valve and a 1/4″ Cajon connector. The calibrated needle valve is set to give a 5 mmol h^{-1} flow of Ar before the deposition window is cooled.

Radicals are generated *in situ* by using a method, based on work by George Pimentel in the late 1960s, where precursor molecules are passed, in a gaseous mixture with Ar, through a microwave discharge.[21] In this work an Evansen microwave cavity (with an Electro-Medical Supplies Microtron 200 power supply operating at ~200 W) is positioned around the inner of the concentric tubes and induces a discharge in a flow of pure Ar. Although slow deposition rates (~2 mmol h^{-1}) are desirable to obtain matrices of high optical quality and avoid an excessive heat load on the deposition window, flows of ~5 mmol h^{-1} were required to maintain the

Ar discharge. The resonance radiation causes the formation of radicals in the matrix mixture flowing simultaneously through the outer tube.[v]

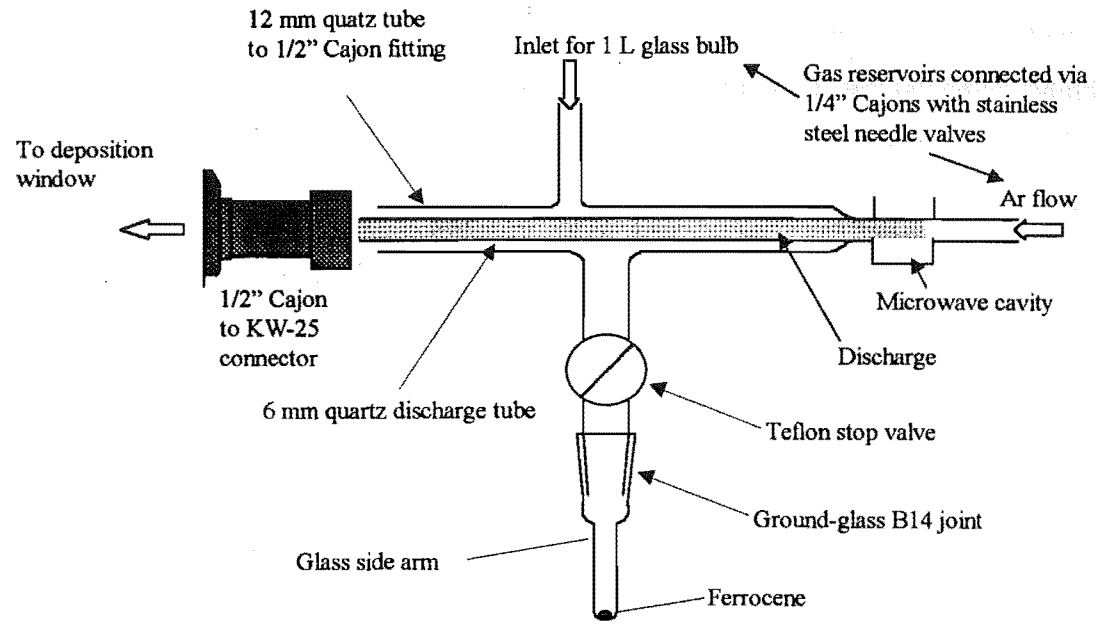

Figure 6.15: Matrix deposition apparatus

6.3.1.1 Cyclopentadienyl

Liquid dicyclopentadiene was degassed by numerous freeze-pump-thaw cycles. The vapour was then mixed in a 1-L pyrex bulb at a 1:25 mole ratio with Ar and the mixture was deposited at a rate of ~1 mmol hr^{-1}. In conjunction with the flow of Ar in the discharge tube, this gives an estimated maximum guest:host matrix ratio of 1:300. Neutral cyclopentadienyl radicals were created by homolytic cleavage with no requirement for an electron trap.

6.3.1.2 Ferricenium

Due to the low volatility of the ferricenium precursor, ferrocene, it was impractical to prepare a gas-phase guest-host mixture. Instead solid ferrocene was place in a side

---

[v] The mechanism by which the Ar resonance radiation induces radical formation has been the subject of dispute.[21,25] Two general possibilities have emerged: the discharge acts as a vacuum-UV lamp and absorption of high-energy photons by the precursor result in ionisation; or the excited Ar atoms undergo collisions with the precursor, and the resulting energy transfer causes ionisation of the precursor. The work done for this Ph.D project (and others from the same research group[1]) support the latter mechanism since the discharge is physically separate from the precursor.

arm connected to the outer tube of the discharge apparatus through a Teflon stop valve Figure 6.15. Sublimed ferrocene, at a flow rate controlled by the valve, was entrained into the flow of host gas. The formation the radical cation ferricenium involves the displacement of an electron from ferrocene, so degassed CCl_4 (in a 1:25 ratio with Ar) was added from the 1-L Pyrex bulb to the host to act as an electron trap. The ratio of trap to host in the final matrix is ≤1: 300.

6.4 Solution Spectra

MCD and absorption spectra of ~10 mmol L^{-1} ferricenium tetrafluoroborate $[Fecp_2][BF_4]$ (prepared according to reference 22) in dichloromethane were collected between ~300 and 180 K (the freezing point of the solvent) using an liquid-N_2-cooled Oxford Instrument CF 1204 continuous-flow cryostat[23] in conjunction with the electromagnet described in Section 6.2.2

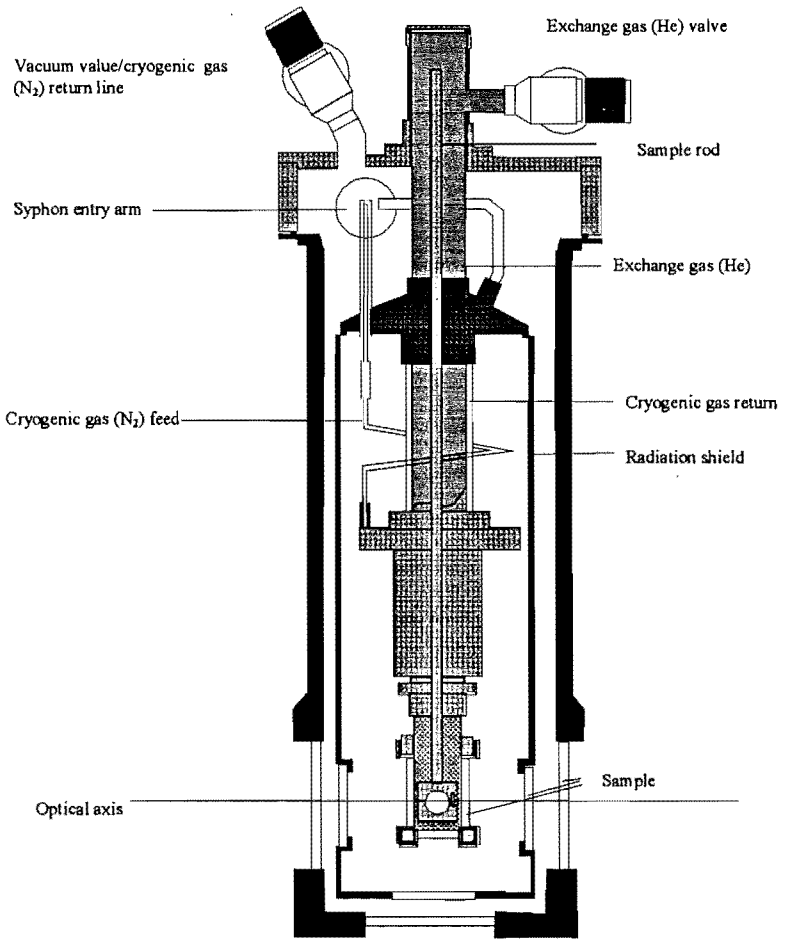

Figure 6.16: Cross section of the continuous-flow cryostat, an additional radiation shield is not shown.

In this set-up, the sample chamber, containing a quartz cell attached to the sample rod, is filled with He exchange gas. The thermal conductivity of this gas means that it comes to equilibrium with the cryostat heat exchanger and the sample. A 27-Ω Rh-Fe resistor and a 34-Ω heater permit accurate temperature measurement and control *via* the ITC4 temperature controller described in Section 6.2.3.

6.5 References

(1) Langford, V. S. Ph.D. Dissertation, University of Canterbury, Christchurch, 1997.

(2) Collingwood, J.C.; Day, P.; Denning, R.G.; Quested, P.N.; Snellgrove, T.R. *J. Phys. E: Sci Instrum.*, **1974**, *7*, 991-996.

(3) Brittain, R.; Powell, D.; Voigtman, E.; Vala, M. *Rev. Sci. Instrum.*, **1980**, *51*, 905-910.

(4) Moore, J. H.; Davis, C. C.; Coplan, M. A. *Building Scientific Apparatus*; Addison-Wesley Publishing Company: London, 1983.

(5) Munroe, D. EG & G Princeton Applied Research.

(6) EG & G Princeton Applied Research. Model 5101 Lock-In-Amplifier operating and service manual.

(7) Warring, R. H. *Understanding Electronics*, 1st ed.; Tab Books Inc.: Blue Ridge Summit, 1978.

(8) Piepho, S. B.; Schatz, P. N. *Group Theory in Spectroscopy-With Applications to Magnetic Circular Dichroism*; John Wiley & Sons Inc:, 1983.

(9) Katz, T. J.; Strauss, H. L. *J. Chem. Phys.* **1960**, *32*, 1873-1875.

(10) Langford, V. S. MOD4 Manual.

(11) Dunkin, I. R. *Matrix-Isolation Techniques. A practical appoach*, 1st ed.; Oxford University Press: Oxford, 1998.

(12) Douglas, I. N.; Grinter, R.; Thomson, A. J. *Mol. Phys.* **1974**, *28*, 1377-1388.

(13) Prince, B. J. Ph.D. Dissertation, University of Canterbury, Christchurch, 1999.

(14) Krausz, E.; McDonald, P. *J. Phys. E: Sci. Instrum.* **1978**, *11*, 801-804.

(15) Dunford, C. L. Ph.D. Dissertation, University of Canterbury, Christchurch, 1997.

(16) Oxford Instruments. Instruction Manual for the Oxford Instruments Spectromag.

(17) Dunford, C. L.; Williamson, B. E. *J. Phys. Chem. A.* **1997**, *101*, 2050-2054.

(18) Upton, A. H. P.; Williamson, B. E. *J. Phys. Chem.* **1994**, *98*, 71-76.

(19) Durieux, M.; Rusby, R. L. *Metrologia* **1983**, *19*, 67-72.

(20) Graham, R. G.; Grinter, R. *J. Phys. Chem.* **1990**, *94*, 6283-6285.

(21) Wright, C. A.; Ault, B. S.; Andrews, L. *J. Chem. Phys.* **1976**, *65*, 1244-1249.

(22) Connelly, N. E.; Geiger, W. E. *Chemical Reviews* **1996**, *96*, 877-910.

(23) Oxford Intruments Limited. Instruction Manual for the Continuous Flow Cryostat CF1204.

(24) Upton, A. H. P. M.Sc. Thesis, University of Canterbury, Christchurch, 1991.

(25) Prochaska, F. T.; Andrews, L. *J. Chem. Phys.* **1977**, *67*, 1091-1099.

7 THE FERRICENIUM RADICAL CATION

7.1 Introduction

The discovery of ferrocene ($Fe(cp)_2$) in 1951,[1,2] and the recognition that it exemplified a new type of bonding,[3] is considered to be the most significant event in the development of organometallic chemistry. It was soon realised that the radical cation of ferrocene, ferricenium ($Fe(cp)_2^+$) was stable, and a good deal of work was performed on this ion, principally as a means of investigating the nature and bonding of ferrocene itself. In this chapter it is the radical species that is of interest.

Despite the fact the its ground and first excited states are orbitally doubly degenerate, and therefore subject to JT effects, there has been very little discussion in the literature of the magnitude or nature of vibronic coupling in ferricenium. One of the reasons for this may be the lack of appropriate experimental data. Another is that the extraction of quantitative information is difficult due to the potential for simultaneous and competing CF, JT and SO effects. One way to simplify the analysis is to eliminate extrinsic (external) effects – especially CFs. While these are inevitably important in crystals, solutions and glasses, they may be much smaller when the species of interest is incorporated into an inert-gas matrix. So although the radical is quite stable and can be easily generated in solution by chemical or electrolytic methods, it might be instructive to study the species in an inert matrix environment. While CFs do exist in such matrices,[4,5] they are generally an order of magnitude smaller than those typically found for ferricenium in other media (Table 7.1). In addition, CF effects on the metal d orbitals in metallocenes may be especially weak, since they are effectively insulated from direct interactions with the environment by the presence of the rings.

In this chapter, absorption and temperature- and magnetic-field-dependent MCD results are presented for $Fe(cp)_2^+$/Ar and for $[Fe(cp)_2^+]BF_4^-$ in a dichloromethane solution. CF and JT effects are investigated by using moment analysis and spectral simulations, which also allows some of the vibrational structure to be assigned. A value for the orbital reduction factor for the ground state is obtained, from which it was possible to derive values for the contribution to the $1e_{2g}$ molecular orbital from the metal orbital (c_d) and for the SO coupling constant. It was also possible to separate contributions from various effects to the ground-state orbital reduction factor.

7.1.1 The Ground States of Ferrocene and Ferricenium

Ferrocene consists of a Fe ion (formally Fe^{2+} in the ground state) sandwiched between two cyclopentadienyl ($C_5H_5^- \equiv cp^-$) rings. Crystal structures[6] indicate that the ligands assume a staggered ($\mathbf{D}_{5d}$) conformation, a result which is supported by vibrational spectroscopy.[7-9] However, there is evidence from electron-diffraction studies that ferrocene takes an eclipsed $\mathbf{D}_{5h}$ conformation in the vapour phase.[10] MO calculations indicate that the energies of the eclipsed and staggered conformations of ferrocene[11,12] are very similar and that the barrier to rotation is small. The $\mathbf{D}_{5d}$ conformation is slightly the more stable because of steric repulsion between carbon atoms on different rings (the perpendicular distance between planes is ~3.32 Å).

The ground-state structure of the ferricenium ion in crystals is found to be either eclipsed, staggered or a mixture, depending on the counter ion.[13-15] Marteniz and Tiripicchio[13] found that the Fe-cp and Fe-C bond distances are similar in the staggered and eclipsed forms. Thus, they suggested that, as with ferrocene, the barriers to rotation of the ligands are small and the conformation in the solid state is ultimately determined crystal packing forces.

From the 1950s through to the early 1970s, a significant amount of theoretical and experimental was done to determine satisfactory molecular-orbital (MO) schemes for the metallocenes.[12,14,16-26] Detailed discussion of these MOs is deferred to Section 7.3.1, but a qualitative energy-level diagram (adapted from reference 20) determined by simple symmetry and energy considerations is shown in Figure 7.1.

Applying the aufbau principle to the MO scheme in Figure 7.1 gives a ground-state configuration for ferrocene of $1e_{2g}^4\,2a_{1g}^2$. The standard text book description of the metal-ligand bonding in ferrocene is then as follows.[27] The $1a_{1g}$ and $1a_{2u}$ orbitals involve donation of electron-pair density from the ligands to the metal forming σ dative bonds, while $1e_{1u}$ and $1e_{1g}$ involve donation in the same direction forming π bonds. In the $1e_{2g}$ orbitals, d-electron density is back donated to the empty higher-lying ligand orbitals of the same symmetry. This so-called retrodative δ-σ bonding is generally weak in metallocenes because the ligand e_{2g} orbitals lie so much higher in energy.

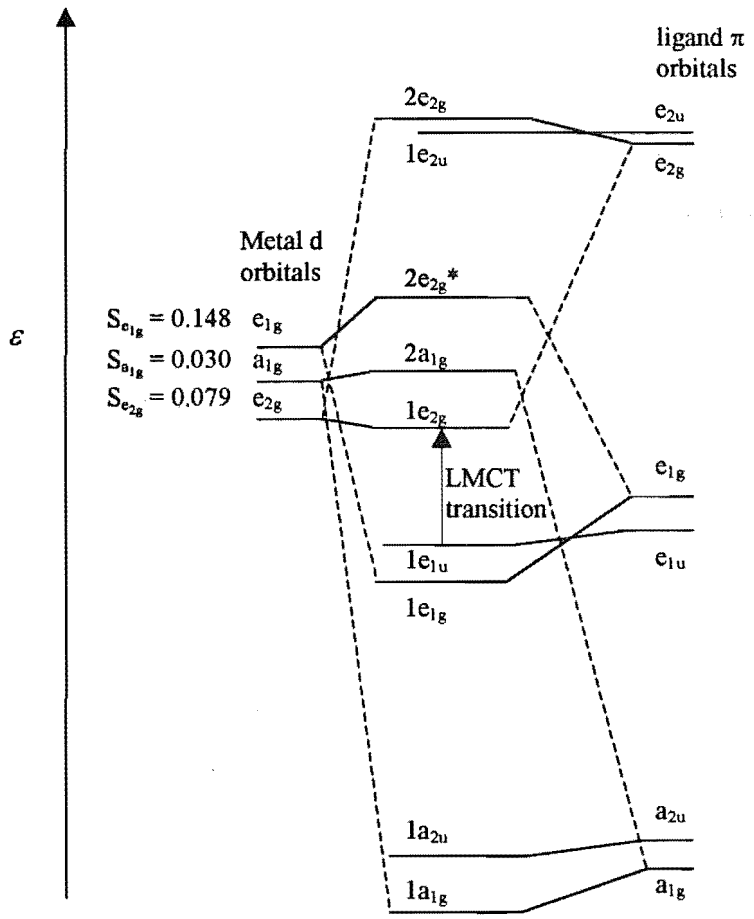

Figure 7.1: The d-π section of a qualitative MO diagram for the metallocenes assuming D_{5d} symmetry. The overlap factors calculated for ferrocene in reference 28 are given on the left.

A broad range of theoretical calculations, from *ab initio* to semi-empirical, have been performed in order to determine a quantitative MO scheme for ferrocene. They have also been concerned with the relative contribution from ligand and metal to the MOs and the extent to which they contribute to ligand-metal bonding. In their 1971 review, Ballhausen and Gray[20] classified the calculations up to that time into four categories – qualitative MO treatments,[11,12] crystal-field treatments,[29,30] extended Wolfsberg-Helmholz calculations[18] and simplified *ab inito* LCAO-MO SCF calculations.[28,31] More recent efforts include *ab inito* LCAO-MO-SCF (including all electrons) calculations performed in 1972[25] and 1976.[14] The results are by no means consistent. In particular, the $1e_{1g}$ – $1e_{1u}$ and $1a_{1g}$ – $2e_{2g}$ orders (both important to the interpretation the optical spectroscopy of ferricenium) have been the subject of contention.

It is clear that the metal and ligand e_{1g} orbitals have similar energies and substantial overlap, and are therefore expected to be most responsible for metal-ligand bonding *via* the d orbitals.[16,28,30,31] The detailed description of other MOs is less certain. For example, the extent to which the metal 4p orbitals are involved in metal-ring bonding is contentious. Early qualitative MO calculations[11] indicated that the contribution from these orbitals could be ignored. However, later calculations[28,31] predicted large amounts of mixing. The extent to which metal-3d and cp-π orbitals mix also varies from study to study. For example, for the $1e_{2g}$ orbital, Shustorovich and Dyatkina calculated a d-orbital contribution of $|c_d|^2 = 0.72$,[31] whereas Ballhausen and Dahl[28] and Prins *et al.*[18] obtained $|c_d|^2 = 0.81$. One of the reasons for this variation is the different types of functions used to describe the metal orbitals – Dahl and Ballhausen used Hartree-Fock orbitals from Watson's calculations for first-row transition metals,[32] while Shustorovich and Dyatkina used Slater-type orbitals. The d-π overlap factors (S values) calculated by Dahl and Ballhausen and described by Sohn *et al.*[33] and Ballhausen and Gray[20] as being the best available, are summarised on the left-hand side of Figure 7.1.

The types of experimental data available to determine a quantitative MO scheme and to further characterise the ground state of ferrocene include photoelectron, Mössbauer,[24] absorption and MCD spectroscopies,[34,35] as well as ESR[21-23,36-41] and magnetic susceptibility measurements.[42] While it is simple to establish the non-degenerate nature of the ground state of ferrocene, the lack of orbital angular momentum means that more detailed treatments are difficult because some of the techniques listed above (ESR, MCD and magnetic susceptibility) are only indirectly useful. Thus, most experimental techniques involve investigation of ferricenium and assume the validity of Koopmans' theorem.[i]

In the photoelectron spectrum of ferrocene obtained in 1968 by Turner,[43] the lowest two ionisation potentials, at 6.85 and 7.2 eV, were respectively assigned to the removal of electrons from e_{2g} and a_{1g} orbitals predominantly localised on the Fe atom. One would thus expect that the orbital sequence to be $a_{1g} < e_{2g}$.[21,25] However, Prins[21] noted that the ionisation potentials are so similar that nothing definite can be said

---

[i] When an electron is removed from an orbital, the remaining electrons do not adjust their distribution. Therefore the experimentally measured ionisation potential can be directly related to the 1-electron energy of the orbital.[57]

about this order – due to the approximations inherent in Koopmans' theorem and neglect of correlation energy in the Hartree-Fock approximation, the only thing that can be said with any certainty is that they lie close together. By considering the photoelectron spectroscopy, Prins[21] established the ordering $1e_{1g} < 1e_{1u}$, commenting that the $1e_{1g}$ orbitals are more stabilised by interaction between π and 3d orbitals than are the $1e_{1u}$ orbitals by π–4p interactions. Overall, he established an experimental MO scheme as

$$1e_{1g} < 1e_{1u} < 2a_{1g} \approx 1e_{2g} < 2e_{1g}^{*}$$

Coutière *et al.*,[25] two years later, explained that discrepancies between the orbital schemes for ferrocene determined by calculations (of the ionisation potentials) and experimental results are due to the fact that Koopmans' theorem is not valid for the ionisation of ferrocene. In particular, the orbital sequences for ferrocene and its cation, ferricenium, are different because of the electronic rearrangement that occurs on ionisation. For the ligand orbitals, this rearrangement is minor so the orbital energies of the neutral and the cation are similar. But for the metal orbitals it is marked, amounting to as much as 6 eV. In fact they found that MO calculations for ferricenium agreed better with experiments aiming to determine the MO scheme of ferrocene than did calculations for ferrocene.

By virtue of its open-shell nature, the ground-state electronic structure of the ferricenium has been has been much easier to establish experimentally. Magnetic susceptibilty[41,42] and ESR[36-38,40] measurements have been conducted on various ferricenium salts and their analogues[37] in solutions[21,36,37,40] and crystals.[38,41,42] In most analyses, $\mathbf{D}_{5d}$ symmetry was assumed and anisotropic, axial ($g_x = g_y \neq g_z$) g matrices were obtained with elements well removed from the spin-only value (columns 3 and 4 of Table 7.1). This indicates a substantial contribution from orbital angular momenta, pointing to a $^2E_{2g}(1e_{2g}^{\ 3}\ 2a_{1g}^{\ 2})$ ground state – the alternative of $^2A_{1g}(1e_{2g}^{\ 4}\ 2a_{1g}^{\ 1})$ has no orbital angular momentum. The apparent paradox that ionisation of ferrocene to give ferricenium may not be from the highest MO of the neutral molecule is explained when two-electron repulsion integrals are taken into account.[16,44]

Table 7.1: Experimental ESR parameters of ferricenium derivatives. δ is the splitting due to a static low-symmetry effect.

species	refs	$g_{\|}$	$g_{\perp}$	κ_{cov}	c_d	δ/cm^{-1}
cations of aryl ferrocenes in various solutions	36	3.62-4.36	1.30-1.75	0.80-0.84		200-450
substituted $Fe(cp)_2^+$ in various solutions	21	3.62-4.35	1.26-1.76	0.76-0.85	0.91	270-610
carborane analogues of $Fe(cp)_2^+$ in various solutions	37	3.70-3.94	1.53-1.80	0.76-0.90	0.87-0.94	364 -750
$Fe(cp)_2^+BF_4^-$ in rigid matrix of methacrylic acid polymer	35	3.21	1.83	0.75		1043
$Fe(cp)_2^+BF_4^-$ in aq solution	26,45	4.35	1.26	1		260

The results in Table 7.1 were explained quantitatively by various authors[35-38,40-42] in terms of a $^2E_{2g}$ ground-state term, split by SO interactions and a static symmetry perturbation (CF and/or JT effects quantified by δ – column 7) of similar magnitude, into a lower-energy Kramers pair ($E_{5/2}$) and a higher-energy Kramers doublet ($E_{3/2}$). That the magnitudes of the SO and CF/JT effects must be similar was evidenced by the fact that the orbital angular momentum is only partially quenched. All investigators considered that the energy difference between these SO-CF levels was too large for the upper states to have an appreciable population, even at room temperature. For the most part, they also determined that the effect of configuration interaction was minimal – the nearest configuration, $^2A_{1g}(1e_{2g}^4\ 2a_{1g}^1)$, is of the wrong symmetry to interact, while second-order perturbation theory indicates that the next-nearest configuration has too small an effect to be of any consequence.[35-37,42] There is evidence in the literature that the CF is temperature dependent. Hendrickson *et al.*[41,42] invoked a CF that increased with temperature as a possible alternative explanation of their magnetic susceptibility results, suggesting that it could be due to the increased motion of the cyclopentadienyl rings. On the other hand, Rowe and McCaffery[35] determined δ = 1043 cm^{-1} from low-temperature (20 K) ESR data, but δ = 263 cm^{-1} from room-temperature MCD data, the implication being that the CF increases with decreasing temperature.

This SO-CF model enabled some groups to determine experimental values for the orbital reduction factor due to covalency, κ_{cov} (Section 3.3.2), as well as the contribution, c_d, of the metal d orbitals to the $1e_{1g}$ MO. These results are given in columns 5 and 6 of Table 7.1. Prins and Reinders[36] calculated $\kappa_{cov} = 0.80$ from the ESR spectra of $Fe(cp)_2^+.BF_4^-$ and $Fe(cp)_2^+.I_3^-$ in acetone at 20 K (Table 7.1 row 1). For a variety of substituted ferricenium ions, Prins[21] found $\kappa_{cov} \approx 0.82$, which gave $c_d \approx 0.91$ (Table 7.1 row 2), indicating that the metal contribution to the open-shell $1e_{2g}$ MO is relatively insensitive to substitution. He noted that this result (in combination with similar ones for vanadocene[22,23]) demonstrated that back-donation *via* $1e_{2g}$ was less important in transition-metal dicyclopentadienyl complexes than in dibenzene complexes. He also suggested the possibility that the reduction of orbital angular momentum could be due to a dynamic (JT) effect, but made no attempt to quantify this. Maki and Berry's[37] earlier experimental results for carborane analogues of ferricenium (Table 7.1, row 3) give similar values. However Rai *et al.*[45] surprisingly suggested that orbital reduction is due entirely to JT or CF effects, with no contribution due to covalency.

Since the pure SO doublets of a ^2E term have vanishing $g_\perp$ values, (the corresponding ESR resonance would be at infinite field) the results of Table 7.1 clearly indicate deviations from rigorous axial ($\mathbf{D}_{5(h/d)}$) symmetry. The authors of these earlier studies generally attributed the symmetry lowering to CFs imposed by the medium (solvent molecules and/or counter ion) and quantified by the parameter δ given in column 8 of Table 7.1. In his study of substituted ferricenium ions, Prins found a CF splittings of $\delta \approx 270$ cm^{-1}.[21] This also helped him to explain the broad linewidths he observed. Hendrickson *et al.*,[42] by comparing measured and calculated temperature dependence of the magnetic susceptibility of substituted ferricenium salts (as glasses), estimated $\delta \approx$ 200-300 cm^{-1}. They noted that distortions responsible for splittings of this magnitude would be difficult to detect by X-ray structure determination, although some evidence had been obtained from infrared studies.[46] In a manner similar to Prins and Reinders[36] and Maki and Berry,[37] Hendrikson *et al.*[42] explained the variations in the magnetic susceptibility data as being due to CF effects of differing magnitude in different environments.

7.1.2 The Red Transition of the Ferricenium Radical

As commonly occurs with the ionisation of molecules, the transformation of ferrocene to ferricenium leads to the appearance of an additional electronic transition to the red of the lowest-energy transition of the neutral precusor.[47] Such transitions arise due to excitations terminating in the now partly occupied LUMO from fully occupied MOs at lower energy.

Early studies (in 1959[44] and 1965[30]) of the red-band system of ferricenium, which peaks at ~16200 cm^{-1} in absorption, suggested that it was a parity-forbidden 3d ← 3d transition $^2A_{1g}(1e_{2g}^4 2a_{1g}^1) \leftarrow {}^2E_{2g}(1e_{2g}^3 2a_{1g}^2)$. But Prins[16,21] pointed that the extinction coefficient of 420 L mol^{-1} cm^{-1} is much higher than the values (typically ~10 L mol^{-1} cm^{-1}) for the d ← d transitions of other sandwich compounds, while Sohn *et al.*[41] noted that, in analogy with ferricyanide, low-energy ligand-to-metal charge-transfer (LMCT) transition are expected for ferricenium. Both research groups observed that substituents on the cp rings lead to band shifts much larger than those of the d ← d bands of substituted neutral ferrocenes and took this to indicate that at least one of the orbitals involved is ligand based. Ligand-to-ligand transitions were ruled out, since other metallocenes exhibit no bands around 16200 cm^{-1}. Furthermore, the observation that the electron-donating methyl group gives a red shift whereas the electron-withdrawing acetyl group gives a blue shift shows that the band is due to a LMCT transition. Lever[47] and Sohn *et al.*[33] noted that the increase in intensity upon cooling (an effect exhibited by the absorption data in Figure 7.7) eliminates the possibility of a d ← d transition.[ii]

In 1970, Prins[16] used evidence from photoelectron spectra of ferrocene[43] to make a definite assignment. Bands at 6.85 and 7.2eV were assigned to removal of electrons from the e_{2g} and a_{1g} metal 3d orbitals. The next two bands, at 8.8 and 9.3 eV were attributed to ionisation from the e_{1u} and e_{1g} ligand π orbitals. Subtraction of the first from the third and fourth gives energy differences corresponding to 15 700 cm^{-1} and 19 800 cm^{-1}, which should be close to the excitation energies for the LMCT processes $1e_{2g} \leftarrow 1e_{1u}$ and $1e_{2g} \leftarrow 1e_{1g}$ in $Fe(cp)_2^+$. Since there is a moderately strong band at 16 200 cm^{-1} in the absorption spectrum and a weak band at 19 000 cm^{-1}, the

---

[ii] Since d-d transitions are necessarily vibronic transitions, their intensity is expected to increase with increasing temperatures

former was attributed to the symmetry-allowed transition $^2E_{1u} \leftarrow {}^2E_{2g}$ and the latter to the symmetry-forbidden transition $^2E_{1g} \leftarrow {}^2E_{2g}$. Investigations of the optical spectrum of ferricenium, also in 1970, led Sohn *et al.*[33,41] to support this conclusion and no data, spectroscopic or otherwise, have since been produced to refute it.

From these considerations and the accumulated experimental evidence, the red transition at ~16 200 cm^{-1} can be confidently assigned to the $^2E_{1u} \leftarrow {}^2E_{2g}$ LMCT transition involving the excitation of an electron from the $1e_{1u}$ orbital, localised mainly on the cp ring system, to the partially occupied $1e_{2g}$ orbital, localised mainly on the metal (see Figure 7.1)

7.1.3 Assignment of Structure in the Absorption Spectrum

Although solution absorption spectra of the $^2E_{1u} \leftarrow {}^2E_{2g}$ LMCT transition of ferricenium salts are broad and almost featureless,[33] Sohn *et al.* observed substantial structure in the 4.2-K spectra of various ferricenium and substituted ferricenium[33] salts as single crystals,[48] in KBr pellets[33,48] and nujol mulls.[48]

For [Fe(*n*-Bu-cp)(cp)]PF_6, [Fe(*n*-Bu-cp)$_2$]PF_6, and [Fe(cp)$_2$]PF_6 in KBr pellets and [Fe(cp)$_2$](CCl_2CO_2H)$_2$(CCl_3CO_2) single crystals[33,48] they observed an apparent doubling of structure, which they explained by proposing that, as well as the ground state, the excited state is also split by a low-symmetry perturbation. This would allow progressions built on two origins $A(1)$ and $A(2)$, which, respectively, represent the transition from the lowest SO-CF level of the ground state to each of two SO-CF levels in the excited state. The magnitude of the excited-state distortion (and therefore the splitting of the levels) varied with the environment (counter-ion and solvent) and ring substitution, but was ~240 cm^{-1} for [Fe(cp)$_2$]PF_6/KBr and ~180 cm^{-1} for [Fe(cp)$_2$](CCl_2CO_2H)$_2$(CCl_3CO_2).

For [Fe(cp)$_2$]BF_4 in a nujol mull, three origin bands were discerned.[48] These, as well as other unassigned peaks in [Fe(cp)$_2$]PF_6/KBr and [Fe(cp)$_2$](CCl_2CO_2H)$_2$(CCl_3CO_2) spectra, were attributed to interactions between the neighbouring ferricenium ions within the crystallites. Their argument was as follows – those crystals whose unit cell contains the greatest number of molecules should show the greatest degree of peak splitting. Using the available X-ray data, (the PF_6^- salt has four molecules per unit cell;[13] [Fe(cp)$_2$](CCl_2CO_2H)$_2$(CCl_3CO_2) has two,[48] no

X-ray data are available for the BF_4^- salt) the spectra of PF_6^- salt should be the most complicated, as observed.

To interpret the vibrational structure to the blue of the origins, Sohn *et al.*[48] used comparisons between the ($^1A_{1g}$) ground-state frequencies of ferrocene, obtained by various workers[7-9] from Raman data, with the excited-state ($^2E_{1u}$) frequencies of ferricenium (Table 7.2). For $[Fe(cp)_2](CCl_2CO_2H)_2(CCl_3CO_2)$, bands at 16 139, 16 218 and 16 708 cm^{-1} were respectively assigned to $A(2)+\nu_{16}$, $A(2)+\nu_{28}$ and $A(2)+2\nu_{28}$. The $\nu_{16} \sim 408$ cm^{-1} mode is an e_{1g} symmetric ring-tilt mode (the ligand planes remain parallel throughout the vibration) and has a ground-state ferrocene frequency of 390 cm^{-1}. $\nu_{28} \sim 490$ cm^{-1} is the e_{2g} in-plane ring distortion (591 cm^{-1} in ground-state ferrocene). In the $[Fe(cp)_2]BF_4$/nujol-mull spectrum, bands are also observed due to $\nu_{16} \sim 398$ cm^{-1} and $\nu_{28} \sim 471$ cm^{-1}.

Built on the origins of all of these ferricenium compounds (BF_4^-, $(CCl_2CO_2H)_2(CCl_3CO_2)^-$, and PF_6^-) are progressions in a mode of ~300 cm^{-1}, assigned to the ν_4 totally symmetric ring-metal-ring stretch (309 cm^{-1} in ferrocene). For the PF_6^- salt, ~300 cm^{-1} progressions also develop from bands $A(1)$+770 cm^{-1} and $A(2)$+770 cm^{-1}. Sohn *et al.*[48] postulated that the 770-cm^{-1} mode is ν_{27}, the e_{2g} out-of plane ring distortion which occurs at ~900 cm^{-1} in ferrocene.

Table 7.2: Excited-state frequencies (cm^{-1}), from optical spectroscopy, for various ferricenium salts.

symmetry and nature of vibrational mode	Ref.	a_{1g} symmetric Fe-cp	e_{1g} symmetric ring tilt	e_{2g} out-of-plane ring distortion	e_{2g} in plane ring distortion
standard notation		ν_4	ν_{16}	ν_{27}	ν_{28}
$[Fe(cp)_2]_{aq}$	7	303	388		
$[Fe(cp)_2]_{aq}$	8	311	393		600
$[Fe(cp)_2]_{aq}$	9	301	390	892	600
$[Fe(cp)_2^+]PF_6^-$	33,48	303	not obs	~770	not obs
$[Fe(cp)_2^+](CCl_2CO_2H)_2$	33,48	307	408		445 from $A(1)$
$-(CCl_3CO_2)^-$					487 from $A(2)$
$[Fe(cp)_2^+]BF_4^-$	48	304	398		471

Sohn *et al.*[48] used their results to comment of the nature of the $1e_{1u}$ molecular orbital. The overall band shape and the observation of both the $A(1)$ and $A(2)$ progressions of ~300 cm^{-1} indicate that the ground- and excited-state geometries are

very similar to each other in both $Fe(cp)_2PF_6$ and $Fe(cp)_2(CCl_2CO_2H)_2(CCl_3CO_2)$. The fact that the totally symmetric ring-metal-ring stretch has approximately the same value for both $^2E_{1u}$ ferricenium and $^1A_{1g}$ ferrocene attests to a close similarity in ring-metal bond strength. Since these states differ by the occupancy of the $1e_{1u}$ orbital, Sohn *et al.* concluded that the Fe $4p_x$ and $4p_y$ orbitals (e_{1u} symmetry in $\mathbf{D}_{5d}$) do not participate strongly in the ring-metal bonding. Additional support for the conclusion that the $1e_{1u}$ orbital is essentially localised on the rings is given by the fact that the frequency of the in-plane ring deformation (ν_{28}) is substantially reduced in $^2E_{1u}$ ferricenium compared to $^1A_{1g}$ ferrocene. This is consistent with the substantial intra-ring bonding character of the $1e_{1u}$ orbital and early qualitative MO calculations,[11] and suggests that later calculations overestimated the extent of mixing.

7.1.4 MCD Studies

Two groups have studied of the MCD of ferrocene[34,35] and its derivatives. However, since ferrocene has a non-degenerate ground state, not much information was gleaned from these studies. The cation, however, is another matter.

The MCD of the $^2E_{1u} \leftarrow {}^2E_{2g}$ transition of $Fe(cp)_2BF_4$ in a rigid matrix of polymethacrylic acid polymer was determined at 290 K and ~9 K by Rowe and McCaffery in 1973.[35] They pointed out that the low-temperature spectrum was best regarded for its qualitative value only, but that low-temperature structure, including the doubling of some bands, was in agreement with absorption data for the same salt in a LiCl glass.[41] They explained the presence of some negative MCD bands (opposite sign to that of the origin) by assuming a ground-state CF perturbation. $\mathscr{C}$-term expressions derived in the linear limit then showed that transition to the Kramers doublets in the $^2E_{1u}$ excited state should show MCD bands of opposite signs. They also calculated $\mathscr{B}$-term contributions to the spectrum but did not use them in their analysis.

7.1.5 The Jahn-Teller Effect in Ferricenium

Despite the fact that e_{1g} and e_{2g} modes are potentially JT active in the $^2E_{2g}$ and $^2E_{1u}$ states, this is rarely mentioned in the literature. Prins[21] discussed qualitatively the possibility of the JT effect contributing to the orbital reduction. Hendrickson *et al.*[42] mentioned a theoretical demonstration by a Russian group that a nearly isotropic g

matrix would result if the ferricenium ion were to experience an extremely large JT distortion (~13 times the SO interaction), but commented that experimental g values (Table 7.1) indicated that the low-symmetry distortion could not be anywhere near this large.

The only workers to consider the JT effect as more than a passing mention were Rai *et al.*[26,45,49] who, between 1969 and 1987, published a series of papers on JT interactions in metallocenes. One paper[45] concerned the predicted ESR behaviour of ferricenium, where (linear and quadratic) JT, CF and SO effects were treated on an equal footing. From the experimental values of $g_{\|} = 4.35$ and $g_{\perp} = 1.26$ for the PF_6 salt,[26] along with the SO parameter $a'_2/2 = 460$ cm^{-1} (corresponding to the free-ion value for Fe(III)), he calculated a ground-state JT stabilisation energy of $\varepsilon_{JT} = 235$ cm^{-1} and $\bar{\nu}_{JT} = 400$ cm^{-1} (for the e_{1g} ring-tilt mode of ferrocene) and orbital reduction factor due to covalency of $\kappa_{cov} = 1$. Since the zero-point energy is ~400 cm^{-1}, the first of these parameters does not represent a large JT effect. The value for κ_{cov} would indicate that covalency of the $1e_{2g}$ orbital is negligible, which he rationalised by saying that the metal e_{2g} orbitals lie in a plane parallel to the rings, making overlap with the ring orbitals insignificant.

7.2 Results

7.2.1 Matrix-isolation Data

Initial matrix-isolation experiments on $Fe(cp)_2^+$/Ar, using the refrigerator/electromagnet system with CCl_4 as the electron trap (Sections 6.2 and 6.3), resulted in fairly simple, structured spectra and a reciprocal MCD temperature dependence indicative of $\mathcal{C}$ terms. Examples of the spectra are shown in Figure 7.2. These spectra show very clear structure, but are less complicated and without the 'doubling' observed by other workers.[33,35,41] This suggests (as commented on above) that excited-state CF effects are less important in an Ar matrix than in crystals, glasses and solution. The MCD spectra clearly shows a negative band shifted by 490 cm^{-1} from, and of opposite sign to, the origin. Other negative bands at intervals of ~480 cm^{-1} are also discernible. Such bands were observed by McCaffery and Rowe,[35] but only as weak dimples superimposed on a congested and much stronger positive signal.

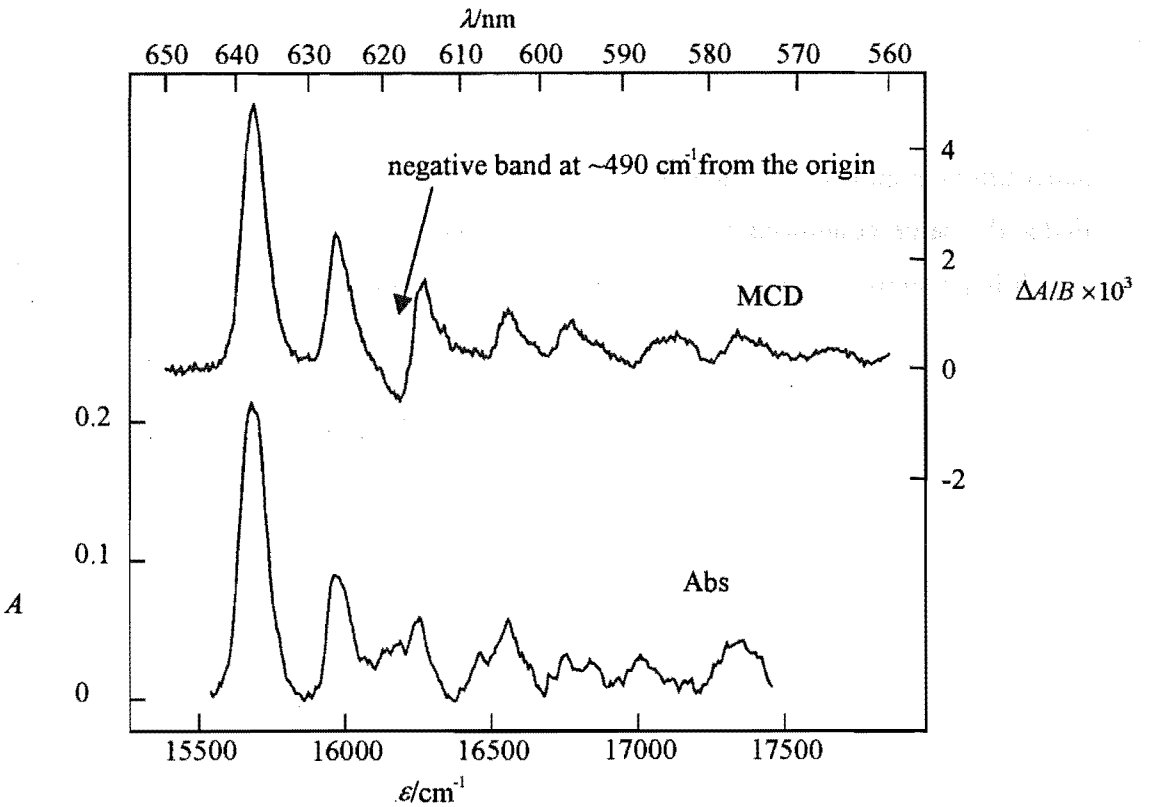

Figure 7.2: Spectra for the $^2E_{1u} \leftarrow {}^2E_{1g}$ transition of $Fe(cp)_2^+/Ar$ (with CCl_4 as the electron trap) obtained using the He refrigerator/electromagnet system. Top: MCD (per tesla) at B = 0.6 T and ~16 K. Bottom: Absorption spectrum at T ≈ 14 K.

To obtain more accurate and precise temperature and magnetic-field dependence data, the spectra were further investigated using the SM4 matrix-injection system (Section 6.2.3). The first few depositions gave spectra that exhibited broad lines without the well-resolved vibrational structure seen with the He refrigerator. This situation was only slightly improved by annealing.[iii] Eventually, by adjusting the mixing and flow rates of $Fe(cp)_2$, CCl_4 and Ar it was possible to get better spectra, although never as well-resolved as obtained with the He refrigerator.

For both experimental systems, the best spectra were obtained after depositing small amounts of material, which meant that the absorption was weak, and, without

---

[iii] Solid material left on the window, after the system had returned to room temperature and pressure, indicated that the matrices contained of substantial amounts of neutral ferrocene, which may have resulted in poor isolation of the species of interest. This is probably less of a problem with He refrigerator since there is a greater capability for cryopumping the deposition mixture, particularly *via* the radiation shield (see Figure 6.7).

the signal-processing advantages of the MCD, its signal-to-noise ratio was poor. Furthermore, the absorption spectrum was superimposed on a strongly sloped background, rising at an increasing rate towards the blue (see for example the top spectrum of Figure 7.3). The baseline spectrum (bottom spectrum, Figure 7.3), taken under the same conditions before matrix deposition, did not exhibit the same slope, which is presumably due to absorption by precursor molecules and other products of the discharge. This, combined with the undulations in the baseline spectrum, made it difficult to obtain objective estimates of the effective baseline for the band of interest. For these reasons the absorption spectra and the moments obtained from them are not highly reliable. Fortunately, the MCD didn't suffer from the same problem, because the species responsible for the sloping absorption baseline do not have strong MCD (they are probably diamagnetic and thus have no $\mathcal{C}$ terms).

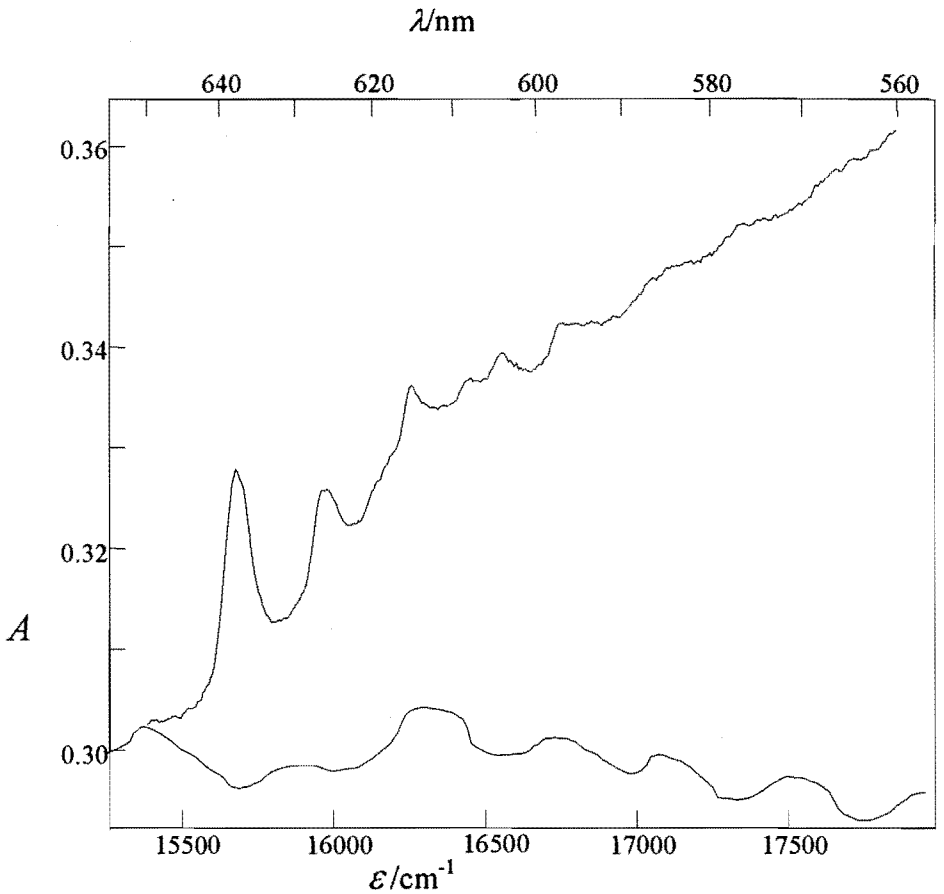

Figure 7.3: Absorption spectra for the $^2E_{1u} \leftarrow {}^2E_{1g}$ transition of $Fe(cp)_2^+/Ar$ (with CCl_4 as the electron trap) obtained using the He refrigerator/electromagnet system at $T \approx 16$ K. The upper line is the same absorption spectrum as in Figure 7.2 before baselining. The lower line is the baseline obtained in the absence of the sample.

Figure 7.4 shows the temperature dependence of the MCD obtained with the SM4. As the temperature decreases the intensity increases, as expected for $\mathcal{C}$ terms. The absorption was not temperature or magnetic-field dependent over the ranges investigated (1.4–12 K and 0–5 T), and the spectrum shown is the average over all temperatures and magnetic field strengths. It is truncated at a higher wavenumber because of the baselining uncertainties outlined above. Although the structure is not nearly as well resolved as in Figure 7.4, the negative MCD band is still evident as a trough marked by an arrow and shifted by ~500 cm^{-1} from the origin.

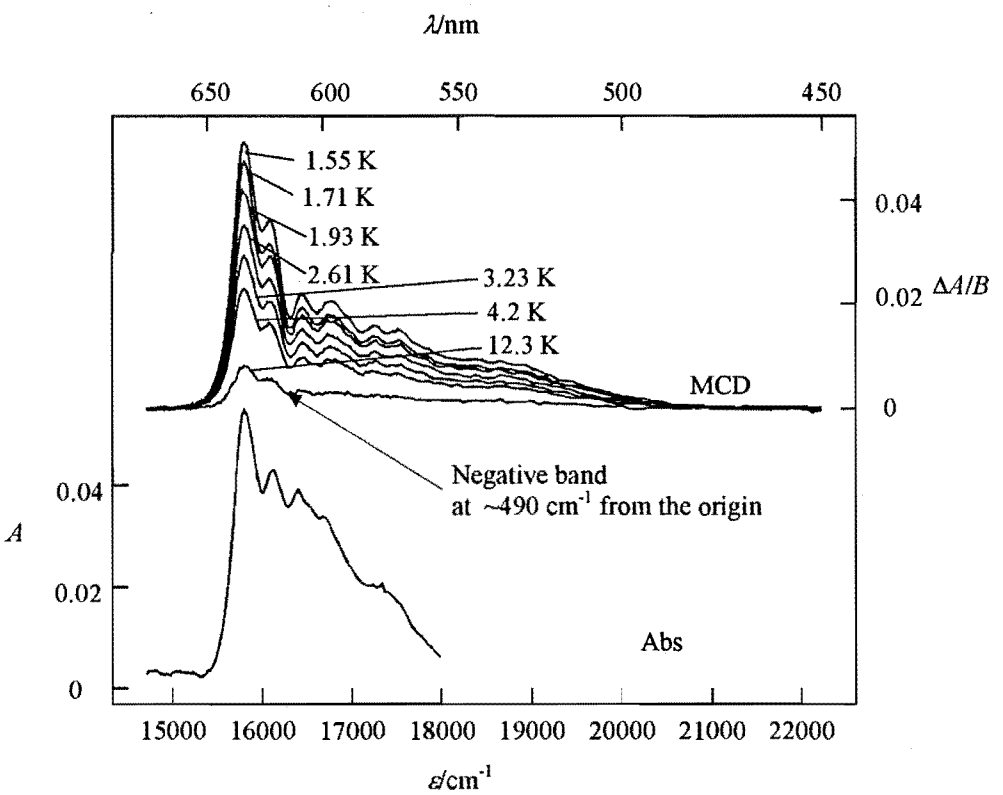

Figure 7.4: Spectra for the $^2E_{1u} \leftarrow {}^2E_{1g}$ transition of $Fe(cp)_2^+/Ar$ (with CCl_4 as the electron trap) obtained using the SM4/matrix-injection system. Top: MCD at various temperature and B = 1 T. Bottom: absorption averaged over all temperatures and magnetic field strengths.

Zeroth MCD and absorption moments ($\mathbf{M}_0$ and $\mathbf{A}_0$) of the experimental spectra were determined over the whole transition envelope by using the computer program MOMENT. In Figure 7.5 $\mathbf{M}_0$ is plotted as a function of $\mu_B B$ at various temperatures. The data show the saturation behaviour expected of $\mathcal{C}$ terms (Section 4.6), with a general decrease of intensity with increasing in temperature. In Figure 7.6 $\mathbf{M}_0$ is plotted against $\mu_B B/kT$ and it is seen that all data fall (within experimental error) on the same curve, irrespective of the temperature at which they were measured. This

immediately indicates that the MCD is strongly dominated by $\mathcal{C}$ terms and that $\mathcal{B}$ terms are insignificant in comparison.

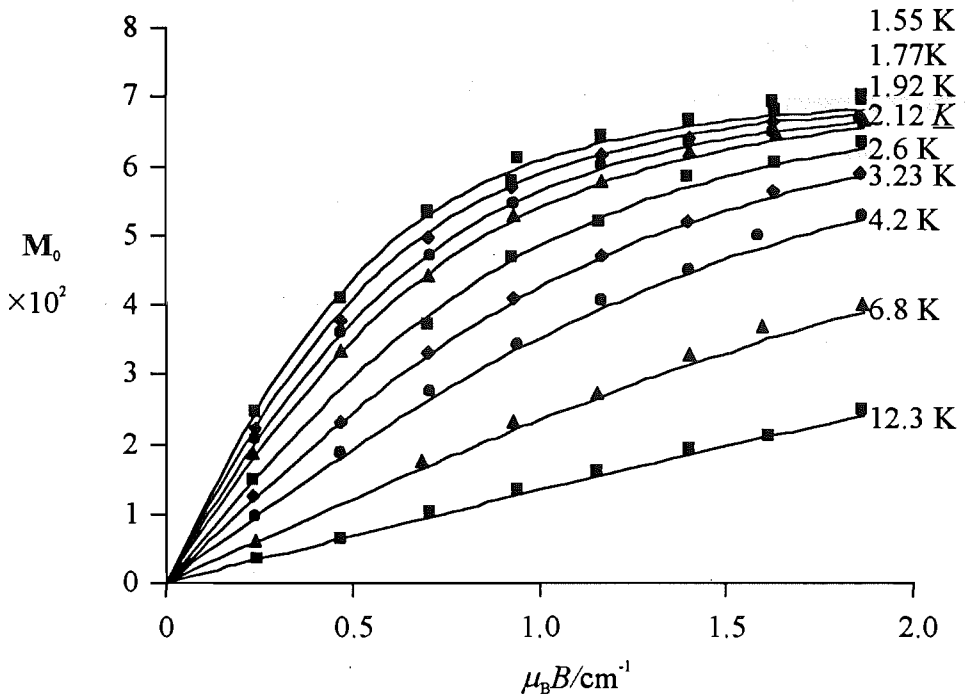

Figure 7.5: M_0 for the $^2E_{1u} \leftarrow {}^2E_{1g}$ transition of $Fe(cp)_2^+$/Ar, obtained using the SM4/matrix-injection system, as a function of $\mu_B B$ at various temperatures. The solid points show the experimental data, while the curve is the fitted function (Section 7.4.3).

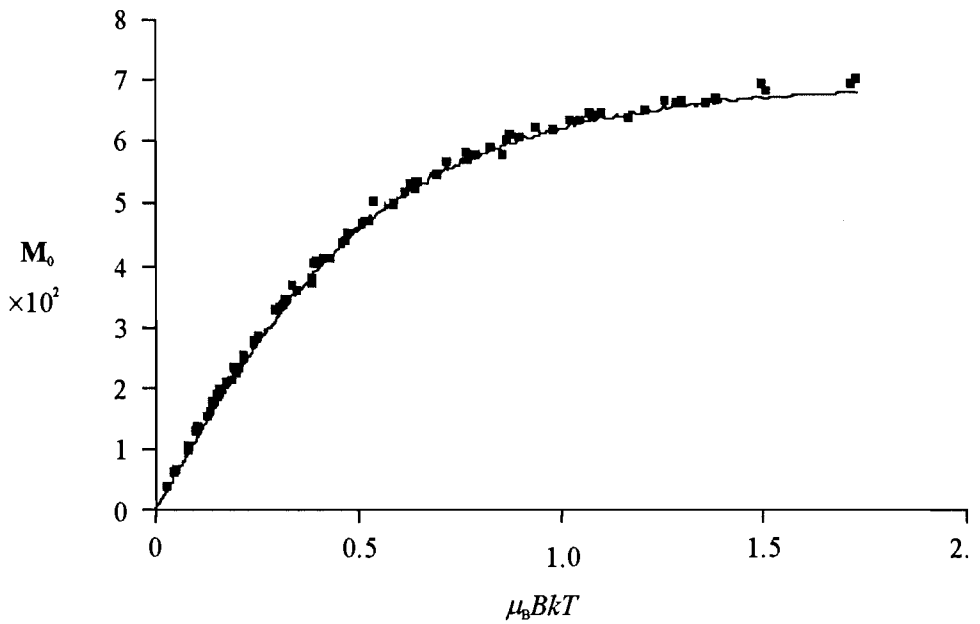

Figure 7.6: M_0 for the $^2E_{1u} \leftarrow {}^2E_{1g}$ transition of $Fe(cp)_2^+$/Ar, obtained using the SM4/matrix-injection system, as a function of $\mu_B B/kT$ for all temperatures. The solid points show the experimental data, while the curve is the fitted function (Section 1.3.3).

7.2.2 Solution Data

The temperature dependence of the MCD and absorption spectra of $Fe(cp)_2^+$ in liquid CH_2Cl_2 solution was investigated over the temperature range 180–280 K, restricted by the freezing point of the solvent. As can be seen from Figure 7.7 the spectra are not nearly as well resolved as those for the matrix-isolated samples. In particular, any signs of the negative band have been almost completely washed out, although the absorption and MCD profiles are different, which would suggest that the negative bands remain but are hidden.

The spectra are very similar to those obtained by Rowe and McCaffrey.[35] The increase in intensity of the absorption with decreasing temperature has previously been seen by others,[33,41] who explained it as in terms of an increase in population at 77 K of the lower SO-CF level.

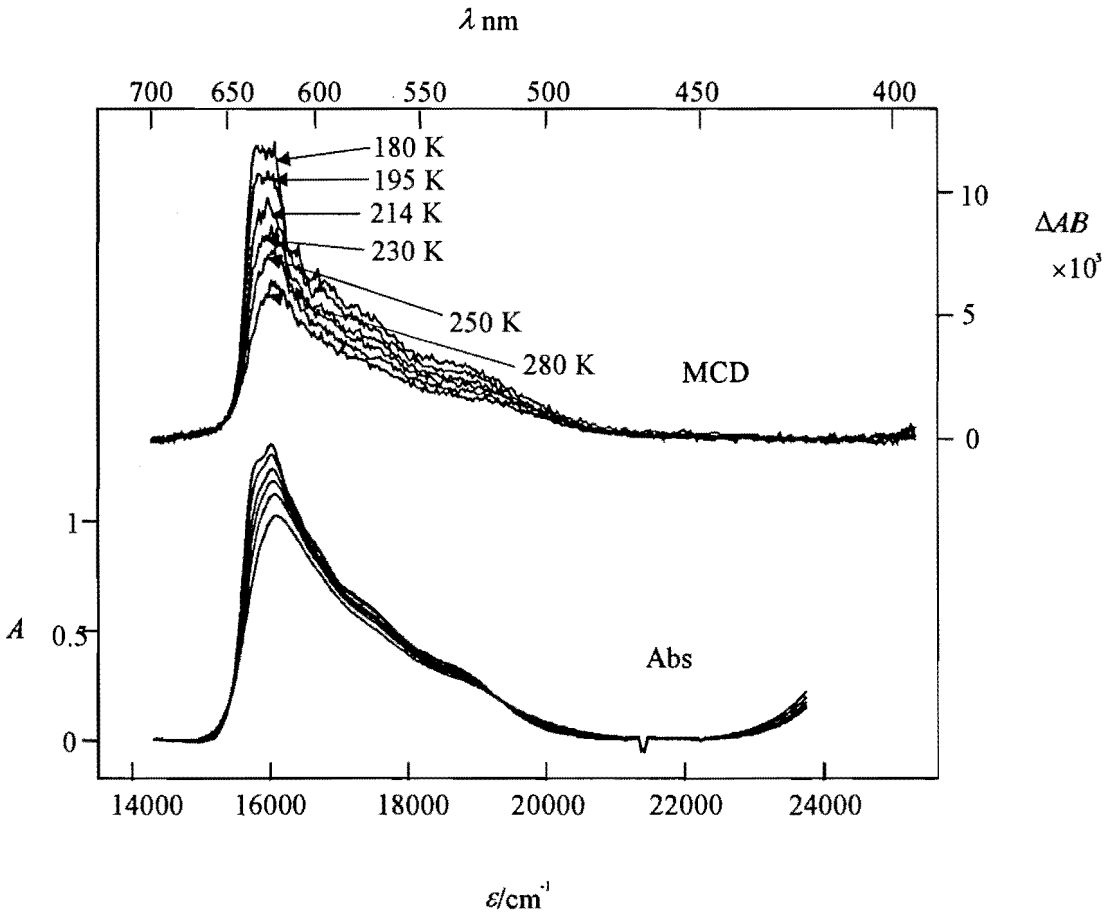

Figure 7.7: Spectra for the $^2E_{1u} \leftarrow {}^2E_{1g}$ transition of $Fe(cp)_2BF_4$ in CH_2Cl_2 solution obtained using the CF1204/electromagnet system at various temperatures. Top: MCD (per tesla) at B = 0.6 T. Bottom: absorption.

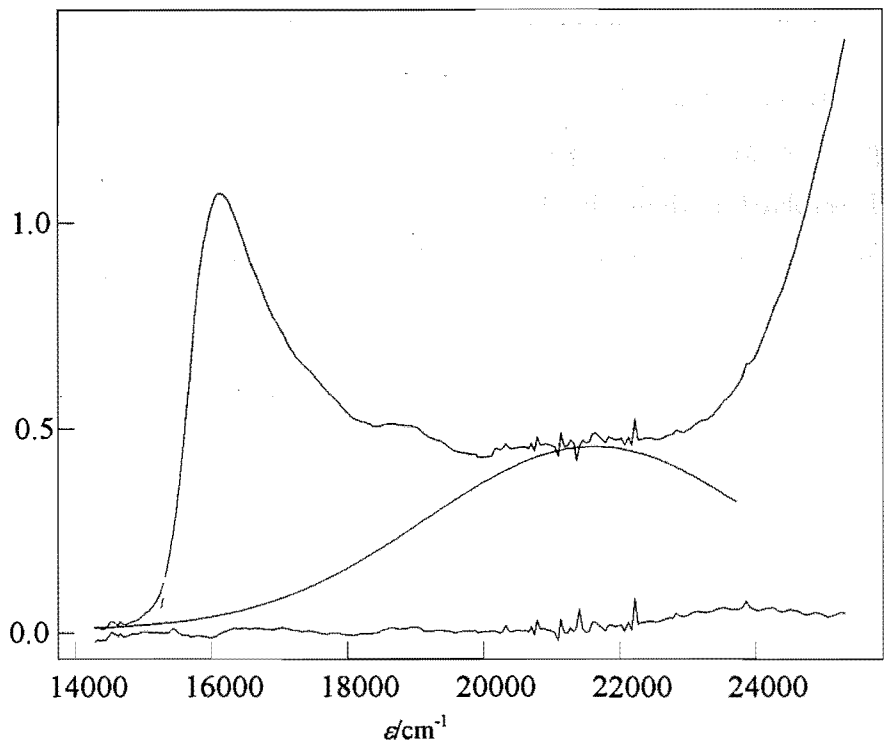

Figure 7.8: Absorption spectra for the $^2E_{1u} \leftarrow {}^2E_{1g}$ transition of $Fe(cp)_2BF_4$ in CH_2Cl_2 solution obtained using the CF1204/electromagnet system at various temperatures. The top curve is an spectrum before baselining. The bottom curve was obtained under the same conditions, but with the sample absent. The middle spectrum was generated artificially to remove a 'hump' in the spectrum due to another transtion.

The moments $\mathbf{M}_0$ and $\mathbf{A}_0$ for three different runs with different samples were determined over the envelope of the transition and their ratio is plotted in Figure 7.9 as a function of $\mu_B B/kT$. The plots are linear since the low field (~0.6 T) and relatively high temperatures used for these runs mean that conditions are well within the linear limit. The slopes of the three runs are very similar but intercepts are not – again this suggests that there are problems with baselining the absorption (Figure 7.9), In particular there is a 'hump' in the spectrum due to a nearby intense ferrocene absorption band. This was removed artificially by generating the baseline spectrum shown as the middle curve in Figure 7.8. Obviously this procedure is quite subjective and that data therefore need to be treated with caution.

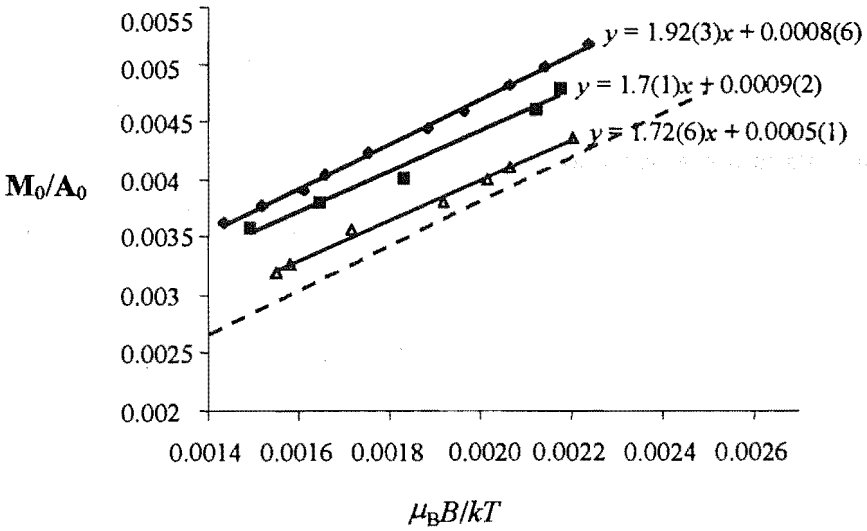

Figure 7.9: M_0/A_0 for the $^2E_{1u} \leftarrow {}^2E_{1g}$ transition of $Fe(cp)_2BF_4$ in CH_2Cl_2 solution (three samples) obtained using the CF1204/electromagnet system as a function of $\mu_B B/kT$. The points show the experimental data and the full, black lines are linear fits to the data, with the best-fit equations indicated. The broken grey line is the extrapolation of the function fitted to the matrix-isolation data shown in Figure 7.4 and obtained according to equation (7.74).

7.3 Theoretical Aspects of Data Analysis

As discussed in Section 7.1.1, the symmetry of ferricenium is known to vary between $\mathbf{D}_{5h}$ and $\mathbf{D}_{5d}$ according to the environment of the radical. Since both are supergroups of $\mathbf{D}_5$, the problem could be treated as the lower-symmetry point group, with the addition of u/g or '/" according to the rules given in the footnotes to Table 2.1. This would confer the advantage that it allows twists about the z axis, which reduce the symmetry to $\mathbf{D}_5$ but don't lower any degeneracies. However the analysis in this chapter assumes $\mathbf{D}_{5d}$ symmetry so as to be in accord with most of the literature on the radical.[21,36,45,48]

As discussed in Section 7.1.2, previous studies on the electronic spectra of ferricenium have lead to the assignment of the band peaking at around 625 nm (16 200 cm^{-1}) to the LMCT transition $^2E_1 \leftarrow {}^2E_{2g}$. Since the both initial and final terms of this transition are degenerate, one might anticipate the MCD to be made up of contributions from all three types of Faraday terms. However the dispersion and the temperature dependence of the spectra indicated that $\mathscr{C}$ terms dominate.

As covered in Chapters 3 and 5, ^{2}E terms are susceptible to SO, JT and Zeeman effects. As will be shown below they are also susceptible to CF effects. The parameters used to quantify these include SO coupling constants, CF splitting parameters, orbital reduction factors, *g* values, *etc.* The extraction of such parameters from experimental data is not always straightforward, and it is normally necessary to assume the value of some constants. In the case of ferricenium, these include SO parameters and orbital angular momenta for the metal ion and cp ring orbitals, as well as integrals for the overlap of these orbitals.

7.3.1 Molecular Orbitals and Orbital Angular Momenta

The free-ion orbital angular momenta of the metal are easily determined, but another important parameter is the effective orbital angular momentum l_π, of the π electron system on the cp rings. In determining a value of κ_{cov}, the contribution to orbital reduction due to covalency, Maki and Berry[37] and Prins[21] assumed that l_π and $S_{e_{2g}}$ (the overlap between metal and π-cp e_{2g} orbital) were equal to zero (so $\kappa_{cov} \approx |c_d|^2$). Their justification was that the orbital angular momentum of the ligand would be severely quenched by symmetry-lowering effects, and that MO calculations had indicated that the $1e_{2g}$ orbital is mostly metal. These approximations are not automatically assumed in this thesis. Instead, a value is calculated for l_π in Section 1.2.1 using simple MO theory, as suggested by Bishop and Dingle.[50] As noted by these authors "the results are subject to the same limitations as the theory, (but) ... sufficient qualitative information is obtained to be of use to the spectroscopist."

Cyclopentadienyl

In this section the π MOs of cyclopentadienyl are constructed from linear combinations of the p_z atomic orbitals (AOs) of the five carbon atoms that make up the molecule. The ring reference frame (*x*, *y*, *z*) is defined in Figure 7.10, with the origin (denoted *o*) at the centre of symmetry, the *z* direction coincident with the five-fold symmetry axis and the *x* passing through one of the carbon atoms.

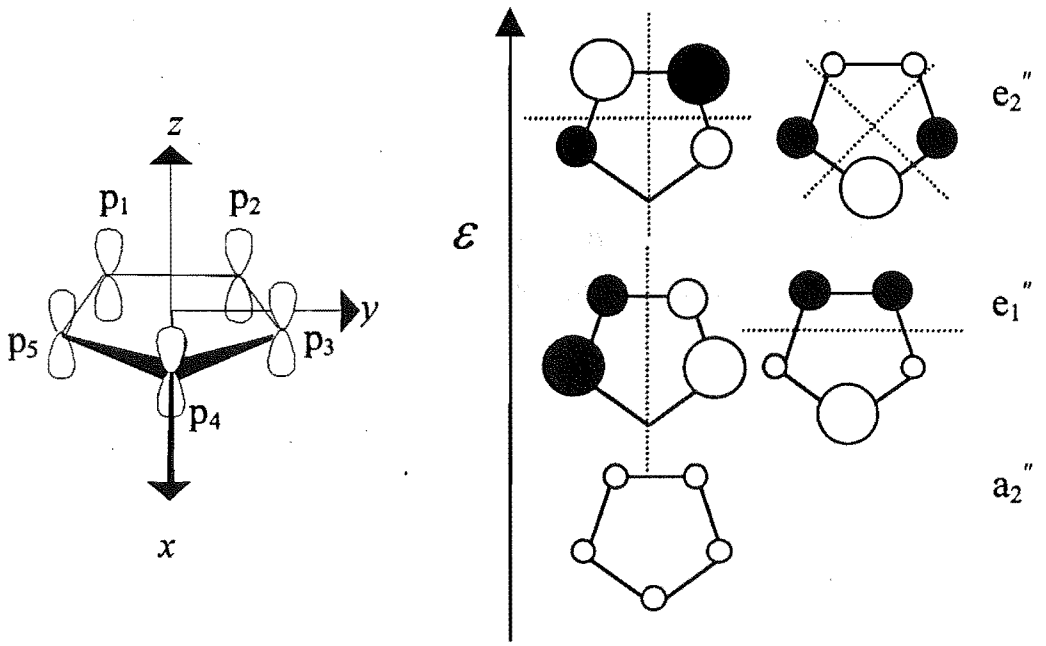

Figure 7.10: Molecular coordinate system (left) and qualitative MO energy-level diagram (right) for cyclopentadienyl ($\mathbf{D}_{5h}$ symmetry). The views on the right are down the molecular z axis. Circles indicate the top lobe of the p_z orbitals with colours indicating relative (+ or –) phases. The sizes of the circles correspond qualitatively to the squares of the coefficients in matrix (7.1).

The appropriate linear combinations of p-orbitals are determined, using the projection-operator method of Section 2.1.1, as those which transform as irreps of the point group, $\mathbf{D}_{5h}$. The transformation matrix, using Mulliken notation and the $\mathbf{D}_{5h} \supset \mathbf{D}_5 \supset \mathbf{C}_2$ chain, is

	$\lvert p_1\rangle$	$\lvert p_2\rangle$	$\lvert p_3\rangle$	$\lvert p_4\rangle$	$\lvert p_6\rangle$
$\langle a_2'' z \rvert$	0.4472	0.4472	0.4472	0.4472	0.4472
$\langle e_1'' x \rvert$	0.6325	0.1954	−0.5117	−0.5117	0.1954
$\langle e_1'' y \rvert$	0.0000	0.6015	0.3718	−0.3718	0.6015
$\langle e_2'' \varepsilon \rvert$	0.6325	−0.5117	0.1954	0.1954	−0.5117
$\langle e_2'' \zeta \rvert$	0.0000	0.3718	0.6015	0.6015	0.3718

(7.1)

where $\varepsilon \sim (x^2 - y^2)$ and $\zeta \sim xy$. These orbitals are represented pictorially to the right of Figure 7.10

The components of orbital angular momentum about the symmetry centre are determined according to the method outlined in Section 3.3.2. There are two types of

two-centre contributions, those due to nearest-neighbour atoms (1,2 interactions) and to next-nearest-neighbour atoms (1,3 interactions). From crystallographic data[6,13] (distances in Bohr radii)

$$D_{o1} = 2.283a_0 \qquad R_{12} = 2.684a_0, \qquad \gamma_{o12} = 54°$$
$$R_{13} = 4.343a_0, \qquad \gamma_{o13} = 18°$$

Using equation (3.59) and the shielding constant k =1.62 for carbon,[51,52] the 1,2 and 1,3 contributions are

$$l_{12} \equiv \langle p_2|l_z^o|p_1\rangle = -0.392i\hbar \tag{7.2}$$

$$l_{13} \equiv \langle p_3|l_z^o|p_1\rangle = -0.035i\hbar \tag{7.3}$$

The angular momentum matrix in the p-orbital basis is (in units of $\hbar$)

l_z^0	$\|p_1\rangle$	$\|p_2\rangle$	$\|p_3\rangle$	$\|p_4\rangle$	$\|p_5\rangle$
$\langle p_1\|$	0	$-0.392i$	$-0.035i$	$0.035i$	$0.392i$
$\langle p_2\|$	$0.392i$	0	$-0.392i$	$-0.035i$	$0.035i$
$\langle p_3\|$	$0.035i$	$0.392i$	0	$-0.392i$	$-0.035i$
$\langle p_4\|$	$-0.035i$	$0.035i$	$0.392i$	0	$-0.392i$
$\langle p_5\|$	$-0.392i$	$-0.035i$	$0.035i$	$0.392i$	0

(7.4)

Transforming into the molecular basis using the similarity transformation defined by matrix (7.1) brings the orbital angular momentum into block diagonal form, according to symmetry, with non-zero matrix elements

$$\langle e_1'' x|l_z^o|e_1'' y\rangle = -\langle e_1'' y|l_z^o|e_1'' x\rangle = -0.79i\hbar \tag{7.5}$$

$$\langle e_2''\varepsilon|l_z^o|e_2''\zeta\rangle = -\langle e_2''\zeta|l_z^o|e_2''\varepsilon\rangle = -0.39i\hbar \tag{7.6}$$

Finally, transforming into the spherical ($\mathbf{D}_{5h} \supset \mathbf{D}_5 \supset \mathbf{C}_5$) basis using the relationships[iv]

$$|e_1'' \pm 1\rangle = \mp\frac{1}{\sqrt{2}}(|e_1'' x\rangle \pm i|e_1'' y\rangle \tag{7.7}$$

$$|e_2'' \pm 2\rangle = \frac{1}{\sqrt{2}}(|e_2'' \varepsilon\rangle \pm i|e_2'' \zeta\rangle \tag{7.8}$$

gives

$$\langle e_1'' \pm 1|\hat{l}_z^o|e_1'' \pm 1\rangle = \pm 0.79\hbar \tag{7.9}$$

$$\langle e_2'' \pm 2|\hat{l}_z^o|e_2'' \pm 2\rangle = \pm 0.39\hbar \tag{7.10}$$

Biscyclopentadienyl

To determine the MOs that the two cyclopentadienyl rings contribute in ferricenium, it is useful to consider the hypothetical molecule biscyclopentadienyl (referred to elsewhere as 'nullocene'[53,v]), in which the two rings are parallel but staggered, giving overall $\mathbf{D}_{5d}$ symmetry. Three reference frames are now required – one for the molecule as a whole and one for each cp ring – as shown in Figure 7.11

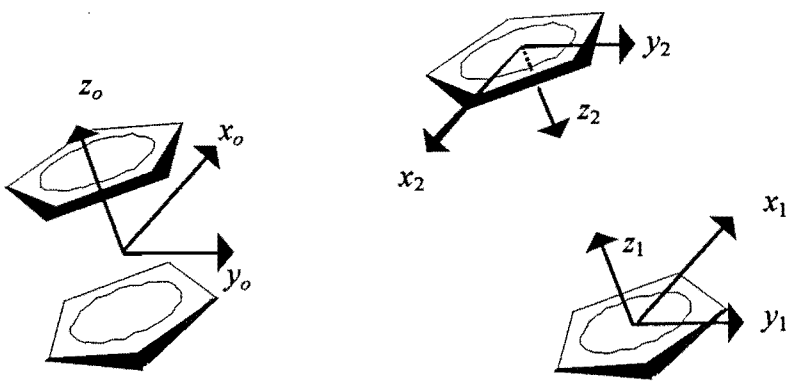

Figure 7.11: Molecular (left) and ring-fixed (right) coordinate systems for biscyclopentadiene.

[iv] The coefficients are determined so that the phases are the same as the corresponding spherical harmonics.

[v] Nullocene has been hypothesised as a metastable intermediate formed when cyclopentadienyl radicals are allowed to dimerise at low temperatures in a rare-gas matrix.[53]

The MOs of biscyclopentadiene are linear combinations of the two sets of $\mathbf{D}_{5h}$ ring orbitals chosen to form bases for the irreps of the point group $\mathbf{D}_{5d}$. Using the method of projection operators, the linear combinations, in matrix form, are

	$\lvert a_2'' z\rangle_1$	$\lvert a_2'' z\rangle_2$	$\lvert e_1'' x\rangle_1$	$\lvert e_1'' x\rangle_2$	$\lvert e_1'' y\rangle_1$	$\lvert e_1'' y\rangle_2$	$\lvert e_2'' \varepsilon\rangle_1$	$\lvert e_2'' \varepsilon\rangle_2$	$\lvert e_2'' \zeta\rangle_1$	$\lvert e_2'' \zeta\rangle_2$
$\langle a_{1g} z^2 \rvert$	$1/\sqrt{2}$	$1/\sqrt{2}$	0	0	0	0	0	0	0	0
$\langle a_{2u} z \rvert$	$1/\sqrt{2}$	$-1/\sqrt{2}$	0	0	0	0	0	0	0	0
$\langle e_{1g} xz \rvert$	0	0	$1/\sqrt{2}$	$1/\sqrt{2}$	0	0	0	0	0	0
$\langle e_{1g} yz \rvert$	0	0	0	0	$1/\sqrt{2}$	$-1/\sqrt{2}$	0	0	0	0
$\langle e_{1u} x \rvert$	0	0	$1/\sqrt{2}$	$-1/\sqrt{2}$	0	0	0	0	0	0
$\langle e_{1u} y \rvert$	0	0	0	0	$1/\sqrt{2}$	$1/\sqrt{2}$	0	0	0	0
$\langle e_{2g} \varepsilon \rvert$	0	0	0	0	0	0	$1/\sqrt{2}$	$1/\sqrt{2}$	0	0
$\langle e_{2g} \zeta \rvert$	0	0	0	0	0	0	0	0	$1/\sqrt{2}$	$-1/\sqrt{2}$
$\langle e_{2u} \alpha \rvert$	0	0	0	0	0	0	$1/\sqrt{2}$	$-1/\sqrt{2}$	0	0
$\langle e_{2u} \beta \rvert$	0	0	0	0	0	0	0	0	$1/\sqrt{2}$	$1/\sqrt{2}$

(7.11)

where $\alpha \sim z(x^2-y^2)$ and $\beta \sim zxy$.

Assuming that overlap between orbitals on different rings is unimportant, their orbital angular momentum matrix elements can be calculated using equations (7.5) and (7.6). The resulting matrix is then transformed into block diagonal form. Using,

$$|e_{1g} \pm 1\rangle = \mp\frac{1}{\sqrt{2}}(|e_{1g}\, xz\rangle \pm i|e_{1g}\, yz\rangle \tag{7.12}$$

$$|e_{1u} \pm 1\rangle = \mp\frac{1}{\sqrt{2}}(|e_{1u}\, x\rangle \pm i|e_{1u}\, z\rangle \tag{7.13}$$

$$|e_{2g} \pm 2\rangle = \frac{1}{\sqrt{2}}(|e_{2g}\, \varepsilon\rangle \pm i|e_{2g}\, \zeta\rangle \tag{7.14}$$

$$|e_{2u} \pm 2\rangle = \frac{1}{\sqrt{2}}(|e_{2u}\, \alpha\rangle \pm i|e_{2u}\, \beta\rangle \tag{7.15}$$

the non-zero matrix elements in the spherical basis are

$$\langle e_{1g} \pm 1|l_z|e_{1g} \pm 1\rangle = \pm i\langle e_{2g}\, \varepsilon|l_z|e_{2g}\, \zeta\rangle = \mp 0.787\hbar \tag{7.16}$$

$$\langle e_{1u} \pm 1|l_z|e_{1u} \pm 1\rangle = \pm i\langle e_{1u}\, x|l_z|e_{1u}\, y\rangle = \mp 0.787\hbar \tag{7.17}$$

$$\langle e_{2g}\ \pm 2|l_z|e_{2g}\ \pm 2\rangle = \pm i\langle e_{2g}\ \varepsilon|l_z|e_{2g}\ \zeta\rangle = \pm 0.394\hbar \tag{7.18}$$

$$\langle e_{2u}\ \pm 2|l_z|e_{2u}\ \pm 2\rangle = \pm i\langle e_{2u}\ \alpha|l_z|e_{2u}\ \beta\rangle = \pm 0.394\hbar \tag{7.19}$$

Ferricenium

In the point group $\mathbf{D}_{5d}$, the transformation properties of the metal d orbitals are

$$\Gamma_d = a_{1g} \oplus e_{1g} \oplus e_{2g}$$

The e_{1g} ($d_{\pm 1}$) and e_{2g} ($d_{\pm 2}$) orbitals can mix with the ligand π orbitals of the same symmetry, as indicated by Figure 7.1, to form MOs of the complex ion. Of these, only the $1e_{2g}$ bonding orbitals are involved in the excitation of interest ($1e_{2g} \leftarrow 1e_{1u}$). In the $\mathbf{D}_{5d} \supset \mathbf{D}_5 \supset \mathbf{C}_5$ basis, they can be represented by

$$|1e_{2g}\ \pm 2\rangle = c_d|e_{2g}{}^d\ \pm 2\rangle + c_\pi|e_{2g}{}^\pi\ \pm 2\rangle \tag{7.20}$$

The mixing coefficients c_d and c_π pertain, respectively, to the metal 3d orbitals and $(cp)_2$ π orbitals. They are related by the requirement

$$|c_d|^2 + |c_\pi|^2 + 2c_d c_\pi S_{e_{2g}} = 1 \tag{7.21}$$

where

$$S_{e_{2g}} = \langle e_{2g}{}^d\ \pm 2|e_{2g}{}^\pi\ \pm 2\rangle \tag{7.22}$$

is an overlap integral. Equation (7.21) is that for an ellipse with major and minor radii of lengths $1/(2 \pm S_{e_{2g}})^{1/2}$. Since the $1e_{2g}$ orbitals are principally of metal-ion parentage, the limit of weak covalent mixing is $c_d = 1$ and $c_\pi = 0$; the strong-mixing limit would be $c_d = c_\pi \lesssim 1/\sqrt{2}$.

In the absence of covalency ($c_d = 1$, $c_\pi = 0$), the orbital angular momentum of the $1e_{2g}$ orbitals would be determined entirely by the metal $e_{2g}{}^d$ ($d_{\pm 2}$) orbitals, for which (in units of $\hbar$)

$$\langle e_{2g}{}^{d} \pm 2|l_z|e_{2g}{}^{d} \pm 2\rangle = \langle d \pm 2|l_z|d \pm 2\rangle = \pm 2 \tag{7.23}$$

But in the presence of covalent interactions

$$\langle 1e_{2g} \pm 2|l_z|1e_{2g} \pm 2\rangle = \pm[2|c_d|^2 + l_\pi|c_\pi|^2 + S_{e_{2g}} c_d c_\pi(2 + l_\pi)] \tag{7.24}$$

where

$$l_\pi = \pm\langle e_{2g}{}^{\pi} \pm 2|l_z|e_{2g}{}^{\pi} \pm 2\rangle \approx 0.39 \tag{7.25}$$

the value being given by equation (7.18). Conventionally, the orbital angular momentum is expressed in terms of the free-metal-ion value times an empirical orbital reduction factor, κ_{cov}

$$\langle 1e_{2g} \pm 2|l_z|1e_{2g} \pm 2\rangle = \kappa_{cov}\langle e_{2g}{}^{d} \pm 2|l_z|e_{2g}{}^{d} \pm 2\rangle = \pm 2\kappa_{cov} \tag{7.26}$$

Comparison of equations (7.26) and (7.24) gives

$$\kappa_{cov} = [(1 - l_\pi/2)(|c_d|^2 - |c_\pi|^2) + (1 + l_\pi/2)]/2 \tag{7.27}$$

The orbital reduction factor is taken to be a measure of the covalency of the metal-ligand bond. In the limit of very weak covalent mixing, $\kappa_{cov} = 1$. If $l_\pi = S_{e_{2g}} = 0$, as assumed by Maki and Berry[37] and Prins,[21] then $|c_\pi|^2 = (1 - |c_d|^2)$ and so $\kappa_{cov} \approx |c_d|^2$, with a strong-mixing (lower) limit of 0.5. However, with $l_\pi = 0.39\hbar$ (equation (7.25)) the strong-mixing limit is slightly higher at $(1+ l_\pi/2)/2 \approx 0.6$. The corresponding orbital g value is

$$g_2 = 2\langle e_{2g} \pm 2|l_z|e_{2g} \pm 2\rangle = 4\kappa_{cov} \tag{7.28}$$

7.3.2 Electronic States of Ferricenium

The initial and final electronic states of the $^2E_{1u} \leftarrow {}^2E_{2g}$ transition derive from $e_\lambda{}^3$-type configurations. The spin-orbit wavefunctions have the forms given by Table 3.5 and are explicitly listed, along with their SO and Zeeman energies, in Table 7.3.

Table 7.3: Anti-symmetrised three-electron spin-orbit wavefunctions for e_{2g}^3 and e_{1u}^3 configurations. The Zeeman energies given in the fourth column are those for a molecule oriented at angle θ with respect to the magnetic field B.

$\|\Gamma_\lambda^{n_e}\ ^{2S+1}\Gamma_\Lambda M_\Lambda \Sigma\rangle$	Normalised Slater determinant	ε_{SO}	$\varepsilon_{Zeeman}/\mu_B B$
$\|e_{2g}^3\ ^2E_{2g}\ 2\ 1/2\rangle$	$\|-2^+\ 2^-\ 2^+\rangle$	$-a'_2/2$	$(g_2 + g_e)\cos\theta/2$
$\|e_{2g}^3\ ^2E_{2g}\ -2\ -1/2\rangle$	$\|-2^-\ -2^+\ 2^-\rangle$	$-a'_2/2$	$-(g_2 + g_e)\cos\theta/2$
$\|e_{2g}^3\ ^2E_{2g}\ 2\ -1/2\rangle$	$\|-2^-\ 2^-\ 2^+\rangle$	$a'_2/2$	$(g_2 - g_e)\cos\theta/2$
$\|e_{2g}^3\ ^2E_{2g}\ -2\ 1/2\rangle$	$\|-2^-\ -2^+\ 2^+\rangle$	$a'_2/2$	$-(g_2 - g_e)\cos\theta/2$
$\|e_{1u}^3\ ^2E_{1u}\ 1\ 1/2\rangle$	$\|-1^+\ 1^-\ 1^+\rangle$	$a'_1/2$	$(g_1 + g_e)\cos\theta/2$
$\|e_{1u}^3\ ^2E_{1u}\ -1\ -1/2\rangle$	$\|-1^-\ -1^+\ 1^-\rangle$	$a'_1/2$	$-(g_1 + g_e)\cos\theta/2$
$\|e_{1u}^3\ ^2E_{1u}\ 1\ -1/2\rangle$	$\|-1^-\ 1^-\ 1^+\rangle$	$-a'_1/2$	$(g_1 - g_e)\cos\theta/2$
$\|e_{1u}^3\ ^2E_{1u}\ -1\ 1/2\rangle$	$\|-1^-\ -1^+\ 1^+\rangle$	$-a'_1/2$	$-(g_1 - g_e)\cos\theta/2$

Since the $1e_{1u}$ orbital is essentially a ligand π orbital then, following the discussion around equation (3.59), the SO splitting parameter, a'_2, for the $^2E_{1u}$ term should be small, a conjecture which is supported by the absence of any obvious splitting of the bands in Figure 7.4 and Figure 7.7. On the other hand, $1e_{2g}$ is principally of metal 3d parentage and can therefore be anticipated to have a much larger SO coupling coefficient. From equation (3.65)

$$a'_2 = 2\langle 1e_{2g}\ 2|\mathcal{H}_{so}|1e_{2g}\ 2\rangle = 2|c_d|^2\langle e_{2g}^{\ d}\ 2|\mathcal{H}_{so}|e_{2g}^{\ d}\ 2\rangle +$$

$$4c_d c_\pi\langle e_{2g}^{\ \pi}\ 2|\mathcal{H}_{so}|e_{2g}^{\ d}\ 2\rangle + 2|c_\pi|^2\langle e_{2g}^{\ \pi}\ 2|\mathcal{H}_{so}|e_{2g}^{\ \pi}\ 2\rangle \qquad (7.29)$$

where $\mathcal{H}_{so}$ was defined in Section 3.3.3.

The second and third terms of equation (7.29) comprise two-centre integrals, which were shown in Section 3.3.2 to be zero, and three-centre integrals (see equation (3.62)), which will be negligible due to the interatomic separation distances.[6] This

leaves the first term, the only important contribution to which involves orbital motion about the Fe nucleus. Thus,

$$a'_2 = 2\,|c_d|^2\,\zeta_{Fe;3d} \qquad (7.30)$$

where $\zeta_{Fe;3d}$ is the one-electron SO parameter for a 3d orbital of the Fe ion.

Equation (7.30) is the same as used by Prins[21] and Maki and Berry,[37] but whereas they ignored the ligand contributions and assumed $\kappa_{cov} = |c_d|^2$, the allowance here for orbital angular momentum of the ligand makes the relationship more complicated (equation (7.27)). Some earlier workers[21,37] used $\zeta_{Fe;3d}$ = 400 cm^{-1}, the value for Fe(II), because analyses[25,28] of the electron distribution in the ferrocene ground state gave a charge close to +1 on the Fe. Formally the iron is in the +3 oxidation state in ferricenium and so, in this work the Fe(III) value of ~460 cm^{-1} is used.[54]

7.3.3 Crystal-field Effects

As outlined in the introduction to this chapter, the results obtained for the ferricienium ion in solutions and crystals indicate substantial CF splittings of the $^2E_{1u}$ excited state term. The absence of obvious splittings in the data shown in Figure 7.2 and Figure 7.4 suggests that such splittings are not important for the excited states of the matrix-isolated radical. However, the possibility of such an effect in the ground state should be considered. For simplicity, CF effects are considered here separately from JT coupling, which is covered in Section 1.2.4.

For an external CF (due to the local environment, Section 6.3) to lower the degeneracy of a E_{2g} orbital level, it must transform as part of the symmetric square, $[E_{2g}^2]$ – that is as e_{1g} ($|1\ \pm1\rangle$ in Butler notation for $\mathbf{D}_{5d} \supset \mathbf{D}_5 \supset \mathbf{C}_5$) – which corresponds to an orthorhombic field. Denoting the CF operator by $V^1_{\pm1}$ (the superscript and subscripts representing the irrep and partner labels, respectively) the WET gives

$$\langle {}^2E_{2g}\ \pm2\ \Sigma|V^1_{\pm1}|{}^2E_{2g}\ \pm2\ \Sigma'\rangle = \frac{1}{\sqrt{2}}\langle {}^2E_{2g}\|V^1\|{}^2E_{2g}\rangle\delta_{\Sigma\Sigma'} \equiv V_{CF}/2 \qquad (7.31)$$

where V_{CF} is the CF interaction parameter ($V_{CF} = \delta$ in the notation of earlier workers). The Hamiltonian matrix for the electronic states of a $^2E_{2g}$ term simultaneously under the influence of SO coupling and a CF effect is

$\mathcal{H}_{SO} + \mathcal{H}_{CF}$	$\lvert^2E_{2g}\ -2\ -1/2\rangle$	$\lvert^2E_{2g}\ 2\ -1/2\rangle$	$\lvert^2E_{2g}\ 21/2\rangle$	$\lvert^2E_{2g}\ -21/2\rangle$
$\langle^2E_{2g}\ -2\ -1/2\rvert$	$-a_2'/2$	$V_{CF}/2$		
$\langle^2E_{2g}\ 2\ -1/2\rvert$	$V_{CF}/2$	$a_2'/2$		
$\langle^2E_{2g}\ 21/2\rvert$			$-a_2'/2$	$V_{CF}/2$
$\langle^2E_{2g}\ -21/2\rvert$			$V_{CF}/2$	$a_2'/2$

(7.32)

Clearly, the problem separates into two identical blocks, according to spin, diagonalisation of which gives the eigenvalues

$$\varepsilon^{\pm} = \pm\sqrt{(a'_2)^2 + (V_{CF})^2}/2 \tag{7.33}$$

So two doubly degenerate SO-CF levels are formed, separated by splitting

$$\Delta = \varepsilon^{+} - \varepsilon^{-} = \sqrt{(a'_2)^2 + (V_{CF})^2} \tag{7.34}$$

The corresponding SO-CF eigenfunctions, where the superscripts ± designate the upper and lower SO-CF levels, are

$$|^2E_{2g}^{+}\ 1/2\rangle = c_\beta|^2E_{2g}\ 2\ 1/2\rangle + c_\alpha|^2E_{2g}\ -2\ 1/2\rangle \tag{7.35}$$

$$|^2E_{2g}^{+}\ -1/2\rangle = c_\beta|^2E_{2g}\ -2\ -1/2\rangle + c_\alpha|^2E_{2g}\ 2\ -1/2\rangle \tag{7.36}$$

$$|^2E_{2g}^{-}\ 1/2\rangle = c_\alpha|^2E_{2g}\ 2\ 1/2\rangle - c_\beta|^2E_{2g}\ -2\ 1/2\rangle \tag{7.37}$$

$$|^2E_{2g}^{-}\ -1/2\rangle = c_\alpha|^2E_{2g}\ -2\ -1/2\rangle - c_\beta|^2E_{2g}\ 2\ -1/2\rangle \tag{7.38}$$

where

$$c_\alpha = V_{CF}/[(V_{CF})^2 + (\Delta - a'_2)^2]^{1/2} \tag{7.39}$$

$$c_\beta = (\Delta - a'_2)/[(V_{CF})^2 + (\Delta - a'_2)^2]^{1/2} \qquad (7.40)$$

These results are shown diagrammatically in Figure 7.12. In the limit of a very strong CF ($V_{CF} >> a'_2$), $|c_\beta|^2 \rightarrow 1/2$ and $|c_\alpha|^2 \rightarrow 1/2$. On the other hand, as $V_{CF} \rightarrow 0$, $c_\alpha \rightarrow 1$ and $c_\beta \rightarrow 0$. Some other useful relationships between these coefficients are

$$|c_\alpha|^2 + |c_\beta|^2 = 1 \qquad (7.41)$$

$$|c_\alpha|^2 - |c_\beta|^2 = a'_2/\Delta \equiv \kappa_{CF} \qquad (7.42)$$

$$2c_\alpha c_\beta = V_{CF}/\Delta \equiv \eta \qquad (7.43)$$

$$\eta^2 + (\kappa_{CF})^2 = 1 \qquad (7.44)$$

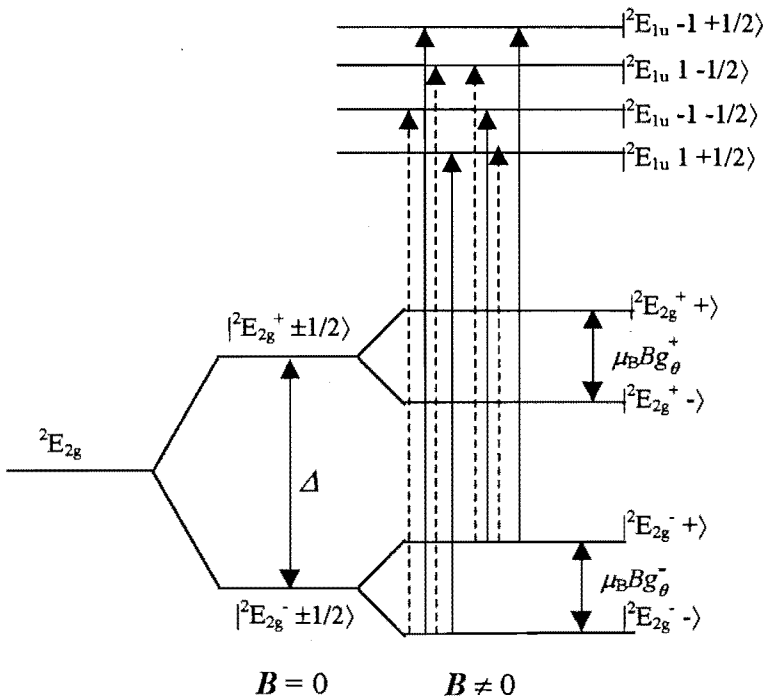

Figure 7.12: Energy level diagram for the SO-CF states of the ground $^2E_{2g}$ ground-state term of $Fe(cp)_2^+$ when the magnetic field is on and off. The dashed lines show *lcp* transitions and the solid lines *rcp* transitions.

It is useful at this point to determine expressions for $g_\parallel$ and $g_\perp$ in terms of g_2 (defined by equation (7.28)) for the two SO-CF levels. Since $g_\parallel$ pertains to the case where the magnetic field is along the molecular z axis, then

$$g_{\|}^{\pm} = 2\langle {}^2E_{2g}^{\pm}\ 1/2|L_z + g_e S_z|{}^2E_{2g}^{\pm}\ 1/2\rangle$$

$$= 2\{|c_\alpha|^2\langle {}^2E_{2g} \mp 2\ 1/2|L_z + g_e S_z|{}^2E_{2g} \mp 2\ 1/2\rangle + |c_\beta|^2\langle {}^2E_{2g} \pm 2\ 1/2|L_z + g_e S_z|{}^2E_{2g} \pm 2\ 1/2\rangle\}$$

$$= \mp(|c_\alpha|^2 - |c_\beta|^2)g_2 + g_e$$

$$= g_e \mp \kappa_{CF} g_2 \qquad (7.45)$$

The matrix elements in the second step are evaluated according to equation (3.74). From the final result, it can be seen that κ_{CF} acts as another orbital reduction factor. When combined with equation (7.25), in the absence of vibronic effects, the total orbital reduction is given by the product of κ_{CF} and κ_{cov}. But whereas κ_{cov} by itself can cause a maximum reduction of only 40 or 50%, κ_{CF} tends to zero in the strong CF limit and can therefore result in essentially complete quenching of the orbital angular momentum, leaving the spin-only value, g_e.

The value of $g_\perp$, corresponding to the case where the magnetic field is perpendicular to the z axis, is determined by the off-diagonal elements connecting states within the same SO-CF manifold. With the help of equation (3.75)

$$g_\perp = 2|\langle {}^2E_{2g}^{\pm}\ -1/2|L_x + g_e S_x|{}^2E_{2g}^{\pm}\ 1/2\rangle|$$

$$= 2c_\alpha c_\beta\{|\langle {}^2E_{2g}\ 2\ -1/2|L_x + g_e S_x|{}^2E_{2g}\ 2\ 1/2\rangle + \langle {}^2E_{2g}\ -2\ -1/2|L_x + g e S_x|{}^2E_{2g}\ -2\ 1/2\rangle|\}$$

$$= \eta g_e \qquad (7.46)$$

Notably, this is independent of the SO-CF level. Moreover, in the limit of a strong CF, η tends to unity and $g_\perp$ approaches the spin-only value.

There are also some important matrix elements between the SO-CF levels. A summary of all matrix elements, for the case where the magnetic field is along the laboratory Z axis, but makes an angle θ with the molecular z axis, is given in matrix (7.47). The Euler angle ψ is defined in Section 4.5.

$L_Z+g_eS_Z$	$\left\|{}^2E_{2g}^--1/2\right\rangle$	$\left\|{}^2E_{2g}^-+1/2\right\rangle$	$\left\|{}^2E_{2g}^+-1/2\right\rangle$	$\left\|{}^2E_{2g}^+-1/2\right\rangle$
$\left\langle{}^2E_{2g}^--1/2\right\|$	$-g_{\|\|}^-\cos\theta/2$	$-i\sin\theta e^{-i\psi}g_\perp/2$	$-(g_2/g_e)\cos\theta g_\perp/2$	$i\sin\theta e^{-i\psi}(\kappa_{CF}/\eta)g_\perp/2$
$\left\langle{}^2E_{2g}^-+1/2\right\|$	$i\sin\theta e^{i\psi}g_\perp/2$	$g_{\|\|}^-\cos\theta/2$	$-i\sin\theta e^{i\psi}(\kappa_{CF}/\eta)g_\perp/2$	$(g_2/g_e)g_\perp\cos\theta/2$
$\left\langle{}^2E_{2g}^+-1/2\right\|$	$-(g_2/g_e)\cos\theta g_\perp/2$	$i\sin\theta e^{-i\psi}(\kappa_{CF}/\eta)g_\perp/2$	$-g_{\|\|}^+\cos\theta/2$	$i\sin\theta e^{-i\psi}g_\perp/2$
$\left\langle{}^2E_{2g}^++1/2\right\|$	$-i\sin\theta e^{i\psi}(\kappa_{CF}/\eta)g_\perp/2$	$(g_2/g_e)\cos\theta g_\perp/2$	$-i\sin\theta e^{i\psi}g_\perp/2$	$g_{\|\|}^+\cos\theta/2$

(7.47)

The electronic Zeeman energies and states are obtained from the eigenvalues and eigenfunctions of $\mathcal{H}_{\text{Zeeman}}$, defined by equation (3.73). To obtain analytical expressions for these, use is made of the fact that the magnetic-field effects will be small compared to the SO-CF splitting. The first step is the used of degenerate perturbation theory to determine first-order expressions for the 2×2 diagonal submatrices of the form.

$\mathcal{H}_{\text{Zeeman}}/\mu_B B$	$\left\|{}^2E_{2g}^\mp-1/2\right\rangle$	$\left\|{}^2E_{2g}^\mp+1/2\right\rangle$
$\left\langle{}^2E_{2g}^\mp-1/2\right\|$	$-g_{\|\|}^\mp\cos\theta/2$	$\mp i\sin\theta e^{-i\psi}g_\perp/2$
$\left\langle{}^2E_{2g}^\mp+1/2\right\|$	$\pm i\sin\theta e^{i\psi}g_\perp/2$	$g_{\|\|}^\mp\cos\theta/2$

(7.48)

The effective g value under these conditions is[vi]

$$g_\theta^\pm \equiv [\cos^2\theta(g_{\|}^\pm)^2 + \sin^2\theta(g_\perp)^2]^{1/2} \tag{7.49}$$

The resulting eigenfunctions are

$$|{}^2E_{2g}^\pm +\rangle^0 = a_\theta^\pm|{}^2E_{2g}^\pm -1/2\rangle + b_\theta^\pm|{}^2E_{2g}^\pm 1/2\rangle \tag{7.50}$$

$$|{}^2E_{2g}^\pm -\rangle^0 = -a_\theta^\pm|{}^2E_{2g}^\pm 1/2\rangle + b_\theta^\pm|{}^2E_{2g}^\pm -1/2\rangle \tag{7.51}$$

where

$$|a_\theta^\pm|^2 = \sin^2\theta\, g_\perp{}^2/(2g_\theta^\pm(g_\theta^\pm + \cos\theta\, g_{\|}^\pm)) \tag{7.52}$$

[vi] Note that when $g_\perp = 0$, equation (7.49) reduces to the same form as equation (3.79), as anticipated in the discussion around that equation.

$$|b_\theta^\pm|^2 = (2\cos\theta g_\parallel^\pm (\cos\theta g_\parallel^\pm + g_\theta^\pm) + \sin^2\theta g_\perp{}^2)/(2g_\theta^\pm(g_\theta^\pm + \cos\theta g_\parallel^\pm) \quad (7.53)$$

$$|a_\theta^\pm|^2 + |b_\theta^\pm|^2 = 1 \quad (7.54)$$

and

$$|b_\theta^\pm|^2 - |a_\theta^\pm|^2 = \cos\theta g_\parallel^\pm/g_\theta^\pm \quad (7.55)$$

The results are shown diagrammatically in Figure 7.12. The corresponding first-order Zeeman energies are

$$\varepsilon_{\text{Zeeman}}({}^2E_{2g}^\pm +) = \mu_B B g_\theta^\pm \quad (7.56)$$

$$\varepsilon_{\text{Zeeman}}({}^2E_{2g}^\pm -) = -\mu_B B g_\theta^\pm \quad (7.57)$$

The remaining off-diagonals, which mix states from different SO-CF levels, can be treated by non-degenerate perturbation theory. They do not contribute to Zeeman splittings (they shift the two states within a SO-CF level by the same amount in the same direction), and hence do not contribute to $\mathcal{C}$ terms. However, as will be shown later, they do contribute to $\mathcal{B}$ terms. The wavefunctions corrected for these contributions are,

$$|{}^2E_{2g}^\pm +\rangle = |{}^2E_{2g}^\pm +\rangle^0 + |{}^2E_{2g}^\pm +\rangle^1 \quad (7.58)$$

$$|{}^2E_{2g}^\pm -\rangle = |{}^2E_{2g}^\pm -\rangle^0 + |{}^2E_{2g}^\pm -\rangle^1 \quad (7.59)$$

where

$$|{}^2E_{2g}^\pm +\rangle^1 = \frac{\pm\mu_B B g_\perp}{2\Delta}((\sin\theta\, b_\theta^\pm(\kappa_{CF}/\eta) - \cos\theta\, a_\theta^\pm g_2/g_e))|{}^2E_{2g}^\mp -1/2\rangle$$

$$+ (\sin\theta\, a_\theta^\pm(\kappa_{CF}/\eta) + \cos\theta\, b_\theta^\pm(g_2/g_e))|\,{}^2E_{2g}^\mp 1/2\rangle \quad (7.60)$$

$$|^2E^{\pm}_{2g} -\rangle^1 = \frac{\pm\mu_B B g_\perp}{2\Delta}((\sin\theta\, b^{\pm}_{\theta}(\kappa_{CF}/\eta) - \cos\theta\, a^{\pm}_{\theta} g_2/g_e))|^2E^{\mp}_{2g}\ 1/2\rangle$$

$$- (\sin\theta\, a^{\pm}_{\theta}(\kappa_{CF}/\eta) + \cos\theta\, b^{\pm}_{\theta}(g_2/g_e))|\,^2E^{\mp}_{2g}\ -1/2\rangle \qquad (7.61)$$

The transition $^2E_{1u} \leftarrow {}^2E_{2g}$ corresponds to $\Delta\Lambda = -1$. The non-zero transition moments between the basis states are therefore given by equation (3.84). Using molecule-based coordinates (Section 4.5), the transition moments, in terms of the SO basis, are

$$\langle^2E_{1u} \mp 1\ \Sigma|m_{\pm 1}|\,^2E_{2g} \mp 2\ \Sigma\rangle = \mathfrak{M}_{\pm 1} \qquad (7.62)$$

where the ± 1 subscripts are retained to keep the polarisation information. In the absence of evidence for CF splittings in the excited state, the $|^2E_{1u} \mp 1\ \Sigma\rangle$ basis states are retained for the $^2E_{1u}$ term. Later, this will be justified by applying the principle of spectroscopic stability (Appendix B).

Keeping terms up to first order, the intensity of a transition $|J\rangle \leftarrow |A\rangle$ induced by interactions involving the operator m_ρ is determined by

$$|\langle J|m_\rho|A\rangle|^2 = |\langle J|m_\rho|A\rangle^0|^2 + 2\mathcal{R}_e\{\langle J|m_\rho|A\rangle^0 (\langle J|m_\rho|A\rangle^1)^*\} \qquad (7.63)$$

where $\mathcal{R}_e$ indicates the real part of everything top the right. Expressions for the first and second terms of equation (7.63) are summarised in Table 7.4 and Table 7.5 respectively. The latter are given in terms of variables $A^{\pm}_{\theta}$ and $B^{\pm}_{\theta}$ defined by

$$A^{\pm}_{\theta} = \frac{\eta g_\perp \mu_B B}{4\Delta}\{a^{\pm}_{\theta} b^{\pm}_{\theta}(\kappa_{CF}/\eta)\sin\theta - |a^{\pm}_{\theta}|^2(g_2/g_e)\cos\theta\} \qquad (7.64)$$

$$B^{\pm}_{\theta} = \frac{\eta g_\perp \mu_B B}{4\Delta}\{a^{\pm}_{\theta} b^{\pm}_{\theta}(\kappa_{CF}/\eta)\sin\theta + |b^{\pm}_{\theta}|^2(g_2/g_e)\cos\theta\} \qquad (7.65)$$

The relationship

$$(B^{\pm}_{\theta} - A^{\pm}_{\theta}) = \frac{\eta g_\perp \mu_B B}{4\Delta}\{|b^{\pm}_{\theta}|^2 + |a^{\pm}_{\theta}|^2\}(g_2/g_e)\cos\theta = \frac{g_\perp{}^2(g^-_\parallel - g_e)\mu_B B}{4g_e{}^2 a'_2}\cos\theta \qquad (7.66)$$

will prove useful later.

Table 7.4: The zeroth-order transition-moment matrix-elements between states comprising the $^2E_{1u}$ and $^2E_{2g}$ terms of $Fe(cp)_2^+$.

$\lvert\langle J\rvert m_\rho\rvert A\rangle^0\rvert^2$	$\lvert^2\bar{E}_{2g}-\rangle$	$\lvert^2\bar{E}_{2g}+\rangle$	$\lvert^2E^+_{2g}-\rangle$	$\lvert^2E^+_{2g}+\rangle$
$\langle^2E_{1u}$ 1 -1/2$\rvert$	$\lvert\bar{b}_\theta c_\beta\rvert^2 \lvert\mathfrak{M}_{-1}\rvert^2$	$\lvert\bar{a}_\theta c_\beta\rvert^2 \lvert\mathfrak{M}_{-1}\rvert^2$	$\lvert b^+_\theta c_\alpha\rvert^2 \lvert\mathfrak{M}_{-1}\rvert^2$	$\lvert a^+_\theta c_\alpha\rvert^2 \lvert\mathfrak{M}_{-1}\rvert^2$
$\langle^2E_{1u}$ -1 -1/2$\rvert$	$\lvert\bar{b}_\theta c_\alpha\rvert^2 \lvert\mathfrak{M}_{+1}\rvert^2$	$\lvert\bar{a}_\theta c_\alpha\rvert^2 \lvert\mathfrak{M}_{+1}\rvert^2$	$\lvert b^+_\theta c_\beta\rvert^2 \lvert\mathfrak{M}_{+1}\rvert^2$	$\lvert a^+_\theta c_\beta\rvert^2 \lvert\mathfrak{M}_{+1}\rvert^2$
$\langle^2E_{1u}$ 1 1/2$\rvert$	$\lvert\bar{a}_\theta c_\alpha\rvert^2 \lvert\mathfrak{M}_{-1}\rvert^2$	$\lvert\bar{b}_\theta c_\alpha\rvert^2 \lvert\mathfrak{M}_{-1}\rvert^2$	$\lvert a^+_\theta c_\beta\rvert^2 \lvert\mathfrak{M}_{-1}\rvert^2$	$\lvert b^+_\theta c_\beta\rvert^2 \lvert\mathfrak{M}_{-1}\rvert^2$
$\langle^2E_{1u}$ -1 1/2$\rvert$	$\lvert\bar{a}_\theta c_\beta\rvert^2 \lvert\mathfrak{M}_{+1}\rvert^2$	$\lvert\bar{b}_\theta c_\beta\rvert^2 \lvert\mathfrak{M}_{+1}\rvert^2$	$\lvert a^+_\theta c_\alpha\rvert^2 \lvert\mathfrak{M}_{+1}\rvert^2$	$\lvert b^+_\theta c_\alpha\rvert^2 \lvert\mathfrak{M}_{+1}\rvert^2$
'sum'[a]	$\lvert\mathfrak{M}\rvert^2$	$\lvert\mathfrak{M}\rvert^2$	$\lvert\mathfrak{M}\rvert^2$	$\lvert\mathfrak{M}\rvert^2$
'difference'[b]	$\kappa_{CF}\cos\theta\, g^-_\parallel/g^-_\theta \lvert\mathfrak{M}\rvert^2$	$-\kappa_{CF}\cos\theta g^-_\parallel/g^-_\theta \lvert\mathfrak{M}\rvert^2$	$-\kappa_{CF}\cos\theta\, g^+_\parallel/g^+_\theta \lvert\mathfrak{M}\rvert^2$	$\kappa_{CF}\cos\theta\, g^+_\parallel/g^+_\theta \lvert\mathfrak{M}\rvert^2$

[a] In this row the matrix elements are added together to obtain the intensity of the absorption

[b] In the difference row, the sum of the *rcp* transitions (m_{-1}) is subtracted from the sum of the *lcp* transitions (m_{+1}) in order to obtain the MCD intensity

Table 7.5: The first-order transition-moment matrix-elements between states comprising the $^2E_{1u}$ and $^2E_{2g}$ terms of $Fe(cp)_2^+$.

$\mathcal{R}e\{\langle J\rvert m_\rho\rvert A\rangle^0$ $(\langle J\rvert m_\rho\rvert A\rangle^1)^*\}$	$\lvert^2\bar{E}_{2g}-\rangle$	$\lvert^2\bar{E}_{2g}+\rangle$	$\lvert^2E^+_{2g}-\rangle$	$\lvert^2E^+_{2g}+\rangle$
$\langle^2E_{1u}$ 1 -1/2$\rvert$	$-\bar{B}_\theta \lvert\mathfrak{M}_{-1}\rvert^2$	$\bar{A}_\theta \lvert\mathfrak{M}_{-1}\rvert^2$	$B^+_\theta \lvert\mathfrak{M}_{-1}\rvert^2$	$-A^+_\theta \lvert\mathfrak{M}_{-1}\rvert^2$
$\langle^2E_{1u}$ 1 1/2$\rvert$	$\bar{A}_\theta \lvert\mathfrak{M}_{-1}\rvert^2$	$-\bar{B}_\theta \lvert\mathfrak{M}_{-1}\rvert^2$	$-A^+_\theta \lvert\mathfrak{M}_{-1}\rvert^2$	$B^+_\theta \lvert\mathfrak{M}_{-1}\rvert^2$
$\langle^2E_{1u}$ -1 -1/2$\rvert$	$\bar{B}_\theta \lvert\mathfrak{M}_{+1}\rvert^2$	$-\bar{A}_\theta \lvert\mathfrak{M}_{+1}\rvert^2$	$-B^+_\theta \lvert\mathfrak{M}_{+1}\rvert^2$	$A^+_\theta \lvert\mathfrak{M}_{+1}\rvert^2$
$\langle^2E_{1u}$ -1 1/2$\rvert$	$-\bar{A}_\theta \lvert\mathfrak{M}_{+1}\rvert^2$	$\bar{B}_\theta \lvert\mathfrak{M}_{+1}\rvert^2$	$A^+_\theta \lvert\mathfrak{M}_{+1}\rvert^2$	$-B^+_\theta \lvert\mathfrak{M}_{+1}\rvert^2$
'sum'[a]	0	0	0	0
'difference'[b]	$2(\bar{B}_\theta - \bar{A}_\theta)$	$2(\bar{B}_\theta - \bar{A}_\theta)$	$2(A^+_\theta - B^+_\theta)$	$2(A^+_\theta - B^+_\theta)$

[a] In this row the matrix elements are added together to obtain the intensity of the absorption

[b] In the difference row, the sum of the *rcp* transitions (m_{-1}) is subtracted from the sum of the *lcp* transitions (m_{+1}) in order to obtain the MCD intensity

Expressions for the absorption and MCD zeroth moments can now be determined. For low temperatures, only the $|^2\bar{E}_{2g}\pm\rangle$ states will be populated, with individual populations given by

$$P_{\pm}^{-} = \frac{\exp(\pm g_{\theta}^{-}\mu_B B/2kT)}{2\cosh(\pm g_{\theta}^{-}\mu_B B/2kT)} \tag{7.67}$$

Integrating over all transitions, for a molecule oriented at angle θ with respect to the field, the moments are given by using equations (4.56), (4.47) and (4.48)

$$(\mathbf{A}_0^{\theta})_{\text{whole band}} = Cl\gamma\frac{1+\cos^2\theta}{4}\sum_J P_{-}^{-}(|\langle J|m_{+1}|^2\bar{E}_{2g}-\rangle|^2 + |\langle J|m_{-1}|^2\bar{E}_{2g}-\rangle|^2)$$

$$+ P_{+}^{-}(|\langle J|m_{+1}|^2\bar{E}_{2g}+\rangle|^2 + |\langle J|m_{-1}|^2\bar{E}_{2g}+\rangle|^2) = Cl\gamma\frac{1+\cos^2\theta}{4}|\mathfrak{M}|^2 \tag{7.68}$$

$$(\mathbf{M}_0^{\theta})_{\text{whole band}} = Cl\gamma\cos\theta\sum_J P_{-}^{-}(|\langle J|m_{+1}|^2\bar{E}_{2g}-\rangle|^2 - |\langle J|m_{-1}|^2\bar{E}_{2g}-\rangle|^2)$$

$$+P_{+}^{-}(|\langle J|m_{+1}|^2\bar{E}_{2g}+\rangle|^2 - |\langle J|m_{-1}|^2\bar{E}_{2g}\rangle|^2)$$

$$= Cl\gamma\cos\theta\{\frac{\kappa_{CF}\,g_{\parallel}^{-}}{g_{\theta}^{-}}\cos\theta\,|\mathfrak{M}|^2(P_{-}^{-} - P_{+}^{-}) + 4(B_{\theta}^{-} - A_{\theta}^{-})(P_{-}^{-} + P_{+}^{-})\}$$

$$= Cl\gamma\cos^2\theta\,|\mathfrak{M}|^2\left(\frac{\kappa_{CF}\,g_{\parallel}^{-}}{g_{\theta}^{-}}\tanh\left(\frac{g_{\theta}^{-}\mu_B B}{2kT}\right) + \frac{g_{\perp}^{2}(g_{\parallel}^{-} - g_e)\mu_B B}{g_e^{2}a'^{2}}\right) \tag{7.69}$$

The absorption moment $\mathbf{A}_0$ is independent of magnetic field and temperature, as long as the temperature is not so high that the upper SO-CF level gains appreciable population. The expression for $\mathbf{M}_0^{\theta}$ contains two terms. The first is responsible for $\mathcal{C}$ terms – it depends on the temperature and field, showing saturation behaviour (Section 4.6) at higher values of B/T. The second term, which is linearly dependent on the field and independent of temperature, is responsible for $\mathcal{B}$ terms. Importantly, the appearance of $\mathcal{B}$ terms requires $g_{\perp} \neq 0$.

Averaging over all θ using equation (4.59) gives

$$(\mathbf{A}_0)_{\text{whole band}} = Cl\gamma|\mathfrak{M}|^2/3 \tag{7.70}$$

$$(\mathbf{M}_0)_{\text{whole band}} = C l\gamma\,|\mathfrak{M}|^2\left(\kappa_{CF}\,\bar{g}_{\parallel}\int_0^1 \frac{\cos^2\theta}{\bar{g}_\theta}\tanh\left(\frac{\bar{g}_\theta\mu_B B}{2kT}\right)d\cos\theta + \frac{g_\perp^{\,2}(\bar{g}_{\parallel} - g_e)\mu_B B}{3g_e^{\,2}a'^2_2}\right) \quad (7.71)$$

$$\left(\frac{\mathbf{M}_0}{\mathbf{A}_0}\right)_{\text{whole band}} = 3\kappa_{CF}\bar{g}_{\parallel}\int_0^1 \frac{\cos^2\theta}{\bar{g}_\theta}\tanh\left(\frac{\bar{g}_\theta\mu_B B}{2kT}\right)d\cos\theta + \frac{g_\perp^{\,2}(\bar{g}_{\parallel} - g_e)\mu_B B}{g_e^{\,2}a'^2_2} \quad (7.72)$$

In the linear limit,

$$(\mathbf{M}_0)_{\substack{\text{whole band}\\ \text{linear limit}}} = C l\gamma\,|\mathfrak{M}|^2\left(\frac{\kappa_{CF}\,\bar{g}_{\parallel}}{6kT} + \frac{g_\perp^{\,2}(\bar{g}_{\parallel} - g_e)}{3g_e^{\,2}a'^2_2}\right)\mu_B B \quad (7.73)$$

and

$$\left(\frac{\mathbf{M}_0}{\mathbf{A}_0}\right)_{\substack{\text{whole band}\\ \text{linear limit}}} = \left(\frac{\kappa_{CF}\,\bar{g}_{\parallel}}{2kT} + \frac{g_\perp^{\,2}(\bar{g}_{\parallel} - g_e)}{g_e^{\,2}a'^2_2}\right)\mu_B B \quad (7.74)$$

7.3.4 Jahn-Teller Effects

The effect of a ground-state JT effect on the spectroscopic moments has been covered in a detailed and general manner in Chapter 5, and the appropriate expression for $\mathbf{M}_0/\mathbf{A}_0$ is given by equation (5.131). In the case of the $^2E_{1u} \leftarrow {}^2E_{2g}$ transition of $Fe(cp)_2^+$, $\Delta\Lambda = -1$, but it is not immediately clear what JT effects might be operating in the ground state. To allow generalisation the following parameters are defined

$$\kappa_{JT} = \bar{\kappa}_{n/2,1} \quad (7.75)$$

$$g_{\parallel} = g_{\parallel}(\psi^{\mp\sigma}_{\mp n/2}) \quad (7.76)$$

Then equation (5.131) can be rewritten

$$\left(\frac{\mathbf{M}_0}{\mathbf{A}_0}\right)_{\text{whole band}} = 3\kappa_{JT}\int_0^1 \cos\theta\tanh\left(\frac{g_{\parallel}\mu_B B}{2kT}\right)d\cos\theta \quad (7.77)$$

This is analogous to equation (7.72) with $g_\perp = 0$, which would give $g_\theta^- = g_\parallel^-$. The $\mathcal{B}$-term contribution (second term in equation (7.72)) would vanish, leaving only the $\mathcal{C}$ terms. Of course, $g_\perp = 0$ corresponds to no CF effect. The reason why $g_\perp = 0$ in the absence of a CF effect is due to the JT branch orthogonality mentioned in Section 5.3.1.

In the linear limit, equation (7.77) reduces to

$$\left(\frac{\mathbf{M}_0}{\mathbf{A}_0}\right)_{\substack{\text{whole band}\\ \text{linear limit}}} = \frac{\kappa_{JT} g_\parallel \mu_B B}{2kT} \tag{7.78}$$

which has exactly the same form as the first term of equation (7.74), except now the extra orbital reduction (in excess over that from covalency) is due to JT coupling (Ham effect) rather than CF interactions.

7.4 Discussion

7.4.1 The Importance of Ground-state Crystal-field Effects in $Fe(cp)_2^+/Ar$

The first step of the analysis is to determine whether CF effects contribute significantly to the orbital reduction. Following the preceding discussion, there are two obvious ways in which CF effects manifest themselves. The first is the occurrence of $\mathcal{B}$ terms due to CF-induced mixing of the ground-state SO levels. The second, which is closely related, is a non-vanishing value of $g_\perp$.

The fact that the MCD moment-analysis data obtained at different temperatures (Figure 1.5) overlap almost exactly when plotted against $\mu_B B/kT$ (Figure 7.6) immediately suggests that $\mathcal{B}$ terms, and therefore CF interactions, are unimportant in the spectra of $Fe(cp)_2^+/Ar$. But a more stringent test is to fit the magnetisation curves in Figure 1.5 and Figure 7.6 with a general function that allows for non-zero $g_\perp$.[55] This was done using the least-squares fitting program SATURATE with the function

$$\mathbf{M}_0 = K\int_0^1 \frac{g_\parallel \cos^2\theta}{g_\theta} \tanh\left(\frac{g_\theta \mu_B B}{2kT}\right) \mathrm{d}\cos\theta \tag{7.79}$$

where

$$g_\theta = [(g_\parallel)^2\cos^2\theta + (g_\perp)^2\sin^2\theta]^{1/2} \tag{7.80}$$

In comparison with equations (7.71) (first term) and (7.77), equation (7.79) can be seen to be a generalisation with

$$K = 3\kappa_X A_0 \tag{7.81}$$

where κ_X is an effective 'extra' reduction factor due to effects other than covalency. The last equation illustrates the point, alluded to in Section 4.6, that magnetisation saturation curves can be used to extract information about the ground-state g values even in the absence of reliable absorption data. Essentially, the absorption can be treated as part of an arbitrary scaling constant.

The best-fit parameter values (with two standard deviation errors in the least significant figures given in the parentheses) obtained by simultaneously fitting the $\mathbf{M}_0$ data for $Fe(cp)_2^+/Ar$ at all field strengths and temperatures, are

$$K = 0.0144(1) \tag{7.82}$$

$$g_\perp = 0.00(4) \tag{7.83}$$

$$g_\parallel = 4.88(8) \tag{7.84}$$

the sum of the squares residuals being 3.893×10^{-7}. The fits to the data are shown as continuous curves in Figure 1.5 and Figure 7.6. The immediately important result is that $g_\perp$ is zero within experimental error, and is certainly very much less than g_e. According to equation (7.46), in absence of JT effects, the upper two-standard-deviation limit of $g_\perp < 0.04$ indicates $\kappa_{CF} > 0.9998$. Given that κ_{CF} can have a maximum value of one (corresponding to no CF), this results reaffirms the suggestion from the absence of $\mathfrak{B}$ terms that CF effects are unimportant in the ground-state of $Fe(cp)_2^+$ in an Ar matrix.

It therefore seems reasonable to treat the MI data as if there were no significant ground-state CF. In that case, from equations (5.108) and (7.28)

$$g_{\|} = \kappa_{JT} g_2 + g_e = 4\kappa_{cov}\kappa_{JT} + g_e \qquad (7.85)$$

which, with $g_e = 2.0023$ and the value of $g_{\|}$ above, gives

$$\kappa_{cov}\kappa_{JT} = 0.72(2) \qquad (7.86)$$

The problem now becomes one of separating contributions to κ from the two sources, the JT effect and covalency. It is here that the JT analysis of individual bands presented in Chapter 5 comes into its own.

An initial estimate for κ_{JT} can be obtained by using equation (5.136), which is independent of temperature and field. The value obtained from a large number of spectra from SM4/matrix-injection system at various temperatures and magnetic field strengths is $\kappa_{JT} \approx 0.93(5)$, which would give $\kappa_{cov} \approx 0.77(4)$ at the lower end of the range of the values obtained by earlier workers (Table 7.1). However, this estimate is subject to an additional and potentially high degree of uncertainty due to the subjectivity of the absorption baselining procedure, as described in Section 7.2.1. The analysis given in Section 1.3.2, using the program DYNAMO, provides more a reliable estimate.

7.4.2 Analysis of Vibrational Structure

Analysis of the vibrational structure in the well-resolved electronic spectra of $Fe(cp)_2^+$ /Ar obtained with the refrigerator/electromagnet system was done by comparison with the vibrational frequencies of ferrocene and simulations made by using the computer program DYNAMO. Agreement between theory and experiment was achieved by trial and error and judged by visual inspection.

As discussed in Section 6.2.2, the temperature in the refrigerator cannot be accurately determined. However, the modelling used here doesn't depend strongly on this parameter, provide the experimental spectrum was obtained under linear-limit conditions – which is true for the refrigerator/electromagnet system. Furthermore, since the absorption is not highly reliable, the focus is on the MCD (Figure 7.13).

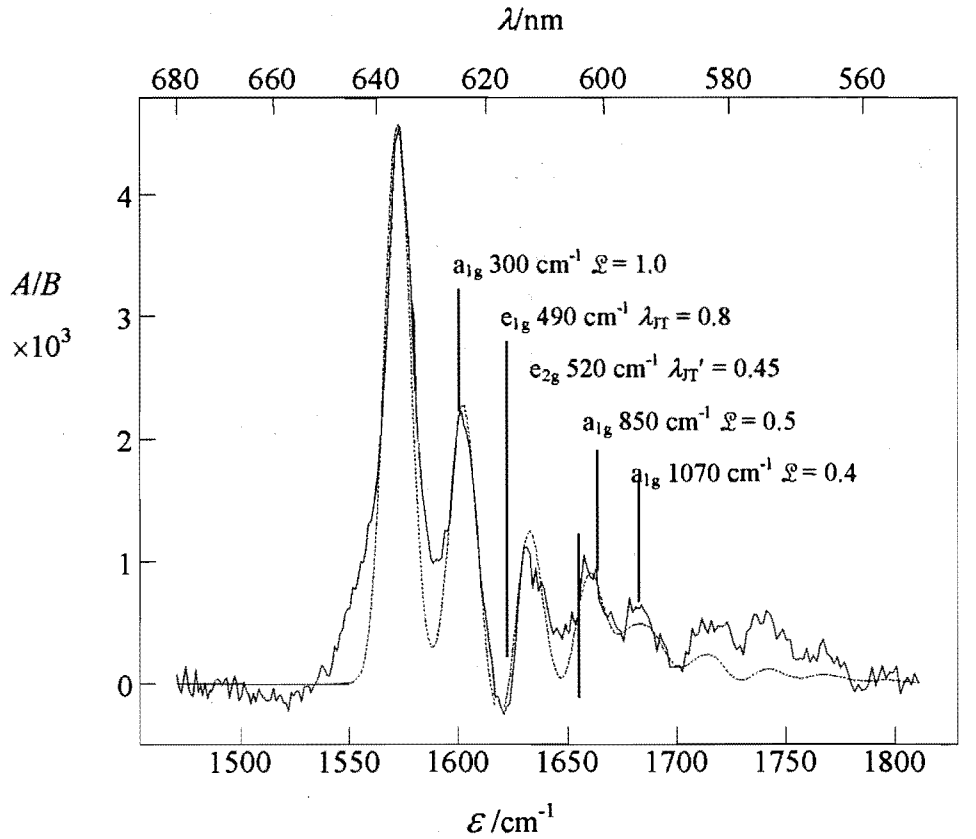

Figure 7.13: Comparison of an experimental spectrum of $Fe(cp)_2^+$/Ar obtained at 15 K and 0.6 T (solid line) with the 'best-fit' spectrum calculated using computer program DYNAMO (dashed line). Parameters are given in Table 7.7.

The vibrational frequencies and assignments for $Fe(cp)_2^+$ are summarised in Table 7.6. Modes with e_{1g} symmetry have the potential be LJT active in the ground state and QJT active in the excited state. Those with e_{2g} symmetry are potentially quadratically active in the ground state and linearly active in the excited state.

As noted by previous workers,[33,48] there is an obvious progression in involving a ~300 cm^{-1} mode, assigned to a totally symmetric metal-ligand stretching mode that occurs at ~305 cm^{-1} in ferrocene. This seems reasonable given that the $1e_{2g} \leftarrow 1e_{1u}$ excitation should lead to a slight decrease in both metal-ligand and inter-ligand bond orders. The fact that the MCD bands are all positive (the same sign as the origin) is also consistent with an a_{1g} progression. Bands with positive MCD shifted by 850 cm^{-1} and 1070 cm^{-1} from the origin are associated here with the first members of further a_{1g} progressions in modes with ground-state ferrocene wavenumbers of 1105 cm^{-1} (CH in-plane deformation) and 1390 cm^{-1} (ring breathing), respectively.

Table 7.6: Vibrational frequencies (cm^{-1}) of ferrocene.[56] || refers to in-plane-modes of the ligand rings while ⊥ refers to out-of-plane modes.

"In-phase" modes			"Out-of-phase" modes	
Irrep	Frequency	Approximate description	Irrep	Frequency
a_{1g}	3110	CH stretch	a_{2u}	3086
	1390	Ring breathing		1408
	306	Fe-cp stretch		478
a_{2u}	1104	CH deform(⊥)	a_{1g}	1105
a_{2g}	1249	CH deform(||)	a_{1u}	1253
		Torsion		—
e_{1g}	818	CH deform(⊥)	e_{1u}	814
	390	Ring tilt		490
		cp-Fe-cp deform		170
e_{1u}	3086	CH stretch	e_{1g}	3089
	1004	CH deform(||)		998
	1408	CC stretch		1412
e_{2g}	3045	CH stretch	e_{2u}	3035
	1361	CH deform(||)		1351
	1527	CC stretch		
	1054	CCC deform(||)		1054
e_{2u}	1188	CH deform(⊥)	e_{2g}	1184
	567	CCC deform(⊥)		591

Table 7.7: Vibrational assignment for the vibronic bands observed in the $^2E_{1u} \leftarrow {}^2E_{2g}$ LMCT transition of $Fe(cp)_2^+/Ar$[a]

symmetry	frequency	displacement	assignment
e_{2g}	520	$\lambda_{JT}' = 0.45$	CCC in-plane deformation
		$\epsilon_{JT} = 0.0$	
e_{1g}	490	$\lambda_{JT} = 0.8$	symmetric ring tilt
		$\epsilon_{JT}' = 0.0$	
a_{1g}	300	$\mathfrak{L} = 1$	Fe-cp symmetric stretch
a_{1g}	1100	$\mathfrak{L} = 0.4$	ring breathing
a_{1g}	830	$\mathfrak{L} = 0.5$	CH in-plane deformation

[a] Primes indicate excited-state JT displacement parameters

These assignments are fairly tentative. Firstly, the ground-state ferrocene frequencies will provide only a rough guide to the ferricenium excited-state values. Secondly both excited-state LJT and QJT effects could contribute positive bands. In particular e_{2g} in- and out-of-plane C-C-C deformations (with ground-state ferrocene frequencies of 1054 cm^{-1} and 1184cm^{-1} respectively) and e_{1g} in- and out-of-plane C-H deformations (818 cm^{-1} and 998 cm^{-1}), are of the correct symmetry in the right frequency range. However there is no other reason to suspect that any of these modes are significantly active and the difference in frequency between ground state ferrocene and excited state ferricenium may be significantly different. Since it doesn't make much difference to that part of the interpretation where real evidence can be brought to bear, namely ground-state JT effects, the simplest and most conservative scenario has been assumed.

The band shifted 490 cm^{-1} from the origin has a negative $\mathcal{C}$ term, and hence, as discussed in Section 5.4.1.2, is the most obvious candidate for a ground-state JT effect. In principle, this could involve either a LJT effect in an e_{1g} mode or a QJT effect in an e_{2g} mode.

First consider the possibility of a ground-state QJT effect (e_{2g} mode). A suitable fit in the region of the negative band was obtained with $\epsilon_{JT} \sim 1$ and $\bar{\nu}_{JT} \approx 200$ cm^{-1}. Consideration of Figure 5.8 shows why the required frequency is only half of the shift from the origin. The lowest vibronic levels of the ground state belongs to the $Q_{\pm 1}$ branches. Since the QJT effect couples states with $\Delta v = \pm 2$, non-zero Franck-Condon overlap factors are only possible with excited-state levels of even v. The first overtone will therefore appear at $\sim 2\nu_{JT}$.) But despite the reasonable fit that could be obtained, there are substantial problems with a QJT interpretation. Firstly, such a large value of ϵ_{JT} is stretching the model to its extreme and therefore very dubious. Secondly it predicts fairly intense bands at higher energy, which are not observed experimentally. And finally, it would require an e_{2g} mode with a frequency of ~ 200 cm^{-1} which (from Table 7.6) seems very unlikely.

A better fit to the negative band was obtained by invoking a ground-state LJT effect with $\lambda_{JT} = 0.8$ and $\bar{\nu}_{JT} = 490$ cm^{-1}. This gives the JT stabilisation energy $\varepsilon_{JT} =$ 157 cm^{-1}. Although such a mode also has the potential to be QJT active in the excited state, the best fit was achieved with $\epsilon_{JT}' = 0$. From Table 1.6, there is only one reasonable candidate for such a vibration – the e_{1g} ring-tilt mode, which occurs at 390

cm^{-1} in ground-state ferrocene. The electronic orbital angular momentum of the $^2E_{2g}$ states arises from the partly filled $1e_{2g}$ orbitals, which are principally metal 3d, so the JT mode should involve distortions of these d orbitals. Since the ligands sit on 'legs' composed of these orbitals, the assignment of the JT mode to the symmetric ring-tilt appears very reasonable.

After all of the above assignments, simulations show a requirement for a further positive band at 520 cm^{-1} from the origin. This could be due to a totally symmetric vibration or an excited-state JT effect. Having already assigned the a_{1g} Fe-cp symmetric stretch and the e_{1g} symmetric ring tilt to other vibronic bands, the only realistic assignment is to an excited-state LJT effect involving the e_{2g} in-plane C-C-C deformation, which occurs at 591 cm^{-1} in ferrocene. Again, this makes sense when the electronic state is considered. Now the orbital angular momentum arises from the partial occupation of the $1e_{1u}$ orbitals, which are principally of ligand π parentage, and the hence distortions of the C_5 frameworks of the ligands would be expected. The 'best fit' was obtained with $\lambda_{JT}' = 0.45$, $\bar{\nu}_{JT} = 520$ cm^{-1} which gives $\varepsilon_{JT}' = 53$ cm^{-1}. Again, although potentially quadratically active in the ground state, the best fit gave $\epsilon_{JT} = 0$.

The final simulation is shown as a dashed curve in Figure 7.13, obtained using 80 basis sets for each JT mode with the parameters listed in Table 7.7, along with ground-state parameters $a'_2 = 820$ cm^{-1} and $g_2 = 3.68$ (see below). Gaussian lineshapes were assumed with a half width at 1/e max of 8.5 cm^{-1}.

It should be reiterated here that very close agreement between the assigned frequencies of Table 7.7 and the ferrocene frequencies in Table 7.6 is not necessarily expected. Firstly, the normal modes of the radical are not necessarily the same as those for neutral precursor, and secondly, their frequencies are likely to be different. Finally, even when it is a ground-state JT effect under consideration, it is the excited-state frequencies that determine the spacings in the absorption and MCD spectra. However, despite the lack of appropriate data, the assignment of the ~490- and ~520-cm^{-1} bands to modes of e_{1g} and e_{2g} symmetries seems to have a reasonably strong basis. In addition they are in agreement with Sohn *et al.*,[48] although those authors did not justify their assignments of non-totally symmetric modes or attempt to determine parameters.

7.4.3 The Ground State of Ferricenium

In this section, attention is focussed on the ground-state parameters and the information they convey about the $1e_{2g}$ orbitals. At this point it is necessary to disclose additional information that was required to perform the fits described in the previous section.

From equation (7.86), κ_{cov} must lie between 1 and ~0.74. This provides a range of values for $|c_d|^2$, which can be obtained by simultaneous solution of equations (7.21) and (7.27), which respectively represent the equations of an ellipse and a pair of hyperbolas (Figure 7.14).

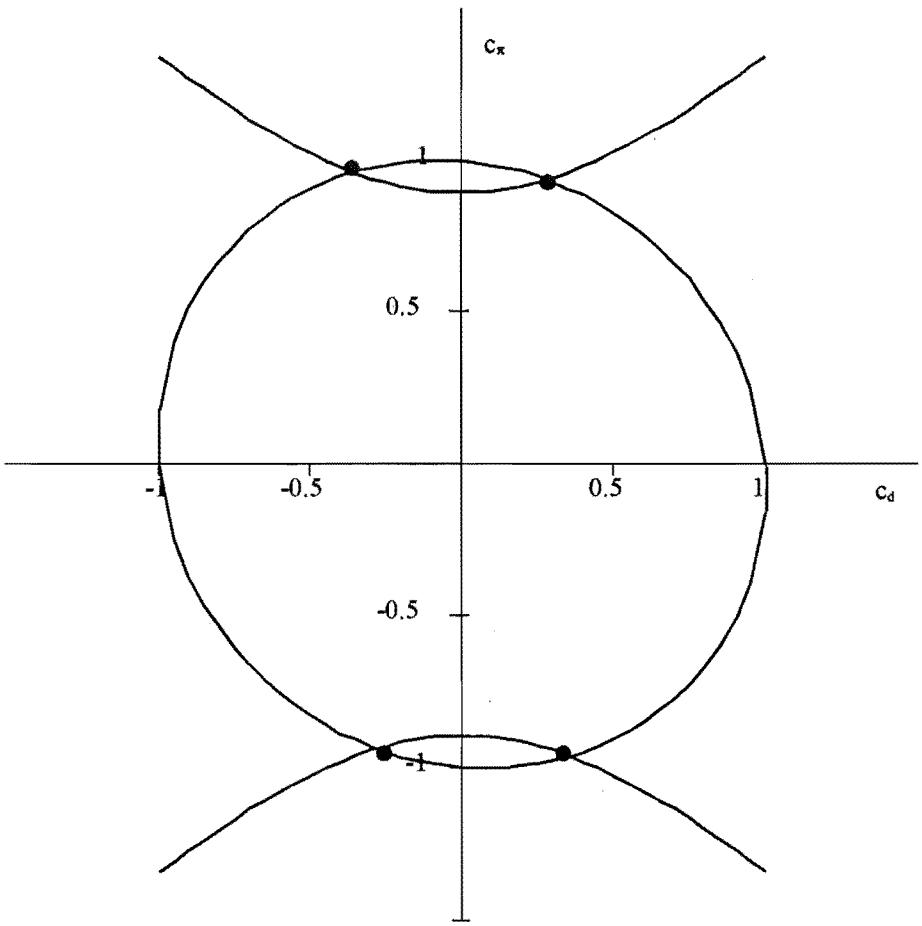

Figure 7.14: Graphical representations of equations (7.21) (an ellipse with the principal axis at 45° to the c_d and c_π axes) and (7.27) (a pair of hyperbolas) for the parameters $l_\pi = 0.4$, $\kappa_{cov} = 0.92$ and $S_{e_{2g}} = 0.079$.

Determination of the four intersections is not a trivial exercise and in fact MATLAB was required to obtain the relevant equations. Defining

$$f = 2S_{e_{2g}} \tag{7.87}$$

$$g = (4\kappa_{cov} - 2 - l_\pi)/(2 - l_\pi) \tag{7.88}$$

and then

$$A = f\sqrt{\{(f^2 - 4)g^2 + 4\}} \tag{7.89}$$

$$B = g(f^2 - 4) - 4 \tag{7.90}$$

$$C = 2f^2 - 8 \tag{7.91}$$

the solutions for c_π are

$$c_\pi = \sqrt{(B \pm A)/C} \tag{7.92}$$

$$c_\pi = -\sqrt{(B \pm A)/C} \tag{7.93}$$

Then for each value of c_π,

$$c_d = \frac{-c_\pi\{(f^2 - 4)\, c_\pi^2 + (f^2 - 2)g + 2\}}{f(g - 1)} \tag{7.94}$$

These equations give two sets of values for $|c_d|^2$ and $|c_\pi|^2$ which can't be distinguished on the basis of the data. The differences between these sets depend on the eccentricity of the ellipse, and therefore by the value of the overlap factor $S_{e_{2g}}$ (see the discussion immediately following equation (7.22)). However, if $S_{e_{2g}}$ is small, then the ellipse tends to a circle and the two sets of solutions converge. In the case considered here, the overlap factor is rather small ($S_{e_{2g}} \approx 0.079$)[28] and so (partly in the absence of a useful alternative approach) it is neglected to give

$$|c_d|^2 \approx \frac{2\kappa_{cov} - l_\pi}{2 - l_\pi} \qquad (S_{e_{2g}} \approx 0) \tag{7.95}$$

With $l_\pi \approx 0.4$ (equation (7.25)), this means that $|c_d|^2$ must lie within the range between 0.65 and 1. Then from equation (7.30) (with $\zeta_{Fe;3d} = 450$ cm^{-1}), a'_2 falls between ~300

and 450 cm^{-1}, while from equation (7.28), g_2 is between ~2.9 and 4.0. Varying these parameters in concert between the upper and lower bounds, the 'best-fits' to the ~490-cm^{-1} negative MCD band obtained using the method in the preceding section consistently give $\lambda_{JT} = 0.8$. However the corresponding value of κ_{JT} changes in the manner indicated by the full curve in Figure 7.15.

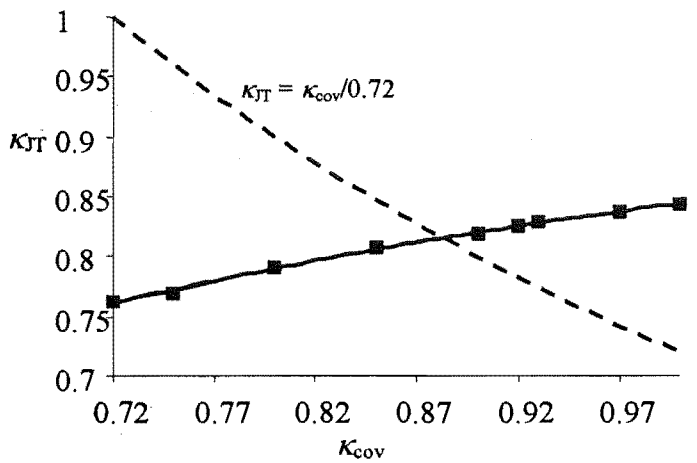

Figure 7.15: Plots of κ_{JT} as a function of κ_{cov}. The broken line is the result obtained by moment analysis which required $\kappa_{JT}\kappa_{cov} = 0.72$. The full line was obtained from spectral simulation with $l_\pi = 0.4$, $S_{e_{2g}} = 0$, $\lambda_{JT} = 0.8$ between the boundary conditions of 0.74 and 1 for κ_{cov}

Figure 7.15 provides a means to separate the contributions to orbital reduction from covalency and the JT effect since equation (7.86) gives the broken curve. The only result consistent with both the moment analysis and the band simulations are given by the intersection of the two curves. The κ values and some of the results determined from them are:

$$\kappa_{cov} = 0.88 \qquad (7.96)$$

$$\kappa_{JT} = 0.82 \qquad (7.97)$$

$$|c_d|^2 = 0.85 \qquad (7.98)$$

$$a'_2 = 765\ cm^{-1} \qquad (7.99)$$

$$g_2 = 3.52 \qquad (7.100)$$

Having determined these parameters, it is worth revisiting a couple of assumption that were made earlier in this treatment.

From the value for a'_2, at the highest temperature of 12.4 K used in the SM4/matrix injection experiments, the upper of the ground-state SO levels will have a negligible population. Thus the assumption following equation (7.69) is justified.

The ground parameters give a ground-state JT stabilisation energy of ε_{JT} = 157 cm^{-1}, about 32% of the zero-point energy for the state. When combined with the evidence for the absence of significant CF effects, the molecule is expected to retain its five-fold symmetry in the matrix. A small CF (~20 cm^{-1}) would be severely quenched by a ground-state SO and JT effects of the magnitude quoted above.

7.4.4 Solution Spectra

In the solution spectra, vibrational structure was not resolved (Figure 7.7). However, since the JT effect is part of the molecular Hamiltonian it should be relatively independent of the host medium. As discussed in the introduction, CFs in solution may be significantly more important than in inert-gas matrices.

To estimate the magnitude of a CF it is useful to compare $\mathbf{M}_0/\mathbf{A}_0$ *vs* $\mu_B B/kT$ plots of the MI data with the same for the solution (Figure 7.9). If a CF is operating in solution, the slopes of such plots would be expected to be less because the effective orbital reduction factor should be decreased by the additional contribution of the CF. The solution data would also be expected to exhibit a positive $\mathbf{M}_0/\mathbf{A}_0$ intercept since a CF introduces $\mathfrak{B}$ terms.

The linear-limit extrapolation (equation (7.74)) of the MI data using the parameters in equations (7.85) and (7.86) is shown as the broken grey line with a slope of 1.90 in Figure 7.9. The solution data are seen to have slopes near or slightly below 1.9 (1.7 – 1.9) and to be shifted to slightly higher values (10^{-4} – 10^{-3}), as expected for the presence of a CF. Unfortunately, the problems of obtaining reproducible data (mainly due to absorption baselining problems) make a detailed analysis difficult. However, assuming that the effective κ_X of equation (7.81) can be approximated (for a weak CF) by the product of κ_{cov} and κ_{CF}, the following values give a reasonable account of the data:

$$V_{CF} = 250 \text{ cm}^{-1} \qquad (7.101)$$

$$\kappa_{CF} = a'_2/((V_{CF}^2) + (a'_2)^2)^{1/2} = 0.96 \quad (7.102)$$

$$g_{\|} = \kappa_{CF}\,\kappa_{JT}\,g_2 + g_e = 4.74 \quad (7.103)$$

$$g_{\perp} = g_e(1 - \kappa_{CF}^2)^{1/2} = 0.59 \quad (7.104)$$

$$\text{slope} = \kappa_{CF}\,\kappa_{JT}(g_{\|} + g_e)/2 = 1.77 \quad (7.105)$$

$$\text{intercept} = g_{\perp}2(g_{\|} - ge)/4a'_2 = 3 \times 10^{-4} \quad (7.106)$$

Although these values should not be taken too seriously, comparison with previous results (Table 7.1) shows that they indicate a CF at the lower end of the range previously indicated (~200 – 1000 cm^{-1}), a result which is reflected by a larger value of $g_{\|}$ (compared with 3.2 – 4.4) and a smaller value of $g_{\perp}$ (1.3 – 1.8). This is perhaps not surprising since the ESR studies used to extract the earlier data were performed below the freezing point of the solvent, where, as noted by Rowe and McCaffery,[35] the decreased volume of the sample is likely to exert stronger crystal fields.

An interesting aspect of the solution spectra that remains unexplained is the temperature dependence of the absorption (Figure 7.7). Prins[41] suggested that this could be due to the population increase of the lower SO level at lower temperature. Between 180 to 280 K, the temperature limits of the solution spectra run here, assuming a splitting of ~800 cm^{-1}, the population of that level should change by only ~1.6%. This is not consistent with the ~20% increase in intensity observed experimentally. On the other hand, if the CF were increasing with (decreasing) temperature, the mixing of the SO levels would change simultaneously, which could also contribute to the change in absorption intensity.

7.5 Conclusions

The JT effect in the $^2E_{2g}$ ground-state of the ferricenium radical cation has been characterised for the first time. It is manifest as negative bands in the MCD spectrum of the species isolated in a solid Ar matrix. By combining moment analysis and

spectral simulation of the MCD data, parameters could be extracted that indicate a linear JT effect in an e_{2g} mode of ~490 cm^{-1}, which is attributed to a symmetric ring tilt mode. Such an assignment fits in with the view that the $1e_{2g}$ orbitals of ferricenium (and ferrocene) are principally of metal-ion parentage. The JT parameters of $\lambda_{JT} \approx 0.8$ and $\varepsilon_{JT} \approx 157$ cm^{-1} are ~25% smaller than the only other determination, by Rai *et al.*,[26,45] of $\lambda_{JT} = 1.08$ cm^{-1} and $\varepsilon_{JT} = 235$ cm^{-1}. In order to achieve agreement between his theoretical model (using $a'_2/2 = 460$ cm^{-1}) and experimental ESR spectra, Rai[45] calculated that a value of the JT frequency of $\bar{\nu}_{JT}$ =400 cm^{-1} (associated with a ring stretch mode) was required. This is remarkably close to the value of 490 cm^{-1} observed in this work.

Combining the moment analysis with predicted orbital angular momentum for the e_{2g} ligand π orbitals, an effective orbital reduction factor of 0.72 was determined for the $^2E_{2g}$ ground state of ferricenium. This is at the lower end of the range of values determined by previous workers who ignored the ligand contributions to the angular momentum. Such a reduction factor can have contributions from CF, JT and covalent effects. Unlike previous workers, the contributions from all three effects were considered in this analysis. Moment analysis of the MCD over the temperature range 1.6–12 K and over magnetic field strengths between 0 and 5 T shows that $g_\perp$ vanishes for the ground state, which in turn indicates that crystal-field effects are inconsequential for the ground state in the matrix. This is consistent with the absence in the matrix spectra of splittings that had previously been seen in glasses.

After establishing that the contribution to ground-state orbital reduction from CFs in the matrix data is negligible, the contributions from JT and covalent effects was determined by comparing experimental and theoretical values of κ_{JT} calculated using different values of κ_{cov} and a'_2. The value of $\kappa_{cov} \approx 0.88$ (and the related value of $|c_d|^2 \approx 0.85$) is in qualitative agreement with the results obtained from analyses of ESR spectra in solutions and single crytals[20-22,36,37] and confirms the general belief that the $1e_{2g}$ orbital is predominantly of metal parentage. However, the magnitude of κ_{cov} is slightly greater than obtained by most previous workers, the difference being their neglect of JT contributions. This indicates that the $1e_{2g}$ orbital has stronger metal-ion parentage and contributes less to metal-ligand bonding than had been previously supposed. More surprising perhaps is result that *most* of the orbital

reduction comes from JT coupling ($\kappa_{JT} \approx 0.82$). The only other worker to made a similar suggestion was Rai,[26,45] who concluded $\kappa_{cov} = 1$ (no covalent contribution).[26,45] The results presented here show that view to be too extreme.

An excited-state linear JT effect is found to be manifest as a positive MCD band (same sign as the origin) shifted by ~490 cm^{-1} to the blue of the origin. This was assigned to an e_{2g} C-C-C in-plane deformation, occurring in ferrocene at 591 cm^{-1}. Since the orbital angular momentum in this $^2E_{1u}$ excited state comes from $1e_{1u}$ orbitals that are mostly of ligand character, it makes sense for the JT effect to be due to a vibration involving distortion of the C_5 framework. Fitting of the spectrum yields $\lambda_{JT}' = 0.45$ and $\varepsilon_{JT}' = 58$ cm^{-1}, so the JT effect in the excited state is weak.

Given the relatively weak ground- and excited-state JT effects ($\lambda_{JT} \approx 0.8$ and $\varepsilon_{JT}/\hbar\omega \approx 0.3$, $\lambda_{JT}' = 0.45$, $\varepsilon_{JT}'/\hbar\omega \approx 0.1$) and the absence of significant CF effects in the matrix, the radical is expected to retain $\mathbf{D}_{5(d)}$ symmetry in both electronic states.

Analysis of the MCD and absorption spectra of ferricenium in dichlormethane solution indicate a CF that is large enough (~250 cm^{-1} in the ground state) to have a bearing on the data, but not as large as those reported from the ESR spectra of glasses and single crystals. It is suggested here, in accord with Rowe and McCaffery,[35] that the CFs in such solutions increases with decreasing temperature. This could be investigated by performing temperature-dependent ESR and MCD studies, which would enable extraction of the relevant ground and excited state parameters. In particular, the $g_\perp$ would be expected to increase with decreasing temperature while $g_\parallel$ is expected to decrease towards the spin-only value of g_e.

7.6 References

(1) Kealy, T. J.; Pauson, P. L. *Nature* **1951**, *168*, 1039.

(2) Millar, S. A.; Tebboth, J. A.; Tremaine, J. F. *J. Chem. Soc.* **1952**, 632.

(3) Wilkinson, G.; Rosenblum, M.; Whiting, M. C.; Woodward, R. B. *J. Amer. Chem. Soc.* **1952**, *74*, 2125.

(4) VanCott, T. C.; Rose, J. L.; Misener, G. C.; Williamson, B. E.; Schrimpf, A. E.; Boyle, M. E.; Schatz, P. N. *J. Phys. Chem.*. **1989**, *93*, 2999-3011.

(5) Langford, V. S.; Williamson, B. E. *J. Phys. Chem. A.* **1998**, *102*, 138-145.

(6) Dunitz, L. E.; Orgel, L. E.; Rich, A. *Acta Cryst.* **1956**, *9*, 373.

(7) Lippincott, E. R.; Nelson, R. D. *Spectrochim. Acta* **1958**, *10*, 307.

(8) Hartley, D.; Ware, M. J. *J. Chem. Soc. A* **1969**, 138.

(9) Long, T. V.; Huege, F. R. *Chem. Com.* **1968**, 1239.

(10) Bohn, R. K.; Haaland, A. *J. Organometal. Chem.* **1966**, *5*, 470.

(11) Moffit, W. *J. Amer. Chem. Soc.* **1954**, *76*, 3386-3392.

(12) Dunitz, J. D.; Orgel, L. E. *J. Chem. Phys.* **1955**, *23*, 954-958.

(13) Martinez, R.; Tripicchio, A. *Acta Cryst.* **1990**, *C46*, 202-205.

(14) Bagus, P. S.; Walgren, U. I.; Almlof, A. *J. Chem. Phys.* **1975**, *64*, 2324-2334.

(15) Mammano, N. J.; Zalkin, A.; Landers, A.; Rheingold, A. L. *Inorg. Chem.* **1976**, *16*, 297-300.

(16) Prins, R. *Chem. Com.* **1970**, 280-281.

(17) Rosenblum, M. *Chemistry of the iron group metallocenes; Part 1*, 1st ed.; John Wiley and Sons: New York, 1965.

(18) Schachtschneider, J. H.; Prins, R.; Ros, P. *Inorg. Chim. Acta.* **1967**, *1*, 462-466.

(19) Hillier, I. H.; Canadine, R. M. *Discuss. Faraday Soc.* **1969**, *47*, 27-36.

(20) Ballhausen, C. J.; Gray, H. B. In *Coordination Chemistry*, 1st ed.; Martell, A. E., Ed.; Van Nostrand Reinhold: New York, 1971.

(21) Prins, R. *Mol. Phys.* **1970**, *19*, 603-620.

(22) Prins, R.; Biloen, P.; van Voorst, J. D. W. *J. Chem. Phys.* **1967**, *46*, 1216-1217.

(23) Prins, R.; van Voorst, J. D. W. *J. Chem. Phys.* **1968**, *49*, 4665-4673.

(24) Collins, R. L. *J. Chem. Phys.* **1965**, *42*, 1072-1080.

(25) Coutiere, M.-M.; Demuyunck, J.; Veillard, A. *Theoret. Chim. Acta.* **1972**, *27*, 281-287.

(26) Anderson, S. E.; Rai, R. *Chem. Phys.* **1973**, *2*, 216.

(27) King, R. B. *Transition-Metal Organometallic Chemistry. An Introduction*, 1st ed.; Acaemic Press, Inc.: New York, 1969.

(28) Dahl, J. P.; Ballhausen, C. J. *Mat. Fys. Medd. Dan. Vid. Selak.* **1961**, *33*, 1-22.

(29) Robertson, R. E.; McConnell, H. M. *J. Phys. Chem.* **1960**, *64*, 70-77.

(30) Scott, D. R.; Becker, R. S. *J. Phys. Chem.* **1969**, *69*, 3207-3208.

(31) Shustorovich, E. M.; Dyatkina, M. E. *Doklady Akademii Nauk. SSR.* **1959**, *128*, 1234.

(32) Watson, R. E. *Physical Review* **1960**, *119*, 1934.

(33) Sohn, Y. S.; Hendrickson, D. N.; Gray, H. B. *J. Amer. Chem. Soc.* **1971**, *93*, 3603-3612.

(34) Nielson, D.; Boone, D.; Eyring, H. *J. Phys. Chem.* **1972**, *76*, 511-515.

(35) Rowe, M. D.; McCaffery, A. J. *J. Chem. Phys.* **1973**, *59*, 3786-3794.

(36) Prins, R.; Reinders, F. J. *J. Amer. Chem. Soc.* **1969**, *91*, 4929.

(37) Maki, A. H.; Berry, T. E. *J. Amer. Chem. Soc.* **1965**, *87*, 4437.

(38) Horsfields, A.; Wassermann, A. **1972**, 187.

(39) Prins, R.; Kortbeek, A. G. T. G. *J. Organometal. Chem.* **1971**, *33*, C33-C34.

(40) Prins, R.; Korswagen, A. R. *J. Organometal. Chem.* **1970**, *25*, C74-C75.

(41) Sohn, Y. S.; Henderickson, D. N.; Gray, H. B. *J. Amer. Chem. Soc.* **1970**, *92*, 2599-3836.

(42) Hendrickson, D. N.; Sohn, Y. S.; Gray, H. B. *Inorg. Chem.* **1971**, *10*, 1559-1563.

(43) Turner, D. W. In *Physical Methods in Advanced Inorganic Chemistry*, 1st ed.; Hill, H. A. O.; Day, P., Eds.; Interscience Publishers: London, 1968.

(44) Levy, D.; Orgel, L. E. *Mol. Phys.* **1961**, *4*, 93-94.

(45) Rai, R. *Physica B* **1988**, *150*, 414-418.

(46) Sohar, P.; Kuszmann, J. *J. Mol. Struct.* **1969**, *3*, 359.

(47) Lever, A. B. P. *Inorganic Electronic Spectroscopy*, 2nd ed.; Elsevier: Amsterdam, 1984.

(48) Hendrickson, D. N.; Sohn, Y. S.; Gray, H. B. *J. Chem. Phys.* **1974**, *58*, 4666-4675.

(49) Rai, R. *Physica B* **1983**, *115*, 247-253.

(50) Bishop, D. M.; Dingle, T. W. *J. Chem. Phys.* **1968**, *48*, 541.

(51) Synder, P. A.; Lund, P. A.; Schatz, P. N.; Rowe, E. M. *Chem. Phys. Lett.* **1981**, *82*, 546-551.

(52) McHugh, A. J.; Gouterman, M.; Weiss, C. *Theoret. Chim. Acta.* **1971**, *24*.

(53) Hedaya, E. *IUPAC 23rd International Congress* **1971**, *4*, 195-214.

(54) Griffith, J. S. *The theory of Transition-Metal Ions*, 1st ed.; Cambridge University Press: London, 1961.

(55) Schatz, P. N.; Mowery, R. L.; Krausz, E. R. *Mol. Phys.* **1978**, *35*, 1537-1557.

(56) Fritz, H. P. In *Advances in Organometallic Chemistry*, 1st ed.; Stone, F. G. A.; West, R., Eds.; Academic Press: New York, 1964; Vol. 1.

(57) Atkins, P. W.; Friedman, R. S. *Molecular Quantum Mechanics*, 3rd ed.; Oxford University Press Inc.: New York, 1997.

8 THE CYCLOOCTATETRAENE RADICAL MONOANION

8.1 Introduction

Cylooctatetraene (C_8H_8; COT) was first synthesised by Willstatter and Waser in 1911 in an attempt to create a new nonbezenoid aromatic system.[1] Unfortunately, the species they produced was devoid of aromaticity, being a $2n$ rather than $2n+2$ π-electron system. It is now generally agreed that ground-state neutral COT is non-planar, taking a $\mathbf{D}_{2d}$ 'tub' conformation with alternating single and double bonds[2-4] However, the ions are found in a number of configurations including crown, chair, tub and octagonal or distorted planar, depending on charge and spin multiplicity.[5] Although the unsubstituted dication has not been observed, proton NMR indicates that the substituted analogues are planar and aromatic.[1-5] NMR evidence[1,5] and semi-empirical calculations[5] also show that the dianion is aromatic with $\mathbf{D}_{8h}$ symmetry. Shida and Iwata report the electronic spectra of the monocation and suggest that the ring is puckered ($\mathbf{D}_{2d}$) symmetry.[6]

It is the radical monoanion, COT^-, that is of interest in this chapter. No experimental work was performed on this system for this thesis. Instead, the theory developed in Chapters 3 and 5 was used to reinterpret some previous spectroscopic results, especially those for COT^- trapped in an Ar matrix, which were published by Samet *et al.*[2,7]

One of the more fundamental questions regarding this molecule is whether the aromatic stabilisation afforded to the radical by going into a planar configuration is sufficient to overcome the tendency of the σ C_8 frame to pucker in order to minimise C-C-C angle strain.[5] Another question that researchers have asked regarding the geometry of the species is the nature and extent of any JT coupling.

8.1.1 The Geometry of COT

Katz and Strauss[1] started their 1960 theoretical and experimental investigation of COT^- by showing that the neutral COT has a higher electron affinity than most molecules containing double bonds. They used this fact, in conjunction with qualitative MO theory (in the Hückel approximation) to predict that the radical

monoanion is planar. Essentially, the extra electron enters a e_{2u} orbital that is non-bonding in the planar structure but antibonding in the tub structure, and therefore the planar form is stabilised. They predicted the resonance energy gained by the monoanion (relative to the neutral) to be half that of the dianion.

Consideration of the hyperfine structure in the ESR spectra of COT^- by the same authors supported these conclusions.[1] They observed nine equidistant hyperfine lines separated by 3.21 gauss, exactly as expected for a planar radical with eight equivalent ring protons and a spin density of 1/8 on each carbon atom. The observed proton hyperfine splitting constant of -25 gauss is the usual value found for the negative ions of planar aromatics.

In 1968, by comparing calculated spectra for different geometries of COT^- with the experimental one in liquid ammonia at ~77 K, Kimmel and Strauss[3] found that permanent distortions of the ground state from D_{8h} are negligible. They also concluded that the radicals are planar and rigid. Later, Dvořák and Michl[8] came to similar view from the interpretation of spectra in 2-methlytetrahydofuran (2-MTHF) glass. These latter authors, however, went further and concluded that rigidity and planarity are preserved in the lowest excited state, whose geometry differs little from that of the ground state. They cited as evidence for this the near mirror-image symmetry between the emission and absorption spectra. Banerjee and Simons[9] found this conclusion to be consistent with their spectroscopic investigation of the species.

In a 1961 paper, McLachlan and Snyder[4] concluded that the values of the spin density fluctuations, as determined by EPR linewidth, were consistent with a planar structure for COT^- with an orbitally degenerate $^2E_{2u}$ ground state.

MO calculations[10] suggest that in COT^-, as in the benzene, coronene and triphenylene negative ions, JT distortions cause changes in electronic energy that are comparable to the energy of vibration, so dynamical coupling is expected. In their 1961 paper McLachlan and Snyder[4] concluded, from MO calculations in which resonance integrals and bond energies were allowed to vary with bond length, that the b_{1g} C-C stretch mode (1124 cm^{-1}) is JT active in the ground state, with $\lambda_{JT} \approx 1$, giving a JT stabilisation of ~824 cm^{-1}. Any JT stabilisation due to the other potentially JT active modes (b_{2g} C-C-C bend at 966 cm^{-1}) was predicted to be very much smaller.

Walsh-diagram analysis and *ab initio* calculations performed more recently by Trindle and Wolfskill[5] indicated, in agreement with the experimental results cited

above, that ground-state COT^- is planar, but that the puckered geometry (D_{2d}) is less stable by only 150 cm^{-1}. They noted that two skeletal modes meet the group-theoretical criteria for JT activity. One of b_{2g} symmetry (in-plane C-C-C bending at 966 cm^{-1}) would be opposed by the σ framework and would not produce significant splitting. The other, a b_{1g} C-C stretch (~1120 cm^{-1}) was predicted to distort the system from D_{8h} to D_{4h} symmetry, with bond-length alternation between 1.36 and 1.44 Å. Some semi-empirical calculation of the MINDO and AM1 type quoted in references 5 and 8 slightly favour a tub configuration.

Table 8.1: Vibrational frequencies (cm^{-1}), symmetries and assignments for COT^-

Calc.[2,a]	Obs.[2,c]	Symmetry			Assignment
		D_{8h}	D_{4h}	D_{2d}	
1180		e_{2u}	$b_{1u} \oplus b_{2u}$	$a_1 \oplus a_2$	
316	270	e_{2g}	$b_{1g} \oplus b_{2g}$	$b_1 \oplus b_2$	ring bend
597		b_{1u}	a_{1u}	b_1	ring pucker
710	720	a_{1g}	a_{1g}	a_1	ring breathe
726		b_{1u}	a_{1u}	b_1	
860		e_{2u}	$b_{1u} \oplus b_{2u}$	a_1 a_2	
966		b_{2g}	a_{2g}	a_2	C-C-C in-plane bend
1131		e_{2g}	$b_{1g} \oplus b_{2g}$	$b_1 \oplus b_2$	
1141	1120[b]	b_{1g}	a_{1g}	a_1	C-C stretch
1296	1600	b_{1g}	a_{1g}	a_1	C-H in plane bend
1504		e_{2g}	$b_{1g} \oplus b_{2g}$	$b_1 \oplus b_2$	
2857		b_{2g}	a_{2g}	a_2	
2927		a_{1g}	a_{1g}	a_1	

[a] *Ab initio* frequencies multiplied by the standard correction of 0.89. Bond lengths used: C–C, 1.403Å; C–H, 1.083Å. Reference coordinates are defined in Figure 8.1.

[b] Reported by Dvořák and Michl[8] and assigned in reference 2 as the ground-state active JT mode.

[c] These data were obtained from absorption and MCD spectra and therefore pertain to the excited state.

It is important to note here that MO calculations of JT coupling can be insensitive to dynamic effects. Although they identify minima in the electronic potential energy surfaces, they do not (normally) take account of dynamical effects that can lead to overall retention of higher symmetry.

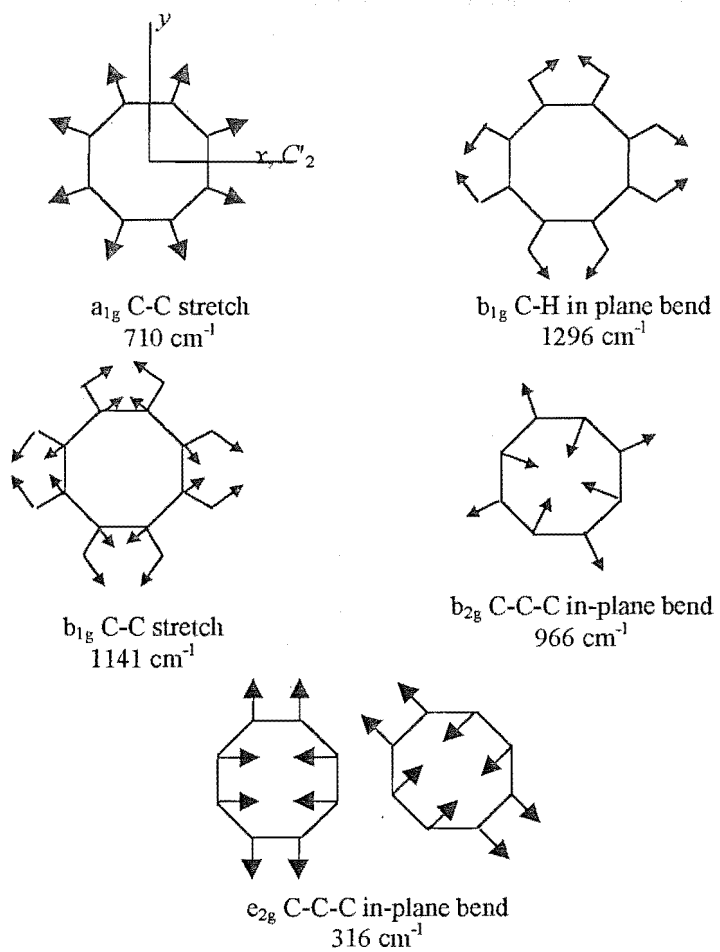

Figure 8.1: Some vibrational modes and calculated frequencies[2] for COT^-. Symmetries are given for $\mathbf{D}_{8h}$, with reference coordinates defined in the diagram for the a_{1g} C-C stretching mode.

8.1.2 Electronic States and Transitions

Assuming $\mathbf{D}_{8h}$ symmetry, COT^- has an open-shell e_{2u}^3 configuration, which corresponds to a $^2E_{2u}$ ground-state term (Section 3.2). The two lowest-energy orbital excitations are $e_{2u} \leftarrow e_{1g}$ and $e_{3g} \leftarrow e_{2u}$ (Figure 8.2). The former gives a $^2E_{1g}$ term, while the latter gives $^2E_{1g}$ and $^2E_{3g}$. Both $^2E_{1g} \leftarrow {}^2E_{2u}$ and $^2E_{3g} \leftarrow {}^2E_{2u}$ are electric-dipole allowed (*x*-*y* polarised) transitions.

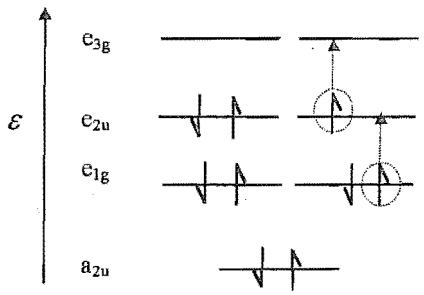

Figure 8.2: Energy level diagram for the π orbitals of COT^- showing the ground-state occupancy and the two lowest-energy orbital excitations.

Transitions have been observed for COT^- at ~395 nm (oscillator strength ~0.0024) and ~325 nm (oscillator strength ~0.028) by various workers.[2,3,8,9,11] Dvořák *et al.*[8] assigned the lower-energy system to a symmetry-allowed transition by noting that the origin bands in absorption and fluorescence were coincident and intense relative to surrounding structure. They also concluded that weaker bands in the ~360–400-nm region constitute vibrational structure built on the ~395-nm origin, since they move as a whole upon perturbation (different counter ions). Banerjee and Simons[9] came to the same conclusion after observing that these bands were uniformly shifted upon changing the solvent from ammonia to 2-MTHF glass. On the basis of theoretical calulations[6,11] (see below) they assigned the electronic transition to the $^2E_{1g} \leftarrow {}^2E_{2u}$.

Calculations of the transition energies and intensities of COT^- using π-electron methods with a zero-differential-overlap approximation (taking into account configuration interaction), were performed in 1968 by Kimmel and Strauss,[3] and found to agree qualitatively with the experimental data for both transitions. However, the oscillator strength of lower-energy transition was calculated to be substantially less than observed, and the authors commented that the excess intensity might be due to a vibronic contribution. Watanabe *et al.*[11] performed SCF-MO/CI calculations for 40 configurations (including some two-electron excitations) predicting that the lower energy transition is $^2E_{1g} \leftarrow {}^2E_{2u}$, comprising ~ 49% $e_{2u} \leftarrow e_{1g}$ and ~17% $e_{3g} \leftarrow e_{2u}$, while the ~325-nm transition is $^2E_{3g} \leftarrow {}^2E_{2u}$, almost entirely (>90%) due to $e_{3g} \leftarrow e_{2u}$.

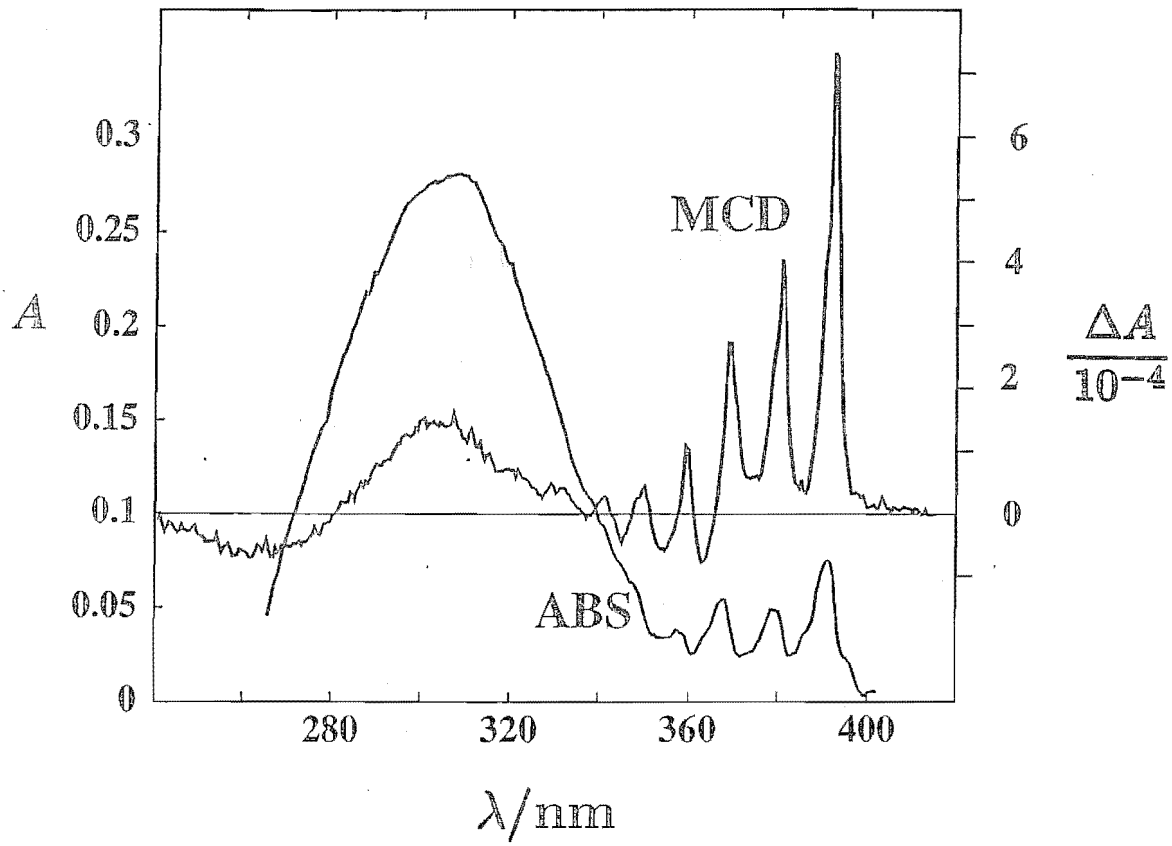

Figure 8.3: Absorption and MCD spectra of COT^-/Ar, adapted from Samet *et al* .[2]

8.1.3 MCD Studies

In 1994 Samet *et al.*[2,7] performed a detailed analysis of the MCD and absorption of COT^- trapped in an Ar matrix. Their sample was prepared by co-deposition of Cs atoms with a COT/Ar mixture (at a ratio of about 1/30). When a Cs atom was in sufficiently close proximity to a COT molecule, electron transfer occurred to form a loose ion pair Cs^+–COT^-. The absorption spectrum so obtained was very similar to those obtained previously for COT^- prepared by photoionisation of COT^{2-} in the presence of alkali metal cations[8] and irradiation with γ-rays[6] in 2-MTHF glass. The MCD of the system attributed to $^2E_{1g} \leftarrow {}^2E_{2u}$ had dispersion that was similar to the absorption, but had a number of negative bands and showed strong temperature-dependent indicating that $\mathcal{C}$ terms were dominant.

They fitted their $\mathbb{M}_0/\mathbb{A}_0$ vs $1/T$ data using equations 4.47 and 4.50 and obtained (in terms of the Faraday parameters described in (Section 4.4.1)) $\mathcal{C}_0/\mathcal{D}_0 \approx 0.02$ and $\mathcal{B}_0/\mathcal{D}_0 = 0.004$ (Figure 8.4).

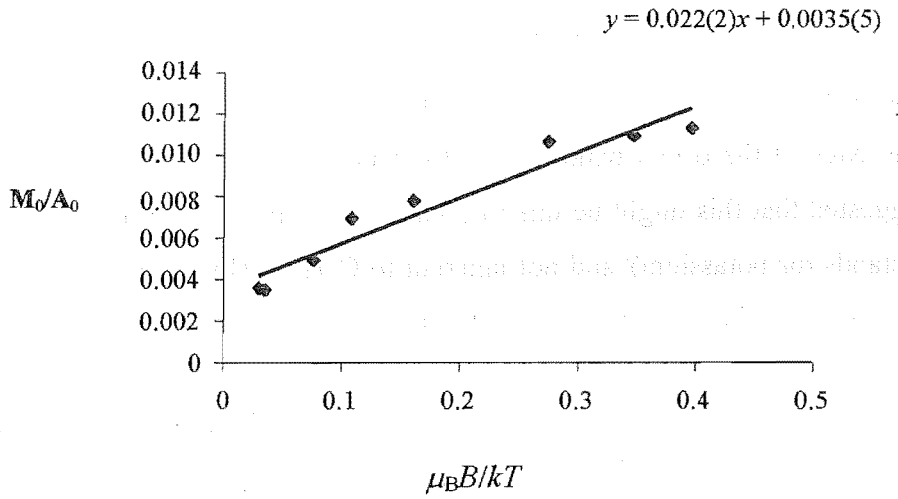

Figure 8.4: The dependence of the experimental M_0/A_0 data for COT^-/Ar^2 on $\mu_B B/kT$. The line is the best linear fit to the data.

8.1.4 Vibronic Structure in the $^2E_{1g} \leftarrow {}^2E_{2u}$ Transition

The $^2E_{3g} \leftarrow {}^2E_{2u}$ transition of COT^-, at ~325 nm, is broad and structureless. However, the $^2E_{1g} \leftarrow {}^2E_{2u}$ transition, extending to the blue from 395 nm, shows well-defined and relatively sharp structure (Figure 8.3). In particular, it exhibits pronounced progressions in modes of ~1600 and ~720 cm^{-1}.[2,8,9] The patterns of these progressions in the absorption spectra are mirrored in the MCD,[2] with the vibronic bands having the same sign as the origin, as is expected for totally symmetric modes.

Samet *et al.*[2] and Dvořák and Michl[8] assigned the 720-cm^{-1} progression to the totally symmetric C-C stretch (ring breathing mode), with a calculated ground-state frequency of 710 cm^{-1}.[2] There are no totally symmetric vibrations near 1600 cm^{-1}, (the only other a_{1g} mode in $\mathbf{D}_{8h}$ is the symmetric C-H stretch which will occur near 3000 cm^{-1}) and most of the authors who have observed the ~1600 cm^{-1} progression did not suggested an assignment. However Samet *et al.* assumed that it appears because the excited state takes a lower symmetry than the ground state, either $\mathbf{D}_{4h}$ or $\mathbf{D}_{2d}$ (their data did not permit them to differentiate between the two possibilities). The b_{1g} C-H stretch mode (calculated frequency of 1296 cm^{-1} in $\mathbf{D}_{8h}$), correlates with a totally symmetric mode in these lower point groups. However, their suggestion contradicts findings by Dvořák and Michl[8] that the excited-state symmetry differs little from that of the ground state.

Of particular interest here is a less-pronounced feature, a shoulder reported with a shift of ~270 cm^{-1} by Samet *et al.* and at ~ 300 cm^{-1} by Dvořák and Michl, on the blue edge of the origin band in the absorption (Figure 8.3).[2,8] Banerjee and Simons suggested that this might be due to a vibration of the ion trio $K^+ COT^- K^+$ (where the K stands for potassium)[i] and not inherent to COT^-.[9] However, in the MCD it appears as a negative band,[2] opposite to the sign of the origin (Figure 8.6), which is the unambiguous signature of a non-totally symmetric vibration. Samet *et al.*[2] decided that this band was due to a linear excited-state JT effect, and assigned the LJT-active vibration to a C-C deformation mode, calculated to have a 316-cm^{-1} ground-state frequency, which transforms as e_{2g} in $\mathbf{D}_{8h}$, correlating to $b_{1(g)} \oplus b_{2(g)}$ in $\mathbf{D}_{2d}$ (or $\mathbf{D}_{4h}$) - symmetry.

Samet *et al.* also found, from the temperature dependence of the zeroth MCD and absorption moments,[2] that the ground-state orbital angular momentum was very low – about 0.02 (in units of $\hbar$) compared to a theoretical value of 1.33 determined from an equation analogous to equation (7.74). They concluded that the quenching mechanism is a ground-state LJT effect involving an antisymmetric C-C stretching mode, with b_{1g} (in $\mathbf{D}_{8h}$) symmetry and ν_{JT} = 1141 cm^{-1}. Although they did not observe this mode in their spectra, they supported the assignment on the basis of theoretical arguments given by other workers,[4,5,8] and the observation, by Dvořák and Michl[8] of a 1120 cm^{-1} mode in the fluorescence spectrum of COT^- in 2-DMTF glass.

To account for the presence of $\mathcal{B}$ terms (non-zero ordinate intercept in Figure 8.4) Samet *et al.*[2] included a CF effect, as required for $\mathcal{B}$ terms in axial systems (Section 7.3.3). While the fit was better when a CF parameter was included, they noted that they could not conclusively prove the existence of a CF, since the addition of any parameter will improve the fit.

Using a model that assumed ground-state SO, CF and LJT effects, they obtained a'_2 = 0.2 cm^{-1},[ii] and V_{CF} = 4.4 cm^{-1}.[7] The JT parameters of the e_{2g} C-C-C in-plane bend were λ_{JT} = 1.30 ν_{JT} = 270 cm^{-1} and ε_{JT} = 964 cm^{-1}.[7] The SO coupling constant is

---

[i] Photoionisation of the salts of COT^{2-} with alkali metal cations in 2-DMTF glass at 77 K led to the formation of these triple ions. These were further transformed into ion pairs M^+COT^- and free COT^-

[ii] In reference 7 Samet *et al.* adjusted the ground state SO parameter from 32 cm^{-1} to less than 0.2 cm^{-1}, thus obtaining a significantly improved least-squares fit to the data was.

very small, as expected for a planar π system,[12] and the CF splitting is also very small, even compared to others results derived from experiment of other molecules inert matrices.[13,14] They noted, that the ground-state radical must be in the dynamic range of $\mathbf{D}_{8h}$ since lower symmetry would require a temperature independent MCD since $\mathbf{D}_{4h}$ and $\mathbf{D}_{2d}$ ground states would have zero orbital angular momenta. However, they also invoked JT effects in the $\mathbf{D}_{4h}$ or $\mathbf{D}_{2d}$ excited state. More detailed discussion of their work is deferred to the next section.

8.2 Discussion

8.2.1 A Ground-state Jahn-Teller Effect?

As explained in Section 5.4.2 an excited-state JT effect cannot cause the appearance of vibronic bands with opposite sign to the origin. Only a ground-state JT effect (or an entirely different mechanism) can achieve this.

To illustrate this point, a calculation was performed using the program DYNAMO (Section 5.5) and the JT parameters published by Samet *et al.* For the ground state these were $\lambda_{JT} = 1.3$, $\bar{\nu}_{JT} = 1140$ cm^{-1}, $g_2 = 0.04$, and $a'_2 = 0.2$ cm^{-1}. The excited-state parameters were $\lambda_{JT}' = 0.99$, $\bar{\nu}_{JT}' = 270$ cm^{-1}. In addition a totally symmetric mode with $\mathcal{L} = 1$, $\bar{\nu}_{a_{1g}} = 720$ cm^{-1} was also incorporated into the calculation. A second totally symmetric mode, meant to simulate an effective totally symmetric mode in a lower-symmetry excited state, with the parameters $\mathcal{L} = 0.85$, $\bar{\nu}_{a_{1g}} = 1600$ cm^{-1} is also included. In Figure 8.5 the result is compared with the experimental MCD spectrum obtained by Samet *et al.* for COT^{-}/Ar at $T = 1.69$ K. Clearly the model does not even approximately reproduce the experimental spectrum. In particular, it predicts a positive band where the first negative band is observed, while the strength of the ground-state LJT effect in a 1140 cm^{-1} mode should cause an intense negative MCD band which is not observed.

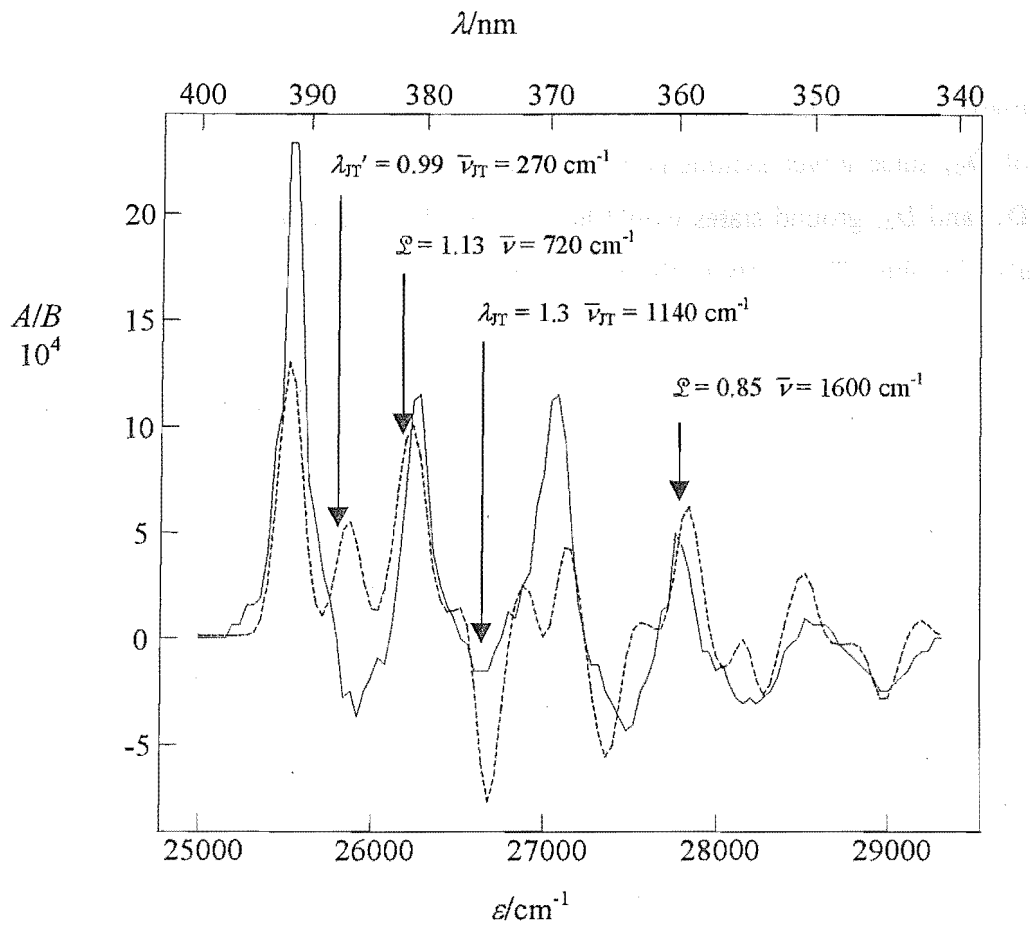

Figure 8.5: The MCD spectra of the $^2E_{1g} \leftarrow {}^2E_{2u}$ transition. The solid line is a reproduction of the spectrum obtained by Samet *et al.*[2] for COT^-/Ar at 1.69 K. The dashed line is a simulation created by DYNAMO assuming a excited-state LJT effect (270 cm^{-1}), a ground-state LJT effect (1140 cm^{-1}) and progressions in two totally symmetry modes (720 and 1600 cm^{-1}).

Next, attempts were made to fit the data (concentrating on the first negative band) using either a linear or quadratic JT effect in the ground state (Figure 8.6). In both cases the values $a'_2 = 0.2$ cm^{-1} and $g_2 = 3.66$ quoted in reference 7 were used.

In the LJT case, a satisfactory fit was found across the whole spectrum with $\bar{\nu}_{JT} = 380$ cm^{-1} and $\lambda_{JT} = 0.5$, which corresponds to $\kappa_{JT} = 0.74$ and $\varepsilon_{JT} = 48$ cm^{-1}. It is worth noting this required 380 cm^{-1} for the JT frequency, although Samet *et al.* used 270 cm^{-1}. Also, an excited-state JT effect was required to fit a band at ~1550 cm^{-1}

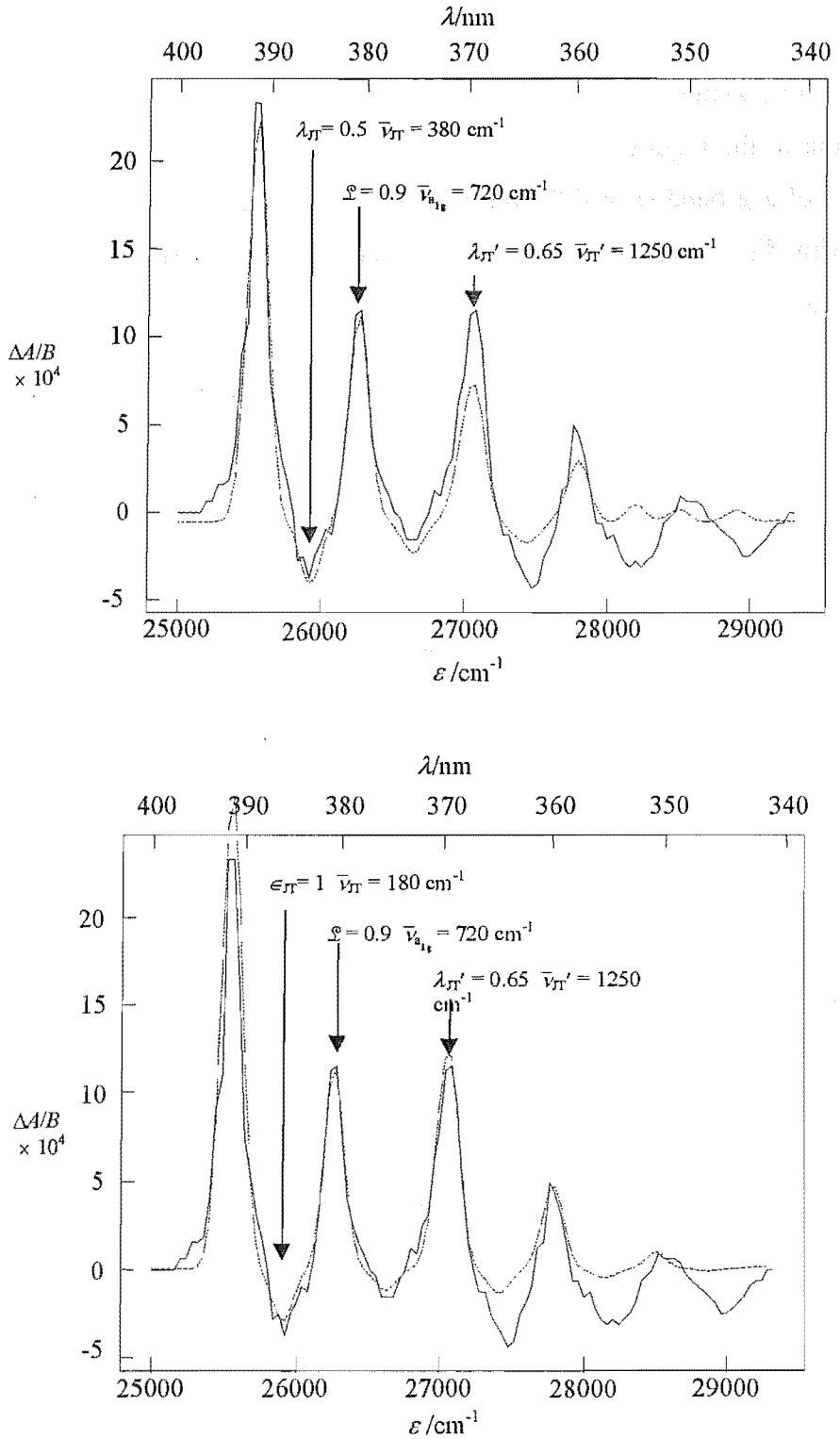

Figure 8.6: The MCD spectra of the $^2E_{1g} \leftarrow {}^2E_{2u}$ transition. The solid lines are the spectrum obtained by Samet *et al.*[2] for COT^-/Ar at 1.69 K. The dashed lines are simulations created by DYNAMO. At the top the negative band is fitted by assuming a linear ground-state JT effect with $\bar{\nu}_{JT} = 400$ cm^{-1} and $\lambda_{JT} = 0.6$. At the bottom it is fitted by a quadratic ground-state JT effect $\bar{\nu}_{JT} = 200$ cm^{-1} with $\epsilon_{JT} = 1$. Other modes are indicated on the figures, with primes indicating excited-state parameters

(see Section 8.2.3). The parameters for this mode were $\bar{\nu}_{JT}' = 1250$ cm^{-1} and $\lambda_{JT}' = 0.65$, corresponding to $\kappa_{JT} = 0.41$ and $\epsilon_{JT} = 265$ cm^{-1}. The reason for the apparent reduction in the required frequency can be seen be considering Figure 5.7. In the absence of a ground-state QJT, the first overtone transition terminates in the $N = 2$ level with $|K_1| = 1/2$, which with $\lambda_{JT} \approx 1$ occurs at a shift substantially greater that $\hbar\omega_{JT}$ above the zero-point level. Thus, for $\lambda_{JT} < 1$ the transition is to a state whose energy is increasing with increasing λ_{JT}. To fit the ~720 cm^{-1} band, a totally symmetry mode, with parameters $\bar{\nu}_{a_{1g}} = 720$ cm^{-1} ($\mathfrak{L} = 1$), corresponding, to the ring breathing mode is used. However, despite the very respectable agreement between the experiment and simulation, and even taking into account a reduction of frequency due to the lower bond order of the excited state, there are no vibrations of the requisite (b_{1g} or b_{2g} in $\mathbf{D}_{8h}$) symmetry required for LJT activity calculated to have the correct energy (Table 8.1).

In the QJT case, the negative band is well reproduced by a mode with $\bar{\nu}_{JT} = 180$ cm^{-1} with $\epsilon_{JT} = 1$, corresponding to a $\kappa_{JT} = 0.16$.[iii] The excited-state JT mode and totally symmetric mode were assigned exactly as in the previous paragraph. The lowest energy e_{2g} (ring bend) mode is predicted at 316 cm^{-1} (Table 8.1),[2] which is probably too high in energy. More importantly, $\epsilon_{JT} = 1$ represents a huge QJT effect, far larger than could reasonable be expected for this system. In the ground state the partially occupied orbital that is responsible for the electronic orbital angular momentum is the e_{2u} non-bonding orbital. So distortion forces should be relatively weak and unable to overcome the rigidity of the framework of σ bonding and six π bonding ($a_{2u}^2\, e_{1g}^4$) electrons.

It is therefore apparent that JT effects, ground or excited state, linear or quadratic, cannot explain the existence of the negative MCD bands, and an alternative explanation is required.

[iii] Consideration of Figure 5.8 shows why, the required frequency for a quadratically active mode is half that for a linearly active mode; the QJT effect couples states with $\Delta v = \pm 2$. The lowest vibronic levels of the ground state belongs to the $Q_{\pm 1}$ branches, which can have non-zero Franck-Condon overlap factors only with excited state levels of even v. The first overtone will therefore appear at $2\nu_{JT}$.

8.2.2 An Alternative Explanation – Herzberg-Teller Coupling

As noted above, Kimmel and Strauss[3] postulated that the intensity of the $^2E_{1g} \leftarrow {}^2E_{2u}$ transition of COT^- could be enhanced by vibronic coupling. In the same vein, it seems possible that the shoulder, with negative MCD, shifted ~ 400 cm^{-1} to the blue of the origin, could be a false origin in a non-totally symmetric mode that gains intensity by vibronic 'stealing' *via* Herzberg-Teller (HT) coupling with a nearby allowed electronic transition. Of the vibrations listed in Table 8.1, it is the e_{2g} ring bending mode with a calculated frequency of 316 cm^{-1} (the one assumed by Samet *et al.* to be responsible for the excited-state JT effect) which is the most likely candidate for a HT-active mode with a frequency of ~400 cm^{-1}.

The treatment starts with equation 3.81. Consideration of matrix elements of the form $\langle {}^2E_{1g}\ \lambda|(\partial V/\partial Q)^{e_{2g}}_{\gamma 0}|{}^2E_A\ \kappa\rangle^0$, using Tables 2.2 and 2.3 indicates that excited-state HT coupling through an e_{2g} mode can occur with $^2E_{3g}$ or $^2E_{1g}$ states. Both $^2E_{1g} \leftarrow {}^2E_{2u}$ and $^2E_{3g} \leftarrow {}^2E_{2u}$ are allowed transitions. MO calculations indicate that the strong ~300-nm band of COT^- is $^2E_{3g} \leftarrow {}^2E_{2u}$.[6,11] Thus, there is a $^2E_{3g}$ state, about 6000 cm^{-1} to higher energy, that fulfils the criteria for HT coupling *via* an e_{2g} mode with the $^2E_{1g}$ excited state. Rewriting equation 3.81 in a form relevant to the current problem gives

$$|{}^2E_{1g}\ \lambda\rangle|\nu\rangle = |{}^2E_{1g}\ \lambda\rangle^0|\nu\rangle^0 + \sum_{\nu',\kappa,\gamma} \frac{\langle {}^2E_{3g}\ \kappa|(\partial V/\partial Q)^{e_{2g}}_{\gamma 0}|{}^2E_{1g}\ \lambda\rangle^0}{W^0_{3,\nu'} - W^0_{1,\nu}} \langle \nu'|Q^{e_{2g}}_{\gamma}|\nu\rangle^0 |{}^2E_{3g}\ \lambda\rangle^0|\nu'\rangle^0 \qquad (8.1)$$

where $W^0_{3,\nu} = W_{3,\nu'}(Q_0)$ *etc* and $\left(\frac{\partial V}{\partial Q}\right)_0 \sim Q^{\dagger}$. For a transition at low temperatures (only the zero-point level of the ground state is significantly occupied) the non-zero electric dipole transition moments for $^2E_{1g} \leftarrow {}^2E_{2u}$ now take the form

$$\langle \nu|\langle {}^2E_{1g}\ \lambda|\boldsymbol{m}|{}^2E_{2u}\ \alpha\rangle|0\rangle = \langle {}^2E_{1g}\ \lambda|\boldsymbol{m}|{}^2E_{2u}\ \alpha\rangle^0 \langle \nu|0\rangle^0$$

$$+ \sum_{\nu',\kappa,\gamma} \frac{\langle {}^2E_{1g}\ \lambda|\left(\frac{\partial V}{\partial Q^{e_{2g}}_{\gamma}}\right)_0|{}^2E_{3g}\ \kappa\rangle^0 \langle {}^2E_{3g}\ \kappa|\boldsymbol{m}|{}^2E_{2u}\ \alpha\rangle^0}{W^0_{3,\nu'} - W^0_{1,\nu}} \langle \nu|Q^{e_{2g}}_{\gamma}|\nu'\rangle^0 \langle \nu'|0\rangle^0 \qquad (8.2)$$

The first term on the right vanishes except when $v = 0$ (the origin band). Since the electronic transition under consideration is $\Delta\Lambda = -1$, Table 5.8 indicates that the origin must have a positive $\mathcal{C}$ term. The second, HT term, is responsible for the 'stealing' of intensity from $^2E_{3g} \leftarrow {}^2E_{2u}$. It vanishes except when $v' = 0$ and $v = 1$, giving

$$\langle v|\langle {}^2E_{1g}\ \lambda|\boldsymbol{m}|{}^2E_{2u}\ \alpha\rangle|0\rangle_{HT} =$$

$$+\sum_{\kappa,\gamma}\frac{\langle {}^2E_{1g}\ \lambda|\left(\frac{\partial V}{\partial Q_\gamma^{e_{2g}}}\right)_0|{}^2E_{3g}\ \kappa\rangle^0\langle {}^2E_{3g}\ \kappa|\boldsymbol{m}|{}^2E_{2u}\ \alpha\rangle^0}{W_3^0 - W_1^0}\langle v|Q_\gamma^{e_{2g}}|0\rangle^0\delta_{v,1} \qquad (8.3)$$

The non-zero vibronic matrix elements and transition moments in equation (1.3) can be determined by using the WET. The appropriate 3*jm*s are (Appendix E)

$$\begin{pmatrix} 3 & 1 & 2 \\ \mp 3 & \pm 1 & \pm 2 \end{pmatrix} = \begin{pmatrix} 1 & 2 & 3 \\ \mp 1 & \mp 2 & \pm 3 \end{pmatrix} = -\frac{1}{\sqrt{2}}$$

which give

$$\frac{\langle {}^2E_{1g}\ \pm 1|\left(\frac{\partial V}{\partial Q_{\mp 2}^{e_{2g}}}\right)_0|{}^2E_{3g}\ \pm 3\rangle^0}{W_3^0 - W_1^0} = \frac{-\frac{1}{\sqrt{2}}\langle {}^2E_{1g}||\left(\frac{\partial V}{\partial Q^{e_{2g}}}\right)_0||{}^2E_{3g}\rangle^0}{W_3^0 - W_1^0} \equiv u \qquad (8.4)$$

and

$$\langle {}^2E_{3g}\ \pm 3|m_{\pm 1}^1|{}^2E_{2u}\ \pm 2\rangle^0 = -\frac{1}{\sqrt{2}}\langle {}^2E_{3g}||m^1||{}^2E_{2u}\rangle^0 \equiv (\mathcal{M}_3)_{\pm 1} \qquad (8.5)$$

so

$$\langle 1|\langle {}^2E_{1g}\ \pm 1|m_{\pm 1}^1|\,{}^2E_{2u}\ \pm 2\rangle|0\rangle_{HT} = u(\mathcal{M}_3)_{\pm 1}\langle 1|Q_{\mp 2}^{e_{2g}}|0\rangle \qquad (8.6)$$

Using equations (4.74), (4.50) and (4.55), the orientationally averaged zeroth absorption and MCD moments in the linear limit are

$$(A_0)_{HT} = \frac{1}{3}|u|^2|\mathcal{M}_3|^2|\langle 1|Q_{\mp 2}^{e_{2g}}|0\rangle|^2 \qquad (8.7)$$

$$(\mathbb{M}_0)_{HT} = \frac{-g_2}{6}|u|^2|\mathfrak{M}_3|^2|\langle 1|Q^{e_{2g}}_{\pm 2}|0\rangle|^2 \qquad (8.8)$$

where g_2 is the orbital g value of the ground state:

$$g_2 = \pm 2\ \langle E_{2u}\ \pm 2|l_z|E_{2u}\ \pm 2\rangle \qquad (8.9)$$

From equation (8.8), the $\mathcal{C}$ term for the HT false origin is negative, and therefore of the opposite sign to the origin. Although the above equations refer to the linear limit this sign is independent of these conditions.

It is useful at this point to check whether the proposed mechanism is reasonable – that is, whether the HT effect can qualitatively account for the observed spectral features. The effect of HT coupling on the spectrum of this transition can be simulated using DYNAMO and some jiggery-pokery.

The origin and JT band and the totally symmetric progression built on them were fitted in the same manner as described for the JT cases above, but with slightly adjusted FC overlap factors (720-cm^{-1} mode has $\mathfrak{L} = 1$). The intensity of the HT false origin is given by equation (8.6), which is essentially the intensity of the origin band multiplied by a (negative) scaling constant. The total HT intensity is then modelled by generating a second (false) origin with progressions multiplied by the scaling factor and shifted by the frequency of the HT-active vibration. The result obtained by adding the 'allowed' and HT spectra, using an arbitrary scaling constant of -0.06, is shown in Figure 8.7.

The fit in Figure 8.7 gives a good account of the data, at least as reasonable as the JT interpretation. However, this model has the advantage over the JT one in that there exists a mode of the correct symmetry (e_{2g}) and the correct frequency (~316 cm^{-1}) (Table 8.1) to give an MCD band of the correct sign. In addition there is an intense, nearby electronic transition, with the right symmetry ($^2E_{3g}$) to donate intensity. The discrepancy between the observed and calculated frequencies can be attributed to limitations of the calculation as well as the fact that the MCD and absorption data give frequencies of excited-state vibrations, which may be significantly different in both their the nature and frequency from those of the ground state.

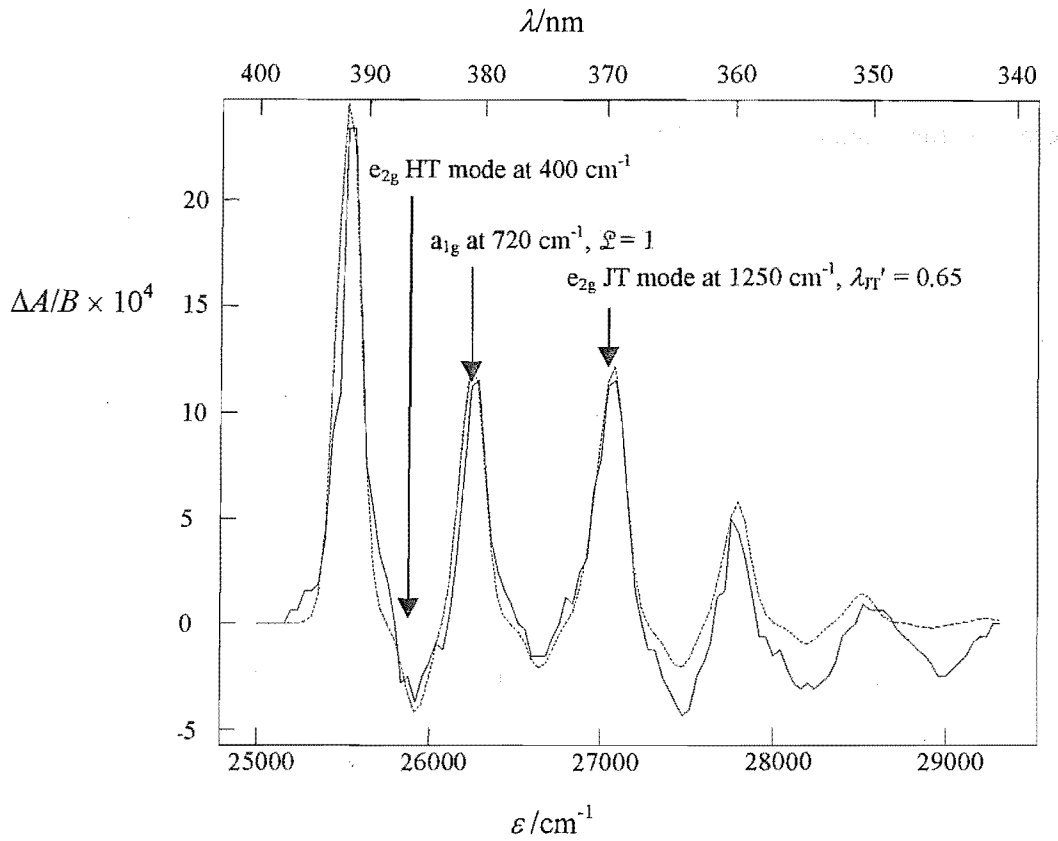

Figure 8.7: The MCD spectra of the $^2E_{1g} \leftarrow {}^2E_{2u}$ transition. The solid line is the spectrum obtained by Samet *et al.*[2] for COT^-/Ar at 1.69 K. The dashed lines are simulations assuming HT coupling of the excited state to a nearby $^2E_{3g}$ state *via* an e_{2g} mode, which causes the appearance of a negative band at 400 cm^{-1}.

A related system in which the HT effects have been well characterised is benzene,[15] in which the formally forbidden $^1B_{1u} \leftarrow {}^1A_{1g}$ transition steals all of its intensity from the nearby allowed $^1E_{1u} \leftarrow {}^1A_{1g}$ transition. In that system, the energy difference between the two HT-coupled excited states is ~8000 cm^{-1} and the percentage of 'stolen' intensity is ~17%. In the case under consideration here, the separation is closer to 6000 cm^{-1} and the stolen intensity is ~3% of the stronger transition, which is certainly not too large to be credible.

8.2.3 An Excited-state Jahn-Teller Effect?

As noted is Section 8.1.3, in their assignment of structure observed in the MCD, Samet *et al.* attributed the band with positive MCD at ~1550 cm^{-1} to an exited-state b_{2g} mode that appeared because of a lowering of excited-state symmetry. They

rejected the more obvious assignment to excited-state LJT activity in the 1504-cm^{-1} e_{2g} mode (Table 8.1) presumably in the erroneous belief that this would cause a negative MCD band. In the fits shown in Figure 8.6, the JT assignment has been preferred, with parameters listed in the figure.

The obvious question that arises is why should there be an excited-state JT effect but no significant ground-state effect? As described in Section 8.1.2 in the ground state of COT^-, the partially occupied orbital is non-bonding, so JT effects should be weak. However, with the promotion $e_{2u} \leftarrow e_{1g}$, not only is the bond order reduced, but the electronic angular momentum involved in JT coupling now comes from a bonding orbital. Therefore, the rigidity of the C_8 skeleton is reduced at the same time as the distortion forces become stronger, facilitating JT effects in the excited state.

8.2.4 Reduction of Ground State Orbital Angular Momentum

As well as an excited-state LJT mechanism to explain the appearance of a negative band in the MCD, Samet *et al.*[2,7] invoked a ground-state effect involving an e_{2g} ring bending mode to account for the quenching of ground-state angular momentum. In Figure 8.6, it was shown that such an assignment should lead to strong negative bands that are not observed. Furthermore, in the preceding section, it was shown that the negative MCD bands that do exist in the $^2E_{1g} \leftarrow {}^2E_{2u}$ transition envelope are probably a consequence of excited-state HT coupling with a higher-lying $^2E_{3g}$ state. So it appears the ground-state JT effects are too weak to be responsible for this orbital reduction, and an alternative explanation is required.

The most obvious choice is a CF effect, especially since the method of sample preparation (codeposition of a COT/Ar mixture with Cs atoms) almost certainly results in Cs^+ counter ions residing nearby in the matrix. In fact Samet *et al.*[2,7] attributed the small CF that they required at least in part to asymmetric placement of the Cs^+ ion(s) with respect to the COT^- C_8 axis.

For the treatment of a CF, the expressions developed for $Fe(cp)_2^+$ in Section 7.3.3 are appropriate. Assuming linear-limit conditions, a linear fit to the data in Figure 8.4 gives

$$\mathbf{M}_0/\mathbf{A}_0 = 0.022\mu_B B/kT + 0.0035 \qquad (8.10)$$

Allowing for ~17% of the intensity arising from HT effects, the first term of equations (8.10) and (7.74) requires

$$\kappa_{CF}(\kappa_{CF} g_2 + g_e)/2 = 0.022 \times 1.17/0.83 = 0.031$$

With $g_2 = 2.66$ (as predicted in reference 2) this gives

$$\kappa_{CF} = 0.030$$

$$g_{\parallel}^{-} = \kappa_{CF} g_2 + g_e = 2.08$$

$$g_{\perp} = \eta g_e = (1 - \kappa_{CF}^2)^{1/2} g_e = 2.00$$

Notably, this value of κ_{CF} is much smaller than the values of κ_{JT} calculated by DYNAMO using the linear and quadratic ground-state JT effects. These g values can be used in conjunction with the intercept and the second term of equation (8.10) to calculate a value for the SOC parameter:

$$a'_2 = \mu_B g_{\perp}^2 (g_{\parallel}^{-} - g_e)/(.0035 \times 1.17\, g_e^2/0.83) = 7.6 \text{ cm}^{-1}$$

The CF is now given by

$$V_{CF} = \sqrt{[(a'_2)^2((1/\kappa_{CF})^2 - 1)]} = 245 \text{ cm}^{-1}$$

Both of the last two parameters are much greater than determined by Samet *et al.* (~0.2 cm^{-1} and 4.4 cm^{-1} in 7). Furthermore $a'_2 \approx 7.6$ cm^{-1} is substantially greater than expected for π ring systems while $V_{CF} \approx 245$ cm^{-1} is large compared with CF splittings generally observed in Ar matrices. The explanation almost certainly lies with the nearby Cs^+ ions. These would not only exert a substantial CF, but also contribute to the SO coupling parameter of the radical *via* the external heavy-atom effect.

8.3 Conclusion

It is shown in this chapter that an excited-state JT effect cannot explain the existence of negative bands observed by Samet *et al.*[2,7] in the MCD of the $^2E_{1g} \leftarrow {}^2E_{2u}$ transition

of the COT^-/Ar. Although a ground-state effect would provide such bands, the absence of any vibrations of the required symmetry and frequency also makes this explanation unlikely. Instead a HT mechanism is suggested that involves vibronic 'stealing' of intensity from the nearby $^2E_{3g} \leftarrow {}^2E_{2u}$ transition *via* an e_{2g} vibrational mode with a frequency of ~400 cm^{-1}, assigned to the ring bending mode with a calculated ground-state frequency of 316 cm^{-1}. This gives an MCD of the correct sign (opposite to the fully allowed origin band). By comparing the HT intensity with that of the $^2E_{3g} \leftarrow {}^2E_{1u}$ transition, only ~3% of the intensity of the latter is stolen. Comparison with $^1B_{1u} \leftarrow {}^1A_{1g}$ of benzene shows this to be reasonable.

For most formally allowed transitions (such as $^2E_{1g} \leftarrow {}^2E_{2u}$), any HT intensity is completely overshadowed by the allowed components and is unobservable. COT^- appears to be a relatively rare case where the formally allowed transition is sufficiently weak that the HT intensity and is observable. Other examples include the porphyrins,[16] where the allowed Q band steals intensity from the higher-energy and much more intense B band, and the d-d transitions of $Co(en)_3^+$,[17] which are Laporte forbidden in octahedral symmetry, but become weakly allowed under the $\mathbf{D_3}$ distortion.

Spectral simulations have shown that there is an excited-state LJT effect involving an e_{2g} mode (calculated ground state frequency of 1504 cm^{-1}). The reason there is an observable excited-state but no ground-state JT effect may be due to the fact that the rigidity of the C_8 skeleton is reduced in the excited state at the same time as the distortion forces become stronger.

When combined with calculations of the CF and SO parameters, the spectroscopic simulations also show that it is not actually necessary to invoke a ground-state JT mechanism, as presumed by Samet *et al.*,[2,7] to effect the orbital quenching observed in this system. Reanalysis of the temperature-dependent moment data, taking into account the ~17% of the intensity attributed to the HT mechanism, gives $V_{CF} \approx 250$ cm^{-1}, but also requires a SO splitting parameters in the order of ~8 cm^{-1}. The former can be explained by invoking a substantial CF caused by a nearby Cs^+ counter ion. The latter is substantially greater than expected for planar delocalise π systems, and probably reflects an external effect due to the heavy counter ion.

8.4 References

(1) Katz, T. J.; Strauss, H. L. *J. Chem. Phys.* **1960**, *32*, 1873-1875.

(2) Samet, C.; Rose, J. L.; Piepho, S. B.; Laurito, J.; Andrews, L.; Schatz, P. N. *J. Amer. Chem. Soc.* **1994**, *116*, 11109-11119.

(3) Kimmel, P. I.; Strauss, H. L. *J. Phys. Chem.* **1968**, *72*, 2813-2817.

(4) McLachlan, A. D.; Snyder, L. C. *J. Chem. Phys.* **1962**, *36*, 1159-1162.

(5) Trindle, C.; Wolfskill, T. *J. Org. Chem.* **1991**, *56*, 5426-5436.

(6) Shida, T.; Iwata, S. *J. Amer. Chem. Soc.* **1973**, *95*, 3473-3483.

(7) Samet, C.; Rose, J.; Piepho, S. B.; Laurito, J.; Andrews, L.; Schatz, P. N. *J. Amer. Chem. Soc.* **1995**, *117*, 9381.

(8) Dvorak, V.; Michl, J. *J. Amer. Chem. Soc.* **1975**, *98*, 1080-1085.

(9) Banerjee, A.; Simons, J. *J. Chem. Phys.* **1978**, *69*, 5538-5544.

(10) Hobey, W. D.; McLachlan, A. D. *J. Chem. Phys.* **1960**, *33*, 1695-1703.

(11) Watanabe, T.; Shida, T.; Iwata, S. *Chem. Phys.* **1967**, *13*, 65-72.

(12) McClure, D. S. *J. Chem. Phys.* **1952**, *20*, 682-686.

(13) VanCott, T. C.; Rose, J. L.; Misener, G. C.; Williamson, B. E.; Schrimpf, A. E.; Boyle, M. E.; Schatz, P. N. *J. Phys. Chem.* **1989**, *93*, 2999-3011.

(14) Langford, V. S.; Williamson, B. E. *J. Phys. Chem. A.* **1998**, *102*, 138-145.

(15) Pitzer, K. S. *Quantum Chemistry*, 1st ed.; Prentice-Hall: New Jersey, 1953.

(16) Dolphin, D., Ed. *Porphryins*; Academic Press: New York, 1978; Vol. 3.

(17) Ferguson, J. In *Progress in Inorganic Chemistry*, 1st ed.; Lippard, S. J., Ed.; Interscience (John Wiley & Sons): New York, 1970; Vol. 12.

9 CYCLOPENTADIENYL

9.1 Introduction

The extent to which Jahn-Teller (JT) coupling modifies the electronic states of the cyclopentadienyl radical (C_5H_5· with $\mathbb{D}_{5h}$ symmetry) has been the subject of controversy. Experiment and theory give conflicting answers to questions regarding the nature and magnitude of the JT effect in these molecules.

In this chapter, absorption and temperature- and magnetic-field dependent MCD spectra are presented for the $^2A_2'' \leftarrow {}^2E_1''$ transition of C_5H_5· trapped in an Ar matrix. The intention was to use the model developed in Chapter 5 to obtain additional information that might illuminate some of the problems the about the JT effect. Unfortunately, it was not possible to obtain spectra of sufficient quality in the vibrational overtone region, so this chapter is largely restricted to a presentation of the results obtained for the origin band. Preliminary moment analysis is presented without any concerted attempt to draw conclusions.

9.1.1 The Cyclopentadienyl Radical

The precursor of cyclopentadienyl is dicyclopentadiene, $C_{10}H_{10}$, which consists of two five-membered carbon rings (each containing two double bonds) connected by a single C-C bond. Homolytic cleavage of this bond gives two C_5H_5· radicals. The five C p_z electrons on each radical occupy two delocalised π MOs (Section 7.3.1), giving a $^2E_1''$ ($a_1''^2\ e_1''^3$) ground state.

The absorption spectrum of C_5H_5· shows a band with vibrational structure which extends from 28 900 to 32 660 cm^{-1} (346 – 306 nm).[1-3] Comparison with calculations performed in the early 1960s[4,5] led to an assignment to the electronically allowed transition $^2A_2'' \leftarrow {}^2E_1''$ deriving from the $e_1'' \leftarrow a_1''$ excitation. Despite a number of efforts[1-3] a complete and unambiguous assignment of the vibrational structure is yet to be made. This is mainly due to the lack of vibrational data for the radical, which

has meant that assignments have generally been made by using the frequencies and assignments for the ground-state anion, $C_5H_5^-$.

The gas-phase absorption spectrum of C_5H_5·, reported by Engleman and Ramsay in 1970,[2] is dominated by two strong bands near 29 570 cm^{-1} and 29 902 cm^{-1}, the one at lower energy being assigned to the origin. The vibrational overtone region exhibits a great deal of complicated and congested structure. No clear progressions can be identified, although the ~330-cm^{-1} doubling of the structure in the origin region is repeated throughout the spectrum. These authors, suggested that the vibrational structure could probably be assigned on the basis of three vibrations with frequencies of 798, 1022, and 1055cm^{-1}. This view was later supported by Purins and Feely,[3] who associated these frequencies with the $C_5H_5^-$ modes given in Table 9.2. The first is a totally symmetric C-C stretching mode, while the other two are e_2' mode (respectively C-C and in-plane C-H deformation), which are potentially LJT active in the ground state.

Engleman and Ramsay[2] suggested that a band at ~330 cm^{-1} might be due to a ground-state JT effect, presumably with the two bands representing transitions originating from different vibronic levels. However Engelking and Lineberger[1] believed this assignment to be incorrect. Firstly, by examination of the structure in UV and IR spectra, obtained by Hedaya,[6,7] of C_5H_5· at low-temperatures in inert gas matrices, they noted that the 330 cm^{-1} band persisted at low temperatures, which eliminates the possibility that it is a hot band. And secondly, a permanent ground-state distortion is not possible because C_5H_5· does not belong to that category of molecules (those with $3n$-fold symmetry – see Section 5.2.1.3) where linear and quadratic effects are possible in a single mode in the same electronic state. Instead, Purins and Feely[3] suggested that, due to its calculated intensity and decreasing frequencies with increasing deuteration, it could be caused by a C-H out-of-plane bending mode. For such a mode to appear, it is necessary to assume that C_5H_5· excited state is non-planar, with a symmetry in which the 330-cm^{-1} mode transforms as a_{1g}. A major problem with this interpretation is the fact that it would predict an extended progression in 330 cm^{-1}, which is not observed.

It can be seen from Table 9.1, that C_5H_5· has four e_2' vibrational coordinates that are potentially LJT active in the ground state. In addition, a further a mode of e_1''

symmetry may be quadratically active. In 1960 Hobey and McLachlan[8] and Synder[9] performed semi-empirical MO (Hückel) calculations of the JT stabilisation of the $C_5H_5^{\cdot}$ ground state, finding the e_2' C-C stretch (ν_{10}, 1447 cm^{-1}) has $\varepsilon_{JT} \approx 500$ cm^{-1}, which corresponds to $\lambda_{JT} \approx 0.831$. As they and others[1,3] have pointed out, this is in the order of magnitude of the zero-point energy of the vibration and so dynamic JT coupling is expected to be significant. *Ab initio* calculations performed later by Meyer *et al*[10] gave a much larger value of $\varepsilon_{JT} \approx 5000$ cm^{-1} in ν_{10} ($\lambda_{JT} \approx 4$) and 2000 cm^{-1} in ν_{13} ($\lambda_{JT} \approx 2.5$).

Table 3.1: Symmetry species of vibrational modes for $C_5H_5^-$ (D_{5h} symmetry) from $K^+[C_5H_5^-]$ data[11] unless otherwise stated.

D_{5h} irrep label	frequency (cm^{-1})	potential ground-state JT activity	approximate type of vibration	mode label
a_1'	3043		C-H stretch	ν_1
a_1'	983		C-C stretch	ν_2
a_2''	710		C-H out-of-plane deformation	ν_3
a_2'	1250[a]		C-H in-plane deformation	ν_4
e_1'	3039		C-H stretch	ν_5
e_1'	1455		C-C stretch	ν_6
e_1'	1003		C-H in-plane deformation	ν_7
e_1''	625	quadratic	C-H out-of-plane deformation	ν_8
e_2'	3096	linear	C-H stretch	ν_9
e_2'	1447	linear	C-C stretch	ν_{10}
e_2'	1020	linear	C-H in-plane stretch	ν_{11}
e_2''	1060[a]		C-H out-of-plane deformation	ν_{12}
e_2'	565	linear	ring in-plane deformation	ν_{13}
e_2''	625[b]		ring stretch	ν_{14}

[a] $Fe(C_5H_5)_2$ frequency[12]

[b] C_5H_5 BeCl frequency[13]

It has been noted[1,3] that spectral simulations for $C_5H_5^{\cdot}$ do not correspond closely to the experimental spectra, particularly with regard to the intensity pattern. A number of theoretical calculations[3,14] suggest that this is because the ground electronic

states are coupled by more than one JT mode. Purins and Feely[3] showed, using LJT coupling parameters (λ_{JT}) calculated by semi-empirical methods for three modes (ν_{10}, ν_{11} and ν_{13}, see Table 9.2), that the activity of several LJT active modes markedly distorts the vibrational pattern of the $^2A_2'' \leftarrow {}^2E_1''$ transition of $C_5H_5^{\cdot}$. Effects include loss of intensity from higher vibrational satellites and the appearance of combination bands.

Engelking and Linberger[1] used evidence from the photoelectron spectra of the anion, $C_5H_5^-$, to argue for a much weaker effect. They concluded that most of the JT coupling occurs in one LJT mode, ν_{11} (C-H in-plane bending mode; 1020 cm^{-1}), with $\lambda_{JT} \approx 0.3$, giving $\varepsilon_{JT} \approx 46$ cm^{-1}. However, they also suggested that ν_{10} (1447 cm^{-1}) may also be weakly JT active, with $\lambda_{JT} < 0.1$. They commented that the weakness may be due to the underlying rigidity of σ-bond system. Only the single unpaired electron in the e_1'' MO will contribute to the JT distortion, which has to compete against restoring forces due to the σ system and remaining four electrons in the π system.

Table 9.2: Vibrational modes attributed responsibility for JT effects in the $^2E_1''$ ground state of $C_5H_5^{\cdot}$

	$C_5H_5^-$ obs. frequency[3] cm^{-1}	λ_{JT}[3]	ε_{JT}/cm^{-1}	λ_{JT}[1]	ε_{JT}/cm^{-1}	λ_{JT}[10]	ε_{JT}/cm^{-1}	λ_{JT}[8,9]	ε_{JT}/cm^{-1}
$\nu_9(e_2')$	3096	0.03	1.4						
$\nu_{10}(e_2')$	1055	1.90	1905	< 0.1	<5	2.6	5064	0.8	495
$\nu_{11}(e_2')$	1022	1.19	724	~ 0.3	~ 46				
$\nu_{13}(e_2')$	565	0.58	95			2.8	2270		

From these results it is abundantly clear that the JT effects in $C_5H_5^{\cdot}$ are far from being well characterised. It was the intention of this work to bring the technique of MCD to bear on the problem.

9.2 Results

Initial MCD spectra of C_5H_5•/Ar were obtained using the closed-cycle He refrigerator and electromagnet using the methods described in Section 6.2.2. As for the case of $Fe(cp)_2^+$ (Chapter 7), the best spectra were obtained after depositing small amounts of material, which meant that the absorption was weak, and the signal-to-noise ratio was poor. The signal-to-noise ratios of both the absorption and MCD suffered by the fact that the spectrometer optics have decreasing transmission at wavelengths below ~300 nm, leading to the steep baseline shown in Figure 3.1.

The origin band of the $^2A_2'' \leftarrow {}^2E_1''$ electronic transition was observed at ~29 800 cm^{-1} (336 nm) (Figure 3.1), shifted slightly to the blue of the gas-phase value. Another band is observed shifted by ~2600 cm^{-1} to the blue, which was not seen in previous spectra.[1,15] There is no sign of the 300 cm^{-1} or 1150 cm^{-1} bands discussed previously but there is a broad band at ~30 770 cm^{-1} (shifted by about 970 cm^{-1} from the origin). The MCD of the origin band shows the dispersion of a negative $\mathcal{A}$ term, whereas the highest-energy band (~2600 cm^{-1}) has a negative absorption-like dispersion, characteristic of a $\mathcal{C}$ or $\mathcal{B}$ term.

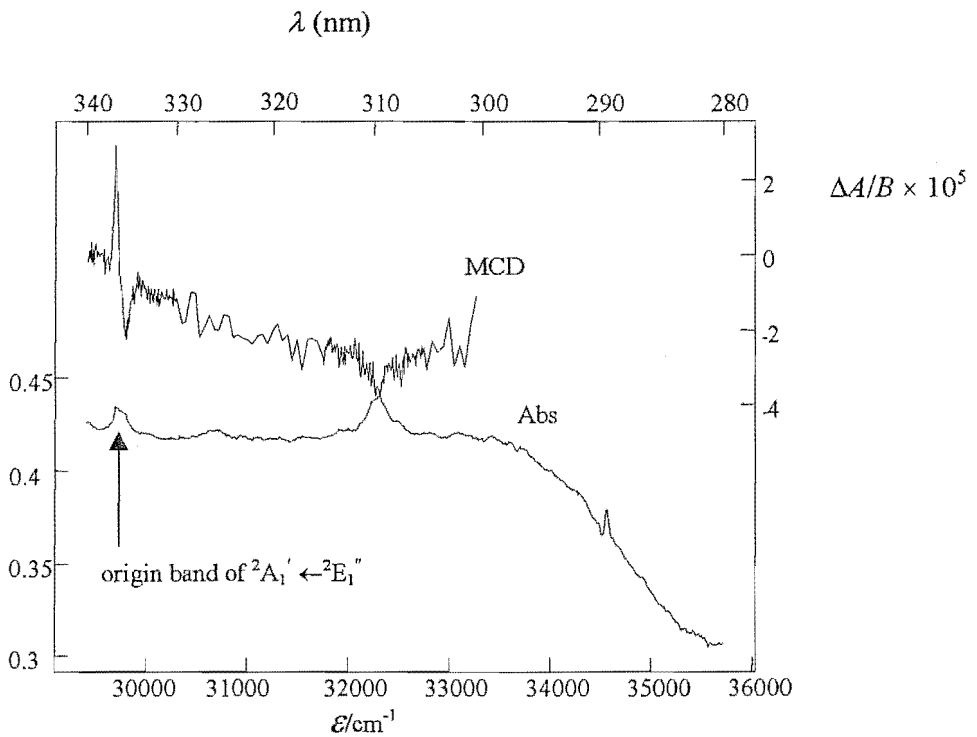

Figure 3.1: Spectra, prior to baselining, of C_5H_5•/Ar obtained on the He refrigerator/electromagnet system at ~12 K and 0.6 T. Top, MCD (per tesla): bottom, absorption.

The highest-energy band was not observed in spectra obtained on the SM4 system. Probably, it is not due to $C_5H_5^{\bullet}$, a conclusion that would also explain the different dispersion forms of the MCD. However, the temperature- and magnetic-field dependence of the origin band were determined, and are shown in Figure 3.2. Clearly the MCD features are not true $\mathscr{A}$ terms since they show inverse temperature dependence. Instead, they constitute pairs of $\mathscr{C}$ terms of opposite sign and similar magnitude separated by ~100 cm^{-1}. The appearance of two bands indicates two levels separated also by ~100 cm^{-1}. These can't be in the ground state since a significant population in the upper state could not be sustained at such low temperatures.

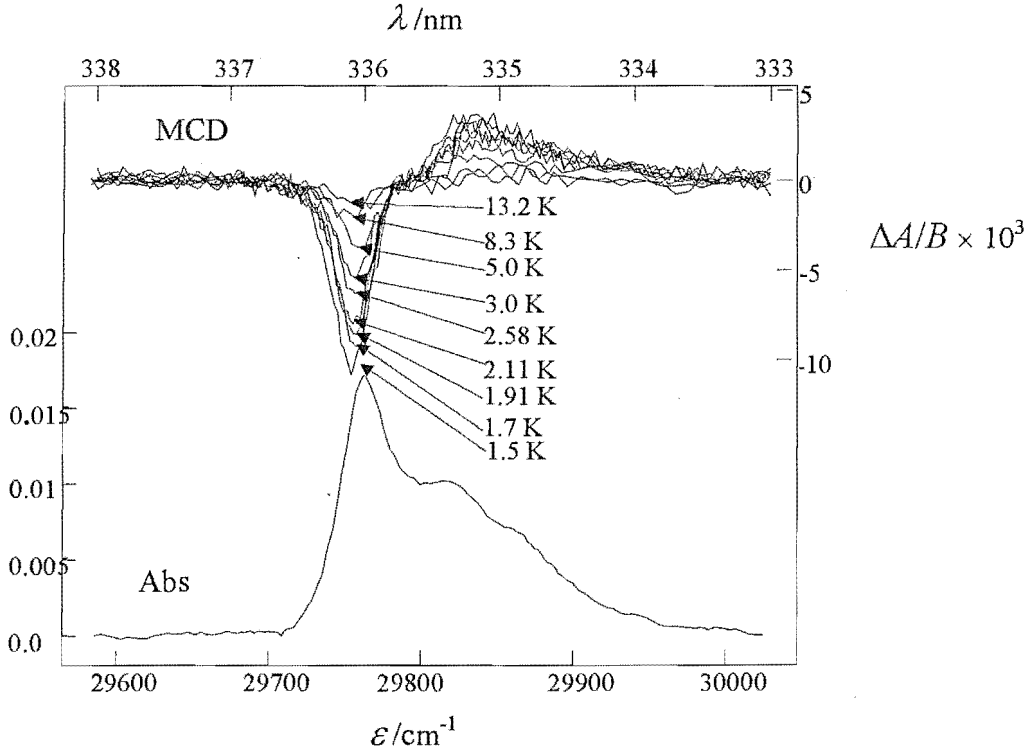

Figure 3.2: Spectra of $C_5H_5^{\bullet}$/Ar obtained at 1 T and the indicated temperatures by using the SM4/matrix-injection system. Top, MCD per tesla: bottom, absorption.

Since the contributions to the zeroth MCD moment, $\mathbf{M}_0$, of the two MCD lobes cancel, it is more convenient to determine the first MCD moment, $\mathbf{M}_1$, defined by equation (4.49). The results are plotted as functions of $\mu_B B$ and $\mu_B B/kT$ in Figure 3.3 and Figure 3.4 respectively, and show the saturation behaviour expected for $\mathscr{C}$ terms. It is difficult to tell, in the second plot, whether the data at different temperatures lie

on the same curve within experimental error. Thus it is not clear whether or not temperature-independent contributions from $\mathcal{A}$ and/or $\mathcal{B}$ terms are significant.

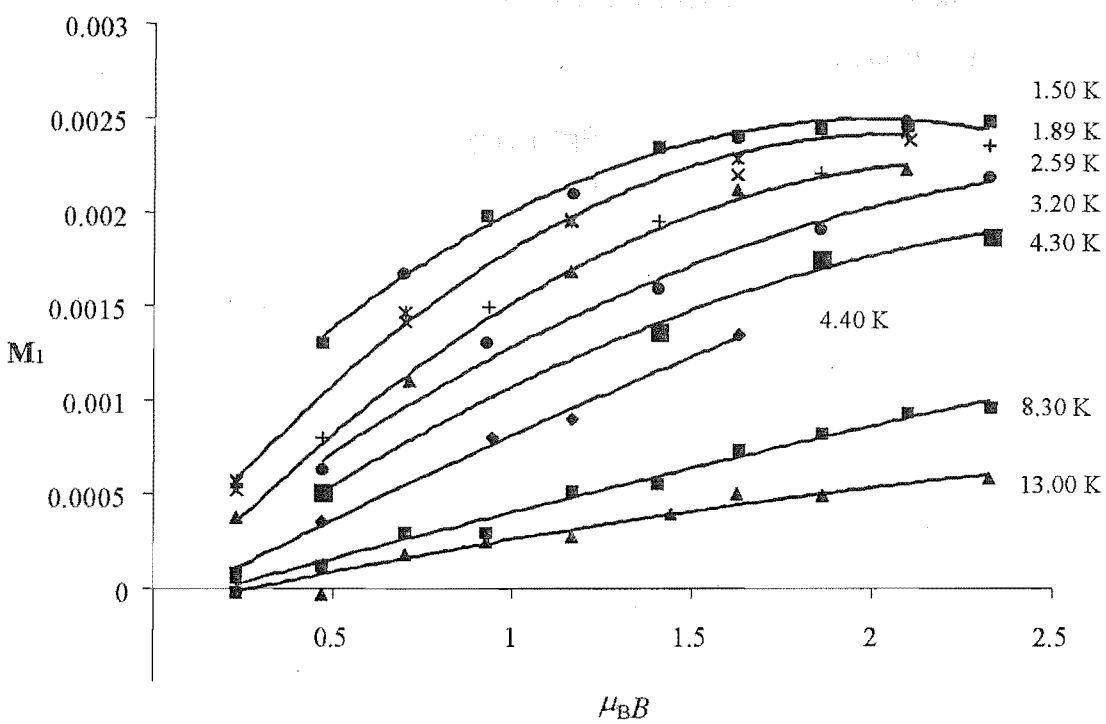

Figure 3.3: First MCD moments for $C_5H_5^{\bullet}$/Ar plotted as a function of $\mu_B B$ at the indicated temperatures. Curves are drawn to guide the eye.

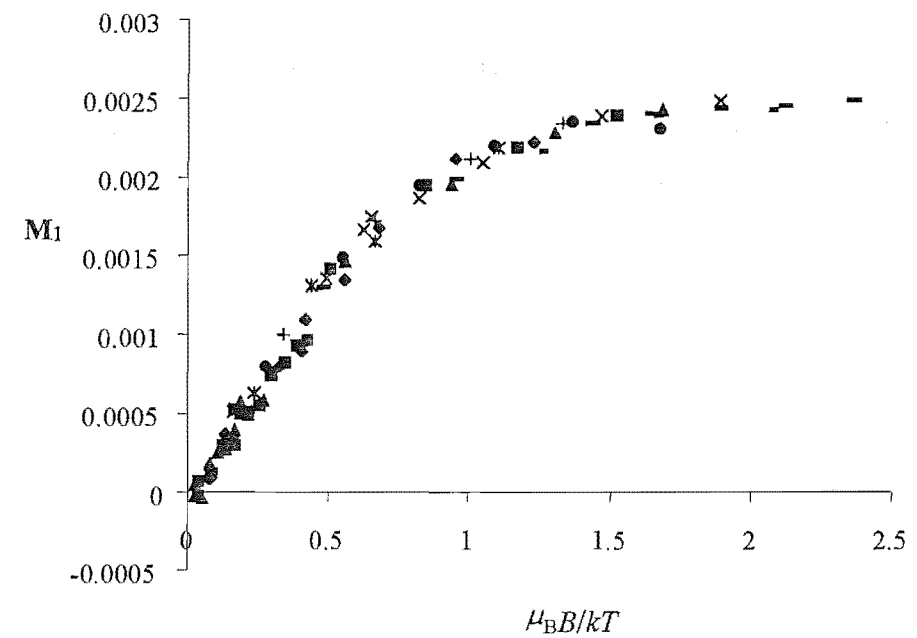

Figure 3.4: First MCD moments for $C_5H_5^{\bullet}$/Ar plotted as a function of $\mu_B B/kT$.

9.3 Discussion and Conclusion

The states of the $^2E_1''$ term are determined according to Section 3.2.2.1. In the $|^{2S+1}E_A\ M_A\ \Sigma\rangle$ basis

$$|^2E_1''\ 1\ -1/2\rangle = |-1^-\ 1^-\ 1^+\rangle$$

$$|^2E_1''\ -1\ -1/2\rangle = |-1^-\ -1^+\ 1^-\rangle$$

$$|^2E_1''\ 1\ 1/2\rangle = |-1^+\ 1^-\ 1^+\rangle$$

$$|^2E_1''\ -1\ 1/2\rangle = |-1^-\ -1^+\ 1^+\rangle$$

These are split by SO coupling with splitting parameter

$$a'_1 = -2\langle ^2E_1''\ 1\ -1/2|\ \mathcal{H}_{so}|\ ^2E_1''\ 1\ -1/2\rangle \qquad (3.1)$$

However, as explained in Section 3.3.2, SO coupling in a planar delocalised π system is expected to be very weak and so a'_1 should be small.

From Section 7.3.1, the orbital g value of the e_1'' orbital is predicted to be

$$g_1 \approx 1.6$$

Then from Table 3.5, for a molecule whose symmetry axis is at angle θ with respect to the magnetic field, the Zeeman shifts (in the absence of CF and/or JT effects) of the states within the ground-state electronic manifold of cyclopentadienyl are

$$\langle ^2E_1''\ \pm1\ \pm1/2\ |\mathcal{H}_{Zeeman}|^2E_1''\ \pm1\ \pm1/2\rangle = \pm(g_1 + g_e)\,\mu_B B\cos\theta\,/2 \qquad (3.2)$$

$$\langle ^2E_1''\ \pm1\ \mp1/2\ |\mathcal{H}_{Zeeman}|^2E_{2g}\ \pm1\ \mp1/2\rangle = \pm(g_1 - g_e)\mu_B B\cos\theta\,/2 \qquad (3.3)$$

The $^2A_2''$ excited-state wavefunctions are

$$|^2A_2''\ 0\ \pm1/2\rangle = |0^{\pm}\rangle$$

Since these have only spin degeneracy, there is no spin-orbit splitting, and the Zeeman shifts are orientation independent, with values

$$\langle {}^2A_2'' \; 0 \; \pm 1/2 | \mathcal{H}_{\text{Zeeman}} | {}^2A_2'' \; 0 \; \pm 1/2 \rangle = \pm g_e \mu_B B/2 \qquad (3.4)$$

In $\mathbf{D}_{5h}$, the electric-dipole operators $m_{\pm 1}$ transform as partners of the irrep e_1'. Using the WET and the HSCC of Appendix D, the non-zero electric dipole moments for the ${}^2A_2'' \leftarrow {}^2E_1''$ transition are

$$\langle {}^2A_2'' \; 0 \; \Sigma | m_{\pm 1} | {}^2E_1'' \; \mp 1 \; \Sigma \rangle = \mathcal{M}_{+1} \qquad (3.5)$$

The SO and Zeeman levels, as well as the allowed transitions between them, are summarised in Figure 3.5.

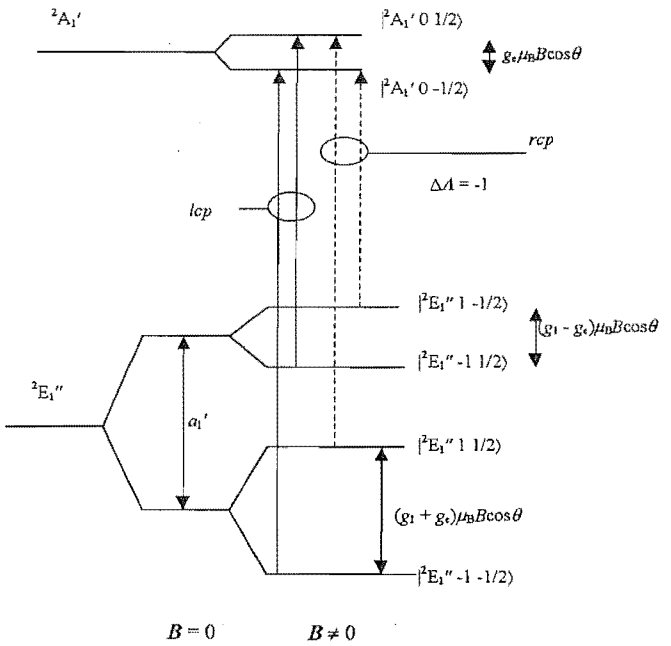

Figure 3.5: Spin-orbit and Zeeman splittings for the ${}^2A_2''$ and ${}^2E_1''$ states of C_5H_5. Transitions are indicated with solid lines for left circular polarisation and the dashed lines for right circular polarisation.

The temperatures at which these experiments were conducted are so low ($\lesssim$13 K) that the only populated levels must lie within a few tens of cm^{-1} of the lowest level. When this is combined with an orbitally non-degenerate excited state, there is no way that the ${}^2A_2'' \leftarrow {}^2E_1''$ assignment can account for a pair of oppositely signed $\mathcal{C}$ terms required to give the temperature-dependence and dispersion seen in Figure 3.2.

There are only two possible conclusions from these observations. Either, the species responsible for the observed transition is not cyclopentadienyl, or the $^2A_2'' \leftarrow {}^2E_1''$ assignment is incorrect.

With respect to the latter possibility, an alternative assignment could be $^2E_2'' \leftarrow {}^2E_1''$ derived from the orbital excitation $e_2'' \leftarrow e_1''$. This would, in some ways, be analogous to the $A^2\Delta \leftarrow X^2\Pi$ transition of CH/Ar,[16] which shows a temperature-dependent pseudo-$\mathcal{Q}$ term at temperatures above ~5 K. If a $^2E_2''$ excited state were distorted to C_s or C_{2v} symmetry (as suggested by Purins and Feely[3]) it would split into to orbitally non-degenerate electronic states, leading to two transitions. This speculation could also possibly account from the 330 cm^{-1} doubling observed in the gas-phase[15] and matrix-isolated[6,7] spectra by previous authors. Although this latter possibility is perhaps worthy of investigation, it is unlikely provide any information about the JT effects in cyclopentadienyl and was not pursued further in this research.

9.4 References

(1) Engelking, P. C.; Lineberger, W. C. *J. Chem. Phys.* **1977**, *67*, 1412-1417.

(2) Engleman, R.; Ramsay, D. A. *Canadian Journal of Physics* **1970**, *48*, 964-969.

(3) Purins, D.; Feeley, H. F. *J. Mol. Struct.* **1973**, *22*, 11-27.

(4) Longuet-Higgins, H. C.; McEwen, K. L. *J. Chem. Phys.* **205**, *26*, 719-723.

(5) Bouman, N. *J. Chem. Phys.* **1961**, *35*, 1661-1664.

(6) Hedaya. *Accounts of Chemical Research* **1969**, *2*, 367-373.

(7) Hedaya, E. *IUPAC 23rd International Congress* **1971**, *4*, 195-214.

(8) Hobey, W. D.; McLachlan, A. D. *J. Chem. Phys.* **1960**, *33*, 1695-1703.

(9) Synder, L. C. *J. Chem. Phys.* **1960**, *33*, 619-620.

(10) Meyer, R.; Graf, F.; Ha, T.-K.; Guthard, H. *Chem. Phys.* **1979**, *66*, 65-71.

(11) Sado, A.; West, R.; Fritz, H. P.; Schafer, L. *Spectrochim. Acta* **1966**, *22*, 509-515.

(12) Rodenheimer, J. S.; Low, W. *Spectrochim. Acta* **1973**, *29*, 1733.

(13) Coe, D. A.; Nibler, J. W.; Cook, T. H.; Drew, D.; Morgan, G. L. *J. Chem. Phys.* **1975**, *63*, 4842.

(14) Sloane, C. S.; Silbey, R. *J. Chem. Phys.* **1972**, *56*, 6031-6043.

(15) Simons, J. *J. Chem. Educ.* **1991**, *68*, 131-132.

(16) Langford, V. S.; Williamson, B. E. *J. Phys. Chem. A.* **1998**, *102*, 138-145.

10 SUMMARY

The objectives of the work described in this thesis were to develop a theoretical framework for using absorption and magnetooptical spectroscopic techniques to characterise the Jahn-Teller (JT) effect in axial molecules, and then to test that formalism. Particular regard was paid to the potential for temperature and magnetic-field dependent magnetic circular dichroism (MCD) and absorption data to yield information about both the ground and excited states.

The theoretical aspects, which took the larger part of the time and effort expended during the project, were described in Chapter 5. Earlier models have been used to explain the absorption spectra of axial molecules,[1-3] but the one presented here is specifically oriented towards MCD spectroscopy. It is also more general than the earlier models, allowing for the possibility of linear and quadratic JT coupling in the ground and excited state, as well as simultaneous spin-orbit effects. One very useful and general result that came out of this model is that MCD bands due to the JT effect and having the opposite sign to the origin band of the transition must be caused by a ground-state JT effect.

A computer program, DYNAMO, based on the theoretical expressions, was written to fit experimental spectra. This enabled the nature (excited or ground state, linear or quadratic, and frequency) of the active modes to be determined and the magnitude of any effect to be quantified (by parameters λ_{JT}, ϵ_{JT} and ε_{JT}). It also enabled the reduction of orbital angular momentum (κ_{JT}) caused by the JT effect to be quantified.

Three case studies were considered to test the effectiveness of this model. One of these (Chapter 9) was the case of the cyclopentadienyl radical, $C_5H_5^{\cdot}$, isolated in an Ar matrix. Unfortunately, the quality of the data was too poor to enable a proper vibronic analysis. The data that were obtained relate only the origin band and nothing can be extracted about JT coupling. However they do suggest that the assignment of the 336 nm transition to $^2A_2'' \leftarrow {}^2E_1''$ could be erroneous, since this cannot possibly the observed two-signed and temperature dependent nature of the MCD. A more definitive conclusion awaits better and more detailed experimental work.

Another case study (described in Chapter 8) employed data for the $^2E_{1g} \leftarrow {}^2E_{2u}$ transition of COT^- (with Cs^+ counter ions) in an Ar matrix obtained from a previously publication.[4,5] It was found necessary to use an excited-state JT effect to explain a positive MCD band shifted about 1600 cm^{-1} from the origin. However, it was also shown that the negative vibronic band at 490 cm^{-1} from the origin could not, as had been previously supposed, be due to an excited-state JT effect and is probably not due to a ground-state JT effect either. Instead, excited-state HT coupling was invoked, involving an e_{2g} mode (ring bend at ~316 cm^{-1}) and resulting in intensity stealing from a nearby $^2E_{3g} \leftarrow {}^2E_{2u}$ allowed transition. Analysis shows that such an effect gives rise to a vibronic side band with the observed MCD sign.

The fact that a JT effect was observed in the excited state of COT^- but not in the ground state was rationalised in terms of the lower bond order and stronger JT distortion forces in the excited state. In the absence of a ground-state effect, the severe quenching of the ground-state orbital angular momentum was explained in terms of a SO-CF model. The CF and SO effects were found to be an order of magnitude larger than previously determined.[4,5] This can be explained by the presence of Cs^+ counter ions, which could exert a large CF and increase the SOC.

The major part of the experimental work (Chapter 6) concerned the radical cation ferricenium, $Fe(cp)_2^+$, generated by photoionisation by a microwave discharge in Ar, and trapped into solid Ar matrices. This radical exemplifies some interesting aspects of metal-ligand bonding but, unlike its precursor, has non-zero ground (and excited) state angular momentum. In fact one of the major problems with studying $Fe(cp)_2^+$ is the large number of potential effects, spin-orbit, vibronic and crystal field, that can be operating in the ground and excited states.

MCD and absorption spectra of the $^2E_{1u} \leftarrow {}^2E_{2g}$ transition of $Fe(cp)_2^+$/Ar were collected at various temperatures (1.6–12 K) and magnetic fields (0–5 T) by using a simultaneous MCD/double-beam absorption spectrometer. The absence of band splittings indicated that both CF and SO effects in the excited state were small, this being expected for a state that is predominately ligand in nature. The presence of negative bands (of the opposite sign to the origin) in the $^2E_{1u} \leftarrow {}^2E_{2g}$ MCD spectrum immediately suggested the possibility of a ground-state JT effect. This was confirmed by an analysis that also showed that CF effects were negligible in the ground state. By combining moment analysis and spectral simulations using the program DYNAMO,

the contribution to the orbital reduction parameter from covalent and JT effects could be separated to give $\kappa_{cov} \approx 0.88$ and $\kappa_{JT} \approx 0.82$. The former result gives $|c_d|^2 \approx 0.85$, which is slightly larger than the results previously published, indicating that the e_{2g} orbital has slightly greater metal d character than has been previously believed. Solution spectra of $Fe(cp)_2^+$ obtained at $B = 0.6$ T and between 180 and 280 K indicate ground-state CF effects become significant in this medium. A tentative determination gives a CF splitting of ~250 cm^{-1}. This is still significantly smaller than values previously deduced for glasses at 77 K and suggests the CF is temperature dependent. This could be further elucidated by measurement of the temperature dependence of the ESR spectrum.

Although the model allows for quadratic JT effects, the case studies presented in this thesis have indicated, in line with most of the existing work in this area, that such second-order JT coupling is inconsequential in comparison with first-order coupling or other (SO and CF) effects.

10.1 Note

The early concept for this project was to use the complementary techniques of ESR, MCD and absorption spectroscopy to maximise the amount and the precision of information about matrix-isolated radical species. Although this aim was not achieved, I conducted preliminary work with the existing (single-crystal) ESR instrument to familiarise myself with the experimental and theoretical techniques. That work resulted in the successful characterisation of a low-symmetry defect centre, $Ti^{3+}(Y^{3+})$, in zircon, which was presented at the 1996 conference of the New Zealand Institute of Chemistry and published in *The Journal of Physics: Condensed Matter*[6] in the same year. Perhaps the major achievement of this work was successful computer interfacing of the ESR spectrometer, which has vastly improved the efficiency with which data can be collected and interpreted.

10.2 References

(1) Child, M. S.; Longuet-Higgins, H. C. *Phil. Trans. Roy. Soc.* **1961**, *254*, 259-294.

(2) Longuet-Higgins, H. C.; Opik, U.; Pryce, M. H. L.; Sack, R. A. *Proc. Roy. Soc. A* **1958**, *244*, 1-16.

(3) Opik, U.; Pryce, M. H. L. *Proc. Roy. Soc.* **1957**, *238*, 425-447.

(4) Samet, C.; Rose, J. L.; Piepho, S. B.; Laurito, J.; Andrews, L.; Schatz, P. N. *J. Amer. Chem. Soc.* **1994**, *116*, 11109-11119.

(5) Samet, C.; Rose, J.; Piepho, S. B.; Laurito, J.; Andrews, L.; Schatz, P. N. *J. Amer. Chem. Soc.* **1995**, *117*, 9381.

(6) Claridge, R. F. C.; Taylor, K. C.; Tennant, W. C.; Walsby, C. J. *J.Phys: Condens. Matter* **1996**, *9*, 3075-3080.

A GROUP THEORETICAL RESULTS FOR SO_3

It is useful to consider the group of all rotations, (SO_3), because spin is often dealt with in this point group.

A.1 Irreps of SO_3

Treatment of the point group SO_3 is complicated by the fact that successive rotations about different axes do not necessarily commute and, consequently, not all irreps are 1-dimensional. However, since C_∞ is a subgroup of SO_3, appropriately chosen sets of basis functions that span the irreps of the lower point group will form valid bases for the irreps of SO_3.[1] Determination of the appropriate sets requires consideration of the transformation properties of the basis functions in the lower point group.

Consider an arbitrary n-dimensional vector space spanned by n linearly independent basis vectors $|M_i\rangle$ (i = 1, 2,..., n) which are chosen to transform as the irreps of C_∞ such that

$$I_z|M_i\rangle = M_i|M_i\rangle \tag{A.1}$$

If the largest value of M for a particular basis in SO_3 is J, the transformation properties (M values) of the other members of the basis can be determined using operators $I_\pm$ related to I_x and I_y by

$$I_\pm = I_x \pm iI_y \tag{A.2}$$

The commutation relations pertaining to these operators and I_z are, in quantum units

$$I_zI_\pm - I_\pm I_z = \pm I_\pm \tag{A.3}$$

$$I_+I_- - I_-I_+ = 2I_z \tag{A.4}$$

If $|M\rangle$ transforms as the Mth irrep of C_∞, then $I_\pm|M\rangle$ must belong to the $(M \pm 1)^{th}$ irrep since

$$I_z(I_\pm|M\rangle) = (I_\pm I_z + I_\pm)|M\rangle = (M\pm 1)I_\pm|M\rangle \tag{A.5}$$

In the same manner it can be shown that $(I_\pm)^p|M\rangle$ (p = 1, 2, ...) belongs to the $(M \pm p)$th irrep of $\mathbb{C}_\infty$, with the proviso that

$$I_+|M = J\rangle = 0 \tag{A.6}$$

since J is the highest value of M for that basis. Since $|M\rangle$ and $(I_\pm)^p|M\rangle$ are related by composite operations of SO_3 (as described by the infinitesimal rotation operators in Section 2.2.1) they must transform as partners of a common irrep in that point group.

The vectors $(I_\pm)^p|M\rangle$ are normalised by introducing $\mathfrak{N}_\pm^M$ such that

$$I_\pm|M\rangle = \mathfrak{N}_\pm^M|M\pm 1\rangle \tag{A.7}$$

To determine explicit expressions for these coefficients, a recurrence relation for $\mathfrak{N}_\pm^M$ must be established.[3] This is

$$(\mathfrak{N}_+^M)^2 + 2M = (\mathfrak{N}_+^{M-1})^2 \tag{A.8}$$

However, when $M = J$, equations (A.6) and (A.8) require $\mathfrak{N}_+^J = 0$, whence

$$(\mathfrak{N}_+^{J-1})^2 = 2J \tag{A.9}$$

From this starting point, equations (A.8) and (A.9) can be used to generate all other normalisation coefficients, with the result that

$$(\mathfrak{N}_+^M)^2 = (\mathfrak{N}_-^{M+1})^2 = J(J+1) - M(M\pm 1) \tag{A.10}$$

Thus if $\mathfrak{N}_+^M$ is chosen to be real and positive

$$I_\pm|M\rangle = \sqrt{J(J+1) - M(M\pm 1)}\,|M\pm 1\rangle \tag{A.11}$$

Continued application of I_- leads to the generation of a set of orthonormal eigenfunctions of I_z with $M = J, J\text{-}1, \ldots, -J$. (The lower limit comes about because vectors with $M < -J$ vanish since the coefficients in equation (A.10) become zero when $M = -J$.) The number of allowed M values, and hence the number of basis vectors, is $2J+1$. For this to be an integer, J must be either integral or half-integral.

To emphasis that these vectors transform as the partners M of a common irrep J, it is conventional to denote them as $|J\,M\rangle$. The basis vectors so chosen are said to belong to the point-group chain $SO_3 \supset C_\infty$. In terms of angular momentum, J is the angular momentum quantum number, and M is the magnetic quantum number according equation (A.1).

$$J_z|J\,M\rangle = M\hbar|J\,M\rangle \tag{A.12}$$

$$J_{\pm1}|J\,M\rangle = [J(J+1)\text{-}M(M\pm1)]^{1/2}\hbar|J\,M\pm1\rangle \tag{A.13}$$

Also by expanding $\boldsymbol{J}^2$ in terms of its components, that is $\boldsymbol{J}^2 = J_x^2 + J_y^2 + J_z^2$, and using equations (A.2), (A.12) and (A.13) an expression for the magnitude of the angular momentum

$$\boldsymbol{J}^2|J\,M\rangle = J(J+1)\hbar|J\,M\rangle \tag{A.14}$$

A.2 Direct-Product Irreps

To further illustrate symmetry-angular momentum equivalence it is useful to consider the irreps contained in the direct-product representation formed by products of the type $|J_1\,M_1\rangle|J_2\,M_2\rangle$. Using equations (2.42) and (2.43) the character of the product under $R_z(\phi)$ is

$$\chi_{J_1\otimes J_2}(\phi) = \chi_{J_1}(\phi)\chi_{J_2}(\phi) = \sum_{M_1=-J_1}^{J_1} e^{-iM_1\phi} \sum_{M_2=-J_2}^{J_2} e^{-iM_2\phi} = \sum_{M_1M_2} e^{-i(M_1+M_2)} \tag{A.15}$$

It is not possible to reduce the representation using equation (2.10) because SO_3 is an infinite group ($h = \infty$). However from equation (2.10)

$$\sum_{M_1 M_2} e^{-i(M_1+M_2)\phi} = \sum_{J=0}^{\infty} a_J \sum_{M=-J}^{J} e^{iM\phi} \tag{A.16}$$

and the a_J can be determined by inspection. Since $|M_1+M_2| \leq J_1 + J_2$, then $|M| \leq J_1 + J_2$ and so $J \leq J_1 + J_2$. Hence, for $J > J_1 + J_2$, $a_J = 0$. The maximum value of M can be only be obtained when $M_1 = J_1$ and $M_2 = J_2$, therefore $a_{j_1+j_2} = 1$. The next value of M can be obtained in two ways – when $M_1 = J_1 - 1$ and $M_2 = J_2$, or when $M_1 = J_1$ and $M_2 = J_2 - 1$. However, one of these combinations is already accounted for by $J = J_1+J_2$, so $a_{j_1+j_2-1} = 1$. This argument can be continued down to $J = |J_1 - J_2|$ and so equation (A.16) can be rewritten as

$$\chi_{J_1 \otimes J_2}(\phi) = \sum_{J=|J_1-J_2|}^{J_1+J_2} \sum_{M=-J}^{J} e^{iM\phi} = \sum_{J=|J_1-J_2|}^{J_1+J_2} \chi_{\Gamma}^{(J)}(\phi) \tag{A.17}$$

and the direct product reduces to

$$\Gamma_{J_1} \otimes \Gamma_{J_2} = \Gamma_{J_1+J_2} \oplus \Gamma_{J_1+J_2-1} \oplus \ldots \oplus \Gamma_{|J_1-J_2|} \tag{A.18}$$

which is equivalent to the *Clebsch-Gordan* series rule for the coupling of two angular momenta in the vector model.[1, 2]

A.3 2jms and Some Useful 3jms in $SO_3 \supset C_\infty$

2*jm*s are obtained using the following rule: $\begin{pmatrix} j \\ m \end{pmatrix} = (-1)^{j-m}$. Some useful 3*jm*s are

1/2	1/2	0	
±1/2	∓1/2	0	$1/\sqrt{2}$

1	1/2	1/2	3*jm*
∓1	±1/2	±1/2	$-1/\sqrt{3}$
0	-1/2	1/2	$1/\sqrt{6}$

A.4 Raising and Lowering Operators

Spherical tensors are defined to have identical transformation properties to the $|j\ m\rangle$ of SO_3 in the angular momentum basis ($SO_3 \supset C_\infty$). Spherical (or complex) vectors are the special case of spherical tensors for which $j = 1$.

$$\mathcal{V}_1 \equiv \frac{1}{\sqrt{2}}(\mathcal{V}_x - i\,\mathcal{V}_y) \sim |1\ {-1}\rangle \tag{A.19}$$

$$\mathcal{V}_0 \equiv \mathcal{V}_z \sim |1\ 0\rangle \tag{A.20}$$

$$\mathcal{V}_{+1} \equiv \frac{-1}{\sqrt{2}}(\mathcal{V}_x + i\,\mathcal{V}_y) \sim |1\ 1\rangle \tag{A.21}$$

These are related to the raising and lowering (also referred to as creation and annihilation or step-up and step-down) operators $\mathcal{V}^{\pm}$ by

$$\mathcal{V}_1 = \frac{1}{\sqrt{2}}\mathcal{V}^- \tag{A.22}$$

$$\mathcal{V}_{+1} = \frac{-1}{\sqrt{2}}\mathcal{V}^+ \tag{A.23}$$

A.5 References

(1) Heine, V. *Group Theory in Quantum Mechanics*, 1st ed.; Pergamon Press: London, 1960.

(2) Atkins, P. W.; Friedman, R. S. *Molecular Quantum Mechanics*, 3rd ed.; Oxford University Press Inc.: New York, 1997.

(3) Petrashen, M. I.; Trifonov, E. D. *Applications of Group Theory in Quantum Mechanics*, English ed.; Iliffe Books Ltd: London, 1969.

B COMPLETENESS, CLOSURE AND SPECTROSCOPIC STABILITY

The eigenfunctions g of any Hermitian operator form a complete orthonormal set[1]

$$|f\rangle = \sum_i |g_i\rangle \langle g_i|f\rangle \tag{B.1}$$

$$\langle f| = \sum_i \langle f|g_i\rangle \langle g_i| \tag{B.2}$$

where $\langle f|g_i\rangle$ and $\langle g_i|f\rangle$ are unitary matrices. These equations imply the closure relation, which is

$$\sum_i |g_i\rangle \langle g_i| = 1 \tag{B.3}$$

which in turn leads to the principle of spectroscopic stability.

$$\sum_i \langle l|O_1|f_i\rangle \langle f_i|O_2|n\rangle = \sum_i \langle l|O_1|g_i\rangle \langle g_i|O_2|n\rangle \tag{B.4}$$

Reference

(1) Levine, I. N. *Quantum Chemistry*, 4th ed.; Prentice Hall, New Jersey, 1991.

C GROUP THEORETICAL RESULTS FOR $\mathbf{D}_\infty$

C.1 2jms for $\mathbf{D}_\infty \supset \mathbf{C}_\infty$

Complex conjugation in $\mathbf{D}_\infty$: $a^* = a$, $\alpha^* = -\alpha$.

2*jm*s are obtained using the following rules:

$$\begin{pmatrix} \tilde{0} \\ 0 \end{pmatrix} = -1,$$

$$\begin{pmatrix} a \\ \alpha \end{pmatrix} = (-1)^{a-\alpha},\ a \neq \tilde{0}$$

C.2 3jms for $\mathbf{D}_\infty \supset \mathbf{C}_\infty$ *(a partial list)*

3*jm* are found using the following rules:

$$\begin{pmatrix} a & b & 0 \\ \alpha & \beta & 0 \end{pmatrix} = \delta_{b,a}\,\delta_{\beta,-\alpha}\,|a|^{-\frac{1}{2}} \begin{pmatrix} a \\ \alpha \end{pmatrix}$$

$$\begin{pmatrix} a & a & \tilde{0} \\ a & -a & 0 \end{pmatrix} \frac{1}{\sqrt{2}},\quad a, b \neq 0, \tilde{0}$$

$$\begin{pmatrix} a+b & a & b \\ a+b & -a & -b \end{pmatrix} = \frac{1}{\sqrt{2}}(-)^{2b};\quad a, b \neq 0, \tilde{0}$$

0	0	0	
0	0	0	1

$\tilde{0}$	$\tilde{0}$	0	
0	0	0	-1

1/2	1/2	0	
$\pm 1/2$	$\mp 1/2$	0	$\pm 1/\sqrt{2}$

1/2	1/2	$\tilde{0}$	
$\pm 1/2$	$\mp 1/2$	0	$1/\sqrt{2}$

1	1/2	1/2	
∓1	±1/2	±1/2	$-1/\sqrt{2}$

1	1	0	
±1	∓1	0	$1/\sqrt{2}$

1	1	$\tilde{0}$	
±1	∓1	0	$1/\sqrt{2}$

3/2	1	1/2	-[a]
±3/2	-1	∓1/2	$-1/\sqrt{2}$

3/2	3/2	0	
±3/2	∓3/2	0	$1/\sqrt{2}$

3/2	3/2	$\tilde{0}$	
±3/2	∓3/2	0	$1/\sqrt{2}$

2	1	1	
±2	∓1	∓1	$1/\sqrt{2}$
2	2	0	
±2	∓2	0	$1/\sqrt{2}$

2	3/2	1/2	+
±2	∓3/2	∓1/2	$-1/\sqrt{2}$
2	2	$\tilde{0}$	
±2	∓2	0	$1/\sqrt{2}$

5/2	2	1/2	-
±5/2	∓2	∓1/2	$-1/\sqrt{2}$

3	2	1	+
±3	∓2	∓1	$1/\sqrt{2}$

[a] + and – signs indicate that the 3jm is respectively even and odd under non-cyclic permutation of columns

D GROUP THEORETICAL RESULTS FOR $\mathbb{D}_5$

D.1 $\mathbb{D}_5 \supset \mathbb{C}_5$ *2jms*

$\begin{pmatrix}0\\0\end{pmatrix} = +1 \quad \begin{pmatrix}1/2\\\pm 1/2\end{pmatrix} = \pm 1 \quad \begin{pmatrix}\tilde{0}\\0\end{pmatrix} = -1 \quad \begin{pmatrix}1\\\pm 1\end{pmatrix} = +1 \quad \begin{pmatrix}3/2\\\pm 3/2\end{pmatrix} = \pm 1 \quad \begin{pmatrix}2\\\pm 2\end{pmatrix} = +1 \quad \begin{pmatrix}\pm 5/2\\5/2\end{pmatrix} = \pm 1$

D.2 $\mathbb{D}_5 \supset \mathbb{C}_5$ *3jms*

0	0	0	
0	0	0	1

0	1/2	1/2	
0	±1/2	∓1/2	±1/√2

$\tilde{0}$	$\tilde{0}$	0	
0	0	0	-1

0	1	1	
0	±1	∓1	1/√2

0	3/2	3/2	
0	±3/2	∓3/2	±1/√2

0	2	2	
0	±2	∓2	1/√2

0	5/2	$\tilde{5/2}$	-
0	5/2	5/2	1

1/2	1/2	$\tilde{0}$	
∓1/2	±1/2	0	1/√2

1/2	1/2	1	
∓1/2	∓1/2	±1	1/√2

1/2	1	3/2	$-^{a}$
±1/2	±1	∓3/2	±1/√2

1/2	3/2	2	+
±1/2	±3/2	∓2	1/√2

1/2	2	$\tilde{5/2}$	-
-1/2	-2	5/2	-1/√2

1/2	2	5/2	-
1/2	2	5/2	-1/√2

2	$\tilde{5/2}$	1/2	-
2	5/2	1/2	$-i/\sqrt{2}$

2	5/2	1/2	-
-2	5/2	-1/2	$-i/\sqrt{2}$

$\widetilde{0}$	1	1	
0	± 1	∓ 1	$\pm 1/\sqrt{2}$

$\widetilde{0}$	3/2	3/2	
0	$\pm 3/2$	$\mp 3/2$	$1/\sqrt{2}$

$\widetilde{0}$	2	2	
0	± 2	∓ 2	$\pm 1/\sqrt{2}$

$\widetilde{0}$	5/2	5/2	
0	5/2	5/2	$-i$

$\widetilde{0}$	$5\widetilde{/2}$	$5\widetilde{/2}$	
0	5/2	5/2	$-i$

1	1	2	
± 1	± 1	∓ 2	$-1/\sqrt{2}$

1	3/2	$5\widetilde{/2}$	-
1	3/2	5/2	$i/\sqrt{2}$

1	3/2	5/2	-
-1	-3/2	5/2	$i/\sqrt{2}$

1	3/2	5/2	-
1	3/2	5/2	$1/\sqrt{2}$

1	3/2	$5\widetilde{/2}$	-
-1	-3/2	5/2	$1/\sqrt{2}$

1	2	2	
± 1	± 2	± 2	$1/\sqrt{2}$

3/2	2	3/2	
$\pm 3/2$	± 2	$\pm 3/2$	$-1/\sqrt{2}$

E GROUP THEORETICAL RESULTS FOR D_8

E.1 D8 ⊃ C8 2jms

$\binom{0}{0} = +1 \quad \binom{1/2}{1/2} = +1 \quad \binom{1/2}{-1/2} = -1 \quad \binom{\tilde{0}}{0} = -1 \quad \binom{1}{1} = +1 \quad \binom{1}{-1} = +1 \quad \binom{3/2}{3/2} = +1 \quad \binom{3/2}{-3/2} = -1 \quad \binom{2}{2}$

$= +1 \quad \binom{2}{-2} = +1 \quad \binom{5/2}{5/2} = +1 \quad \binom{5/2}{-5/2} = -1 \quad \binom{3}{3} = +1 \quad \binom{3}{-3} = +1 \quad \binom{7/2}{7/2} = +1 \quad \binom{7/2}{-7/2} = -1 \quad \binom{4}{4} =$

$+1 \quad \binom{\tilde{4}}{4} = -1$

E.2 $\mathbf{D_8 \supset C_8}$ *3jms*

0	0	0	
0	0	0	1

0	1/2	1/2	
0	±1/2	∓1/2	±1/√2

$\tilde{0}$	$\tilde{0}$	0	
0	0	0	-1

0	1	1	
0	±1	∓1	1/√2

0	3/2	3/2	
0	±3/2	∓3/2	±1/√2

0	2	2	
0	±2	∓2	1/√2

0	5/2	5/2	
0	±5/2	∓5/2	±1/√2

0	3	3	
0	±3	∓3	1/√2

0	7/2	7/2	
0	±7/2	∓7/2	±1/√2

0	4	4	
0	4	4	1

0	$\tilde{4}$	$\tilde{4}$	
0	4	4	-1

1/2	1/2	$\widetilde{0}$	
±1/2	∓1/2	0	1/√2

1/2	1/2	1	
±1/2	±1/2	-1	1/√2

1/2	1	3/2	-[a]
±1/2	±1	∓3/2	±1/√2

1/2	3/2	2	+
±1/2	±3/2	∓2	±1/√2

1/2	2	5/2	-
±1/2	±2	∓5/2	±1/√2

1/2	5/2	3	+
±1/2	±5/2	∓3	1/√2

1/2	3	7/2	-
±1/2	±3	∓7/2	±1/√2

1/2	7/2	4	+
±1/2	±7/2	4	+1/√2

1/2	7/2	$\widetilde{4}$	+
±1/2	±7/2	4	±1/√2

$\widetilde{0}$	1	1	
0	±1	∓1	±1/√2

$\widetilde{0}$	3/2	3/2	
0	±3/2	∓3/2	1/√2

$\widetilde{0}$	2	2	
0	±2	∓2	±1/√2

$\widetilde{0}$	5/2	5/2	
0	±5/2	∓5/2	1/√2

$\widetilde{0}$	3	3	
0	±3	∓3	±1/√2

$\widetilde{0}$	7/2	7/2	
0	±7/2	∓7/2	1/√2

$\widetilde{0}$	4	$\widetilde{4}$	-
0	4	4	1

1	1	2	
±1	±1	∓2	-1/√2

1	3/2	5/2	-
±1	±3/2	∓5/2	∓1/√2

1	2	3	+
±1	±2	∓3	-1/√2

1	5/2	7/2	-
±1	±5/2	∓7/2	∓1/√2

1	3	4	+
±1	±3	4	-1/√2

1	3	$\widetilde{4}$	+
±1	±3	4	∓1/√2

1	7/2	7/2	+
±1	±7/2	±7/2	-1/√2

3/2	3/2	3	+
±3/2	±3/2	∓3	1/√2

3/2	2	7/2	-
±3/2	±2	∓7/2	±1/√2

3/2	5/2	4	+
±3/2	±5/2	4	1/√2

3/2	5/2	$\widetilde{4}$	+
±3/2	±5/2	4	±1/√2

3/2	3	7/2	+
±3/2	±3	±7/2	1/√2

2	2	4	
±2	±2	4	-1/√2

2	2	$\widetilde{4}$	
±2	±2	4	∓1/√2

2	5/2	7/2	+
±2	±5/2	±7/2	-1/√2

2	3	3	+
±2	±3	±3	1/√2

5/2	5/2	3	+
±5/2	±5/2	∓3	-1/√2